OVERFLOW
Turbulence Modeling Resource Validation Results

Dennis C. Jespersen
Thomas H. Pulliam
Marissa L. Childs

NASA Ames Research Center
Mail Stop 258-5
Bldg. 258, Rm. 214
P.O. Box 1
Moffett Field, CA 94035-0001

Abstract

We exercise the computational fluid dynamics code OVERFLOW on 16 turbulence model validation cases from the NASA Langley Turbulence Model Resource website. We give some information about the OVERFLOW options used to run these cases, and compare OVERFLOW results with results from other codes and with experiment. The goal is turbulence model validation for OVERFLOW.

Table of Contents

List of Figures

1. Introduction

The purpose of this study is to perform turbulence model validation for OVERFLOW [1] using the NASA Langley Research Center (LaRC) Turbulence Modeling Resource (TMR) test cases [2]. Some of the discussion and text given below is taken directly from the TMR website, which was created and is maintained by Dr. Christopher Rumsey of LaRC and his colleagues. The approach described here uses the TMR-provided cases and grids. For OVERFLOW we made every attempt to apply the same flow conditions and boundary conditions as prescribed on the TMR website, to enable comparison with results from CFL3D [3] and FUN3D [4]. We assess the OVERFLOW implementation of the Spalart-Allmaras (SA) and Menter Shear Stress Transport (SST) turbulence models, with specific versions and modifications detailed below. We used versions 2.2h, 2.2i, and 2.2k of OVERFLOW. While we were doing this work, new versions of OVERFLOW were released and we generally opted to use the latest official release, as we judged that for the TMR validation cases, the differences between these code versions was negligible. The CFL3D and FUN3D results given here are taken directly from the TMR website.

This report relies heavily on the TMR website. We suggest that readers would do well to have the TMR website available in a browser for easy reference.

The specific version of the SA model used in all the OVERFLOW calculations is referred to on the TMR website as the "SA-noft2" model. In this report, whenever we refer to SA calculations with OVERFLOW, we mean the SA-noft2 model.

Validation is defined on the TMR website: "Unlike verification, which seeks to establish that a model has been implemented correctly, validation compares CFD results against data in an effort to establish a model's ability to reproduce physics." In [5] we reported on a turbulence model verification study for Overflow.

To the best of our knowledge, there has been no previous systematic attempt at turbulence model validation for Overflow. We aim to check that results from Overflow agree with experiment and with other codes for a well-defined set of validation cases.

For many of the test cases in this report, a very fine structured grid was given, from which coarser grids were created by deleting every other grid line. Overflow is a node-centered code that uses overlapping structured grids, Cfl3d is a cell-centered code that uses structured grids, and Fun3d is a node-centered unstructured grid code. In some cases the grid for Overflow was constructed by adding additional grid lines for overlapping, but the computational nodes were not varied from those of the grids provided on the TMR website.

2. Specifying Boundary and Initial Conditions

Many of the TMR test cases require specification of quantities such as pressure or total temperature on some boundary surface, and freestream turbulent eddy viscosity or turbulence intensity. Here we will document how these specifications are translated into inputs for OVERFLOW. It is important to note that OVERFLOW refers to both “reference” values and “freestream” values; the former are used for non-dimensionalization, the latter are far-field values. In general, reference values may differ from freestream values, for example, a case with a hovering vehicle might have zero freestream velocity but nonzero reference velocity.

For some of the TMR validation cases, there are boundaries which are to have both the quantities p_t/p_{ref} and T_t/T_{ref} specified. This means a specified ratio of total pressure (also denoted as stagnation pressure) to pressure at reference conditions, and a specified ratio of total temperature (or stagnation temperature) to temperature at reference conditions. This corresponds to OVERFLOW boundary condition type 41, `IBTYP=41`. This boundary condition in OVERFLOW needs two parameters, `BCPAR1` and `BCPAR2`. These quantities are defined by `BCPAR1` $= p_t/p_{t,\infty}$ and `BCPAR2` $= T_t/T_{t,\infty}$ where the ∞ subscript refers to freestream. For the TMR validation cases, terms that are labeled on the TMR website as reference conditions are what OVERFLOW calls freestream conditions.

The problem then is, given ratios $r_1 = p_t/p_{ref}$ and $r_2 = T_t/T_{ref}$, determine the parameters `BCPAR1` and `BCPAR2` for OVERFLOW. To do so, one invokes fluid dynamics theory for a thermally and calorically perfect gas in isentropic flow [6]. For such a fluid, one has the relations

$$p_t/p = \left(1 + \frac{\gamma - 1}{2} M^2\right)^{\gamma/(\gamma-1)}$$

and

$$T_t/T = 1 + \frac{\gamma - 1}{2} M^2,$$

where M denotes Mach number. Thus, the total pressure is determined by the local dynamic pressure and the local Mach number, and the total temperature is determined by the local temperature and Mach number. Then, if we define a quantity F by

$$F = (1 + \frac{\gamma - 1}{2} M^2),$$

we have

$$\begin{aligned} p_t &= pF^{\gamma/(\gamma-1)} \\ T_t &= TF. \end{aligned}$$

In particular, if we evaluate at freestream conditions, then

$$\begin{aligned} p_{t,\infty} &= p_\infty F_\infty^{\gamma/(\gamma-1)} \\ T_{t,\infty} &= T_\infty F_\infty. \end{aligned}$$

Thus the input parameters `BCPAR1` and `BCPAR2` are given by

$$\begin{aligned} \texttt{BCPAR1} &= p_t/p_{t,\infty} \\ &= (p_t/p_{ref}) \cdot (p_{ref}/p_{t,\infty}) \\ &= r_1 \cdot (p/p_t)_\infty \\ &= r_1/F_\infty^{\gamma/(\gamma-1)} \end{aligned}$$

and

$$\begin{aligned} \texttt{BCPAR2} &= T_t/T_{t,\infty} \\ &= (T_t/T_{ref}) \cdot (T_{ref}/T_{t,\infty}) \\ &= r_2 \cdot (T/T_t)_\infty \\ &= r_2/F_\infty. \end{aligned}$$

In summary,

$$\begin{aligned} \texttt{BCPAR1} &= r_1/F_\infty^{(\gamma-1)/\gamma} \\ \texttt{BCPAR2} &= 1/F_\infty. \end{aligned}$$

For example, if the OVERFLOW input parameter `FSMACH`=0.5 and $\gamma = 1.4$, we find that $F = 1.05$. If the case in question specifies $r_1 = 1.1862$ and $r_2 = 1.05$, then `BCPAR1` would be given by

$$\texttt{BCPAR1} = 1.1862/1.05^{1.4/0.4} = 1$$

and `BCPAR2` would be given by

$$\texttt{BCPAR2} = 1.05/1.05 = 1.$$

Or, if the case in question specifies $r_1 = 1.046$ and $r_2 = 1$, then `BCPAR1` would be given by

$$\texttt{BCPAR1} = 1.046/1.05^{1.4/0.4} = 1.046/1.18621 = 0.881807$$

and `BCPAR2` would be given by

$$\texttt{BCPAR2} = 1/1.05 = 0.952381.$$

Another possible boundary condition from the TMR validation cases is to give the ratio of dynamic pressure to reference pressure, p/p_{ref}. For OVERFLOW this is implemented by `IBTYP=33` and the value for `BCPAR1` should be just the given ratio p/p_{ref}.

The SA and SST turbulence models require specification of some freestream quantities for normalization. Both require a value of the ratio of freestream turbulent viscosity to laminar viscosity. For the SST model as implemented in OVERFLOW, this quantity is the input variable `MUTINF`, i.e., `MUTINF`=$(\mu_t/\mu)_\infty$. For the SA model in OVERFLOW, μ_t is computed as $\rho\tilde{\nu}f_1$, where $f_1 = \chi^3/(\chi^3 + 7.1^3)$, with $\chi = \tilde{\nu}/\nu$. The SA field variable is $\tilde{\nu}$. Freestream values are $\rho = 1$ and $\nu = 1$, so `MUTINF` is given by

$$\texttt{MUTINF} = \tilde{\nu}_\infty^4/(\tilde{\nu}_\infty^3 + 7.1^3),$$

which gives, for example, `MUTINF` = 0.210438 if $\tilde{\nu}_\infty = 3$ and `MUTINF` = 1.294234 if $\tilde{\nu}_\infty = 5$.

For the two-equation SST model, OVERFLOW also asks for a value `XKINF`, the freestream turbulent kinetic energy normalized by reference velocity, k_∞/V_{ref}^2. Again we are assuming that freestream and reference conditions are the same. To translate from a given freestream turbulence intensity percentage `FSTI` to `XKINF`, we assume that the far-field turbulent velocity fluctuations u'_∞, v'_∞, and w'_∞ satisfy

$$u'_\infty = v'_\infty = w'_\infty,$$

and far-field turbulent kinetic energy k_∞ is given by

$$k^2_\infty = \left((u'_\infty)^2 + (v'_\infty)^2 + (w'_\infty)^2\right)/2 = 3(u'_\infty)^2/2,$$

so

$$\texttt{XKINF} = 1.5 \cdot (\texttt{FSTI}/100)^2.$$

For example, a freestream turbulence intensity of 0.088% results in

$$\texttt{XKINF} = 1.16 \cdot 10^{-6}.$$

If the freestream and reference conditions are not the same, then `XKINF` is given by

$$\texttt{XKINF} = 1.5 \cdot \left((\texttt{FSTI}/100) \cdot (\texttt{FSMACH}/\texttt{REFMACH})\right)^2.$$

3. Extracting the Turbulent Shear Stress

Many of the validation cases involve comparison with experimental values of turbulent shear stress $\overline{u_i' u_j'}$. As pointed out at the TMR website, for low-speed flows one has

$$\overline{u_i' u_j'} \approx -\tau_{ij}/\overline{\rho},$$

where τ_{ij} is defined as $-\overline{\rho u_i'' u_j''}$ (see the TMR website for further information). If the Boussinesq relation

$$\tau_{ij} = 2\hat{\mu}_t \left(\hat{S}_{ij} - \frac{1}{3} \frac{\partial \hat{u}_k}{\partial x_k} \delta_{ij} \right) - \frac{2}{3} \overline{\rho} k \delta_{ij}$$

is assumed, where $\hat{S}_{ij} = (\partial \hat{u}_i / \partial x + \partial \hat{u}_j / \partial x_k)/2$ is the strain tensor and $\hat{\mu}_t$ is the eddy viscosity from the turbulence model, then $\overline{u'v'}$ is approximately given by

$$\overline{u'v'} \approx -\frac{\hat{\mu}_t}{\overline{\rho}} \left(\frac{\partial \hat{u}}{\partial y} + \frac{\partial \hat{v}}{\partial x} \right) = -2 \frac{\hat{\mu}_t}{\overline{\rho}} \hat{S}_{12}.$$

Overflow computes the strain tensor as part of its turbulence model computation, so the turbulent shear stress $\overline{u'v'}$ can be obtained by capturing the strain tensor and multiplying by $-2\hat{\mu}_t/\overline{\rho}$. If it is given the input parameter `DEBUG`=1, Overflow will compute and write some turbulence quantities of interest. We modified Overflow to include $\hat{S}_{12}$ multiplied by $-2\hat{\mu}_t/\overline{\rho}$. as one quantity to write if `DEBUG=1`.

Further scaling is necessary, since the nondimensionalization used by Overflow results in multiplying the viscous terms of the momentum equation by Re/M_{ref}, where M_{ref} is a reference Mach number, denoted `REFMACH` in an Overflow input file, and Re is the Reynolds number. So the output from Overflow needs to be divided by Re/M_{ref}.

To compare these quantities with experimental results, yet another scaling may be necessary. If the experimental values of $\overline{u'v'}$ are presented as scaled by some reference velocity V_{ref}, then (since OVERFLOW scales velocities by a reference sound speed a_∞) we have for any velocity V^* from OVERFLOW,

$$V^* = V/a_\infty = (V/U_{ref}) \cdot (U_{ref}/a_\infty) = (V/U_{ref}) \cdot M_{ref}$$

and so OVERFLOW velocities must be divided by M_{ref} to get quantities directly comparable to experimental values. Since the shear stress is quadratic in velocity, OVERFLOW numbers need to be divided by M_{ref}^2. Summarizing, output from OVERFLOW needs to be divided by $(Re/M_{ref}) \cdot M_{ref}^2 = Re \cdot M_{ref}$.

4. 2D Zero Pressure Gradient Flat Plate

In this section we present turbulence model validation for Overflow using the LaRC Turbulence Modeling Resource (TMR) 2D Zero Pressure Gradient Flat Plate validation case. This case has $M = 0.2$, and Reynolds number $Re = 5,000,000$ based on a unit length of 1. This geometry and flow conditions are the same as for the TMR flat plate verification case, but different quantities are of interest. Here the quantities of interest are skin friction coefficient vs. Re_θ for $4000 < \mathrm{Re}_\theta < 13000$ and u^+ vs. y^+ at $\mathrm{Re}_\theta = 10000$. Re_θ is defined on the TMR website; for convenience we repeat the definition here. Freestream quantities are denoted by a subscript ∞. Define θ by

$$\theta = \int_0^\infty \frac{\rho}{\rho_\infty} \frac{u}{U_\infty} \left(1 - \frac{u}{U_\infty}\right) \, dy,$$

then Re_θ is defined by

$$\mathrm{Re}_\theta = \rho_\infty U_\infty \theta / \mu_\infty.$$

When numerically computing the integral that defines θ, it is important to have the upper limit of the integral near the edge of the boundary layer and *not* the full extent of the grid. This is because a quadrature scheme that uses the entire grid can produce a significant contribution from the part of the flow that is nominally freestream. In our work we defined the upper limit of integration as the smallest value of y for which u is 99.5% of its freestream value.

The Overflow input files prescribed central differencing with low-Mach preconditioning [13]. The coefficient of second-order dissipation, `DIS2`, was set to 0. The boundary condition type at inflow was `IBTYP=47` with parameters `BCPAR1=BCPAR2=1`, and the boundary condition at outflow was `IBTYP=31` with parameter `BCPAR1=1`. For each of the SA, SST, and SST-V models, both the flow and turbulence model residuals were reduced from their initial values by at least 13 orders of magnitude in about 10,000 time steps.

For the SA, SST, and SST-V models, Figure 4.1 shows Overflow and Cfl3d skin friction coefficient vs. Re_θ along with the theoretical Karman-Schoenherr (K-S) relation. For each of the three turbulence models, the Overflow and Cfl3d results plot atop one another.

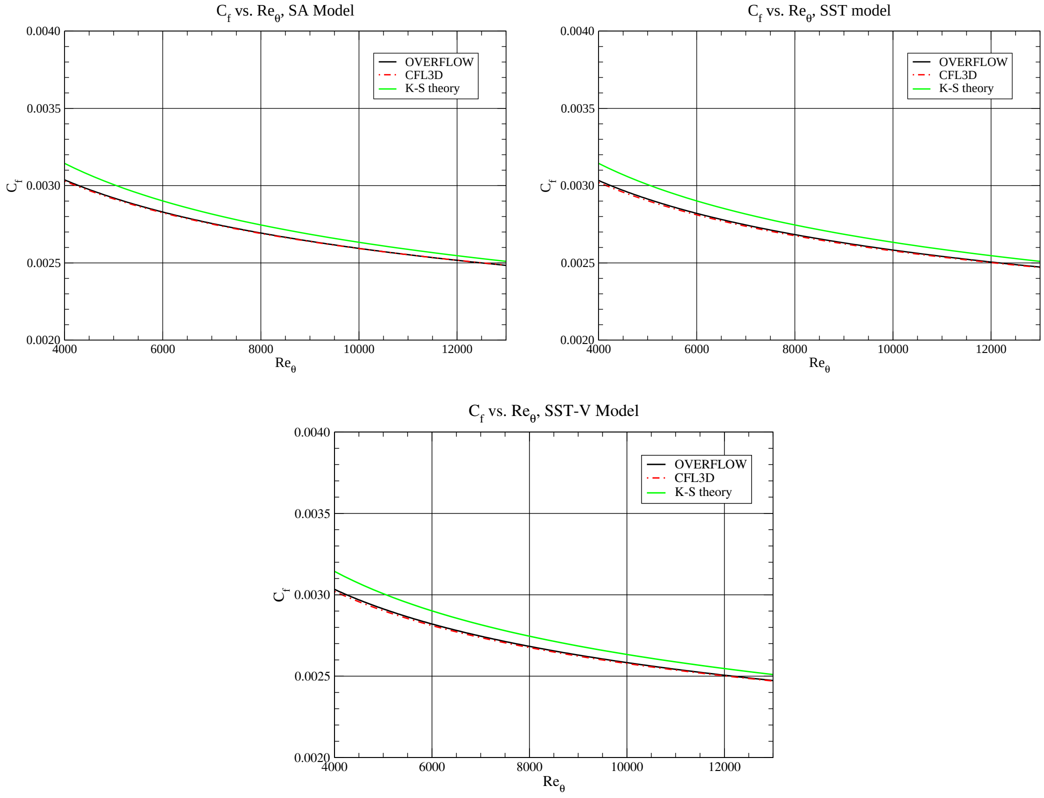

Figure 4.1: Skin friction coefficient, SA, SST, SST-V models.

The next set of plots shows u^+ vs. $\log_{10}(y^+)$ for the three turbulence models. Each plot shows computed results from Overflow and Cfl3d along with an analytical result based on Coles' mean velocity profile [7], [8]. In each case the Overflow and Cfl3d results plot atop one another.

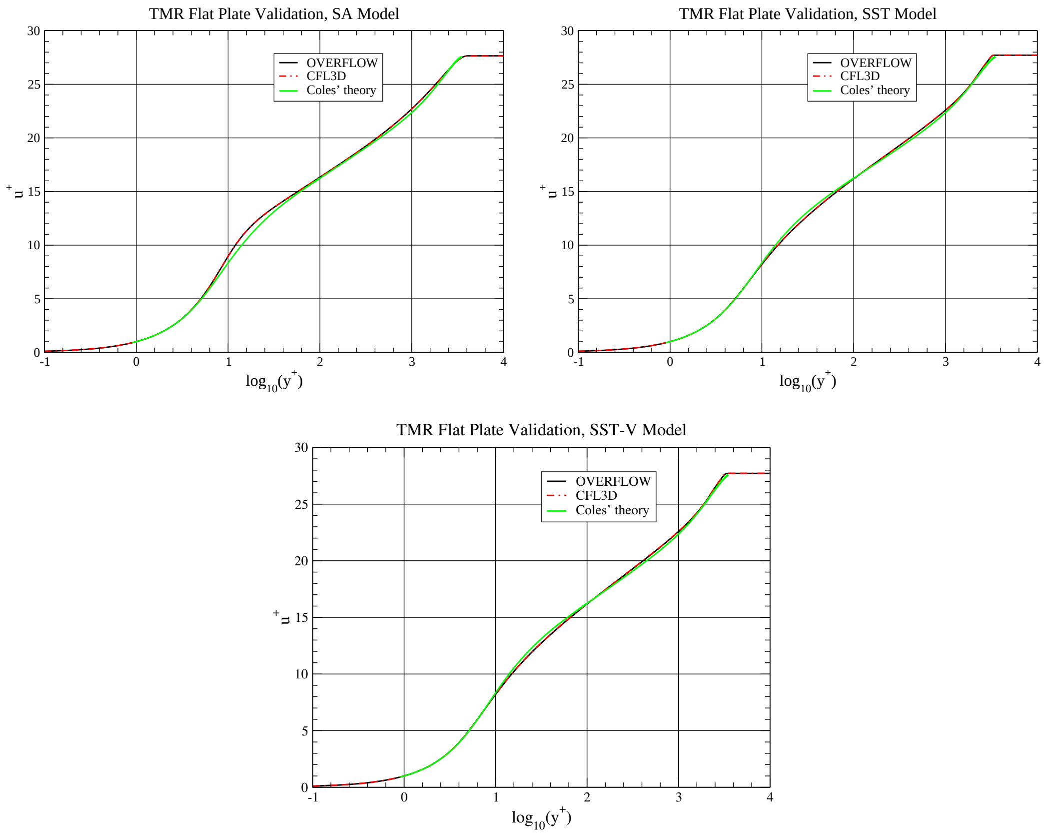

Figure 4.2: u^+ vs. $\log_{10}(y^+)$, SA, SST, and SST-V models.

5. 2D Mixing Layer

In this section we present turbulence model validation for OVERFLOW using the LaRC Turbulence Modeling Resource (TMR) 2D Mixing Layer validation case. This case has $M = 0.121108$ and Reynolds number $Re = 2900$. The geometry and flow conditions are shown in Figure 5.1, taken from the TMR website.

The grid system provided for this case is indicated in Figure 5.2. To prepare grids for OVERFLOW, overlap points were added to the region where zones 2 and 3 meet zone 1. No special preprocessing to define interzone interpolation was needed, as OVERFLOW can determine how information is to be transferred between zones.

Also, as a convenience, data surface grids (line segments in this case) at $x = 1$, 50, 200, 650, and 950 were adjoined. When a zone has at least one of its extents equal to 1, OVERFLOW treats that zone as a data surface and does not compute on the zone but does interpolate flow variable data to the grid points of that zone; thus no special postprocessing capability is needed to extract data values.

For OVERFLOW, boundary condition `IBTYP`=41 (nozzle inflow with fixed total pressure and total temperature, and one Riemann invariant extrapolated from the interior) was used for inflow and `IBTYP`=33 (fixed pressure, other quantities extrapolated from the interior) was used at outflow. The input parameters for these boundary conditions, which involve total pressure, total temperature, and static pressure, were determined as noted in Section 2. We used Roe spatial differencing, two multigrid levels, and the scalar pentadiagonal option for the implicit time-stepping. The flow residuals were converged to, or almost to, machine zero and the turbulence model residuals were decreased at least 10 orders of magnitude from their maximum values.

The turbulent shear stress $\overline{u'v'}$ is given by a slightly modified version of

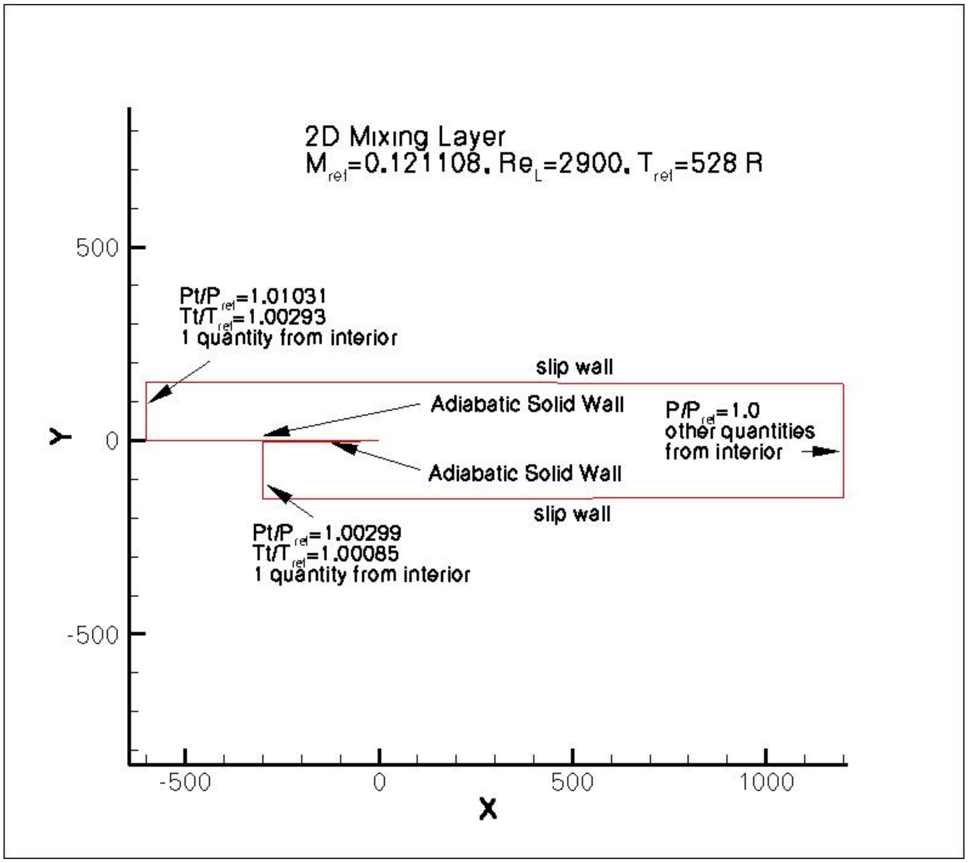

Figure 5.1: Mixing layer geometry.

OVERFLOW using the input parameter `DEBUG`=1, as noted in Section 3 above.

The first set of figures (5.3–5.5) shows OVERFLOW results with the SA model, compared with results from CFL3D and from experiment. Both the OVERFLOW and the CFL3D results are from the second-finest grid system. The OVERFLOW and CFL3D results plot atop one another.

The next set of figures (5.6–5.8) shows OVERFLOW results with the SST model compared with results from CFL3D and from experiment. As with the SA model, the OVERFLOW and CFL3D results plot atop one another.

The final set of figures (5.9–5.11) shows OVERFLOW results with the SST-V model, compared with results from CFL3D and from experiment. As with the other models, the OVERFLOW and CFL3D results plot atop one another.

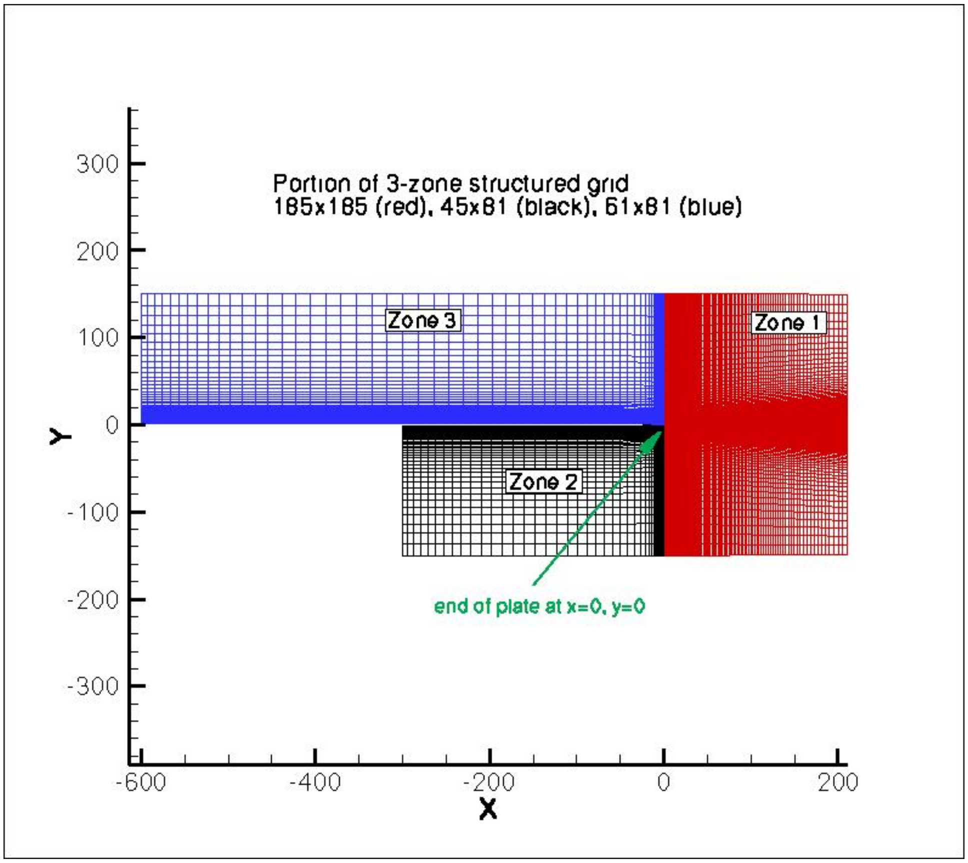

Figure 5.2: Mixing layer grid system.

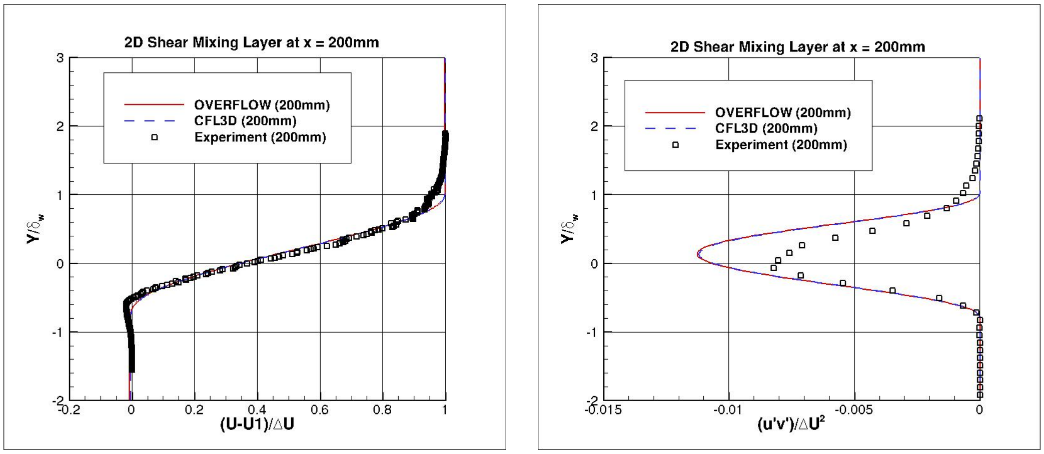

Figure 5.3: SA model at $x = 200$ mm.

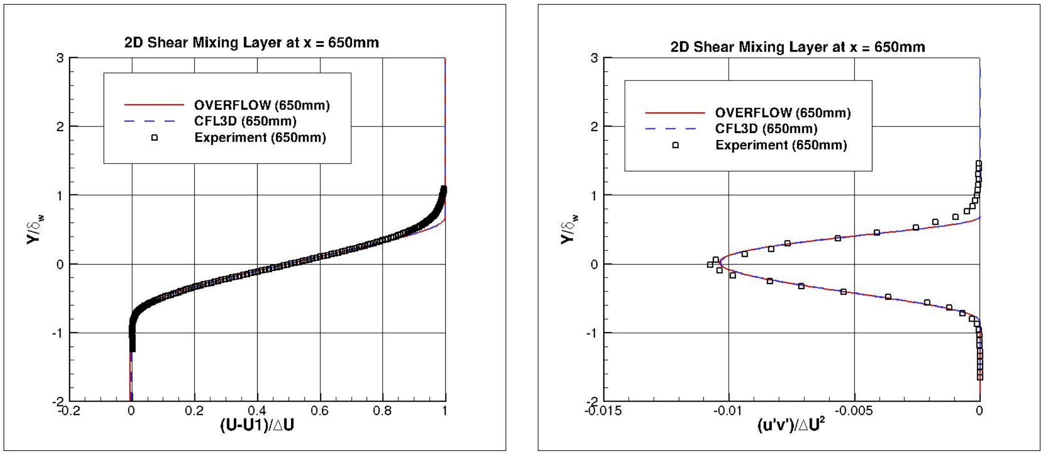

Figure 5.4: SA model at $x = 650$ mm.

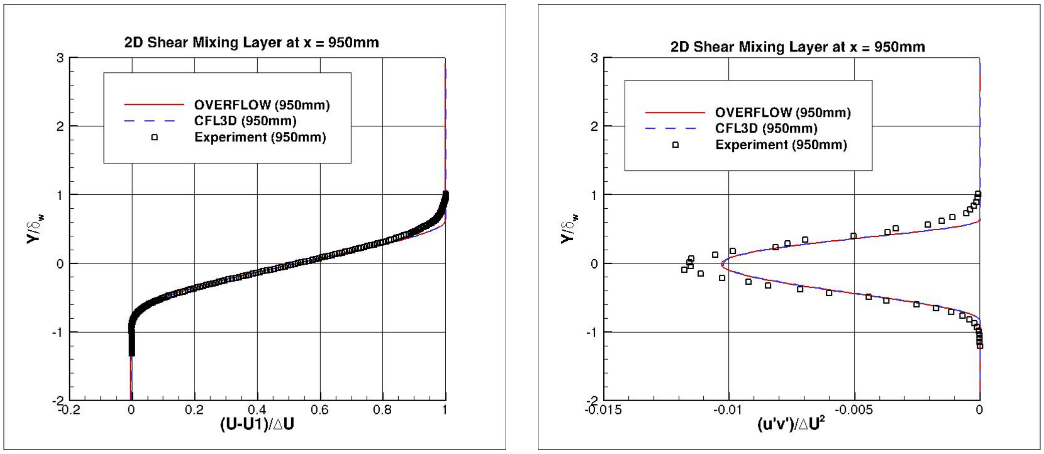

Figure 5.5: SA model at $x = 950$ mm.

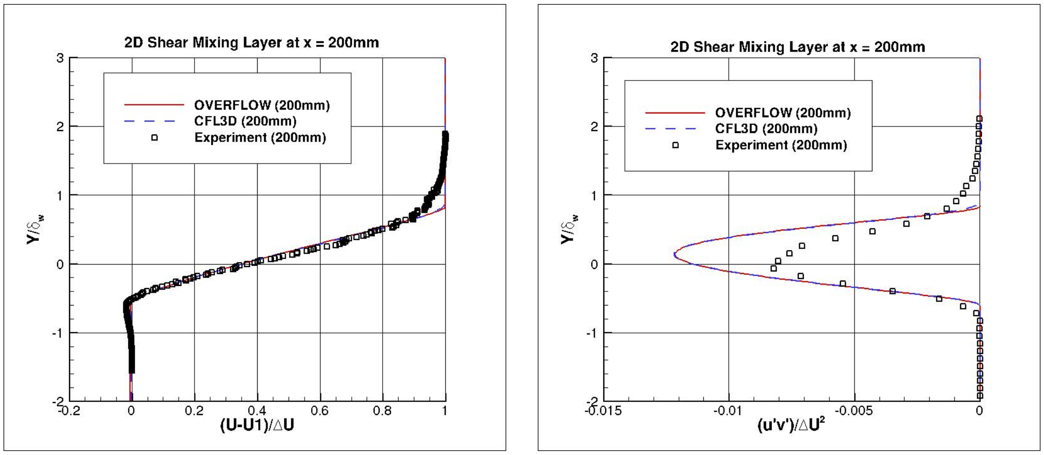

Figure 5.6: SST model at $x = 200$ mm.

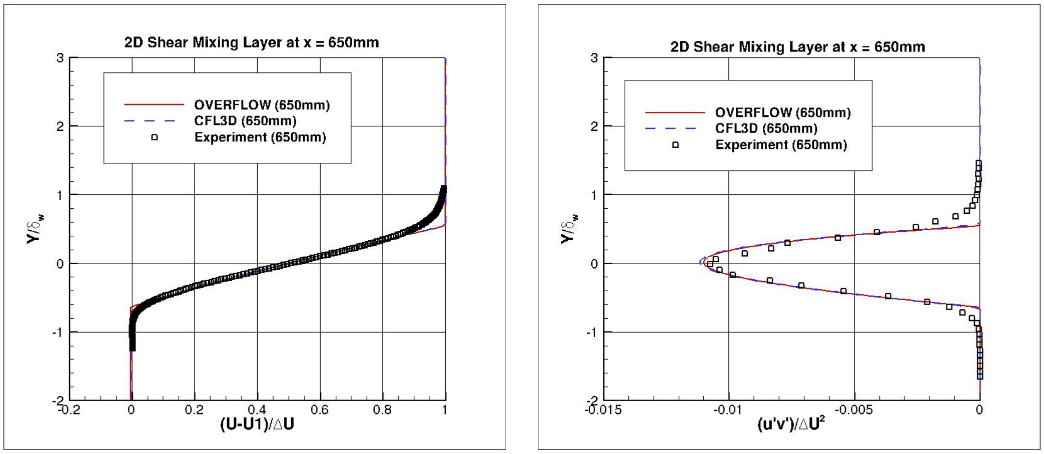

Figure 5.7: SST model at $x = 650$ mm.

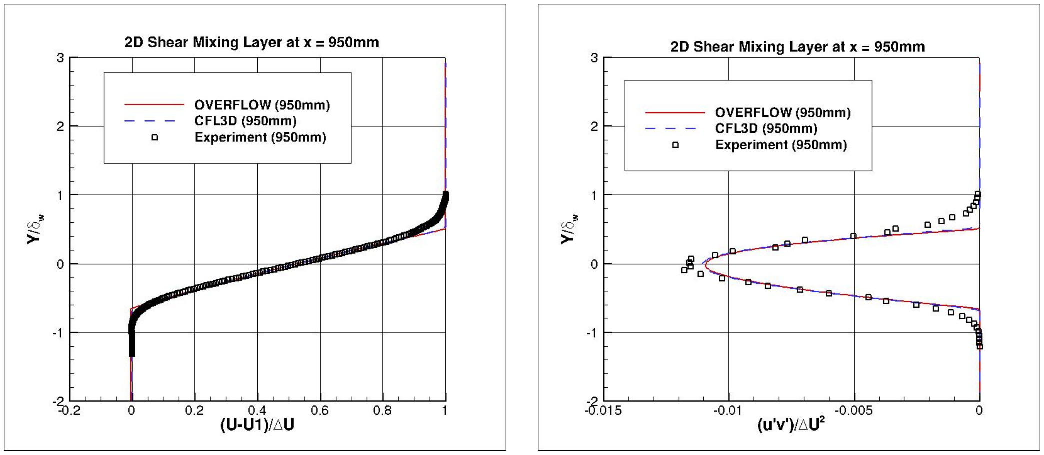

Figure 5.8: SST model at $x = 950$ mm.

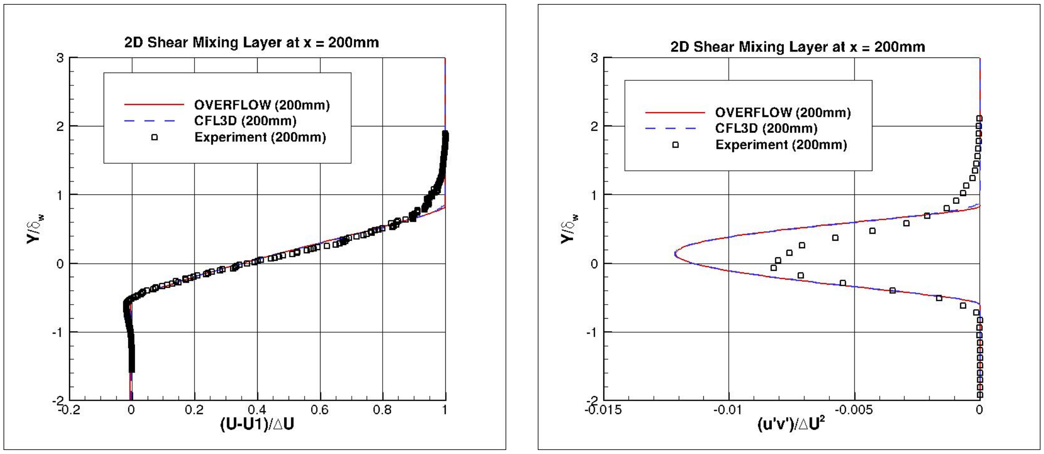

Figure 5.9: SST-V model at $x = 200$ mm.

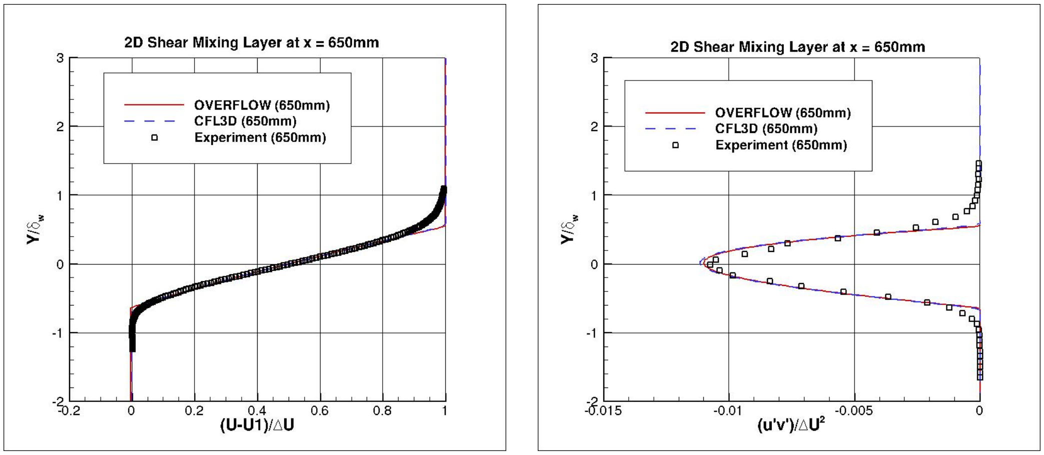

Figure 5.10: SST-V model at $x = 650$ mm.

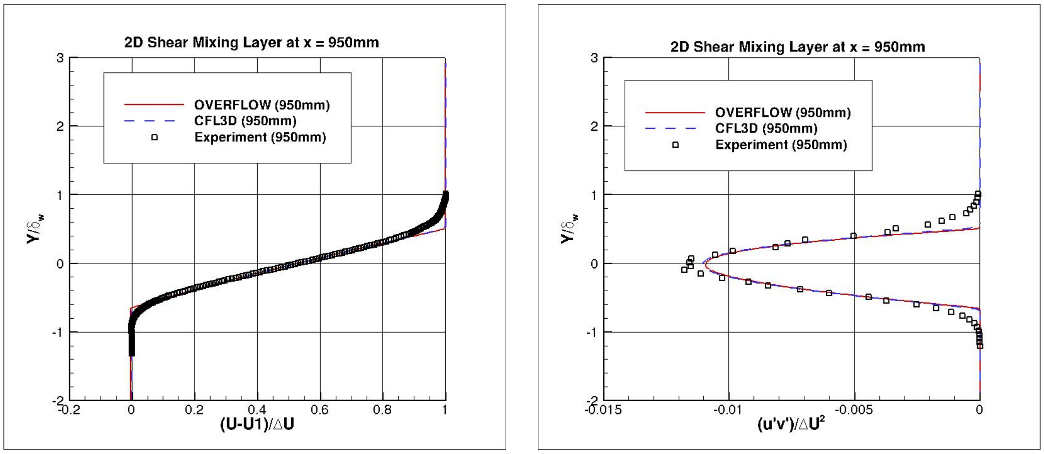

Figure 5.11: SST-V model at $x = 950$ mm.

6. 2D Airfoil Near-Wake

In this section we present turbulence model validation for Overflow using the LaRC Turbulence Modeling Resource (TMR) 2D Airfoil Near-Wake validation case. This case has Mach number $M = 0.088$ and Reynolds number $Re = 2,000,000$ based on a chord length of 1. The geometry and flow conditions are shown in Figure 6.1, taken from the TMR website. The grid system provided for this case is indicated in Figure 6.2.

To prepare the grid for use with Overflow, data surface grids (line segments in this case) at x = 1.01, 1.05, 1.20, 1.40, 1.80, and 2.19 were adjoined. Each line segment consisted of 121 equally-spaced points between −0.06 and 0.06. As mentioned in Section 5, Overflow does not compute on the data surface grids but instead interpolates flow variable data to the grid points of those zones so that no special postprocessing capability is needed to extract data values.

The Overflow input files prescribed central differencing with low-Mach preconditioning and matrix dissipation. The second-order dissipation coefficient `DIS2` was set to 0 and the fourth-order dissipation coefficient `DIS4` was set to 0.01. The code was run until the L_2 residuals of the flow equations were decreased to machine roundoff level.

The first set of plots, figures 6.3–6.5, shows velocity profiles in the wake from experiment and for Overflow and Cfl3d with the SA model. The Overflow and Cfl3d data are from the second-finest grid and the Overflow and Cfl3d results are in very close agreement. With the SA model on this grid, the lift and drag coefficients are $C_L = 0.1606$ and $C_D = 0.01011$ for Cfl3d, $C_L = 0.1589$ and $C_D = 0.01014$ for Fun3d, and $C_L = 0.1567$ and $C_D = 0.01021$ for Overflow. We also ran Overflow on the finest grid and got lift and drag coefficients of $C_L = 0.1569$ and $C_D = 0.01020$.

The second set of plots, figures 6.6–6.8, shows turbulent shear stresses in the wake from experiment and for Overflow and Cfl3d with the SA

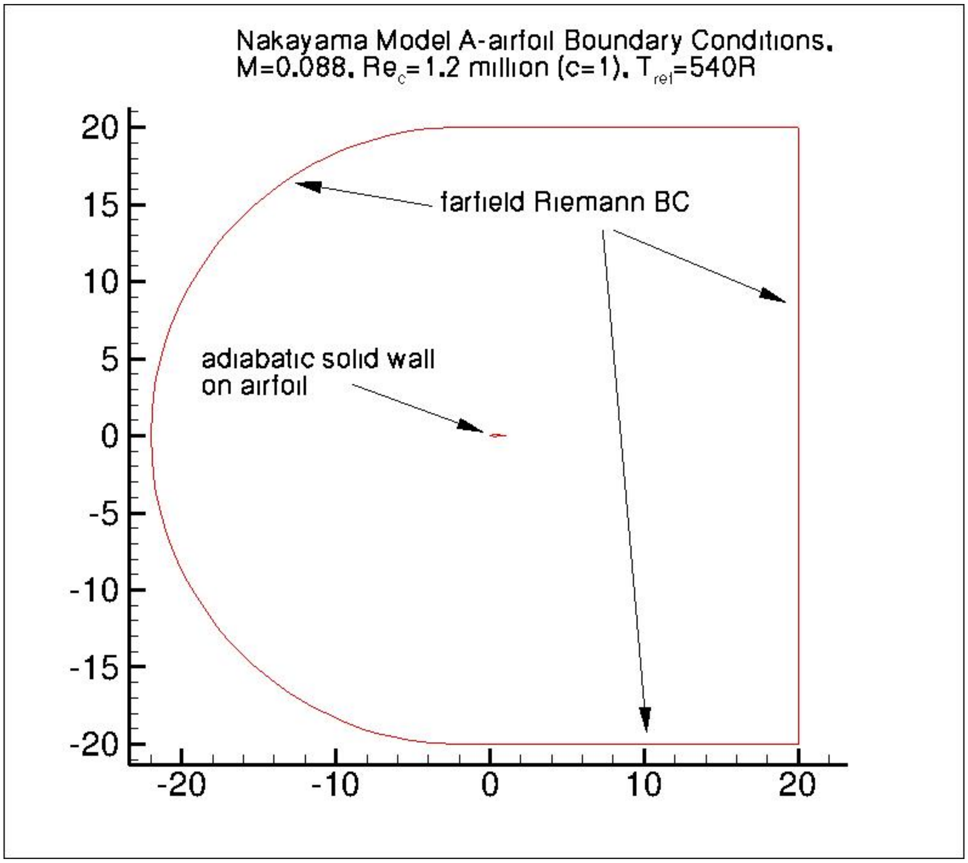

Figure 6.1: Airfoil wake geometry.

model. Again the Overflow and Cfl3d results agree closely.

The next set of plots, figures 6.9–6.11, shows velocity profiles in the wake from experiment and for Overflow and Cfl3d with the SST model, and the Overflow and Cfl3d results are in very close agreement. With the SST model, the lift and drag coefficients are $C_L = 0.1574$ and $C_D = 0.01011$ for Cfl3d, $C_L = 0.1556$ and $C_D = 0.01015$ for Fun3d, and $C_L = 0.1535$ and $C_D = 0.01018$ for Overflow. For Overflow on the finest grid, the lift and drag coefficients were found to be $C_L = 0.1536$ and $C_D = 0.01020$.

The final set of plots, figures 6.12–6.14, shows turbulent shear stress profiles in the wake from experiment and for Overflow and Cfl3d with the SST model. Again Overflow and Cfl3d are in very close agreement.

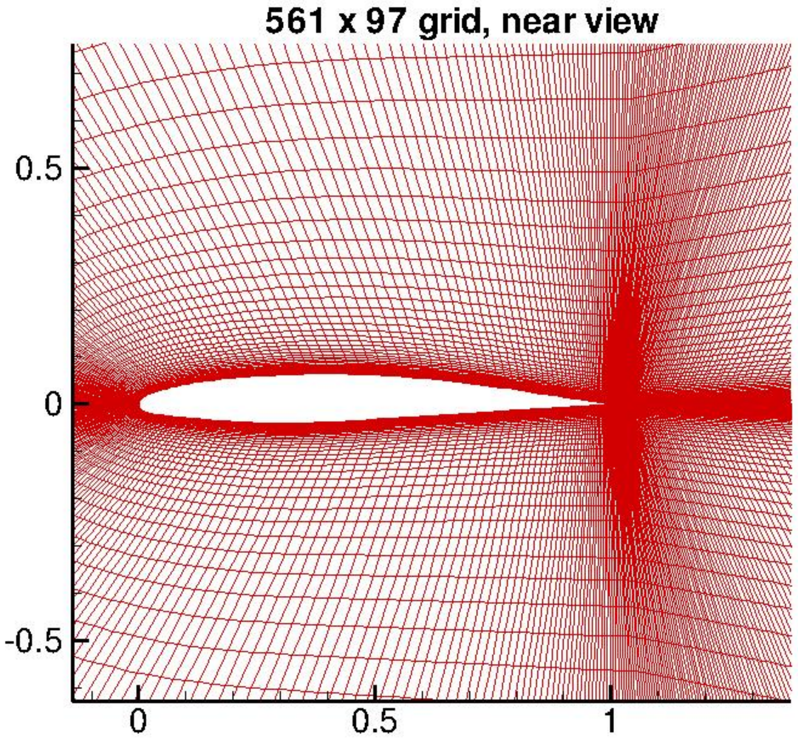

Figure 6.2: Airfoil wake geometry, near view.

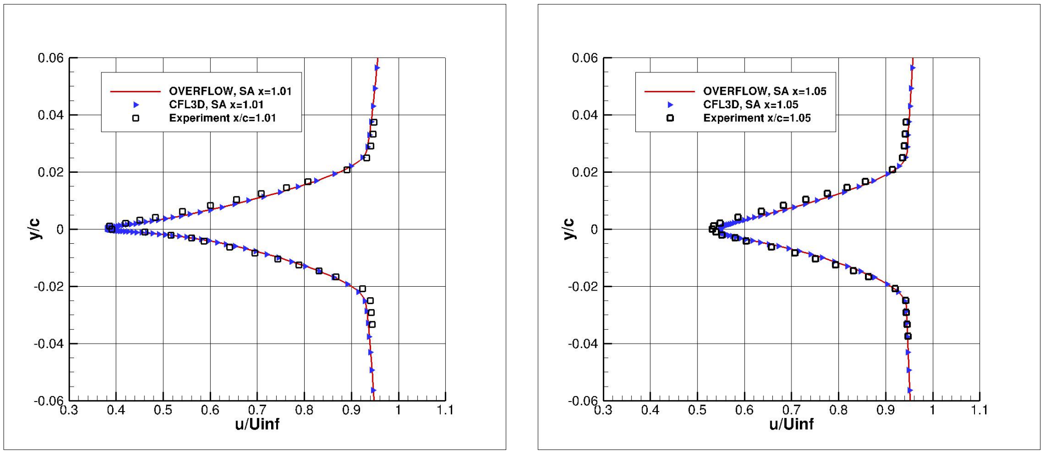

Figure 6.3: Velocity profiles, SA model, $x = 1.01$ and $x = 1.05$.

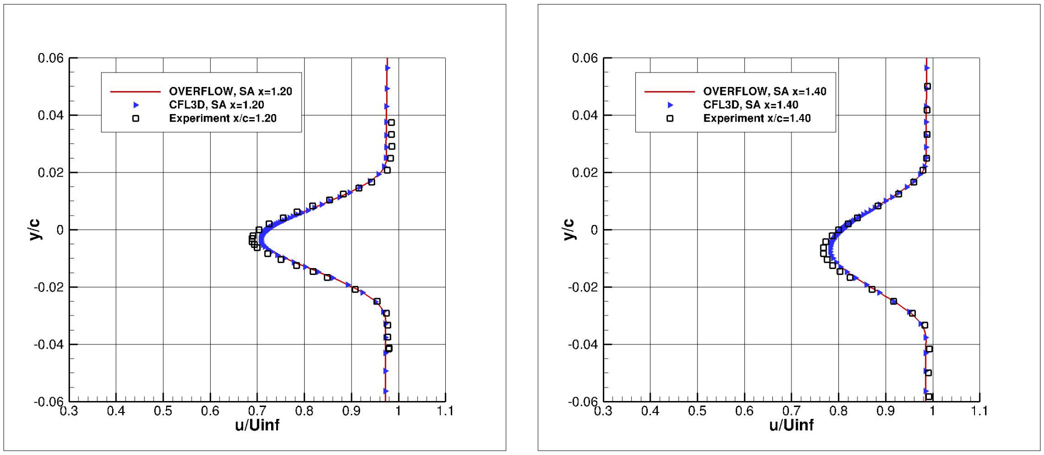

Figure 6.4: Velocity profiles, SA model, $x = 1.20$ and $x = 1.40$.

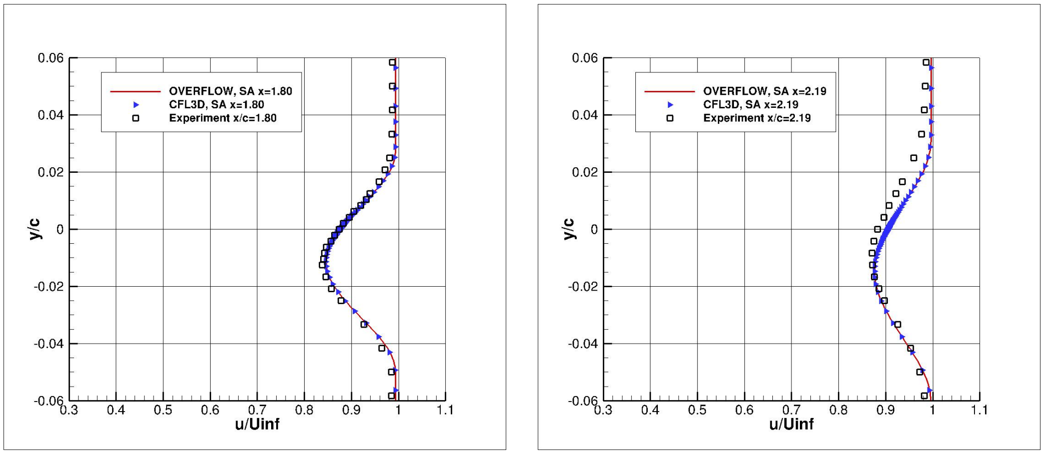

Figure 6.5: Velocity profiles, SA model, $x = 1.80$ and $x = 2.19$.

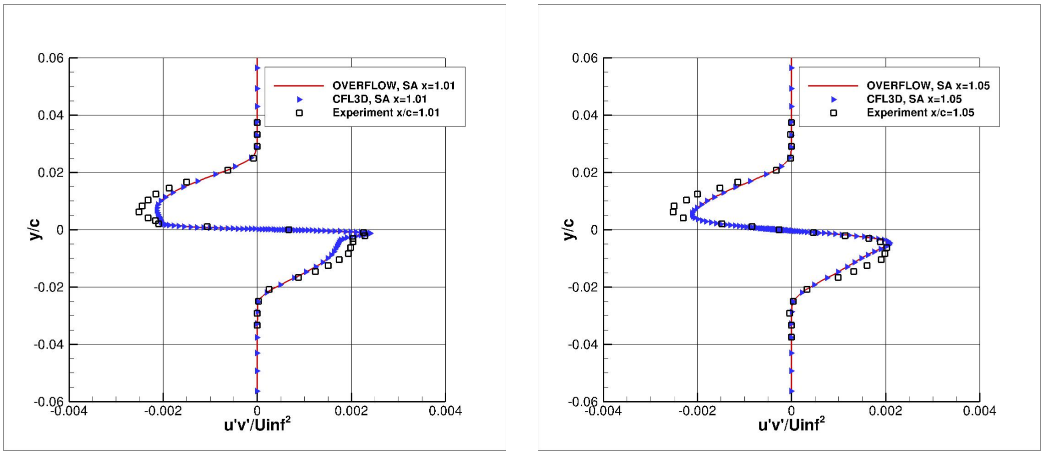

Figure 6.6: Turbulent shear stress profiles, SA model, $x = 1.01, 1.05$.

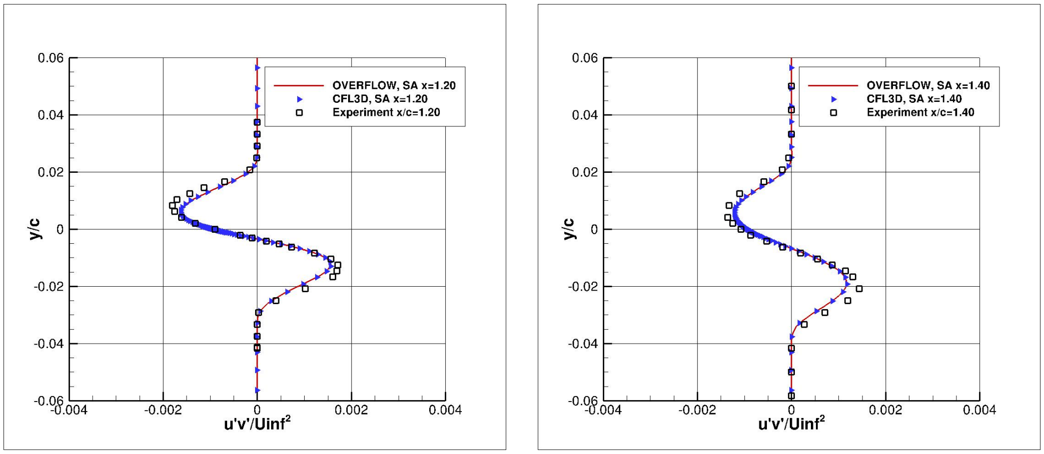

Figure 6.7: Turbulent shear stress profiles, SA model, $x = 1.20, 1.40$.

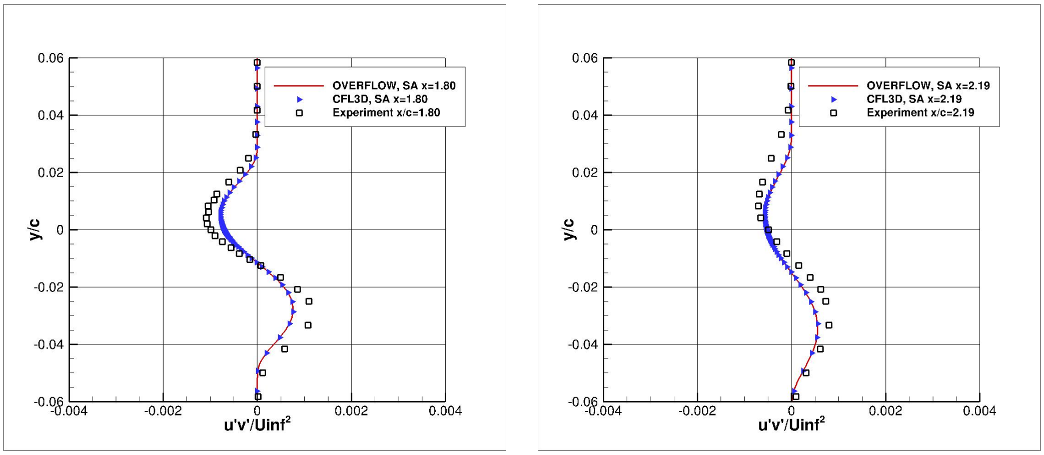

Figure 6.8: Turbulent shear stress profiles, SA model, $x = 1.80, 2.19$.

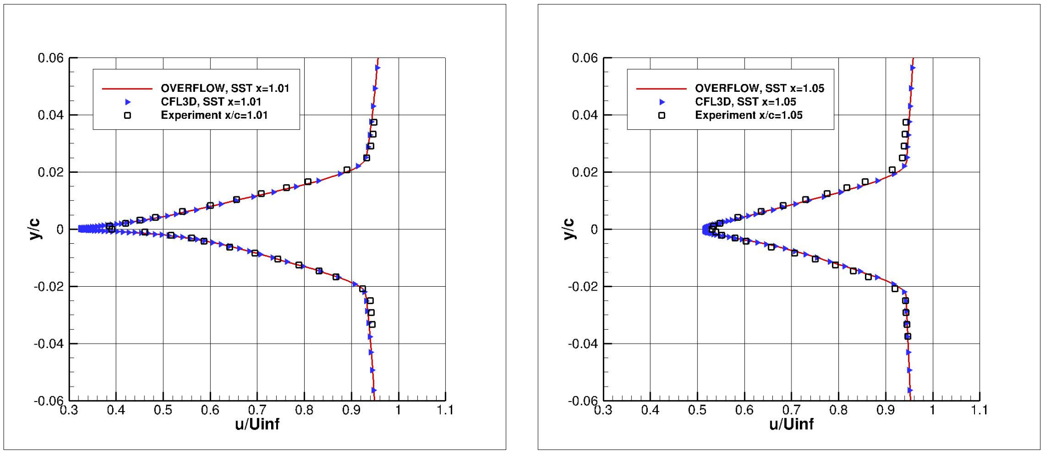

Figure 6.9: Velocity profiles, SST model, $x = 1.01$ and $x = 1.05$.

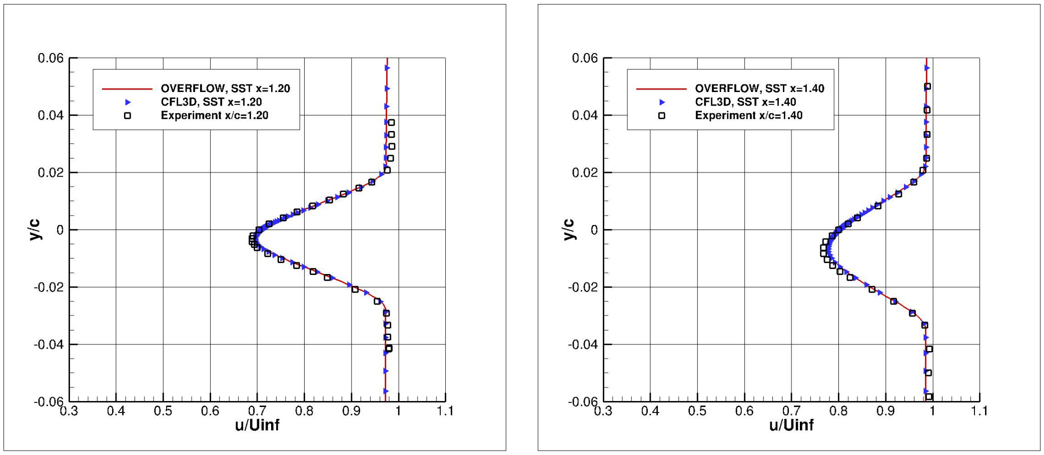

Figure 6.10: Velocity profiles, SST model, $x = 1.20$ and $x = 1.40$.

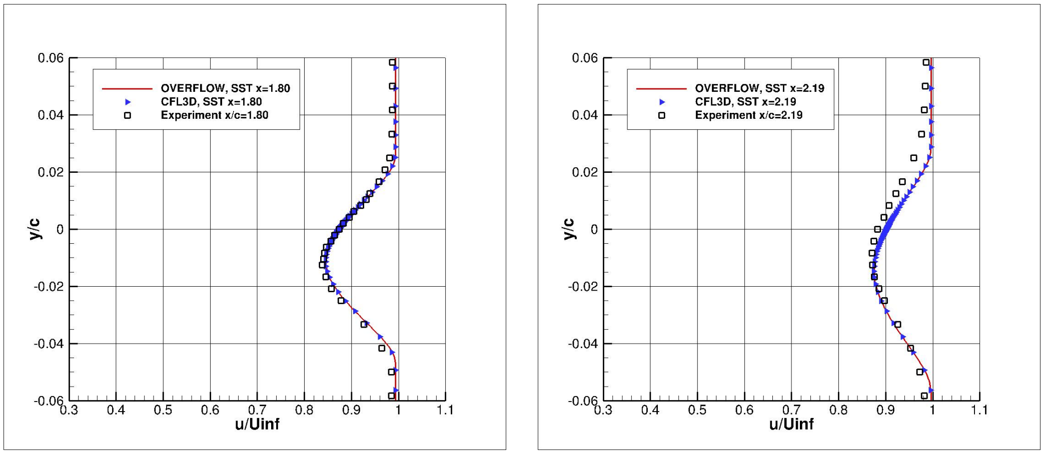

Figure 6.11: Velocity profiles, SST model, $x = 1.80$ and $x = 2.19$.

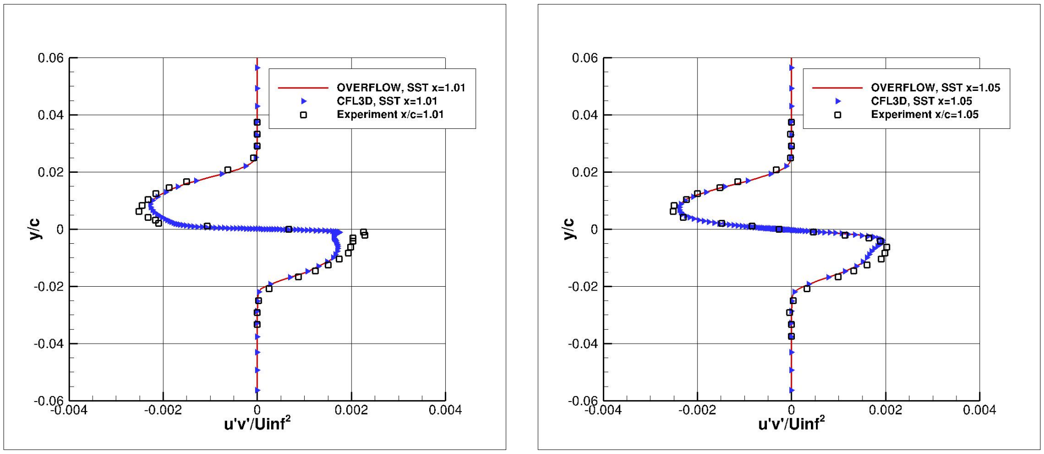

Figure 6.12: Turbulent shear stress profiles, SST model, $x = 1.01$ and $x = 1.05$.

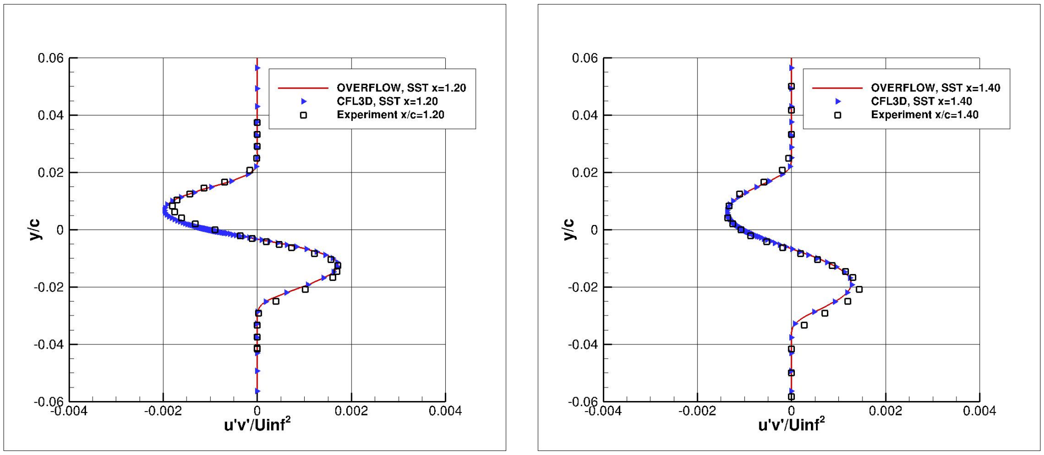

Figure 6.13: Turbulent shear stress profiles, SST model, $x = 1.20$ and $x = 1.40$.

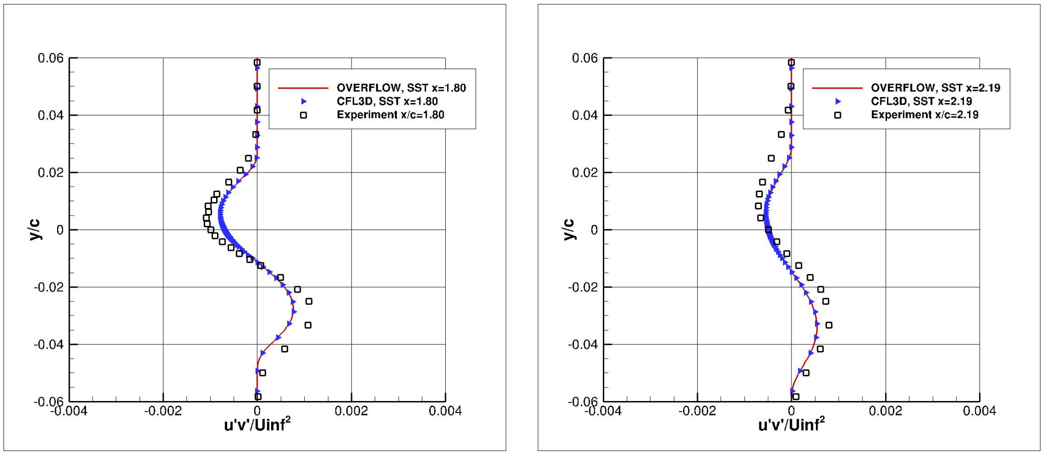

Figure 6.14: Turbulent shear stress profiles, SST model, $x = 1.80$ and $x = 2.19$.

7. NACA0012 Airfoil

In this section we present turbulence model validation for OVERFLOW using the LaRC Turbulence Modeling Resource (TMR) NACA0012 Airfoil validation case. This case has Mach number $M = 0.15$ and Reynolds number $Re = 6,000,000$ based on a chord of 1. The geometry and flow conditions are shown in Figure 7.1, taken from the TMR website. A close-up view of the grid system provided for this case is indicated in Figure 7.2. For the flow equations, the OVERFLOW calculations used third-order Roe differencing on the right-hand side and the scalar pentadiagonal solver on the left-hand side.

The first plots, Figure 7, are for calculations with the Spalart-Allmaras model on the second-finest (897 × 257) grid. OVERFLOW was run for three angles of attack, $\alpha = 0°$, $\alpha = 10°$, and $\alpha = 15°$. The figure shows lift coefficient as a function of angle of attack and also shows a drag polar. The OVERFLOW and CFL3D results are in close agreement.

The numerical values of lift and drag are given in Table 7.1, where we have adjoined data from OVERFLOW to data from the TMR website.

Figure 7 shows pressure coefficient C_p over the airfoil surface and skin friction coefficient C_f over the upper surface of the airfoil for the three angles of attack. The OVERFLOW and CFL3D results are very close to one another.

The next plots, Figure 7.5 are for calculations with the SST model on the second-finest (897 × 257) grid. OVERFLOW was run for three angles of attack, $\alpha = 0°$, $\alpha = 10°$, and $\alpha = 15°$. The figure shows lift coefficient as a function of angle of attack and also shows a drag polar. The OVERFLOW and CFL3D results are in close agreement.

The numerical values of lift and drag are given in Table 7.2, where we have adjoined data from OVERFLOW to data from the TMR website.

Figure 7.6 shows pressure coefficient C_p over the airfoil surface and skin friction coefficient C_f over the upper surface of the airfoil for the three angles of attack. The OVERFLOW and CFL3D results are very close to one another.

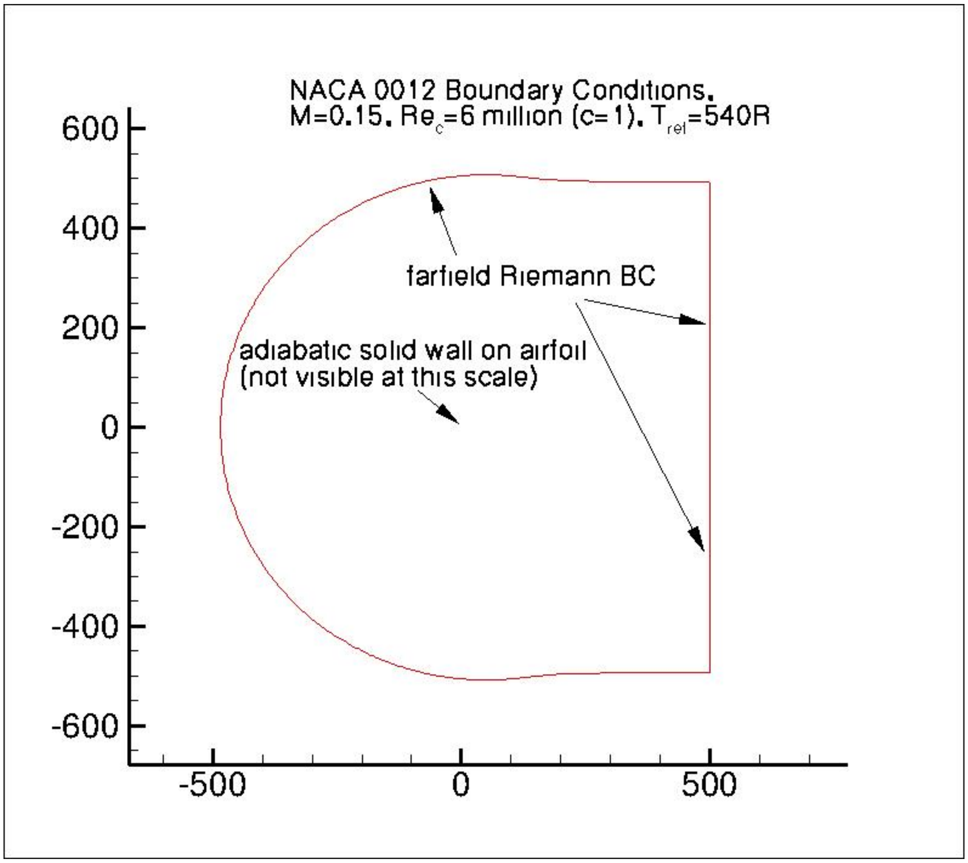

Figure 7.1: NACA0012 airfoil geometry.

At $\alpha = 15°$, the data file from the TMR website shows that the skin friction coefficient from CFL3D decreases to zero at about $x/c = 0.9868$, while the OVERFLOW computation has the skin friction coefficient decreasing to zero at about $x/c = 0.9882$.

The last set of plots shows calculations with the SST-V model on the second-finest (897 × 257) grid. As for the SST model, OVERFLOW was run for $\alpha = 0°$, $\alpha = 10°$, and $\alpha = 15°$. Figure 7.7 shows lift coefficient as a function of angle of attack and a drag polar. The OVERFLOW and CFL3D results are in close agreement.

The numerical values of lift and drag are given in Table 7.3, where we have adjoined data from OVERFLOW to data from the TMR website.

Table 7.1: Lift and drag for SA

	C_L			C_D		
Code	$\alpha = 0°$	$\alpha = 10°$	$\alpha = 15°$	$\alpha = 0°$	$\alpha = 10°$	$\alpha = 15°$
CFL3D	≈ 0	1.0909	1.5461	0.00819	0.01231	0.02124
FUN3D	≈ 0	1.0983	1.5547	0.00812	0.01242	0.02159
NTS	≈ 0	1.0891	1.5461	0.00813	0.01243	0.02105
JOE	≈ 0	1.0918	1.5490	0.00812	0.01245	0.02148
SUMB	≈ 0	1.0904	1.5446	0.00813	0.01233	0.02141
TURNS	≈ 0	1.1000	1.5642	0.00830	0.01230	0.02140
GGNS	≈ 0	1.0941	1.5576	0.00817	0.01225	0.02073
OVERFLOW	≈ 0	1.0990	1.5576	0.00838	0.01251	0.02149

Table 7.2: Lift and drag for SST

	C_L			C_D		
Code	$\alpha = 0°$	$\alpha = 10°$	$\alpha = 15°$	$\alpha = 0°$	$\alpha = 10°$	$\alpha = 15°$
CFL3D	≈ 0	1.0778	1.5068	0.00809	0.01236	0.02219
FUN3D	≈ 0	1.0840	1.5109	0.00808	0.01253	0.02275
NTS	≈ 0	1.0765	1.5100	0.00809	0.01251	0.02187
OVERFLOW	≈ 0	1.0847	1.5094	0.00821	0.01262	0.02288

Table 7.3: Lift and drag for SST-V

	C_L			C_D		
Code	$\alpha = 0°$	$\alpha = 10°$	$\alpha = 15°$	$\alpha = 0°$	$\alpha = 10°$	$\alpha = 15°$
JOE	≈ 0	1.0805	1.5079	0.00805	0.01257	0.02280
SUMB	≈ 0	1.0773	1.5046	0.00807	0.01230	0.02214
CFL3D	≈ 0	1.0778	1.5060	0.00828	0.01245	0.02224
OVERFLOW	≈ 0	1.0847	1.5094	0.00821	0.01262	0.02288

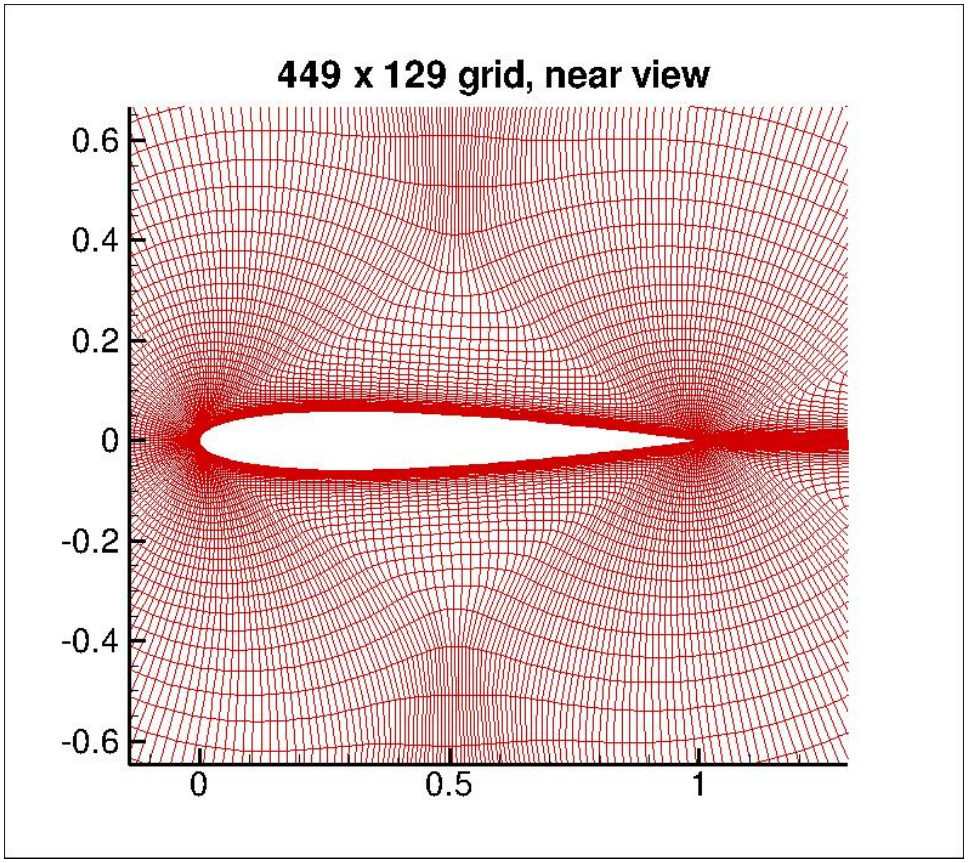

Figure 7.2: NACA0012 airfoil grid, near view.

Figure 7.8 shows pressure coefficient C_p over the airfoil surface and skin friction coefficient C_f over the upper surface of the airfoil for the three angles of attack. The OVERFLOW and CFL3D results are very close to one another.

At $\alpha = 15°$, the data file from the TMR website shows that the skin friction coefficient from CFL3D decreases to zero at about $x/c = 0.9870$, while the OVERFLOW computation has the skin friction coefficient decreasing to zero at about $x/c = 0.9879$.

For OVERFLOW and the SA model, we show in Table 7.4 values for lift and drag coefficient as functions of the grid dimensions. For this case, the drag coefficient appears to decrease monotonically as the grid is refined.

Next, in Table 7.5, we show lift and drag coefficient for OVERFLOW and

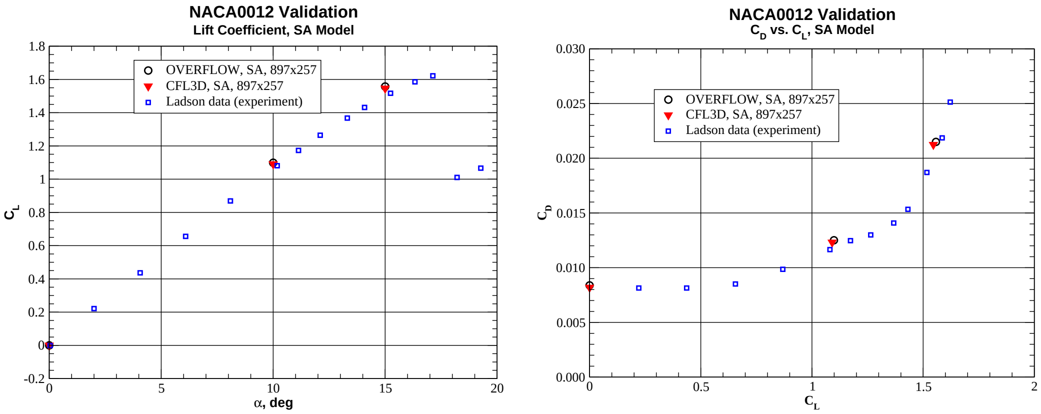

Figure 7.3: Lift and drag, NACA0012, SA model.

Table 7.4: Lift and drag for Overflow, SA model, mesh size varying

	$\alpha = 0°$		$\alpha = 10°$		$\alpha = 15°$	
Grid	C_L	C_D	C_L	C_D	C_L	C_D
113 × 33	≈ 0	0.00978291	1.08324	0.0225240	1.44781	0.0584944
225 × 65	≈ 0	0.00878727	1.10542	0.0146783	1.55786	0.0262086
449 × 129	≈ 0	0.00841582	1.10316	0.0129701	1.55931	0.0225324
897 × 257	≈ 0	0.00838221	1.09895	0.0125069	1.55756	0.0214924
1793 × 513	≈ 0	0.00820996	1.09553	0.0123648	1.55498	0.0212017

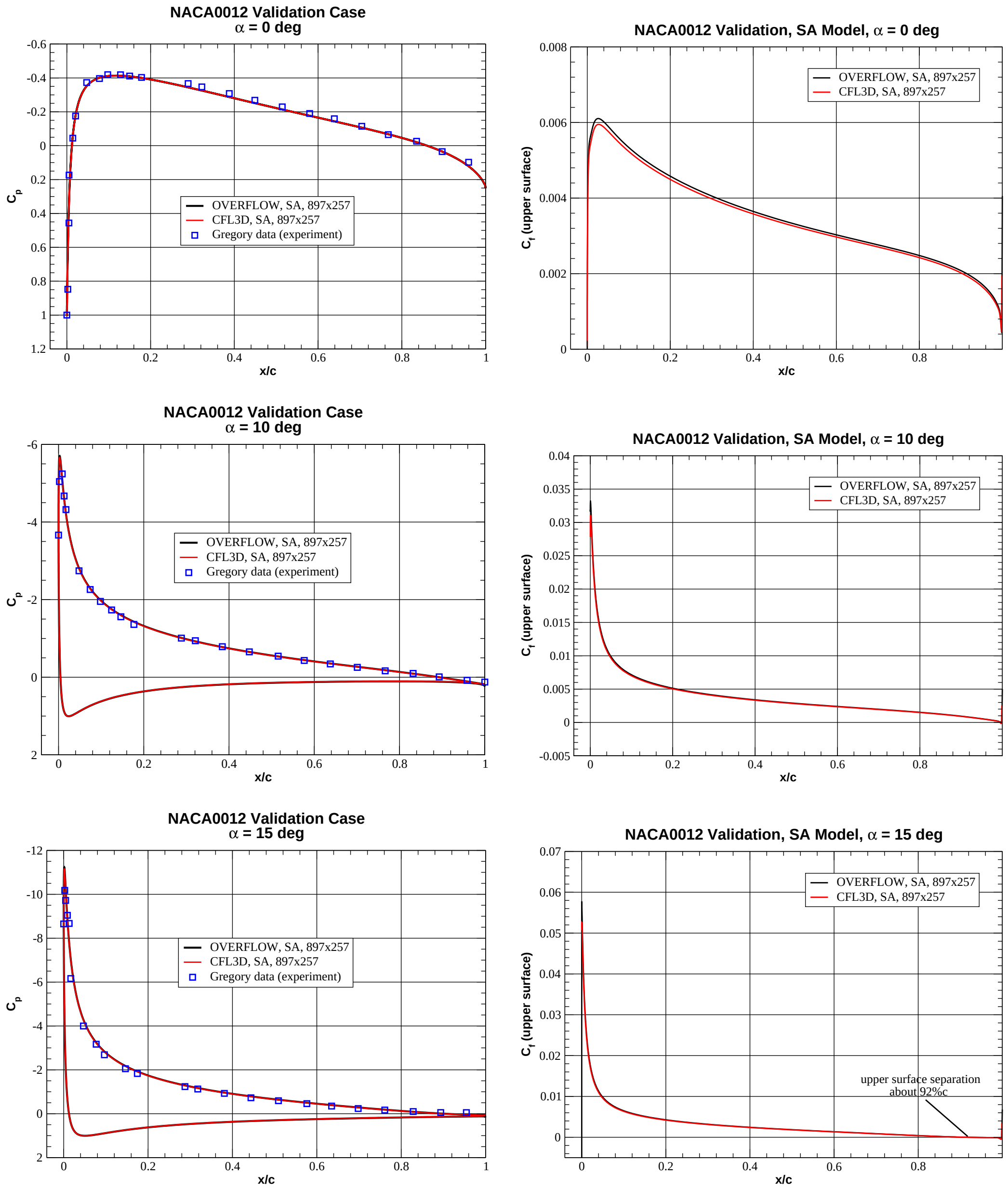

Figure 7.4: Pressure coefficient and skin friction, NACA0012, SA model.

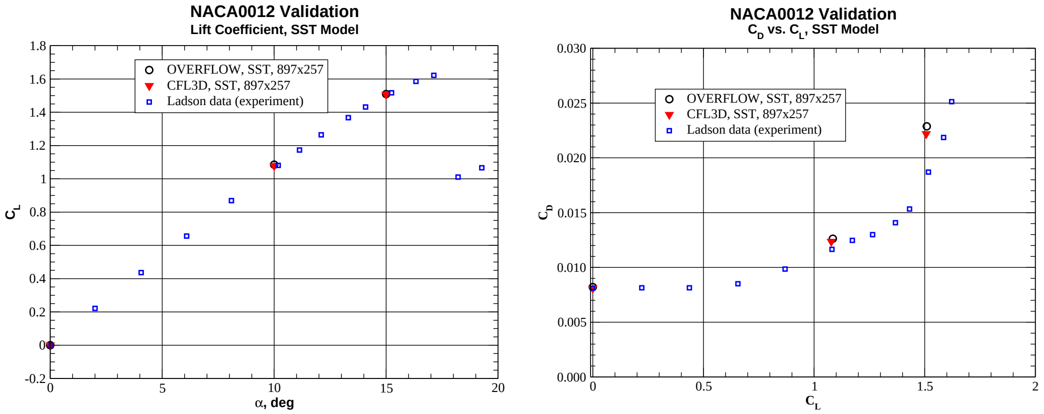

Figure 7.5: Lift and drag, NACA0012, SST model.

the SST model as functions of grid dimension. For each fixed α, the drag coefficient is monotone decreasing as the grid is refined, except for the $\alpha = 15°$ case and the two finest grids.

Table 7.5: Lift and drag for OVERFLOW, SST model, mesh size varying

	$\alpha = 0°$		$\alpha = 10°$		$\alpha = 15°$	
Grid	C_L	C_D	C_L	C_D	C_L	C_D
113×33	≈ 0	0.00951145	1.00805	0.0340621	1.12402	0.123347
225×65	≈ 0	0.00846612	1.09366	0.0142877	1.51237	0.0275199
449×129	≈ 0	0.00826384	1.09011	0.0128840	1.51599	0.0234893
897×257	≈ 0	0.00820820	1.08473	0.0126228	1.50944	0.0228792
1793×513	≈ 0	0.00816992	1.08083	0.0125676	1.50202	0.0229112

Finally, in Table 7.6, we show lift and drag coefficients for OVERFLOW and the SST-V model as functions of grid dimension.

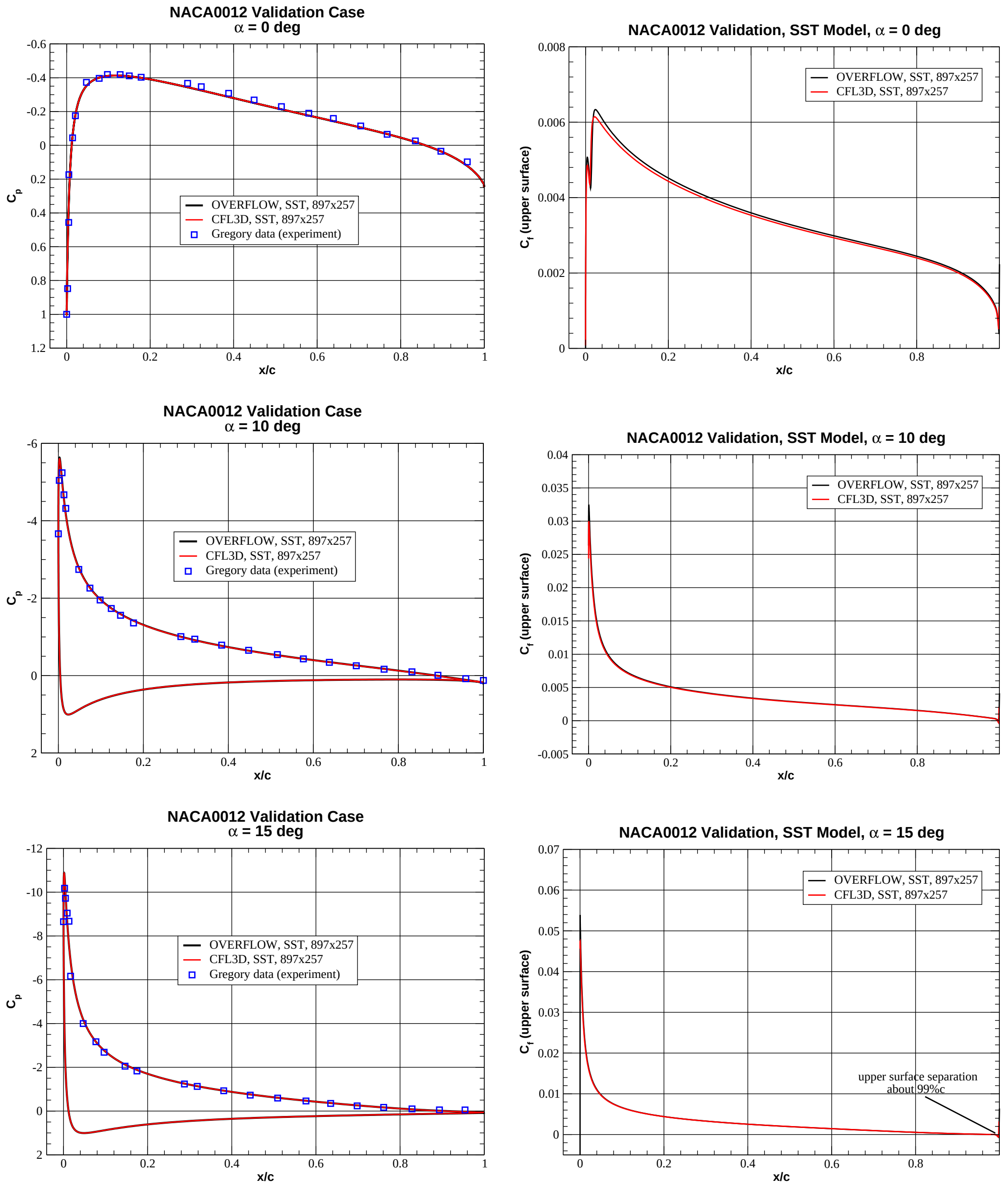

Figure 7.6: Pressure coefficient and skin friction, NACA0012, SST model.

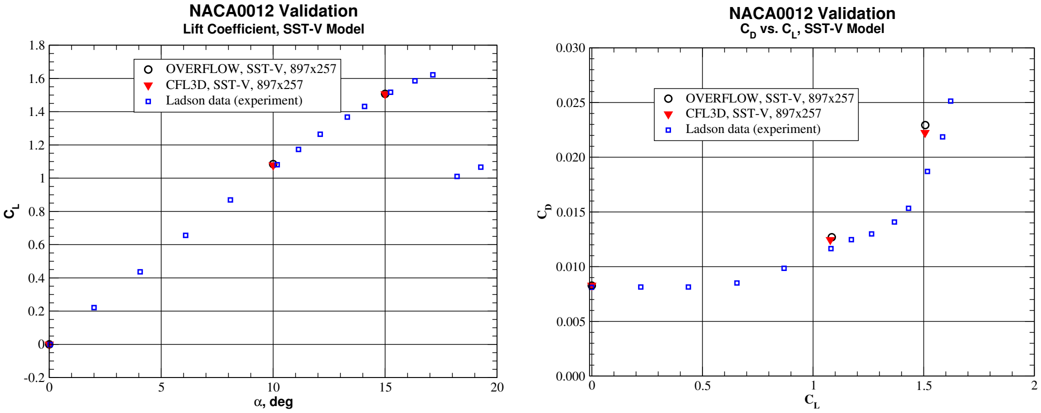

Figure 7.7: Lift and drag, NACA0012, SST-V model.

Table 7.6: Lift and drag for Overflow, SST-V model, mesh size varying

	$\alpha = 0°$		$\alpha = 10°$		$\alpha = 15°$	
Grid	C_L	C_D	C_L	C_D	C_L	C_D
113 × 33	≈ 0	0.00951145	1.00805	0.0340621	1.12402	0.123347
225 × 65	≈ 0	0.00846612	1.09366	0.0142877	1.51237	0.0275199
449 × 129	≈ 0	0.00826384	1.09011	0.0128840	1.51599	0.0234893
897 × 257	≈ 0	0.00820820	1.08473	0.0126228	1.50944	0.0228792
1793 × 513	≈ 0	0.00821664	1.08064	0.0126308	1.49935	0.0229634

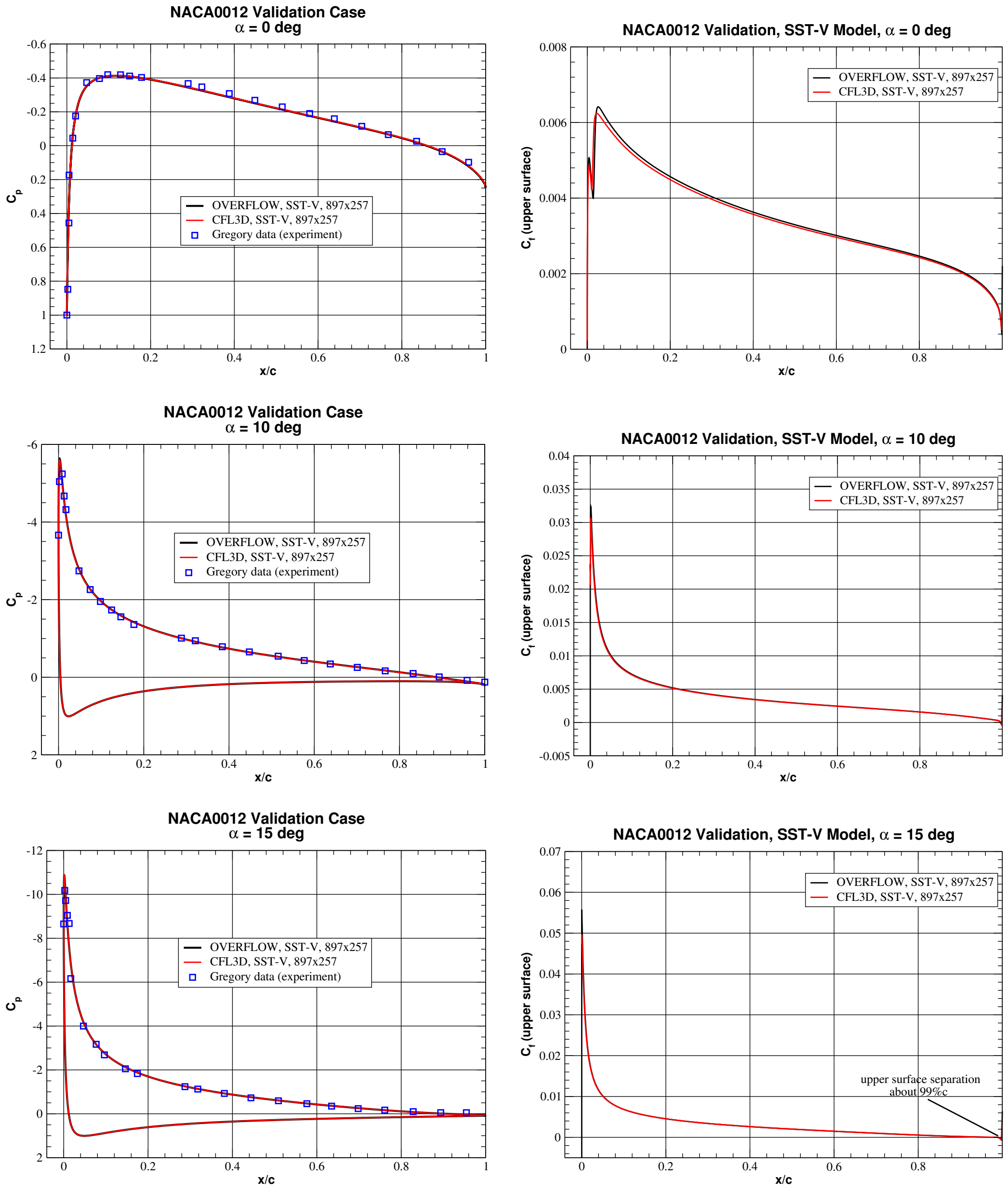

Figure 7.8: Pressure coefficient and skin friction, NACA0012, SST-V model.

8. Axisymmetric Subsonic Jet

In this section we present turbulence model validation for OVERFLOW using the LaRC Turbulence Modeling Resource (TMR) Axisymmetric Subsonic Jet validation case. This case has Mach number $M = 0.01$ and Reynolds number $Re = 5601$ based on the jet radius. The geometry and flow conditions are shown in Figure 8.1, taken from the TMR website. The grid system provided for this case is indicated in Figure 8.2.

To prepare the grids for use with OVERFLOW, for each of the two left-hand grids, we adjoined four line segments from the right-hand grid to create the necessary grid overlapping. In addition, we created data surface grids at the locations where plotting is to be done, with five normal line segments in the wake and one along the jet axis.

For both the SA and SST-V models, we used Roe spatial differencing along with time-accurate time stepping. The boundary condition at the upstream boundary of the plenum was the nozzle inflow condition `IBTYP=41` with parameters `BCPAR1=1.19671` and `BCPAR2=1`. The condition at the downstream boundary was the fixed pressure ratio condition `IBTYP=33` with parameter `BCPAR1=1`. For the SST-V model we used OVERFLOW input parameters `MUTINF=0.001` and `XKINF=1.62E-6`, which correspond to the freestream turbulent viscosity and freestream turbulence intensity as used with the WIND code [9] for the TMR website results.

Convergence to a steady state was difficult to achieve for these cases. When run in time-accurate mode, the flow eventually became reasonably steady.

For this validation case, the TMR website provides plots comparing the two codes CFL3D and WIND, and the results of the two codes are very close to one another. The TMR website also provides data files from WIND but not from CFL3D, so in our plots we compare OVERFLOW results with WIND results.

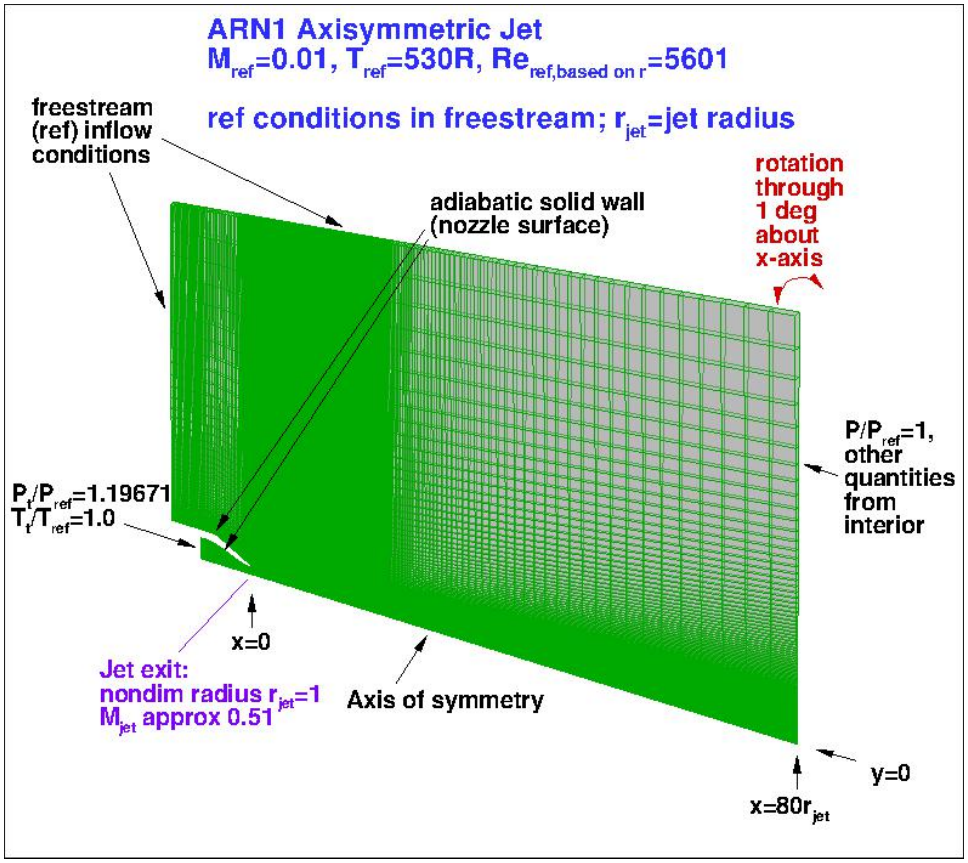

Figure 8.1: Axisymmetric jet geometry.

The first set of plots, Figure 8.3, shows streamwise velocity profiles in the wake from experiment and for OVERFLOW and the WIND code with the SA model. The OVERFLOW and WIND data are from the second-finest grid, and the OVERFLOW and WIND results are in good agreement.

The second set of plots, Figure 8.4, shows normal velocity profiles in the wake from experiment and for OVERFLOW and the WIND code with the SA model. Again the OVERFLOW and WIND results are in good agreement.

The next set of plots, Figure 8.5, shows turbulent shear stress profiles in the wake from experiment and for OVERFLOW and the WIND code with the SA model. The OVERFLOW and WIND results agree closely.

The next three sets of plots, figures 8.6, 8.7, and 8.8, show streamwise ve-

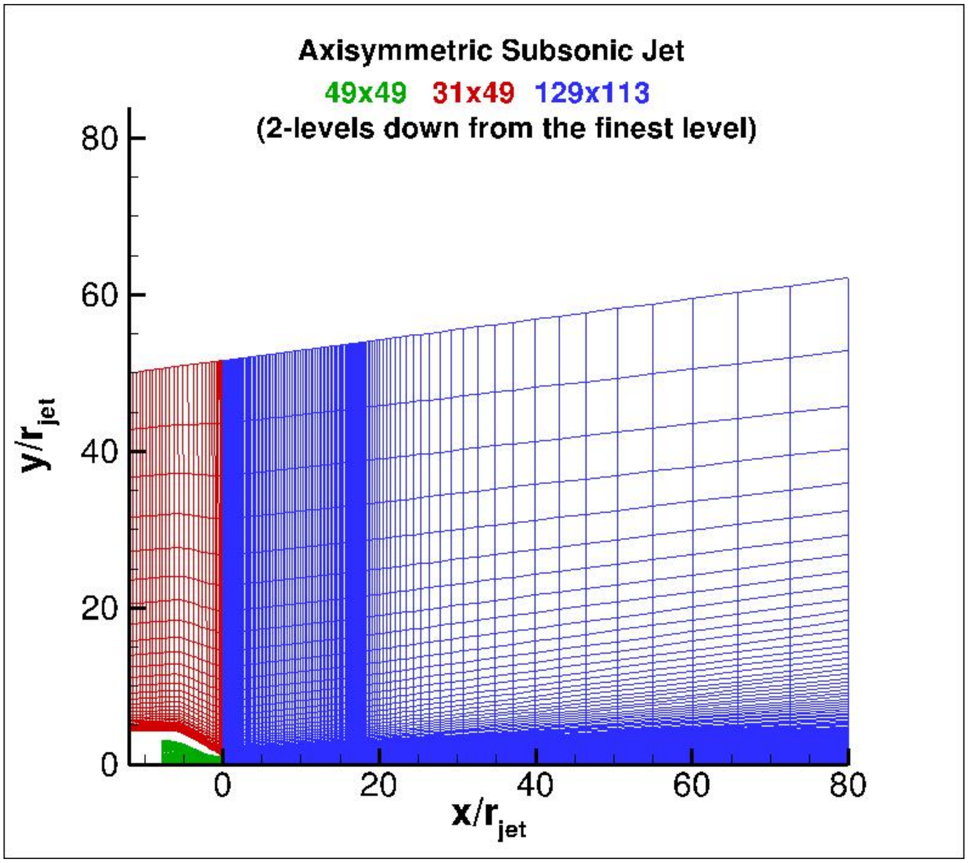

Figure 8.2: Axisymmetric jet grid system.

locity profiles in the wake, normal velocity profiles in the wake, and turbulent shear stress profiles in the wake, respectively, comparing Overflow and the Wind code using the SST-V model with experiment. The Overflow and Wind data are from the second-finest grid, and the Overflow and Wind results are in good agreement.

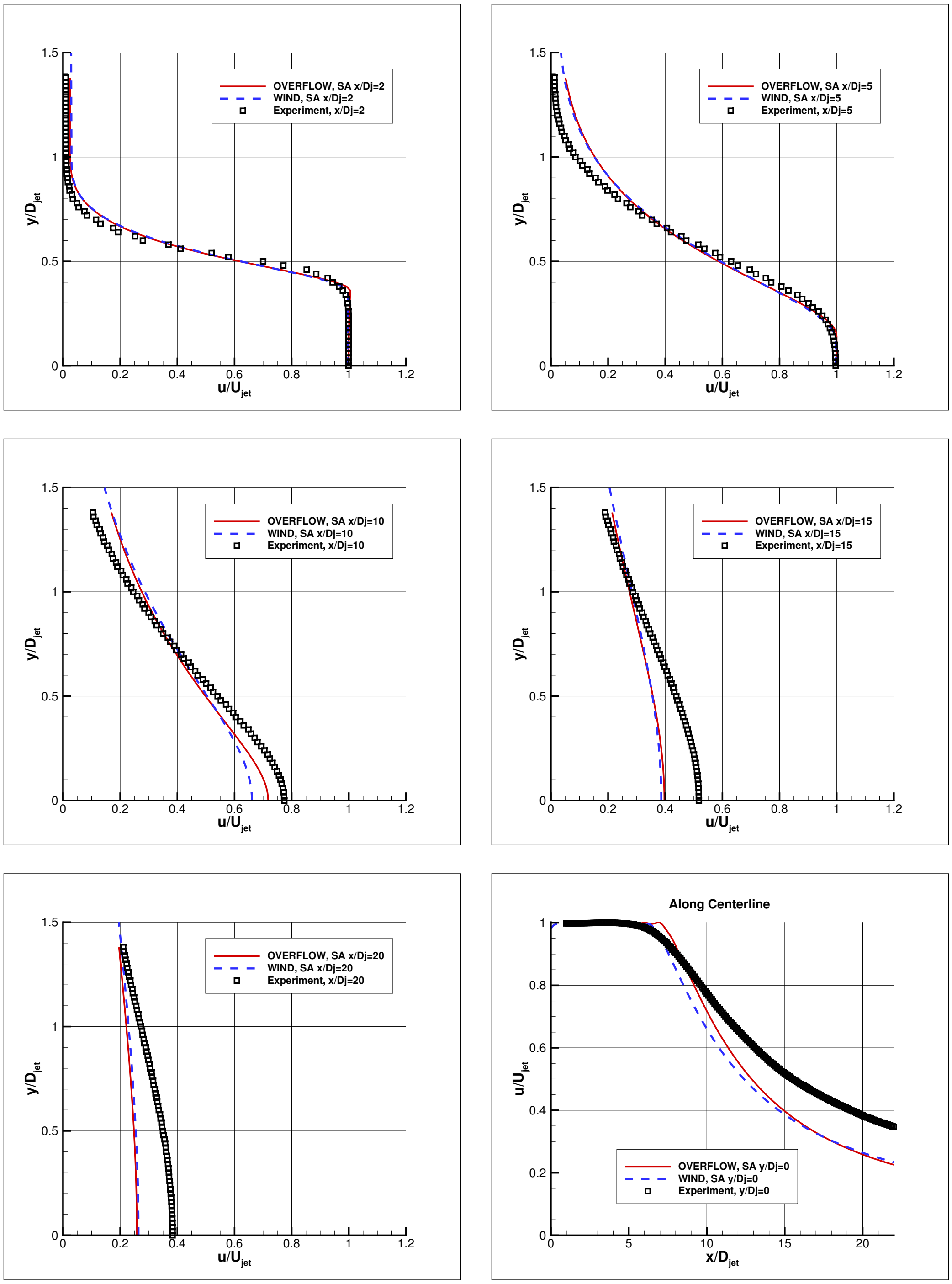

Figure 8.3: Streamwise velocity profiles, SA model, x/D_{jet} = 2, 5, 10, 15, 20, and along centerline.

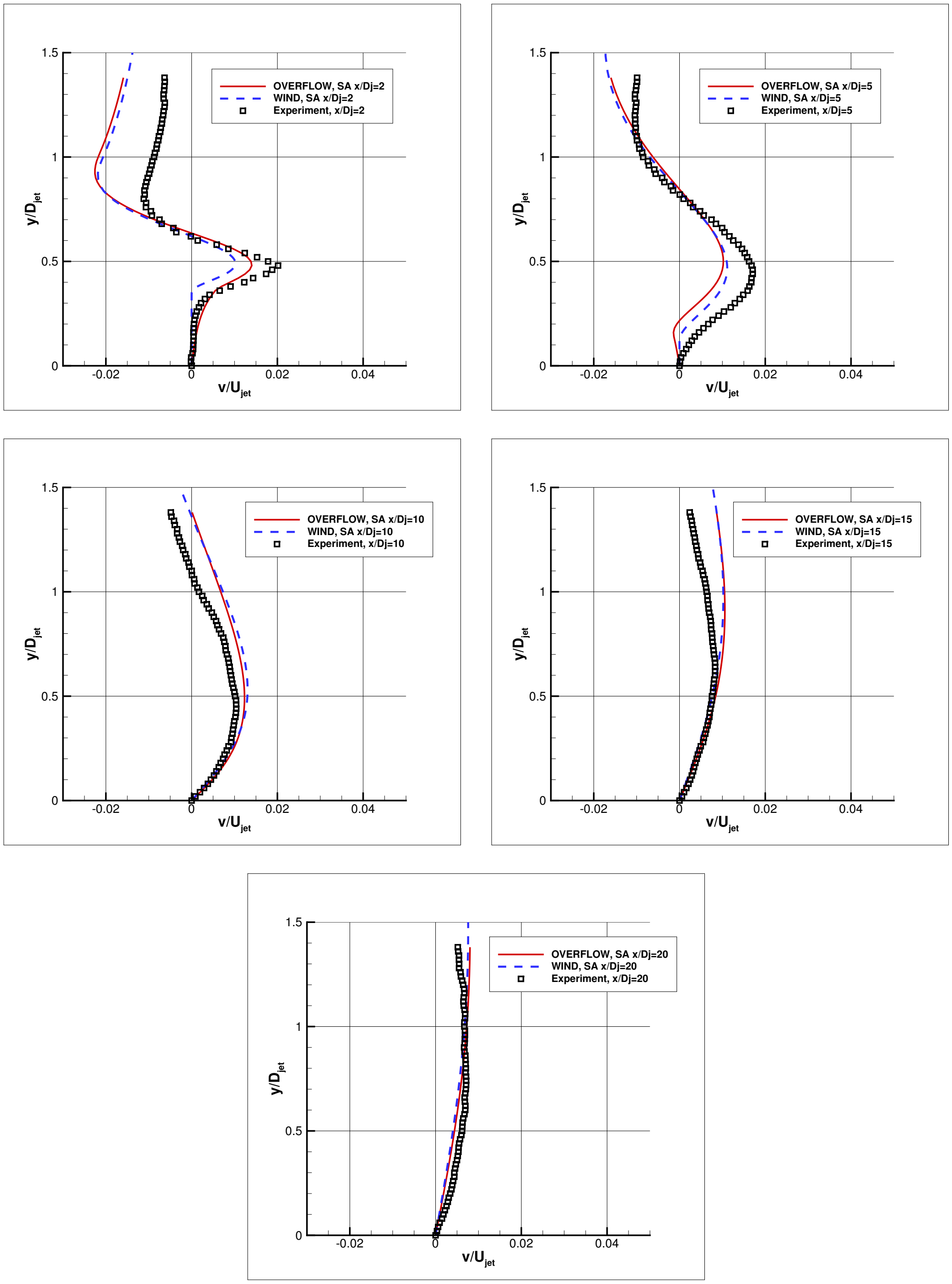

Figure 8.4: Normal velocity profiles, SA model, $x/D_{jet} = 2$, 5, 10, 15 and 20.

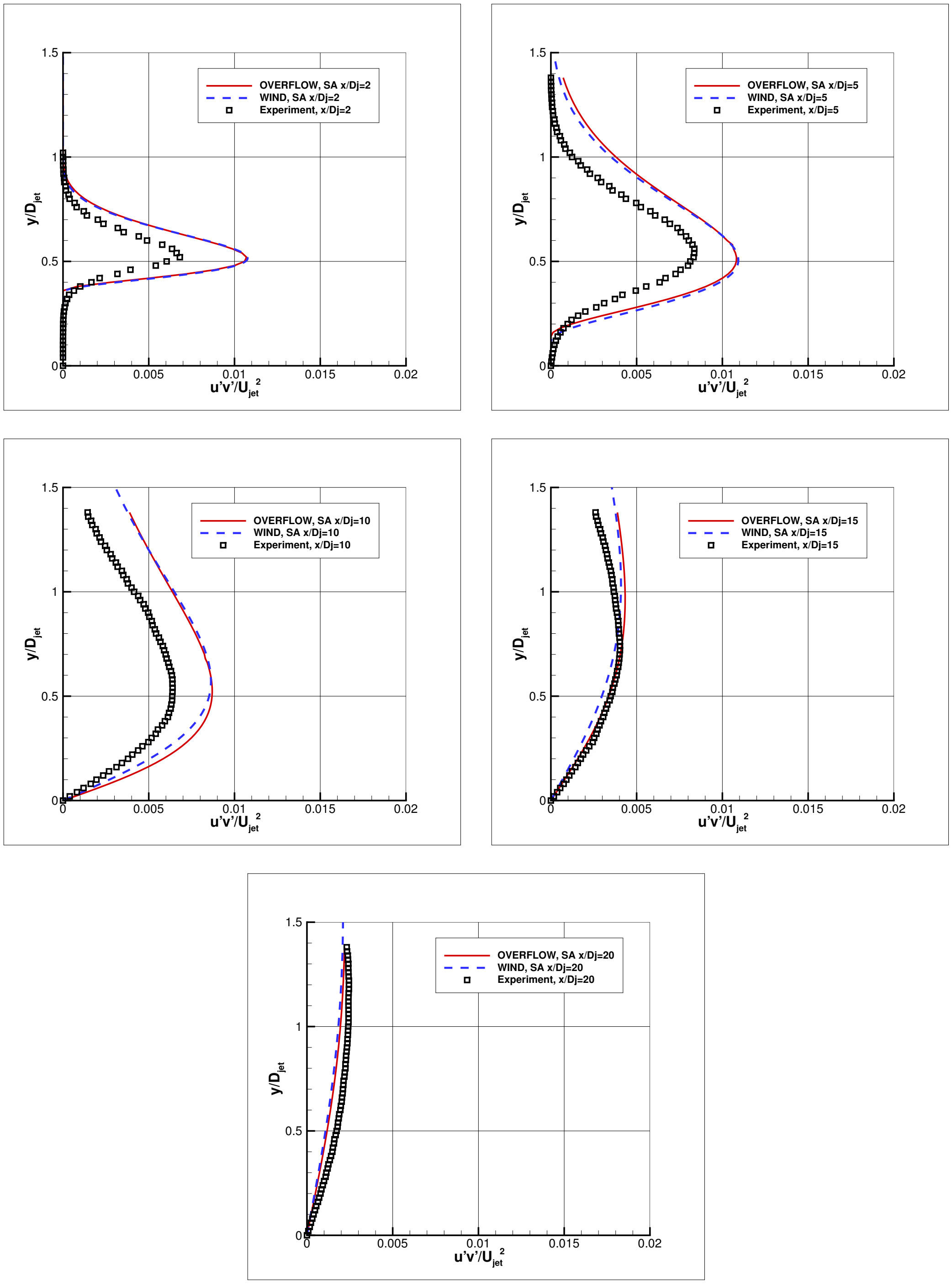

Figure 8.5: Turbulent shear stress profiles, SA model, $x/D_{jet} = 2, 5, 10, 15$ and 20.

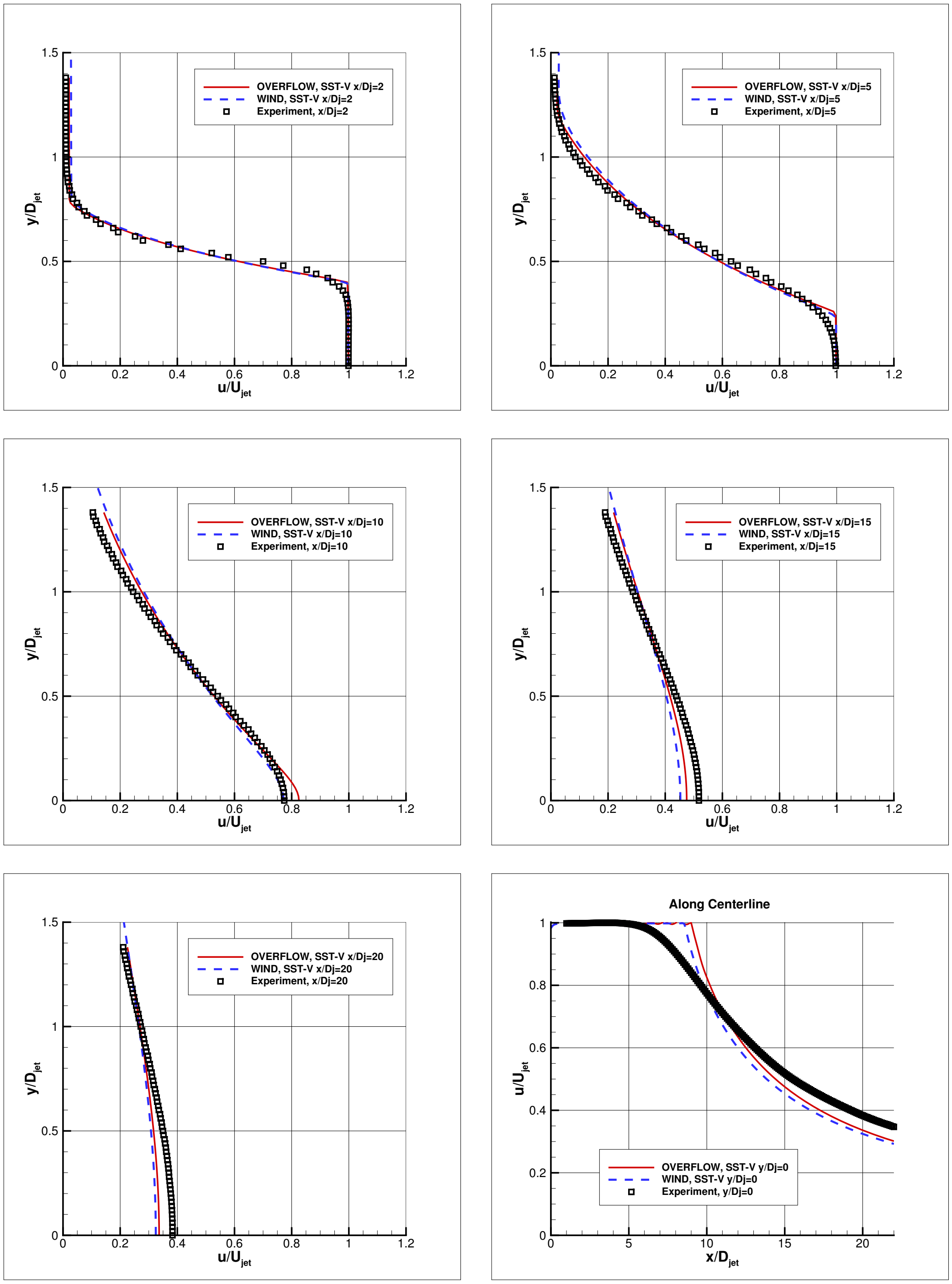

Figure 8.6: Streamwise velocity profiles, SST-V model, x/D_{jet} = 2, 5, 10, 15, 20, and along centerline.

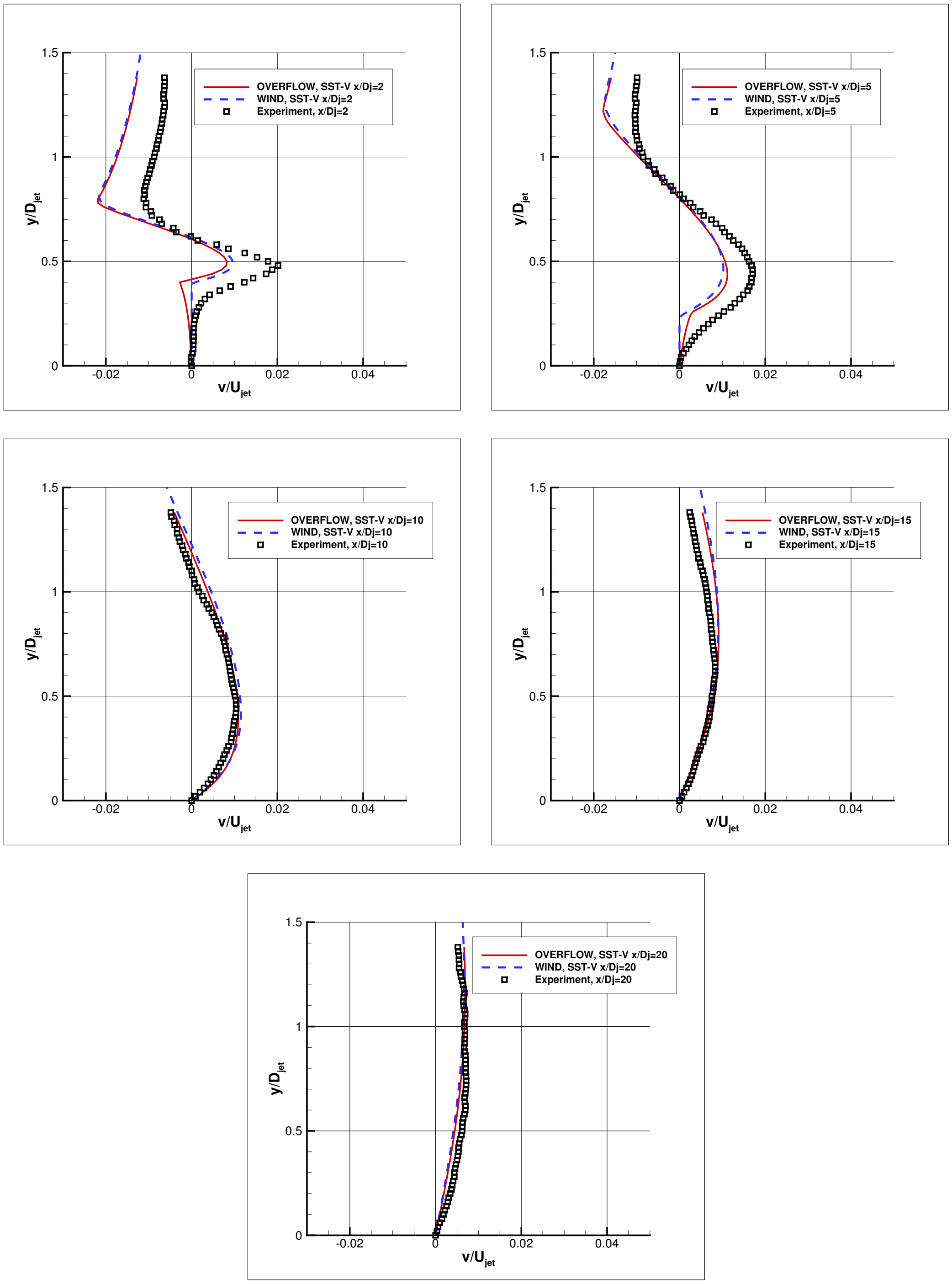

Figure 8.7: Normal velocity profiles, SST-V model, $x/D_{jet} = 2$, 5, 10, 15, 20.

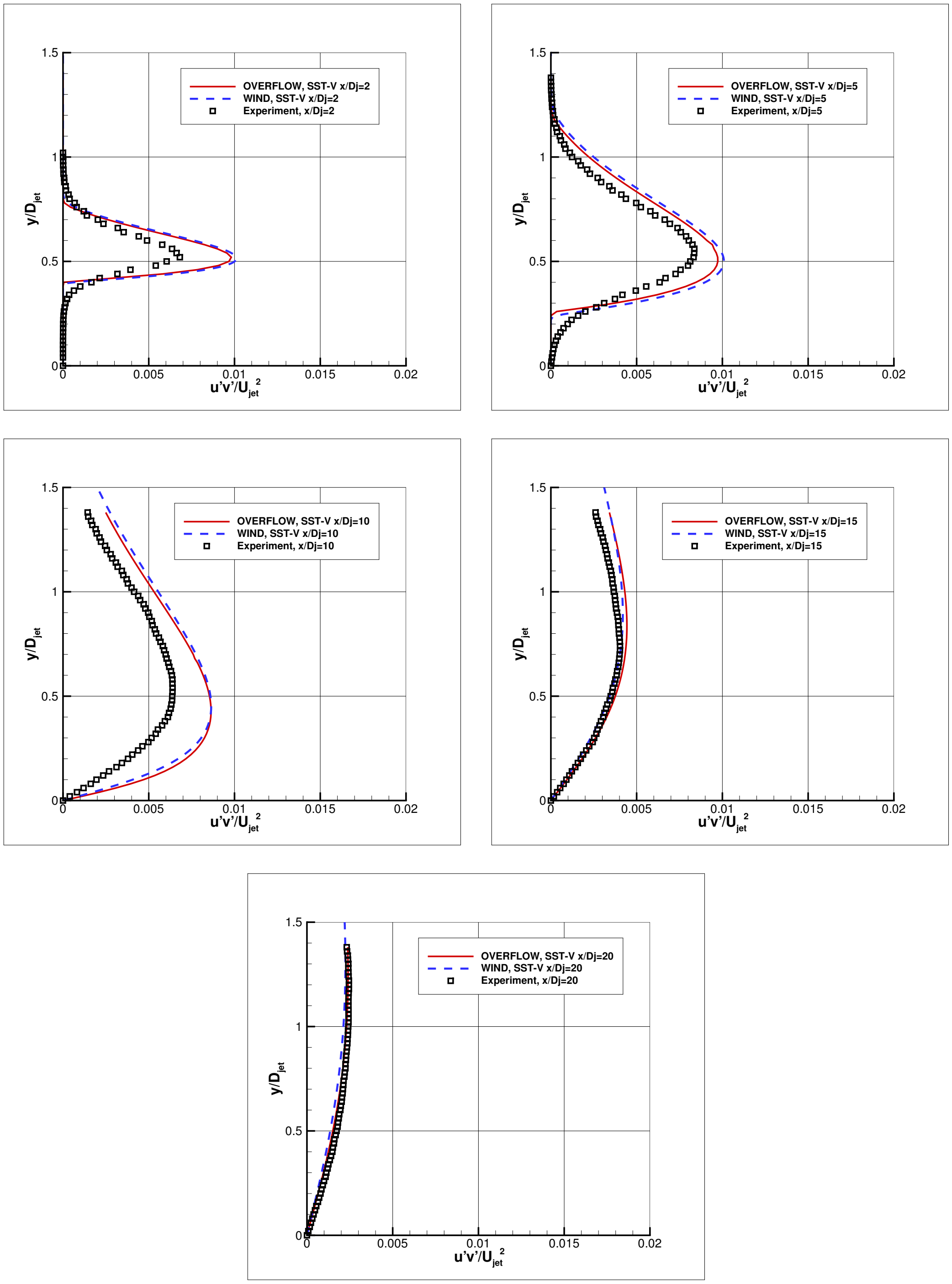

Figure 8.8: Turbulent shear stress profiles, SST-V model, $x/D_{jet} = 2$, 5, 10, 15 and 20.

9. Axisymmetric Hot Subsonic Jet

In this section we present turbulence model validation for OVERFLOW using the LaRC Turbulence Modeling Resource (TMR) Axisymmetric Hot Subsonic Jet validation case. This case has Mach number $M = 0.01$ and Reynolds number $Re = 5601$ based on the jet radius. The geometry and flow conditions are shown in Figure 9.1, taken from the TMR website. The grid system provided for this case is the same as for the axisymmetric subsonic jet.

The grids for OVERFLOW were the same for this case as for the subsonic jet case of the previous section.

For both the SA and SST-V models, we used Roe spatial differencing along with time-accurate time stepping. The boundary condition at the upstream boundary of the plenum was the nozzle inflow condition `IBTYP=41` with parameters `BCPAR1=1.10203` and `BCPAR2=1.81388`. The condition at the downstream boundary was the fixed pressure ratio condition `IBTYP=33` with parameter `BCPAR1=1`. For the SST-V model we used OVERFLOW input parameters `MUTINF=0.001` and `XKINF=1.622E-6`, which correspond to the freestream turbulent viscosity and freestream turbulence intensity used with the WIND code for the TMR website results.

Convergence to a steady state was difficult to achieve for these cases. When run in time-accurate mode, the flow eventually became reasonably steady.

The first set of plots, Figure 9.2, shows streamwise velocity profiles in the wake from experiment and for OVERFLOW and the WIND code with the SA model. The OVERFLOW and WIND data are from the second-finest grid, and the OVERFLOW and WIND results are in good agreement.

The second set of plots, Figure 9.3, shows normal velocity profiles in the

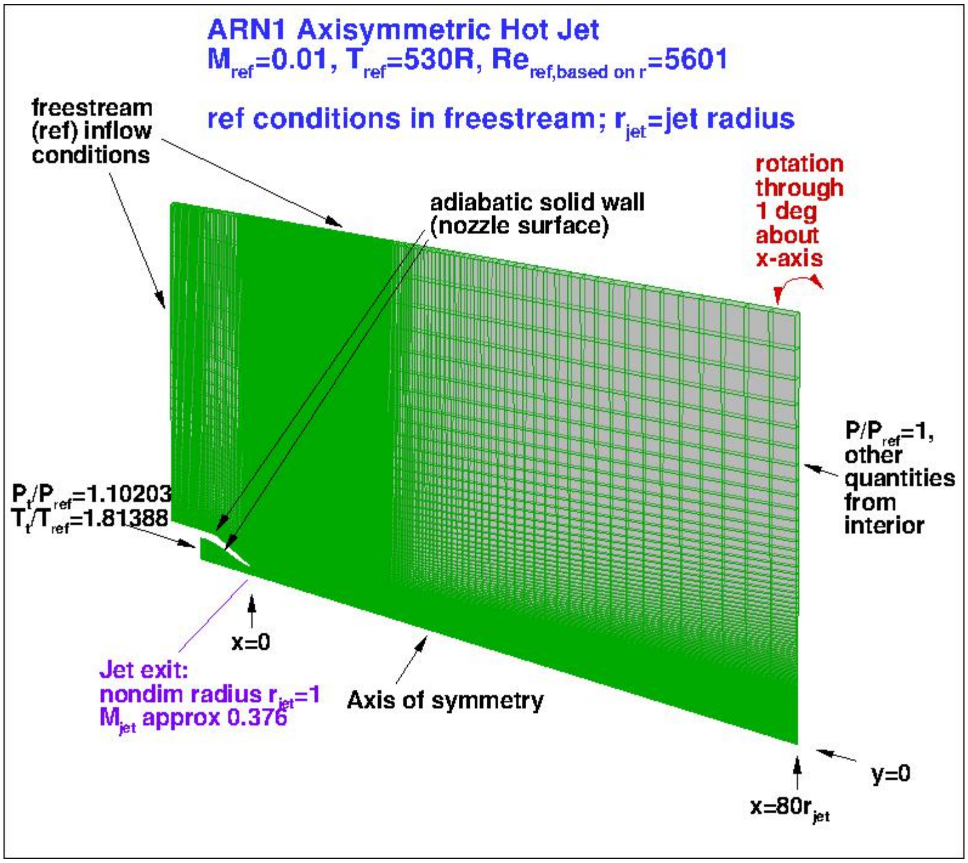

Figure 9.1: Axisymmetric jet geometry.

wake from experiment and for Overflow and the Wind code with the SA model. Again the Overflow and Wind results are in good agreement.

The next set of plots, Figure 9.4, shows turbulent shear stress profiles in the wake from experiment and for Overflow and the Wind code with the SA model. The Overflow and Wind results agree closely.

The next set of plots, Figure 9.5, shows streamwise velocity profiles in the wake from experiment and for Overflow and the Wind code with the SST-V model. The Overflow and Wind data are from the second-finest grid. The Overflow and Wind results are in good agreement.

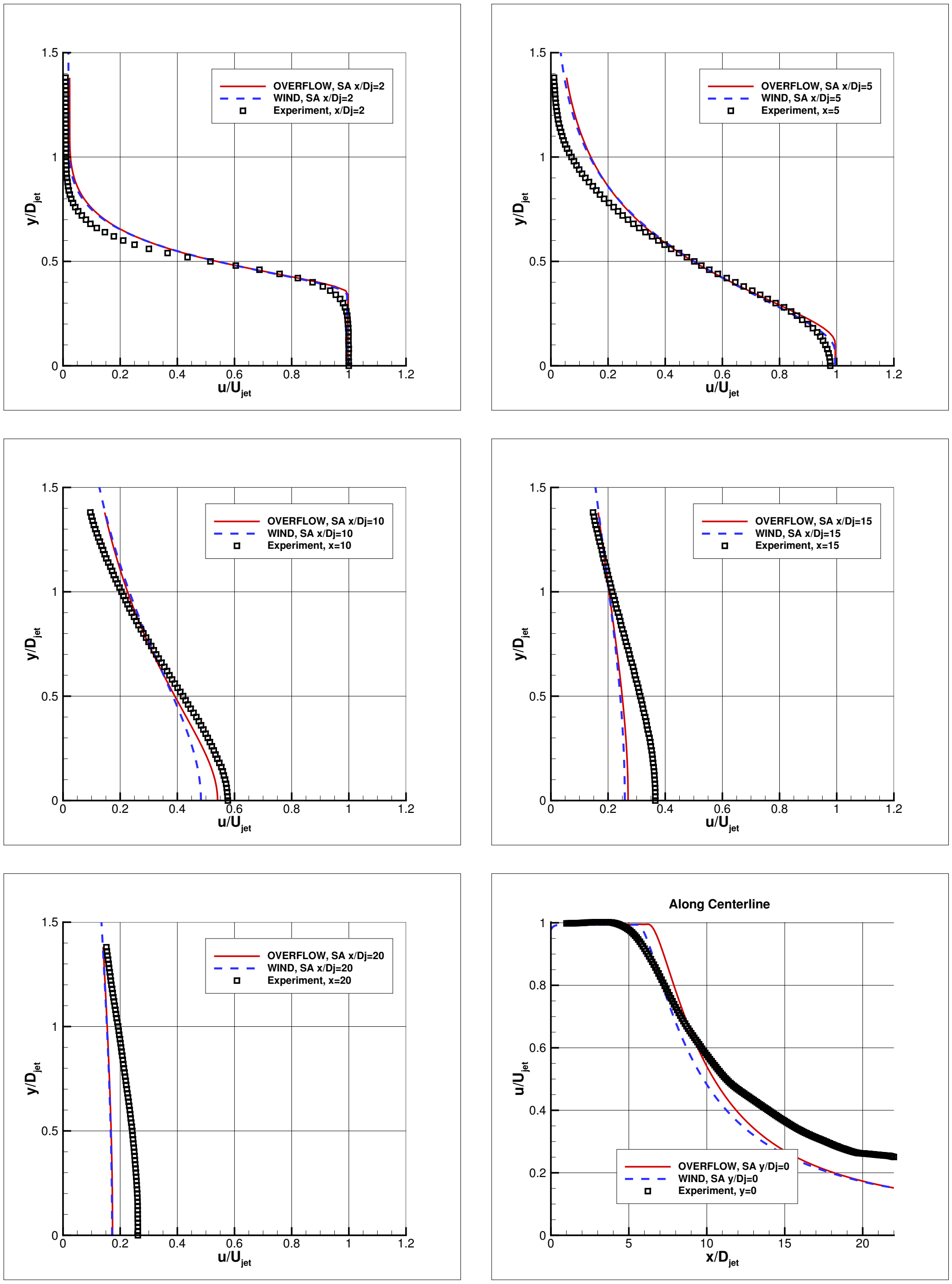

Figure 9.2: Streamwise velocity profiles, SA model, x/D_{jet} = 2, 5, 10, 15, 20, and along centerline.

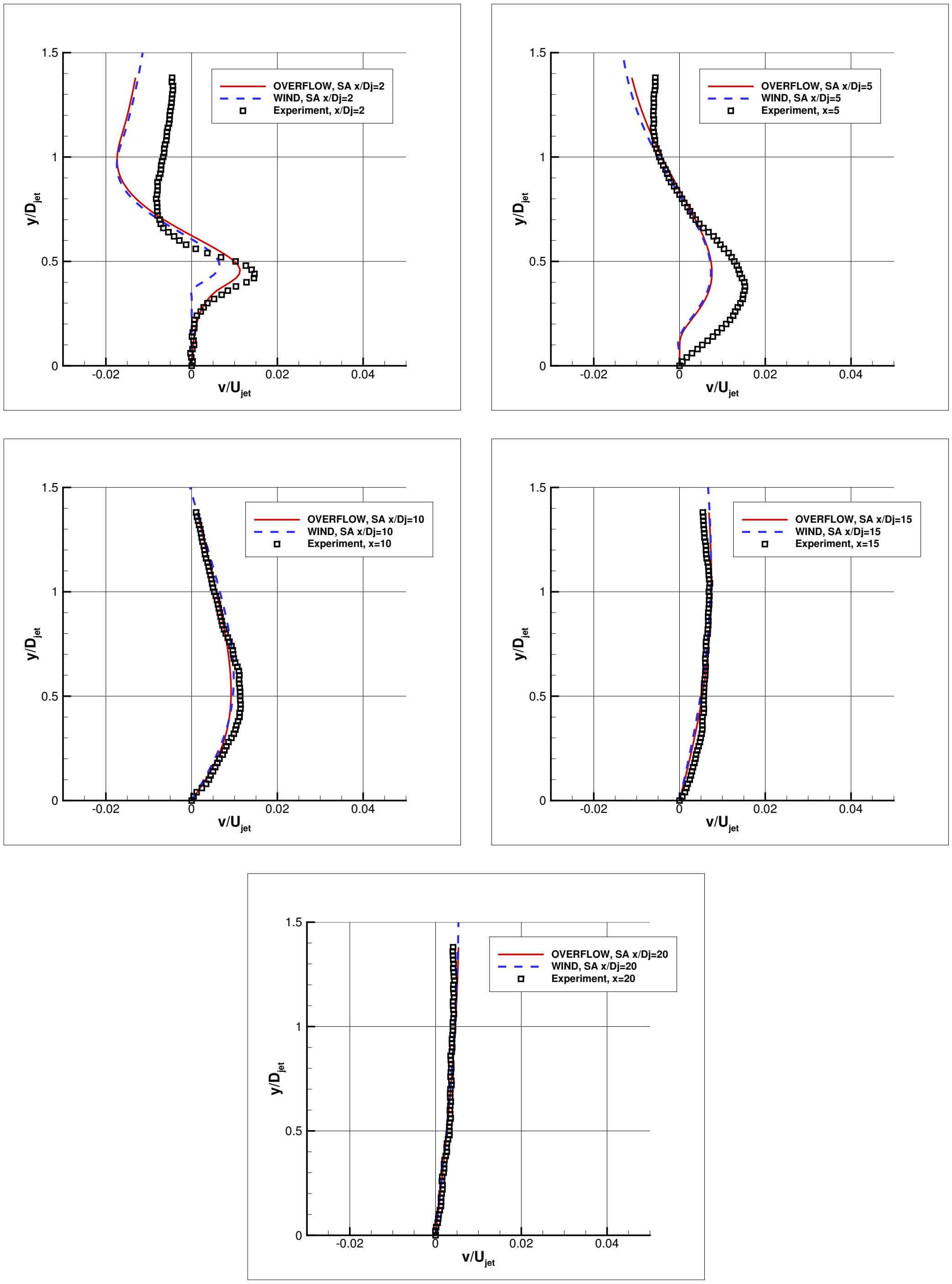

Figure 9.3: Normal velocity profiles, SA model, $x/D_{jet} = 2, 5, 10, 15, 20$.

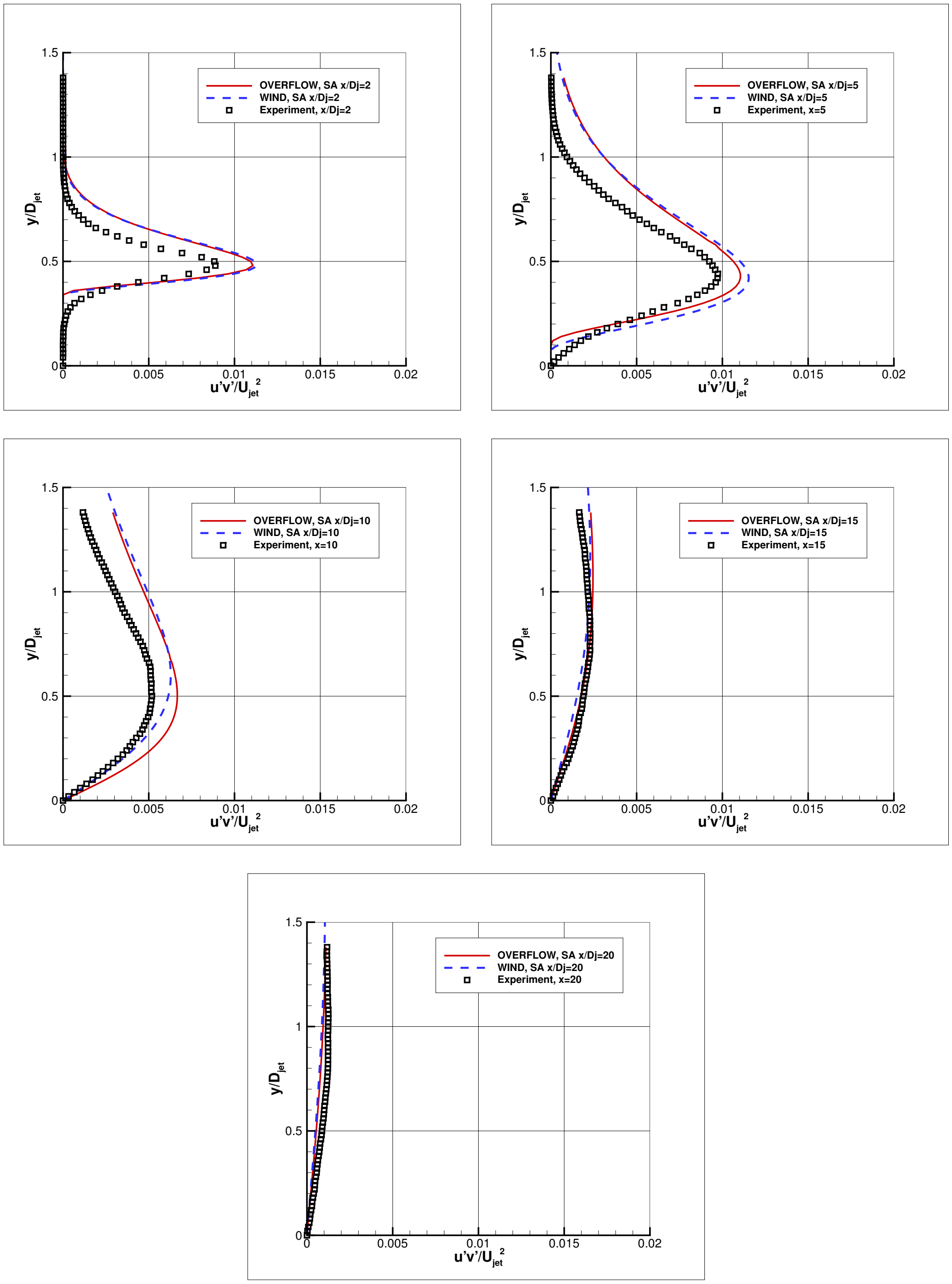

Figure 9.4: Turbulent shear stress profiles, SA model, $x/D_{jet} = 2$, 5, 10, 15 and 20.

The next set of plots, Figure 9.6, shows normal velocity profiles in the wake from experiment and for OVERFLOW and the WIND code with the SST-V model. Again the OVERFLOW and WIND results are in good agreement.

The final set of plots, Figure 9.7, shows turbulent shear stress profiles in the wake from experiment and for OVERFLOW and the WIND code with the SST-V model. The OVERFLOW and WIND results are in good agreement.

We also ran the SST model on the second-finest grid. Plots from the SST solution are very similar to plots from the SST-V solution.

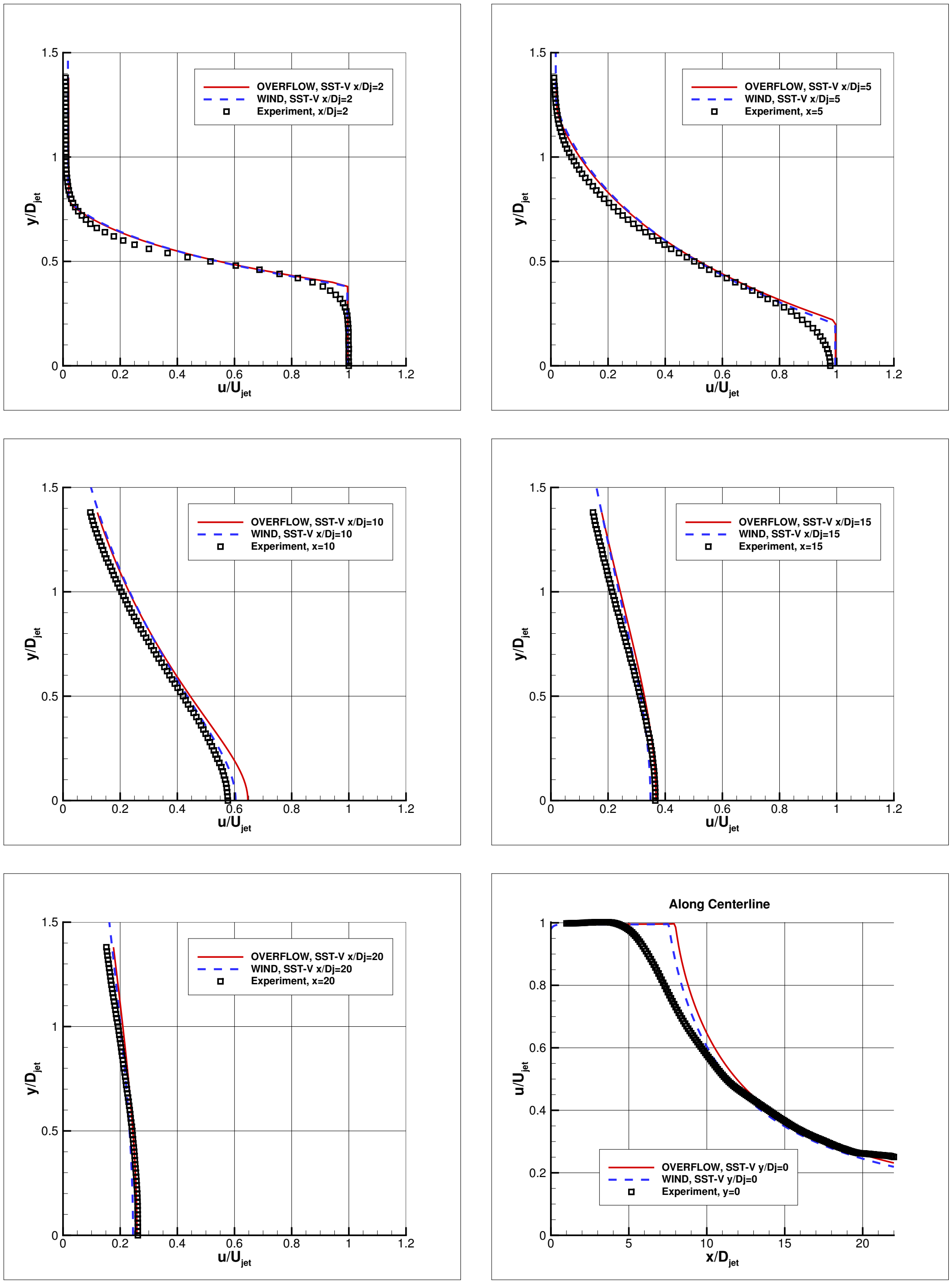

Figure 9.5: Streamwise velocity profiles, SST-V model, x/D_{jet} = 2, 5, 10, 15, and along centerline.

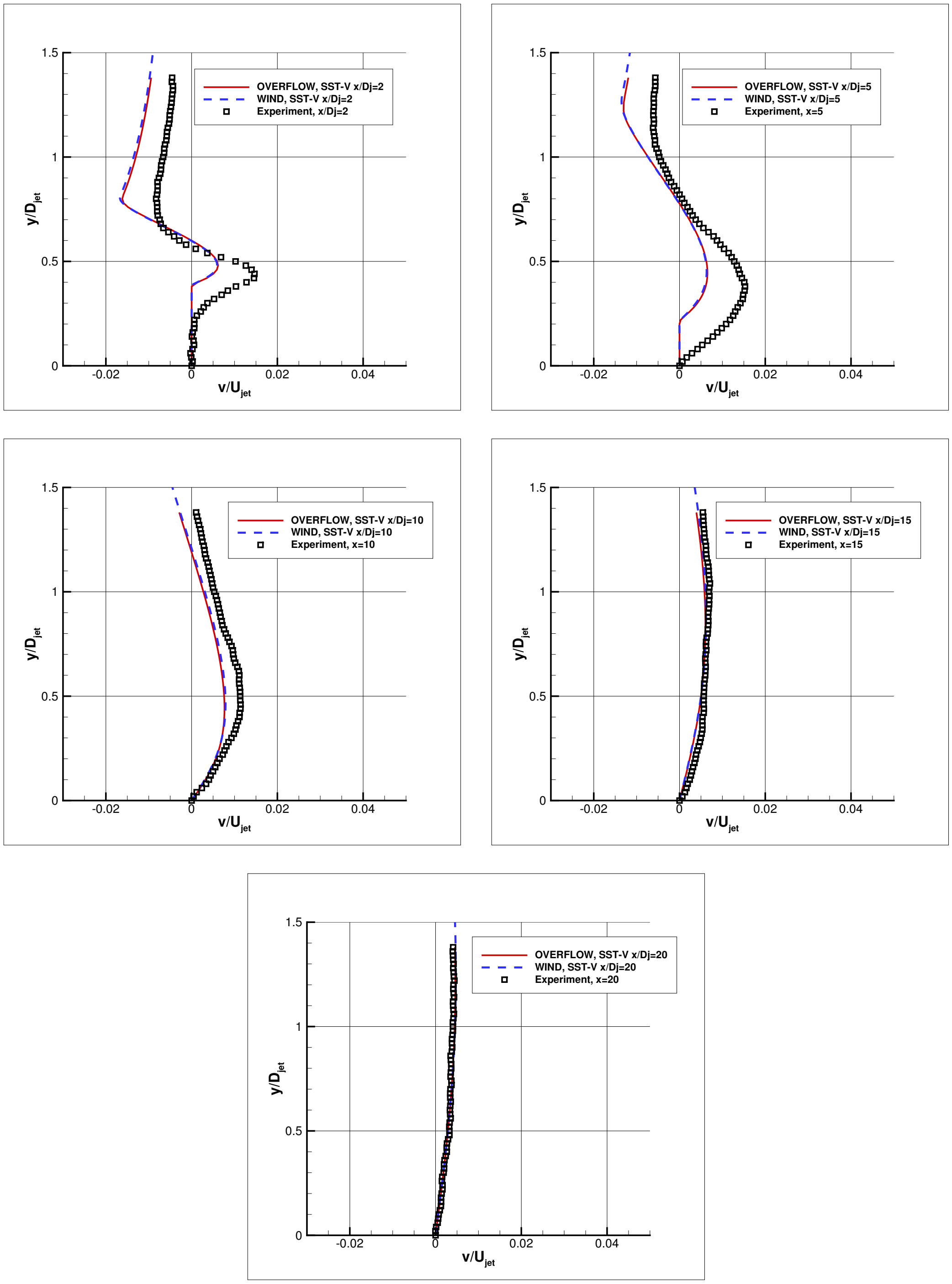

Figure 9.6: Normal velocity profiles, SST-V model, $x/D_{jet} = 2, 5, 10, 15, 20$.

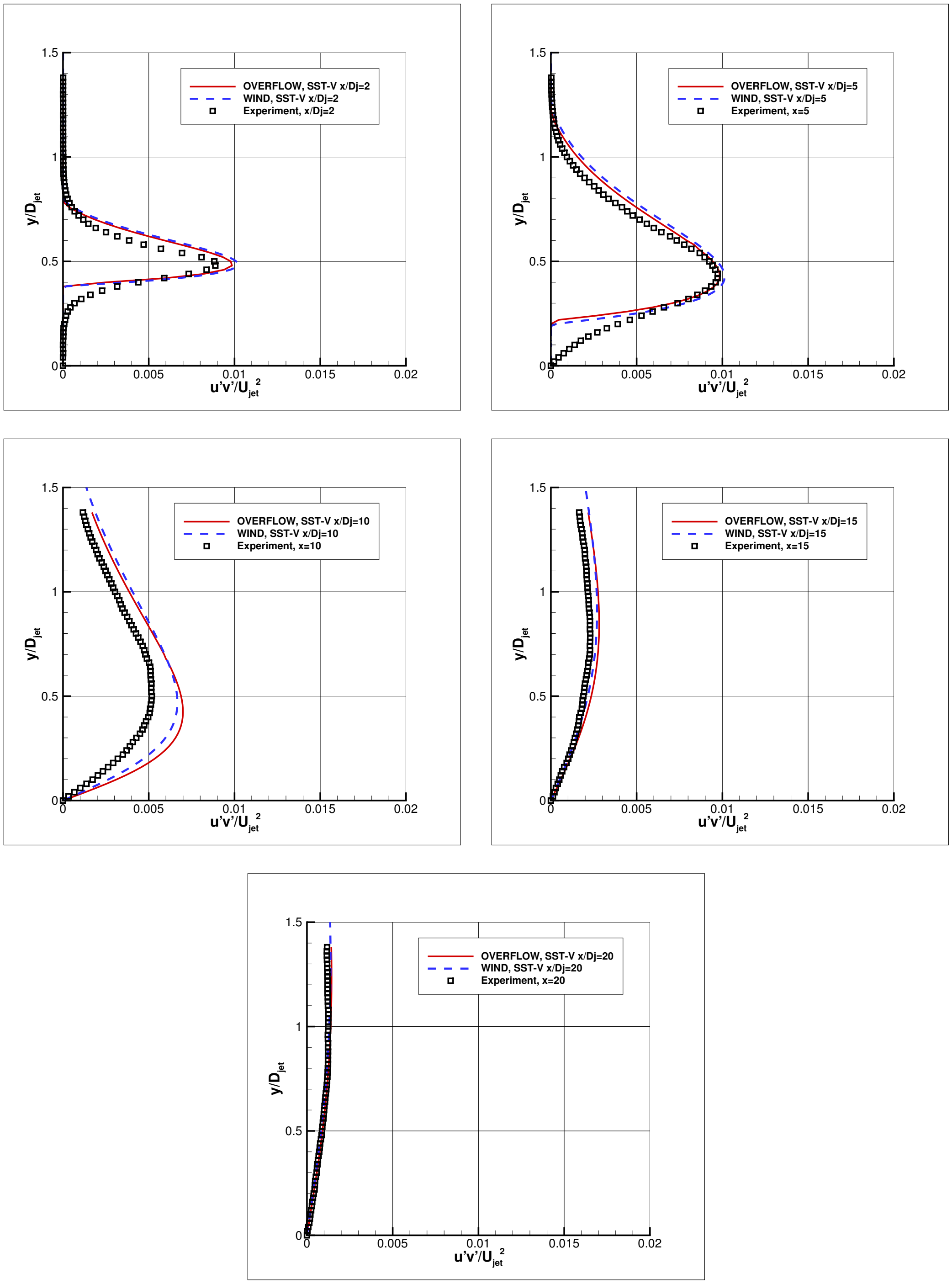

Figure 9.7: Turbulent shear stress profiles, SST-V model, $x/D_{jet} = 2$, 5, 10, 15 and 20.

10. Axisymmetric Nearsonic Jet

In this section we present turbulence model validation for Overflow using the LaRC Turbulence Modeling Resource (TMR) Axisymmetric Nearsonic Jet validation case. This case is the same as the subsonic jet validation case discussed in Section 9 except that the total pressure ratio at the jet inlet is such that the Mach number at the jet exit is approximately 0.985. The geometry and grid system are the same as for the subsonic jet validation case.

For both the SA and SST-V models, we used Roe spatial differencing along with time-accurate time stepping. The boundary condition at the upstream boundary of the plenum was the nozzle inflow condition `IBTYP=41` with parameters `BCPAR1=1.861` and `BCPAR2=1`. The condition at the downstream boundary was the fixed pressure ratio condition `IBTYP=33` with parameter `BCPAR1=1`. For the SST-V model we used Overflow input parameters `MUTINF=0.001` and `XKINF=1.622E-6`, which correspond to the freestream turbulent viscosity and freestream turbulence intensity used with the Wind code for the TMR website results. For SST-V, we used Overflow both without and with compressibility correction.

Convergence to a steady state was difficult to achieve for these cases. When run time-accurately, the flow eventually became reasonably steady.

The first set of plots, Figure 10.1, shows streamwise velocity profiles in the wake from experiment and for Overflow and the Wind code with the SA model. The Overflow and Wind data are from the second-finest grid, and the Overflow and Wind results are in good agreement.

The second set of plots, Figures 10.2, shows normal velocity profiles in the wake from experiment and for Overflow and the Wind code with the SA model. Again the Overflow and Wind results are in good agreement.

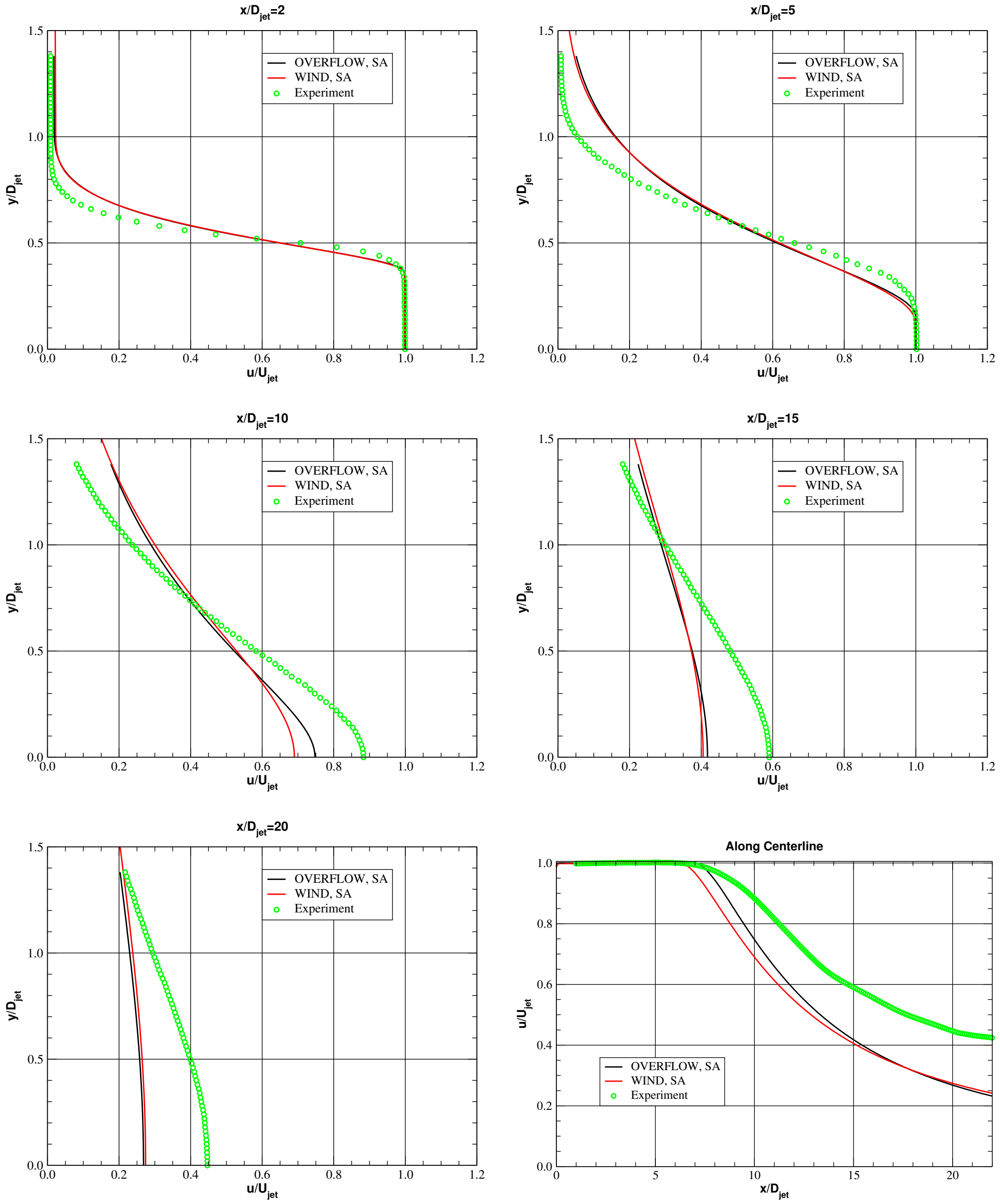

Figure 10.1: Streamwise velocity profiles, SA model, x/D_{jet} = 2, 5, 10, 15, 20, and along centerline.

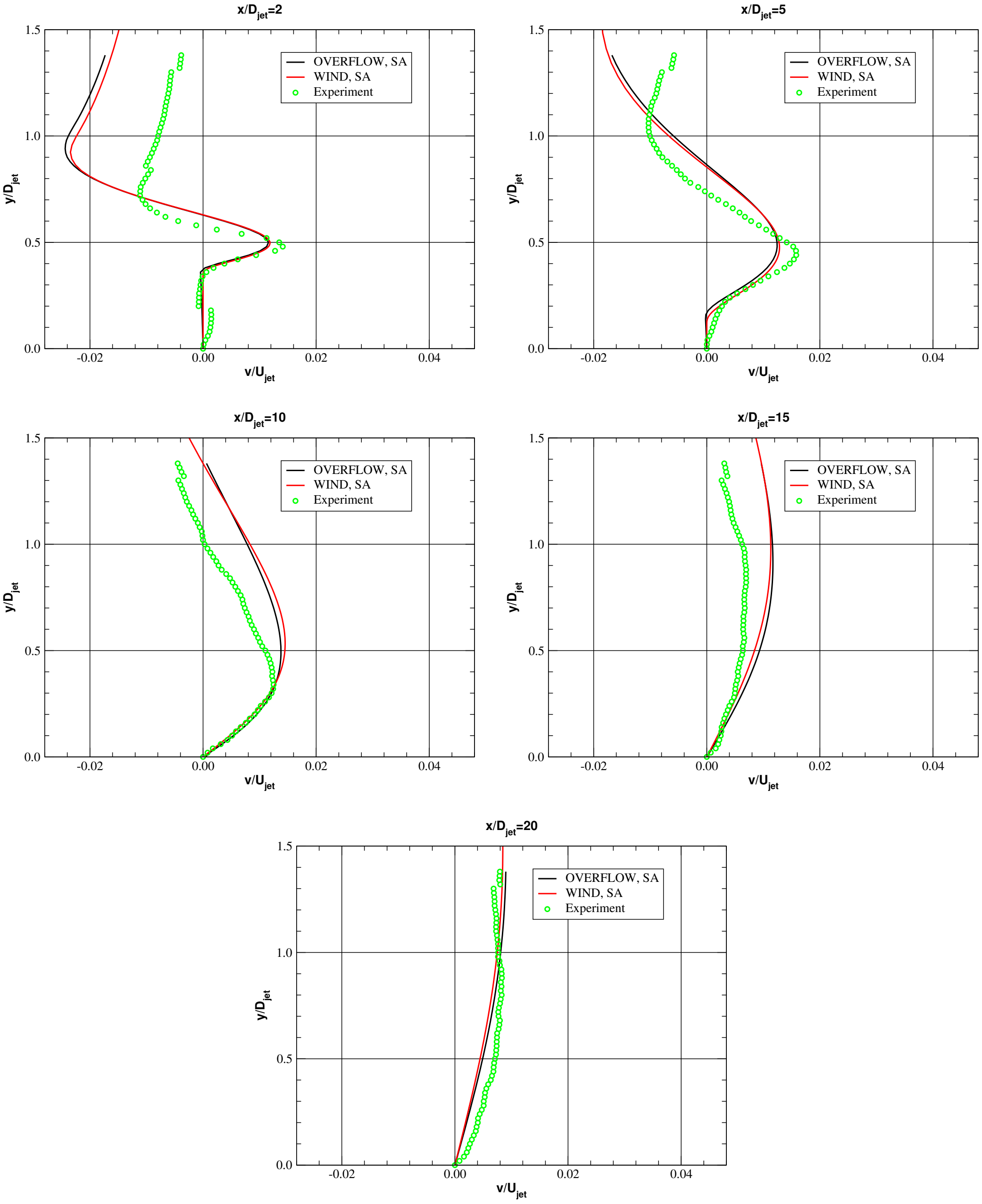

Figure 10.2: Vertical velocity profiles, SA model, $x/D_{jet} = 2, 5, 10, 15, 20$.

The next set of plots, Figures 10.3, shows turbulent shear stress profiles in the wake from experiment and for OVERFLOW and the WIND code with the SA model. Again the OVERFLOW and WIND results are in good agreement.

The next set of plots, Figure 10.4, shows streamwise velocity profiles in the wake from experiment and for OVERFLOW and the WIND code with the SST-V model. The OVERFLOW and WIND data are from the second-finest grid. The OVERFLOW computations did not use compressibility correction.

The next set of plots, Figure 10.5, shows vertical velocity profiles in the wake from experiment and for OVERFLOW and the WIND code with the SST-V model. Again the OVERFLOW computations did not use compressibility correction.

The next set of plots, Figure 10.6, shows turbulent shear stress profiles in the wake from experiment and for OVERFLOW and the WIND code with the SST-V model.

The next set of plots, Figure 10.7, shows turbulent kinetic energy profiles, comparing OVERFLOW with SST-V with the WIND code and experiment.

The next sets of plots show OVERFLOW computations with SST-V using compressibility correction. In general, it seems that using the compressibility correction gives results that are closer to experiment compared with not using compressibility correction.

We also ran OVERFLOW with the SST model. We found that OVERFLOW results with SST and no compressibility correction were very similar to OVERFLOW results with SST-V and no compressibility correction. Also, OVERFLOW results with SST and compressibility correction were very similar to OVERFLOW results with SST-V and compressibility correction. We only noticed differences in the turbulent kinetic energy profiles at the two downstream stations; see Figure 10.12.

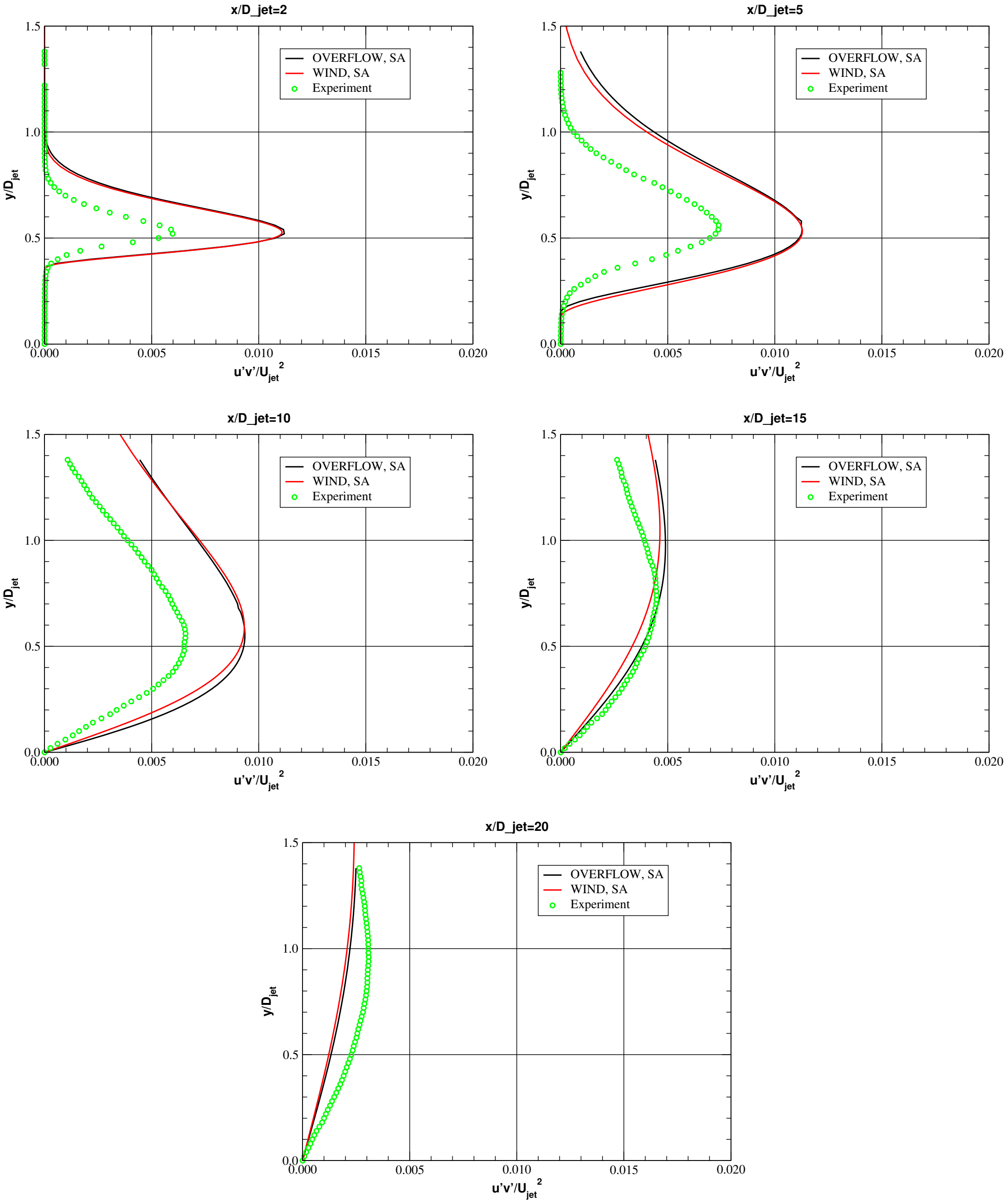

Figure 10.3: Turbulent shear stress profiles, SA model, $x/D_{jet} = 2$, 5, 10, 15, and 20.

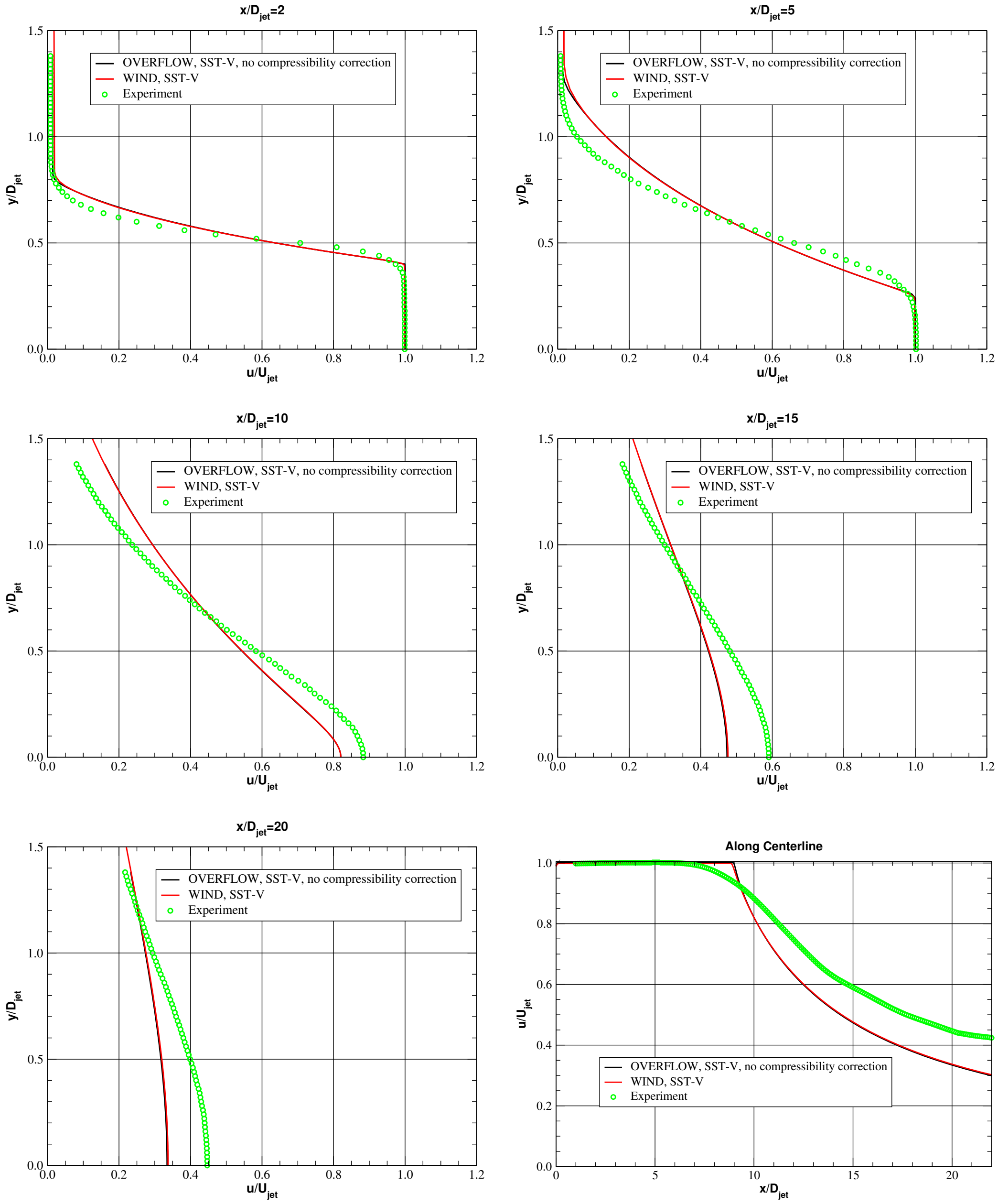

Figure 10.4: Streamwise velocity profiles, SST-V model, x/D_{jet} = 2, 5, 10, 15, 20, and along centerline.

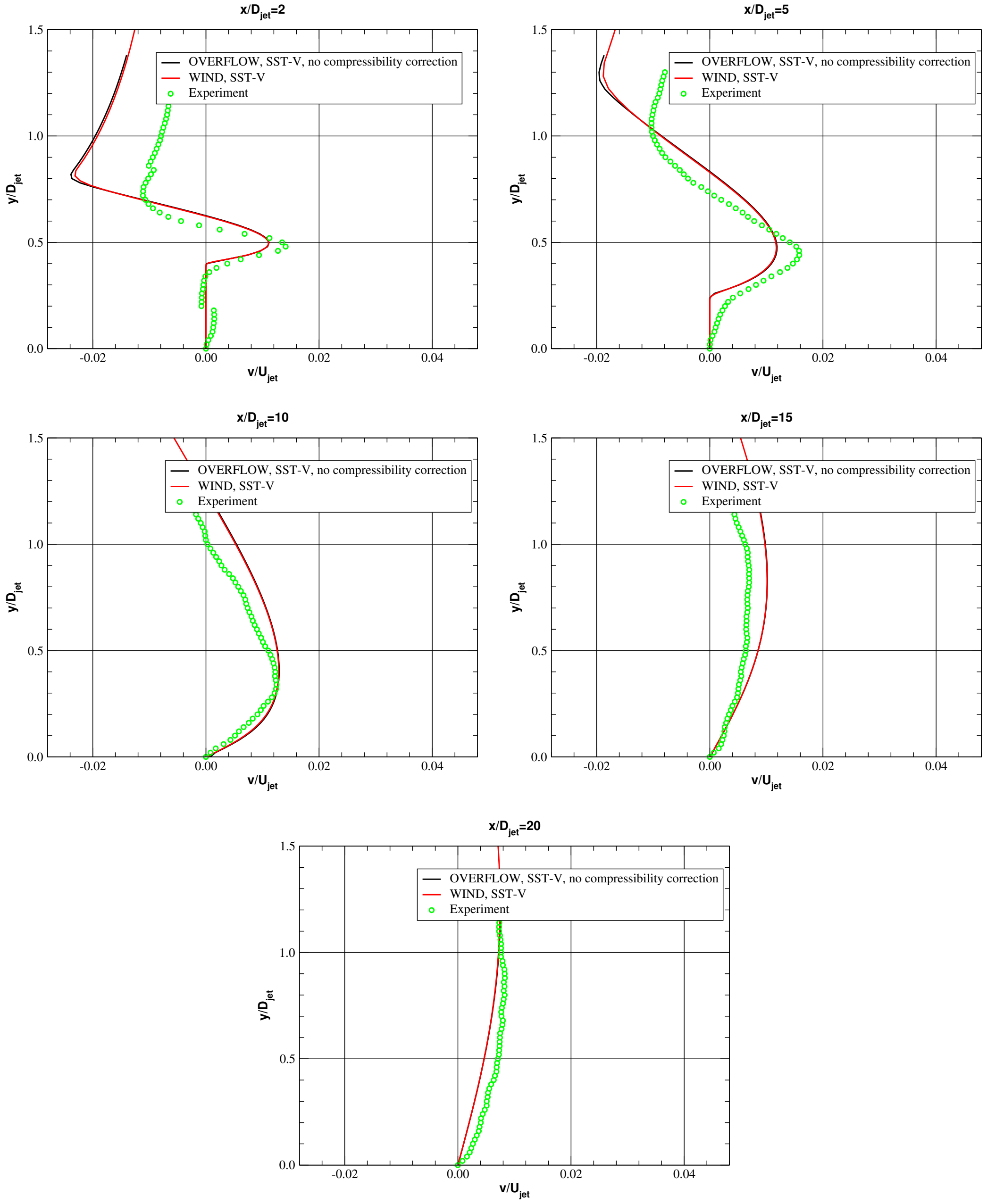

Figure 10.5: Vertical velocity profiles, SST-V, $x/D_{jet} = 2$, 5, 10, 15, and 20.

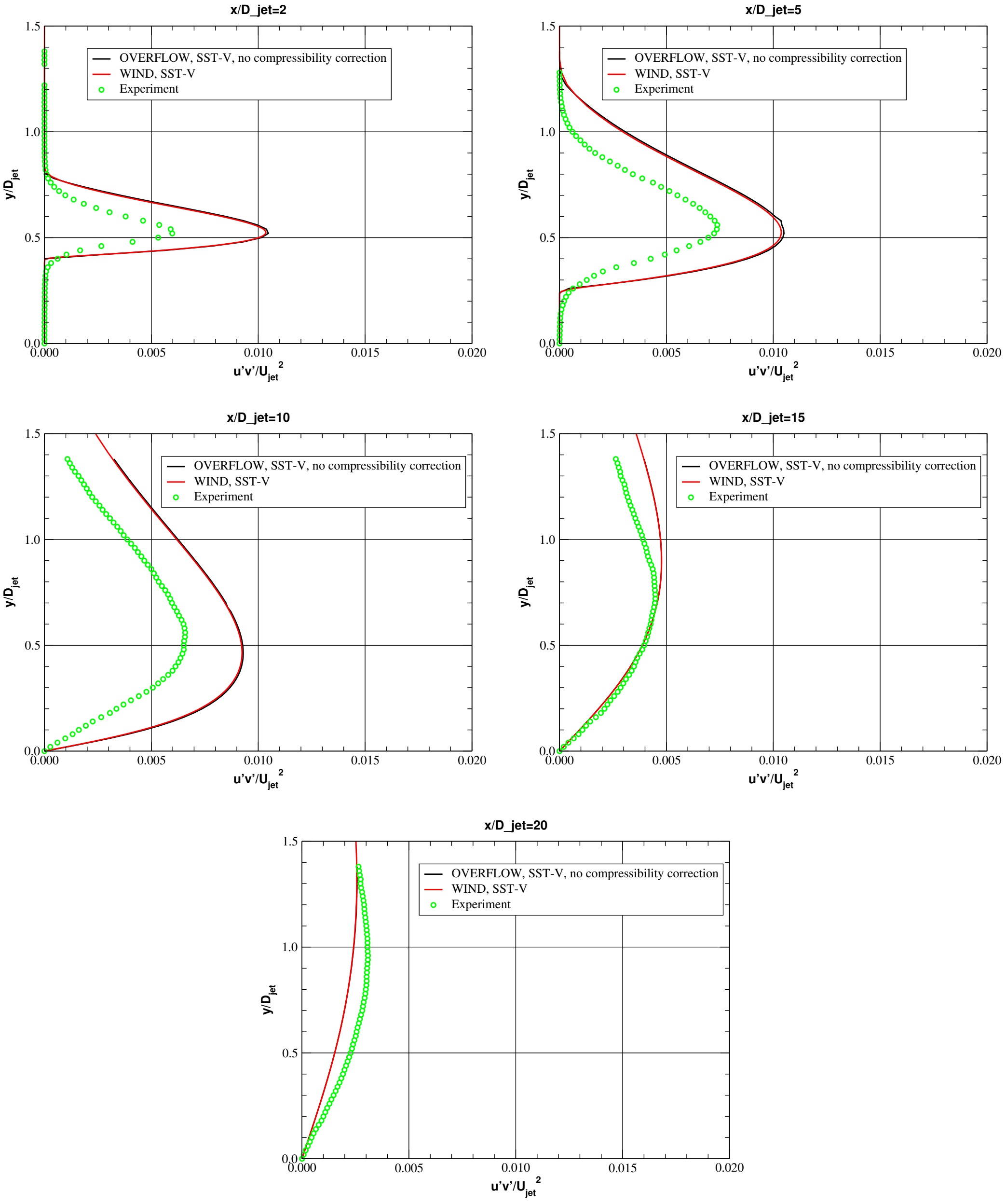

Figure 10.6: Turbulent shear stress profiles, SST-V, x/D_{jet} = 2, 5, 10, 15, and 20.

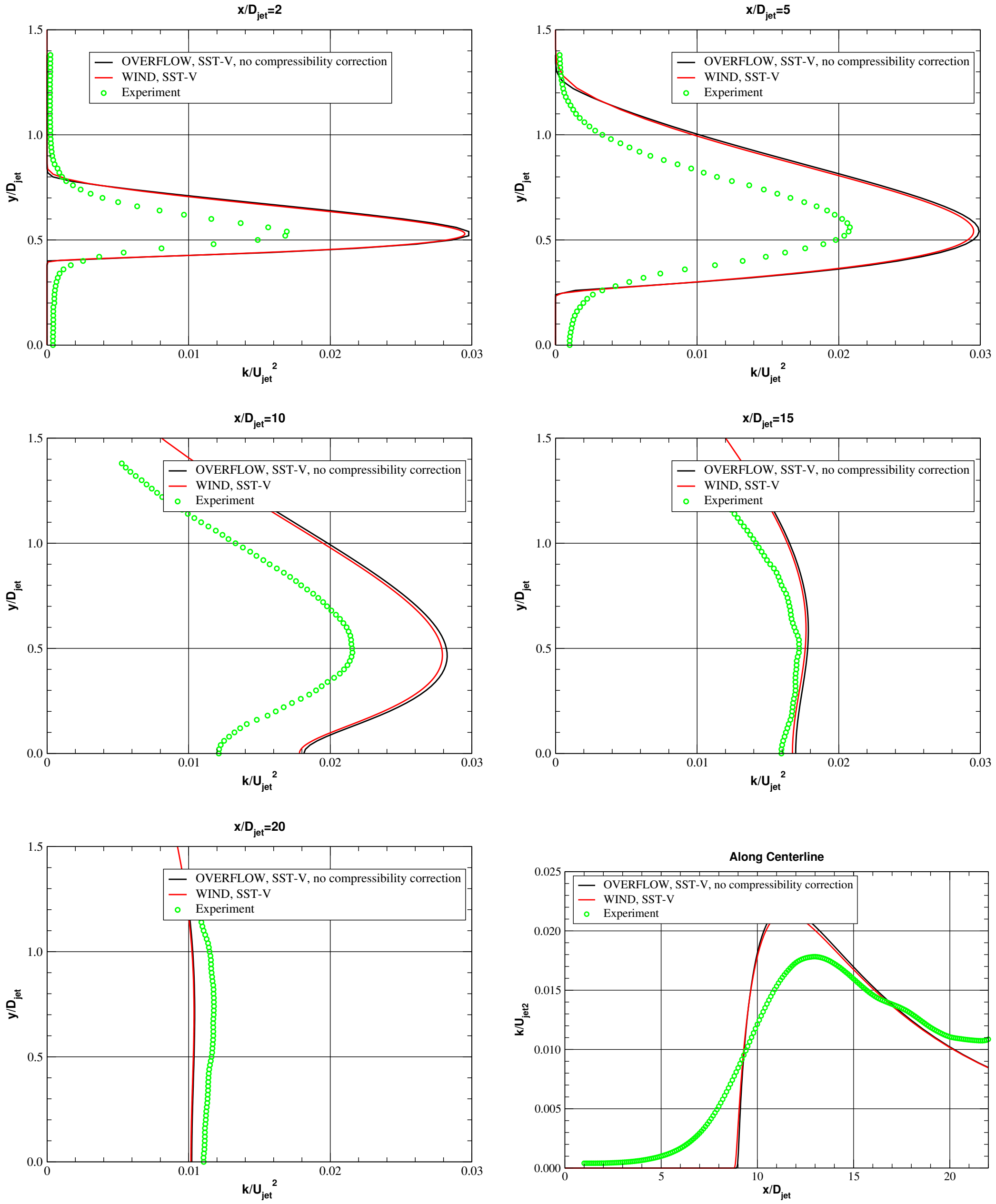

Figure 10.7: Turbulent kinetic energy profiles, SST-V model, $x/D_{jet} = 2, 5, 10, 15, 20$, and along centerline.

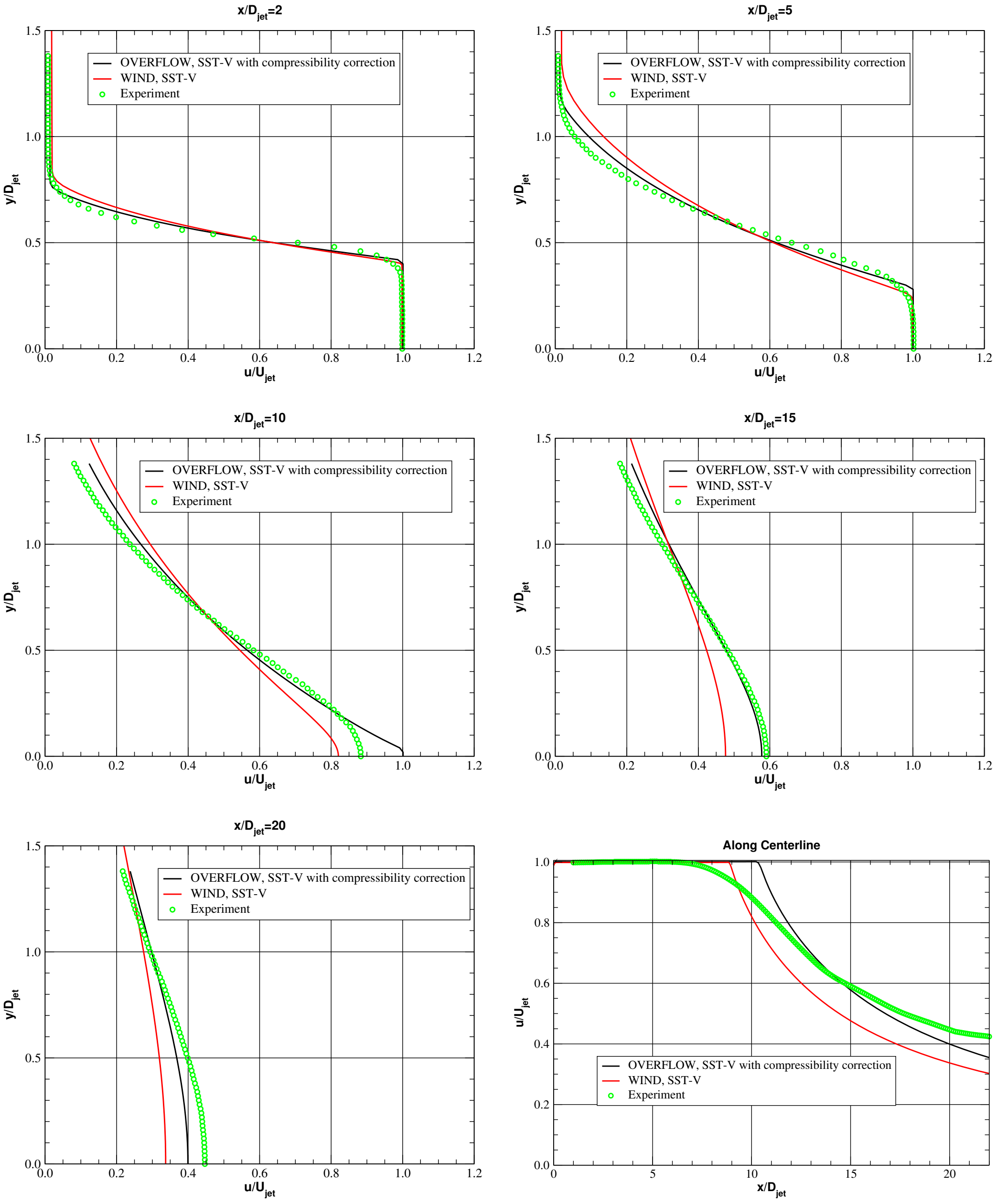

Figure 10.8: Streamwise velocity profiles, SST-V model, x/D_{jet} = 2, 5, 10, 15, 20, and along centerline.

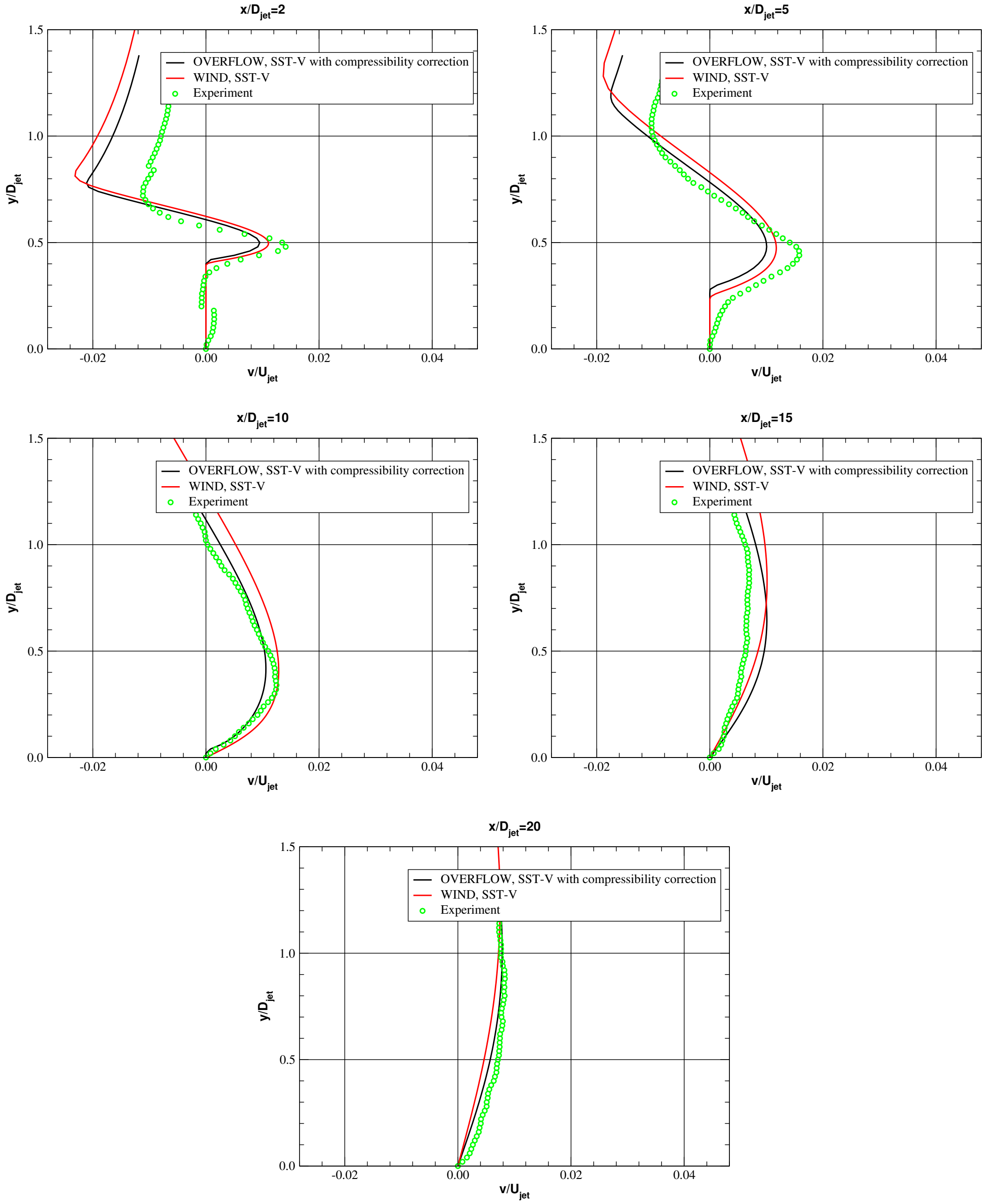

Figure 10.9: Vertical velocity profiles, SST-V, $x/D_{jet} = 2$, 5, 10, 15, and 20.

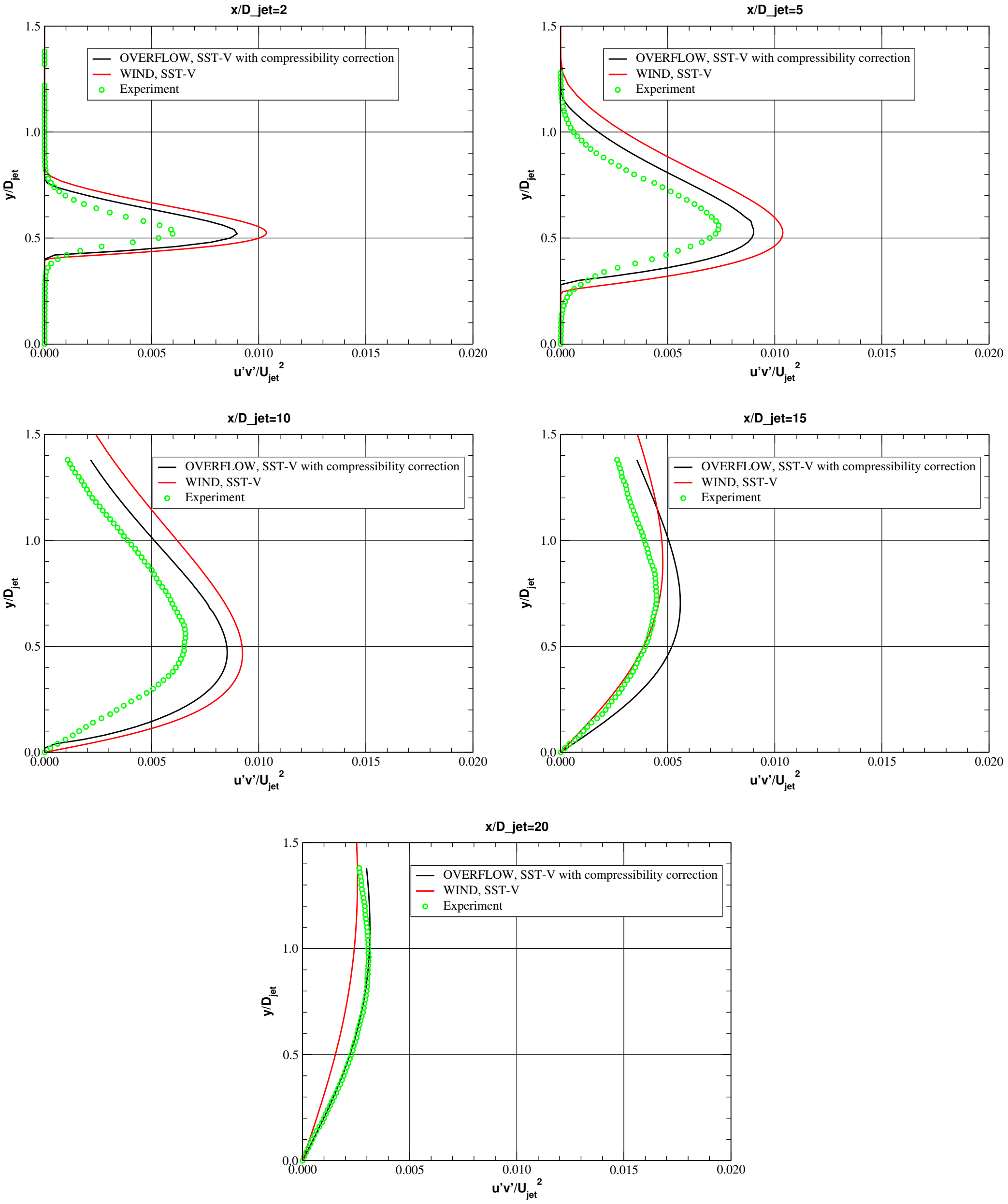

Figure 10.10: Turbulent shear stress profiles, SST-V, x/D_{jet} = 2, 5, 10, 15, and 20.

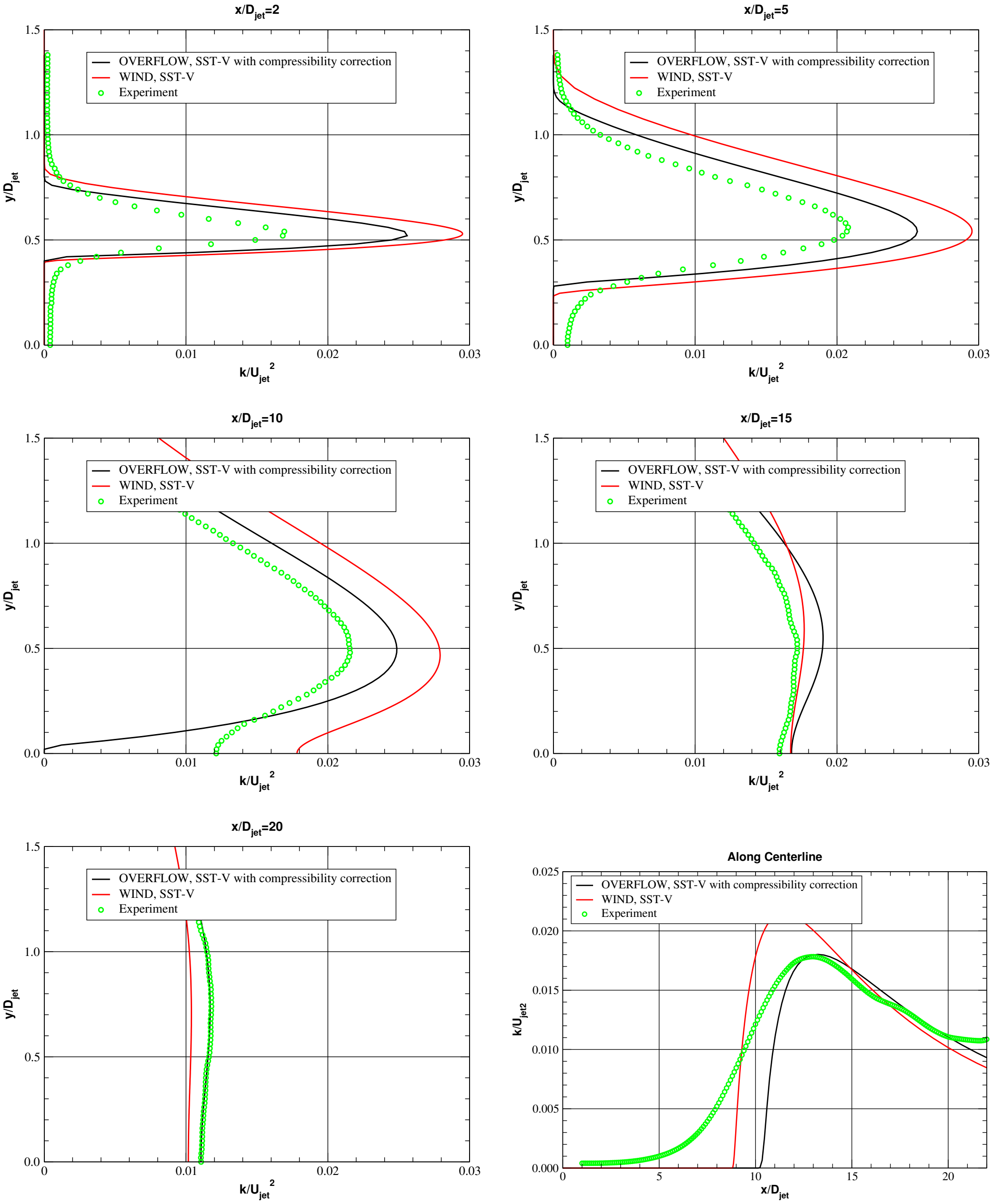

Figure 10.11: Turbulent kinetic energy profiles, SST-V model, $x/D_{jet} = 2$, 5, 10, 15, 20, and along centerline.

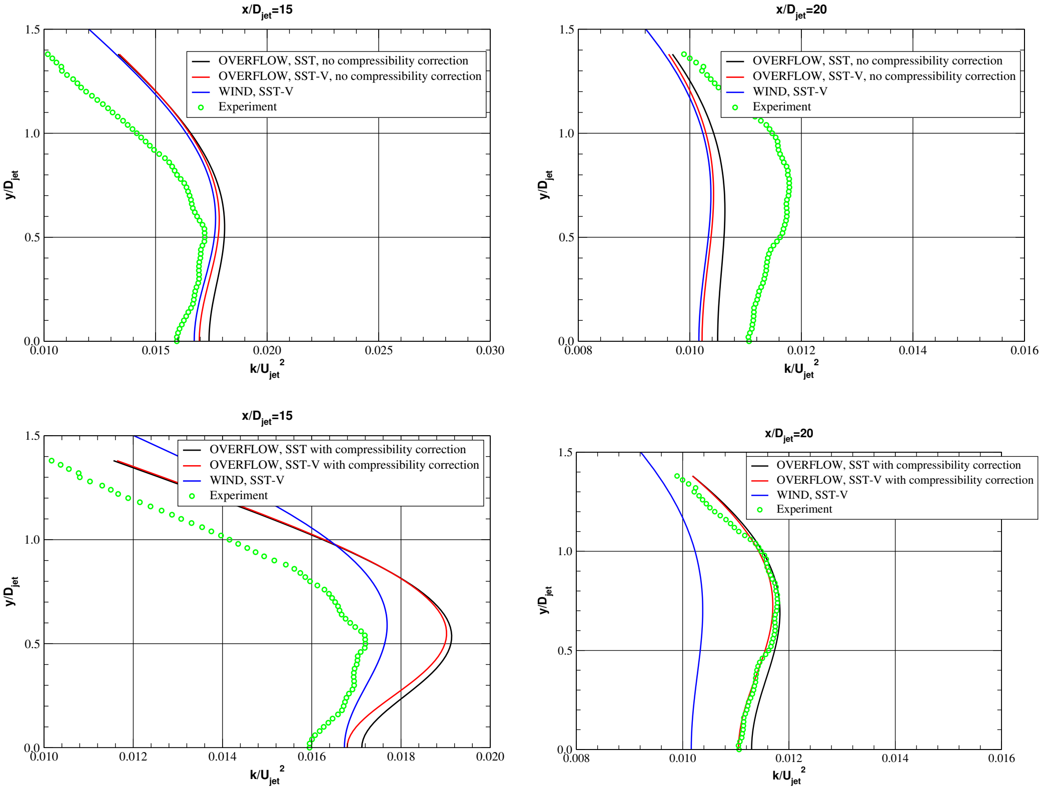

Figure 10.12: Turbulent kinetic energy profiles, $x/D_{jet} = 15$, 20, comparing SST and SST-V.

11. Axisymmetric Separated Boundary Layer

In this section we present turbulence model validation for Overflow using the LaRC Turbulence Modeling Resource (TMR) Axisymmetric Separated Boundary Layer validation case. This case has Mach number $M = 0.08812$ and Reynolds number $Re = 2,000,000$ based on a length of 1 meter. The geometry and flow conditions are shown in Figure 11.1, taken from the TMR website.

The grid system provided for this case is indicated in Figure 11.2. For Overflow, to simplify the task of plotting velocity and turbulent shear stress profiles, we adjoined seven line segments as data surface grids where data was to be plotted. The input files for Overflow specified axisymmetric mode, multigrid, Roe differencing, low-Mach preconditioning and matrix dissipation. We used `DT=0.1`, `SMOO=0`, and `CFLT=4`. For the SA model we used `CFLMIN=25` and for the SST model we used `CFLMIN=15`. The boundary conditions at inflow were fixed at freestream values (`IBTYP=40`) and the boundary conditions at outflow were fixed pressure conditions (`IBTYP=33` with corresponding `BCPAR=1`). On the second-finest grid we used two MPI ranks, and the root mean square residuals of the mean flow equations converged to machine zero in about 17,000 time steps.

Figure 11.3 shows pressure coefficient and skin friction for the SA model. The Overflow and Cfl3d data are from the second-finest grid. The Overflow and Cfl3d results are in good agreement with experiment.

The next plots, Figure 11.4, show streamwise velocity profiles in the wake from experiment and for Overflow and Cfl3d with the SA model. The codes are in good agreement with experiment.

Figure 11.5 shows turbulent shear stress profiles in the wake from experiment and for Overflow and Cfl3d using the SA model.

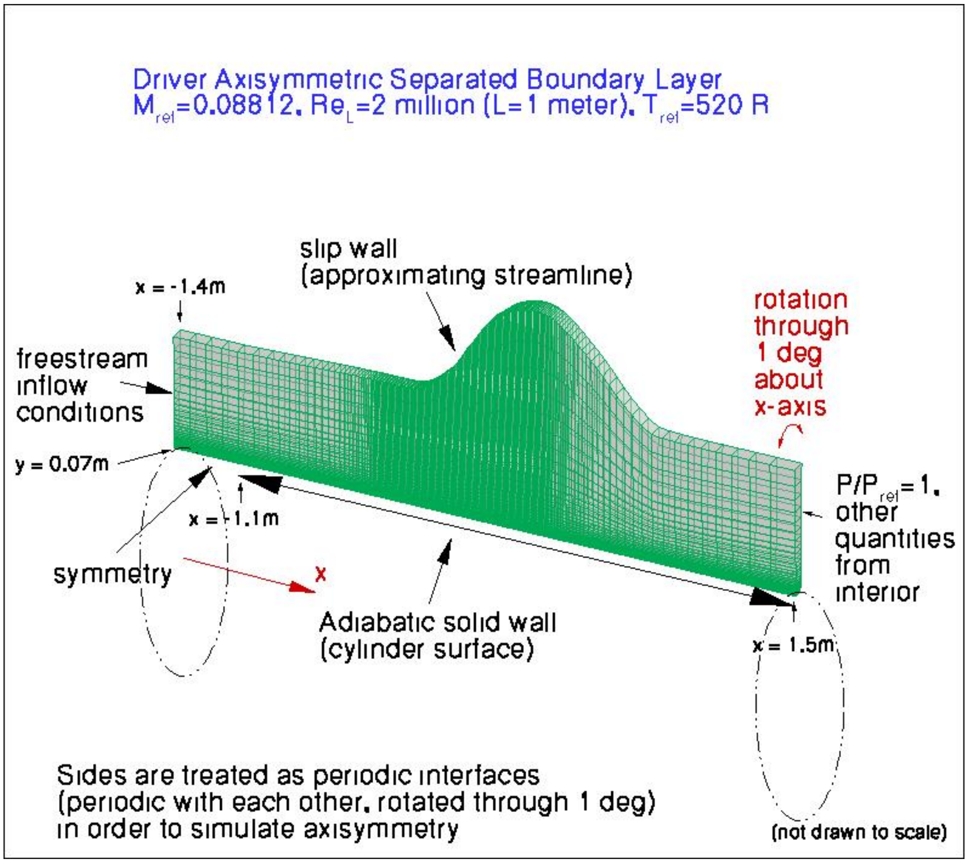

Figure 11.1: Axisymmetric separated boundary layer geometry.

Figure 11.6 shows pressure coefficient and skin friction for the SST model.

The next plots, Figure 11.7, show streamwise velocity profiles in the wake from experiment and for Overflow and Cfl3d with the SST model.

The final plots, Figure 11.8, show turbulent shear stress profiles in the wake from experiment and for Overflow and Cfl3d using the SST model.

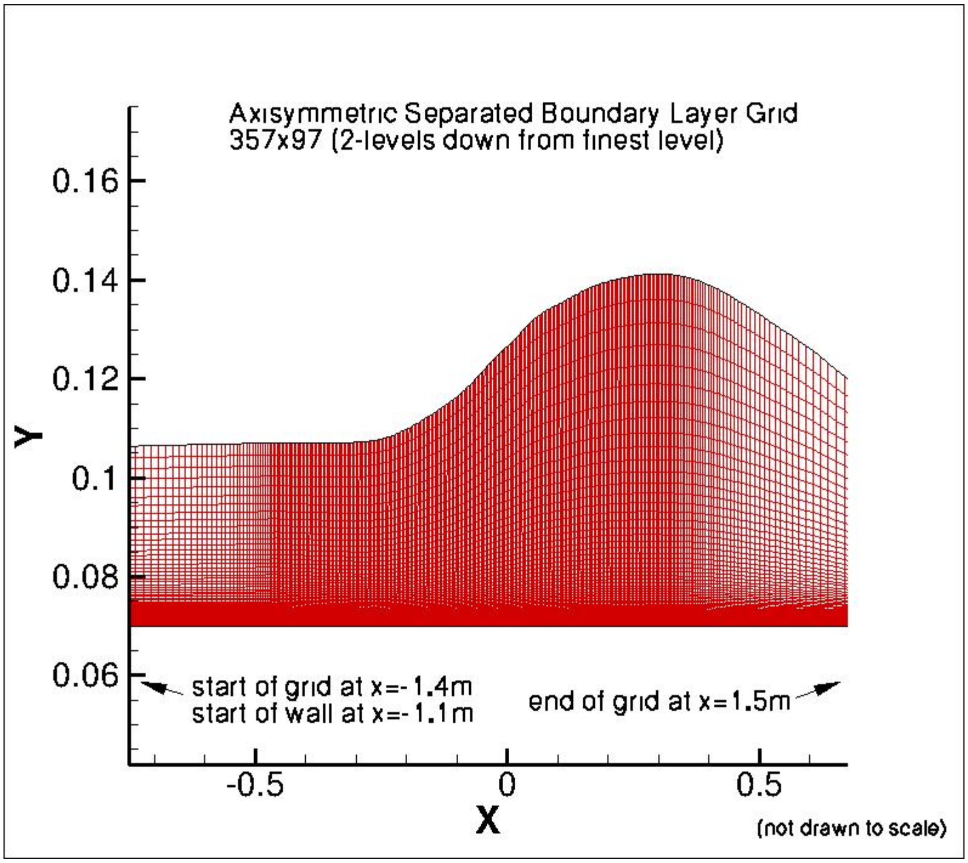

Figure 11.2: Portion of axisymmetric separated boundary layer grid.

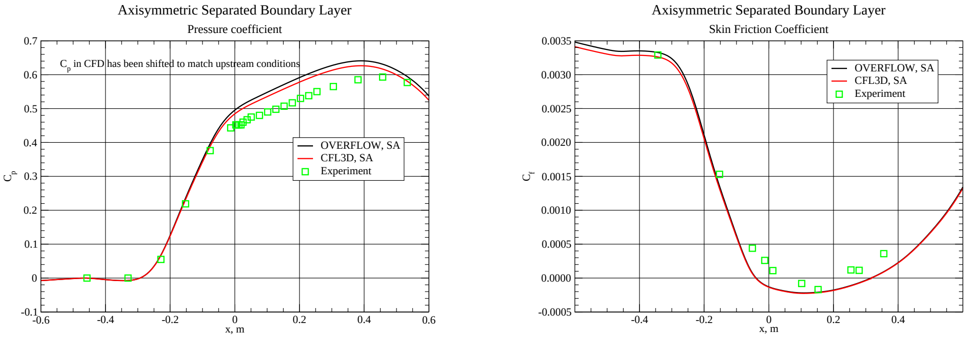

Figure 11.3: Pressure coefficient and skin friction, SA model.

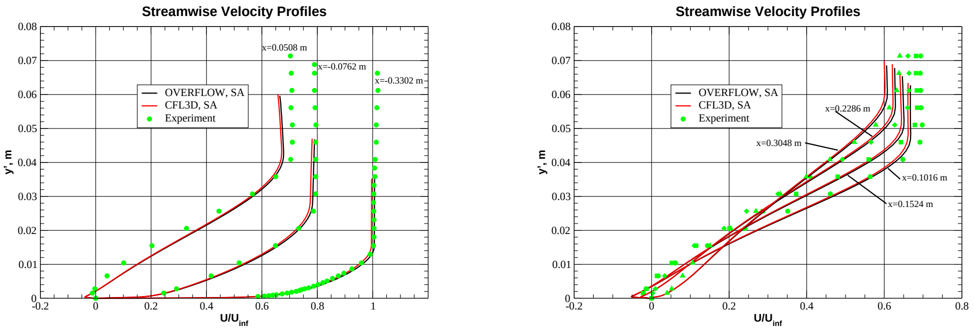

Figure 11.4: Streamwise velocity profiles, SA model.

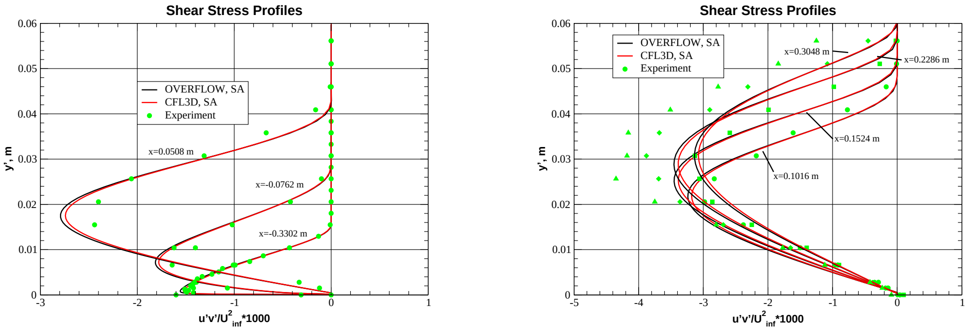

Figure 11.5: Turbulent shear stress profiles, SA model.

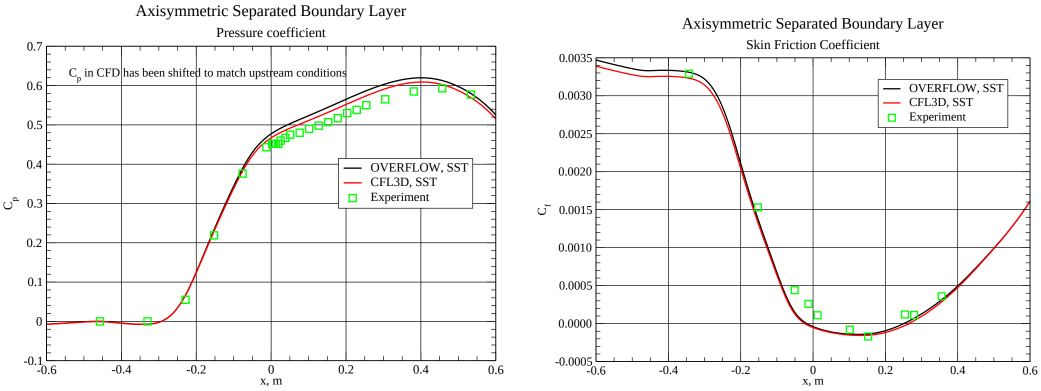

Figure 11.6: Pressure coefficient and skin friction, SST model.

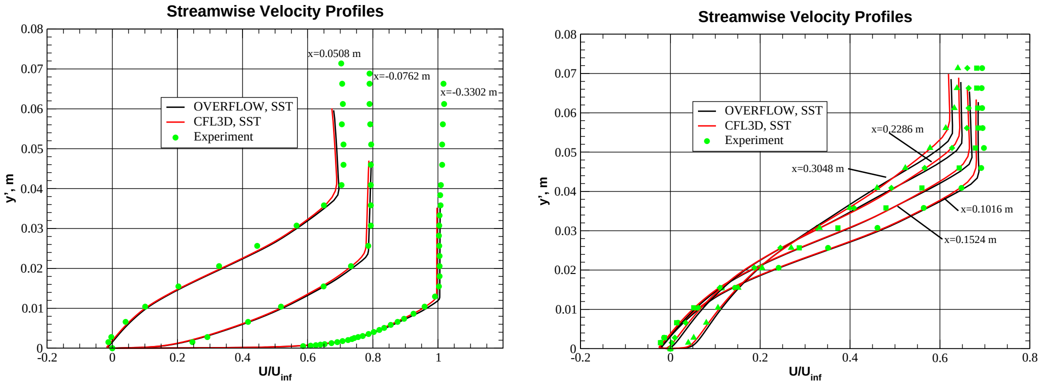

Figure 11.7: Streamwise velocity profiles, SST model.

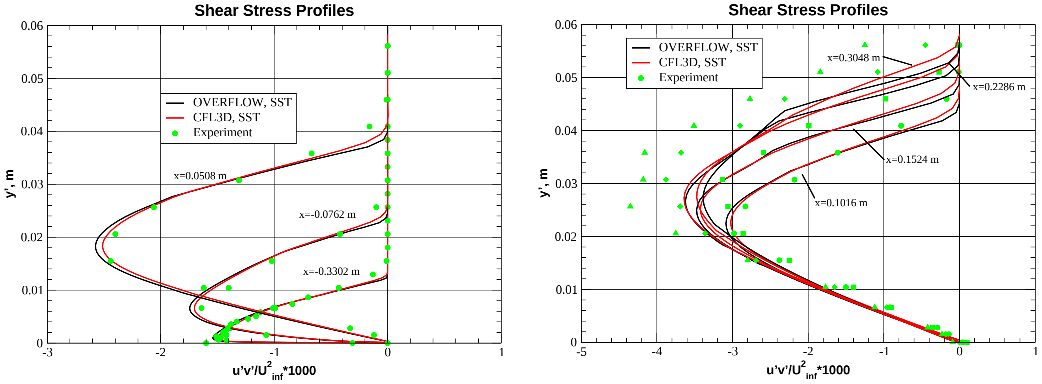

Figure 11.8: Turbulent shear stress profiles, SST model.

12. Axisymmetric Transonic Bump

In this section we present turbulence model validation for Overflow using the LaRC Turbulence Modeling Resource (TMR) Axisymmetric Transonic Bump validation case. This case has Mach number $M = 0.875$ and Reynolds number $Re = 2.763$ million. The geometry and flow conditions are shown in Figure 12.1, taken from the TMR website.

The grid system provided for this case is indicated in Figure 12.2. For Overflow, to simplify the task of plotting velocity and turbulent shear stress profiles, we adjoined 6 line segments as data surface grids where data was to be plotted. The input files for Overflow specified axisymmetric mode, multigrid, and central differencing. We had `DT=0.01`, `SMOO=0.04` and `CFLT=4`. For the SA model we had `CFLMIN=10` and for the SST model we took `CFLMIN=5`. The boundary conditions at inflow were fixed at freestream values (`IBTYP=40`), the boundary conditions at outflow were pure extrapolation (`IBTYP=30`), and the boundary condition at the far field was `IBTYP=47`, the freestream/characteristic condition. On the second-finest grid we used six MPI ranks. On this grid, the root-mean-square flow residuals decreased about nine orders of magnitude for the SA model and about four orders of magnitude for the SST model in 10,000 time steps.

Figure 12.3 shows pressure coefficient and skin friction for the SA model. The Overflow and Cfl3d data are from the second-finest grid. The Overflow and Cfl3d results are indistinguishable to plotting accuracy.

The next plots, Figure 12.4, show streamwise velocity profiles in the wake from experiment and for Overflow and Cfl3d with the SA model. The results from the two codes plot atop one another.

Figure 12.5, shows turbulent shear stress profiles in the wake from experiment and for Overflow and Cfl3d using the SA model. The two codes

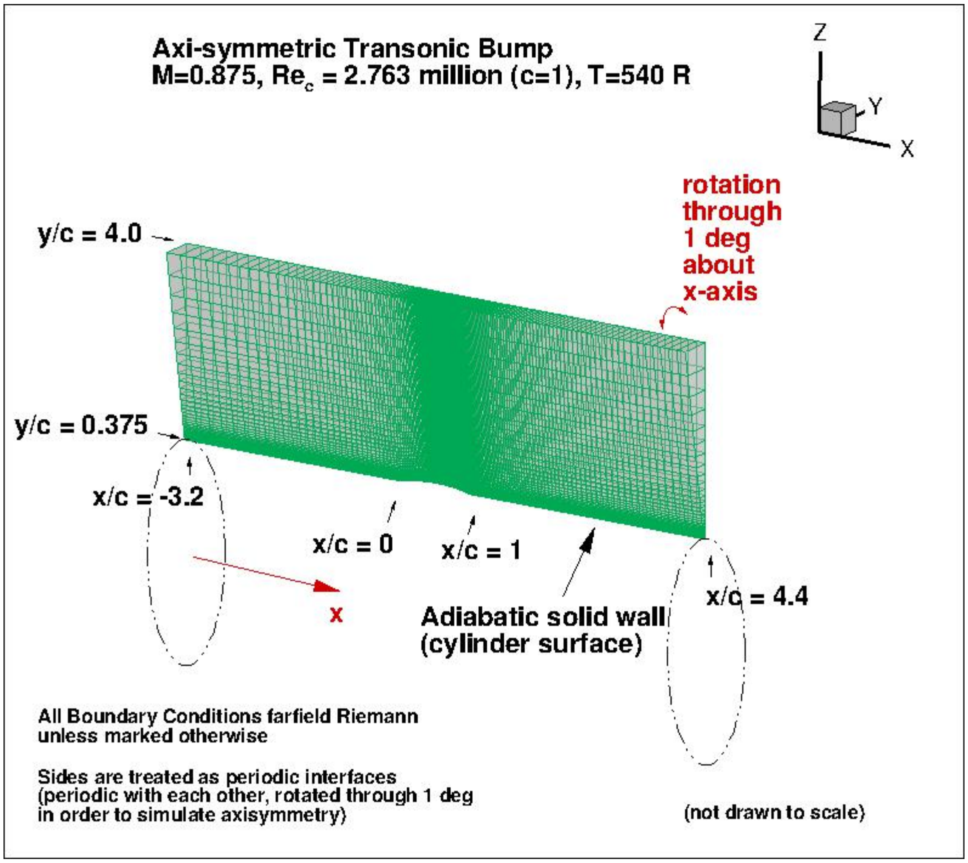

Figure 12.1: Axisymmetric transonic bump geometry.

give results that are nearly indistinguishable.

Figure 12.6 shows pressure coefficient and skin friction for the SST model. The two codes agree very well with one another.

The next plots, Figure 12.7, show streamwise velocity profiles in the wake from experiment and for Overflow and Cfl3d with the SST model.

The final plots, Figure 12.8, show turbulent shear stress profiles in the wake from experiment and for Overflow and Cfl3d using the SST model.

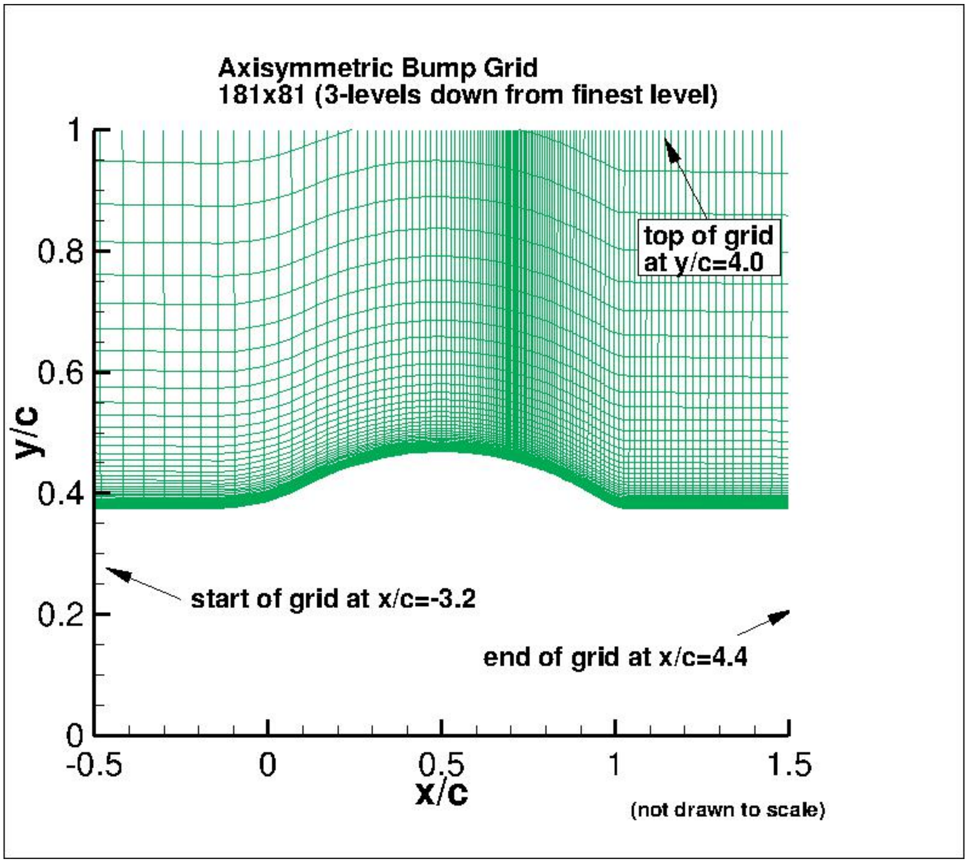

Figure 12.2: Portion of axisymmetric transonic bump grid.

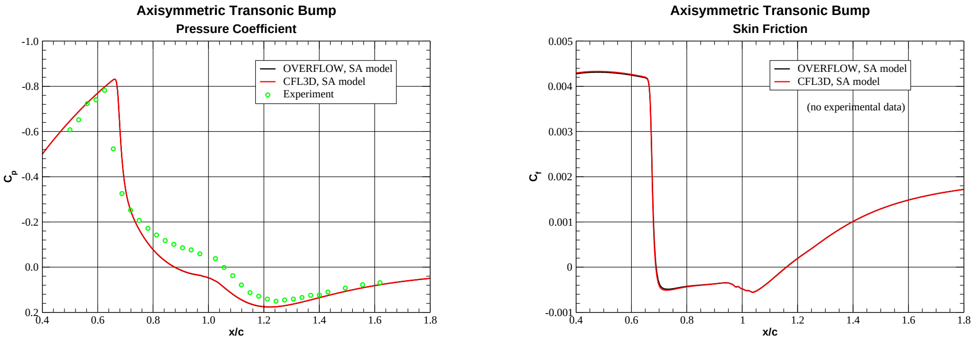

Figure 12.3: Pressure coefficient and skin friction, SA model.

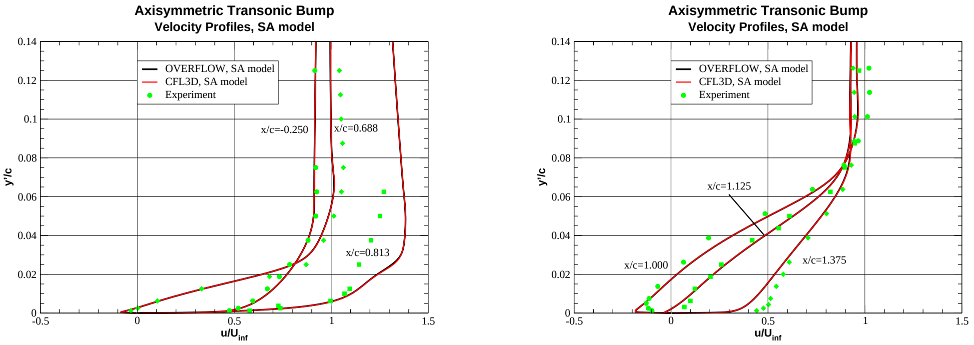

Figure 12.4: Streamwise velocity profiles, SA model.

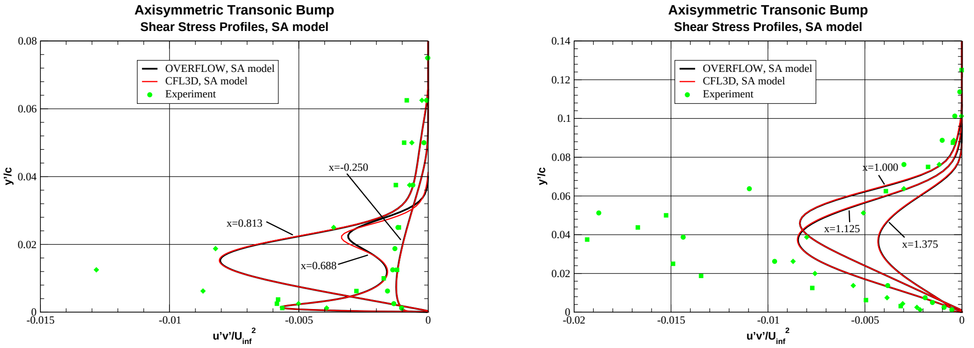

Figure 12.5: Turbulent shear stress profiles, SA model.

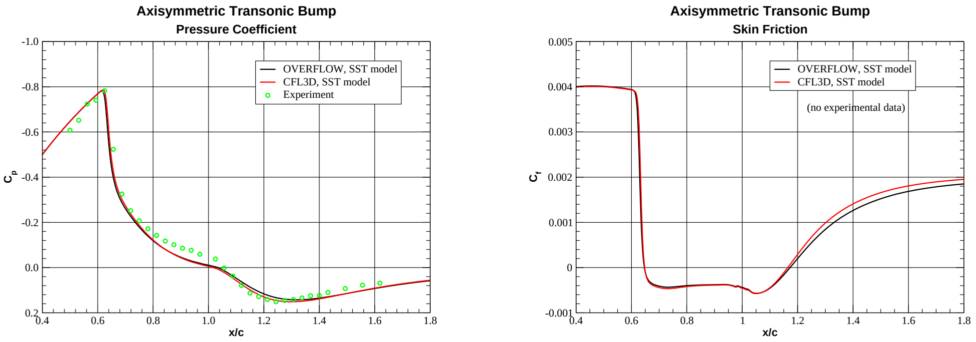

Figure 12.6: Pressure coefficient and skin friction, SST model.

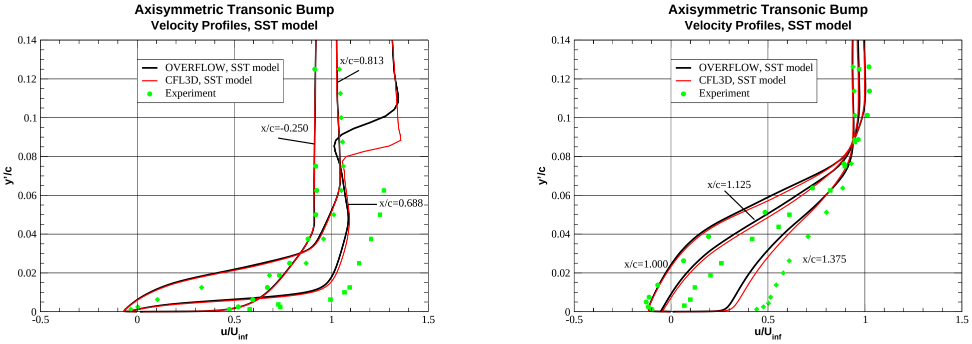

Figure 12.7: Streamwise velocity profiles, SST model.

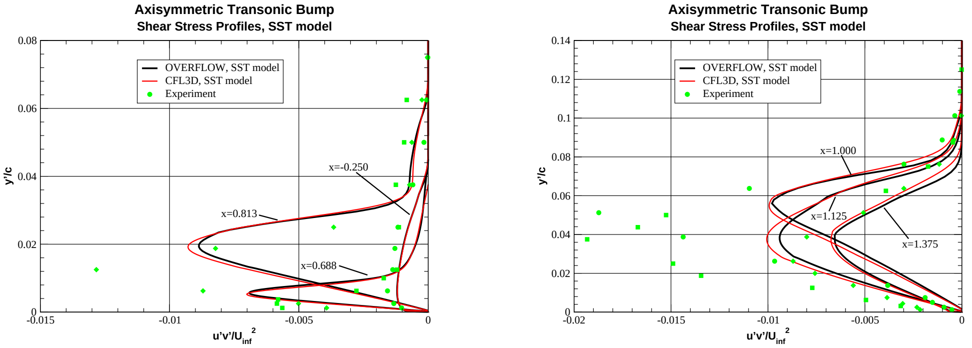

Figure 12.8: Turbulent shear stress profiles, SST model.

13. High Mach Number Flat Plate

In this section we present turbulence model validation for OVERFLOW using the LaRC Turbulence Modeling Resource (TMR) High Mach Number Flat Plate validation case. This case involves a Reynolds number based on unit length of 15 million and four flow conditions, with Mach numbers and wall temperatures varying. The four flow conditions are:

- $M_\infty = 2$, $T_{wall}/T_\infty = 1.712$
- $M_\infty = 5$, $T_{wall}/T_\infty = 1.090$
- $M_\infty = 5$, $T_{wall}/T_\infty = 2.725$
- $M_\infty = 5$, $T_{wall}/T_\infty = 5.450$

The geometry and boundary conditions for this case are shown in Figure 13.1, taken from the TMR web site. The grid is the same as the finest grid for the flat plate validation case, with dimensions 545×385.

The input files for OVERFLOW specified multigrid, HLLE++ upwind differencing [12] (`IRHS=6`), and SSOR (`ILHS=17`) for the left-hand side operator; we used `DT=1.0` and `CFLMIN=1`. The boundary conditions at inflow were taken as freestream values (`IBTYP=40`), the boundary conditions at outflow were pure extrapolation (`IBTYP=30`) and the boundary condition at the far field was `IBTYP=47`, the freestream/characteristic condition. The wall boundary condition was the viscous wall constant temperature condition `IBTYP=7` with `BCPAR1` set to the wall temperature. We used 12 MPI ranks.

Drag convergence for these cases is shown in figures 13.2 and 13.3. Convergence is clear for all cases.

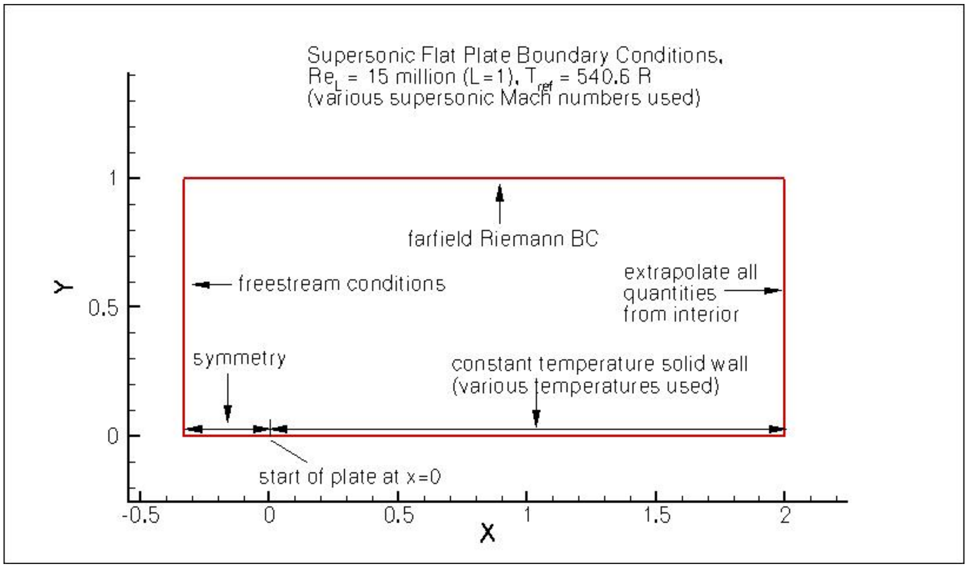

Figure 13.1: High Mach number flat plate geometry.

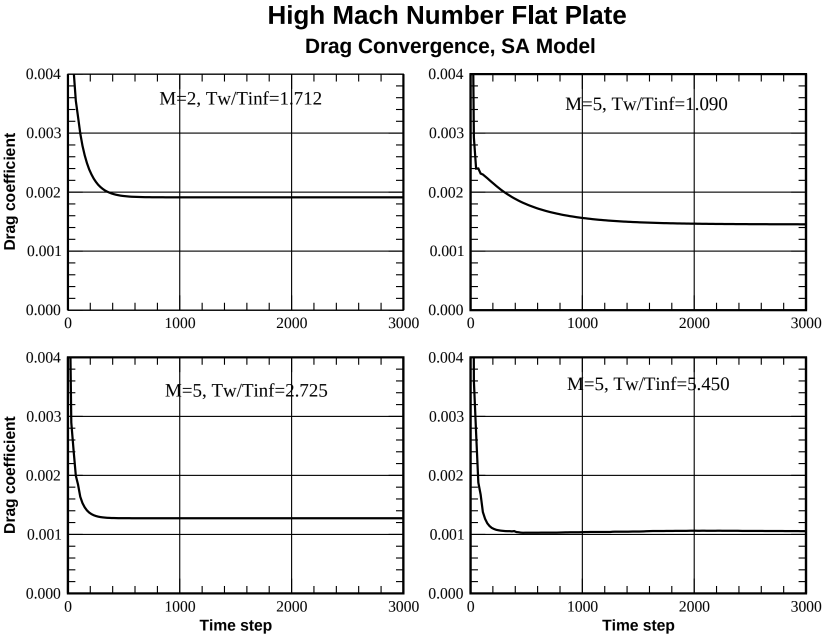

Figure 13.2: Drag convergence, Overflow, SA model.

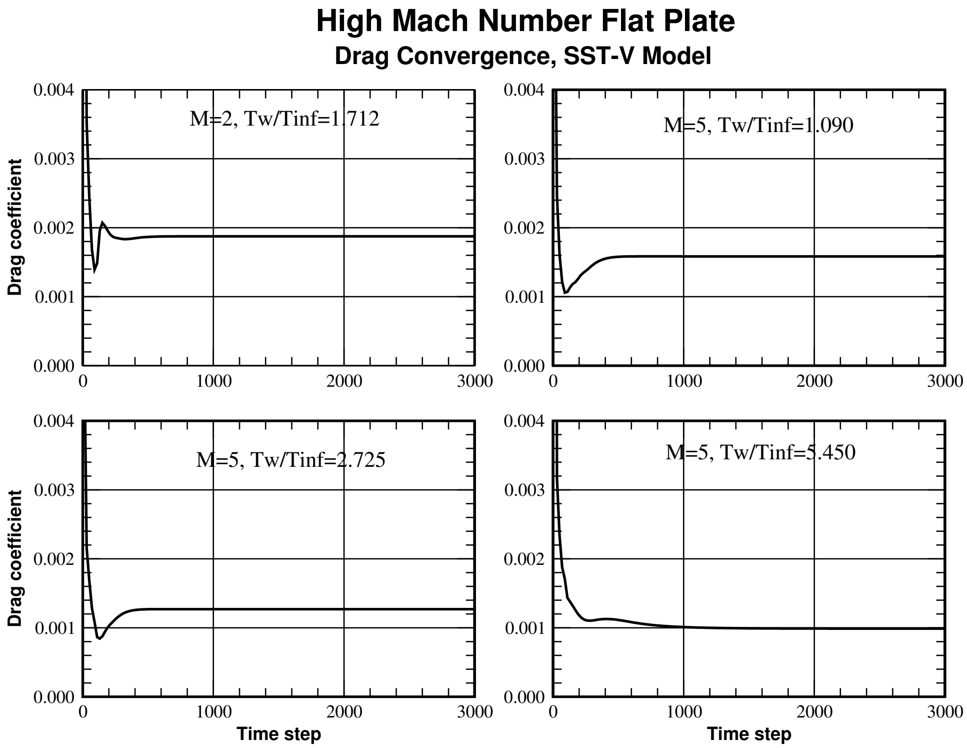

Figure 13.3: Drag convergence, OVERFLOW, SST-V model.

Next, figures 13.4 and 13.5 show plots of skin friction coefficient computed with the SA and SST-V models for the four cases. The OVERFLOW and CFL3D results are very close. With regard to the discrepancy between theory and computation for the SA model at $M = 5$, $T_w/T_\infty = 1.090$, the TMR website and its references mention that the theoretical results are somewhat uncertain, especially for the strongly cooled case: $T_w/T_\infty = 1.090$ corresponds to $T_{\text{wall}}/T_{\text{adiabatic wall}} \approx 0.2$.

The final plots, figures 13.6 and 13.7, show u^+ vs. $\log_{10}(y^+)$ for SA and SST-V. The OVERFLOW and CFL3D results are very close to one another.

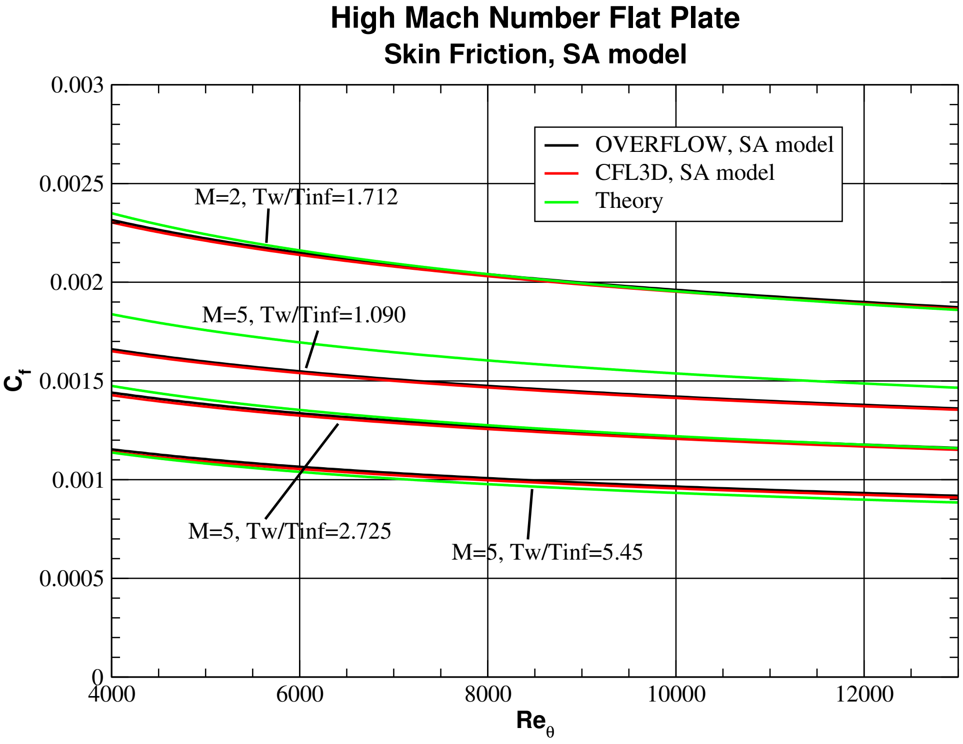

Figure 13.4: Skin friction, SA model.

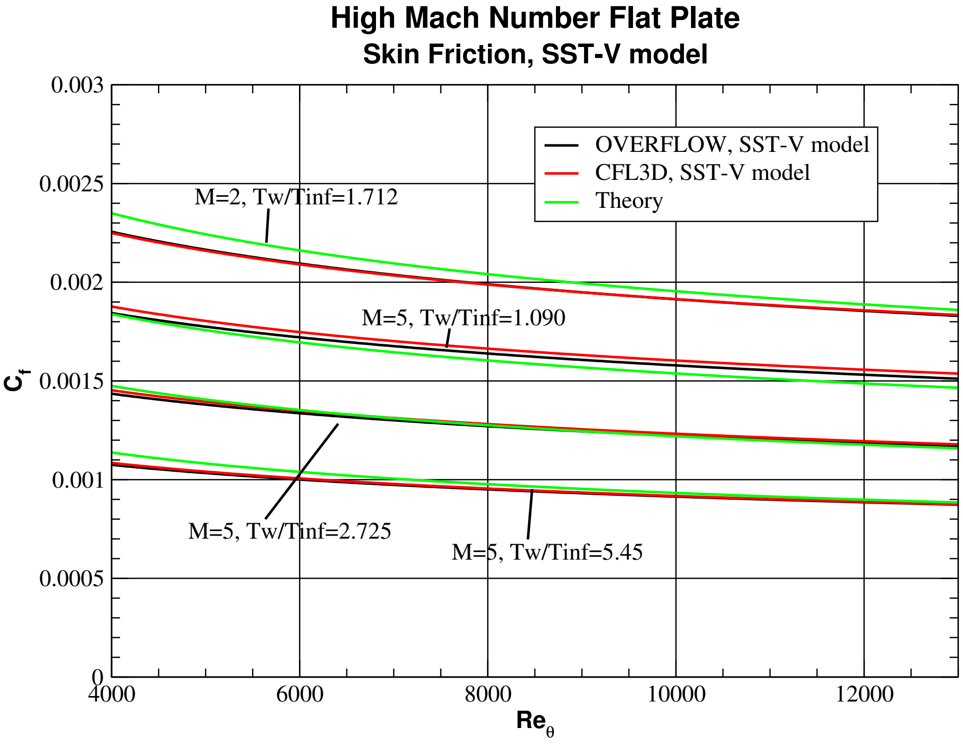

Figure 13.5: Skin friction, SST-V model.

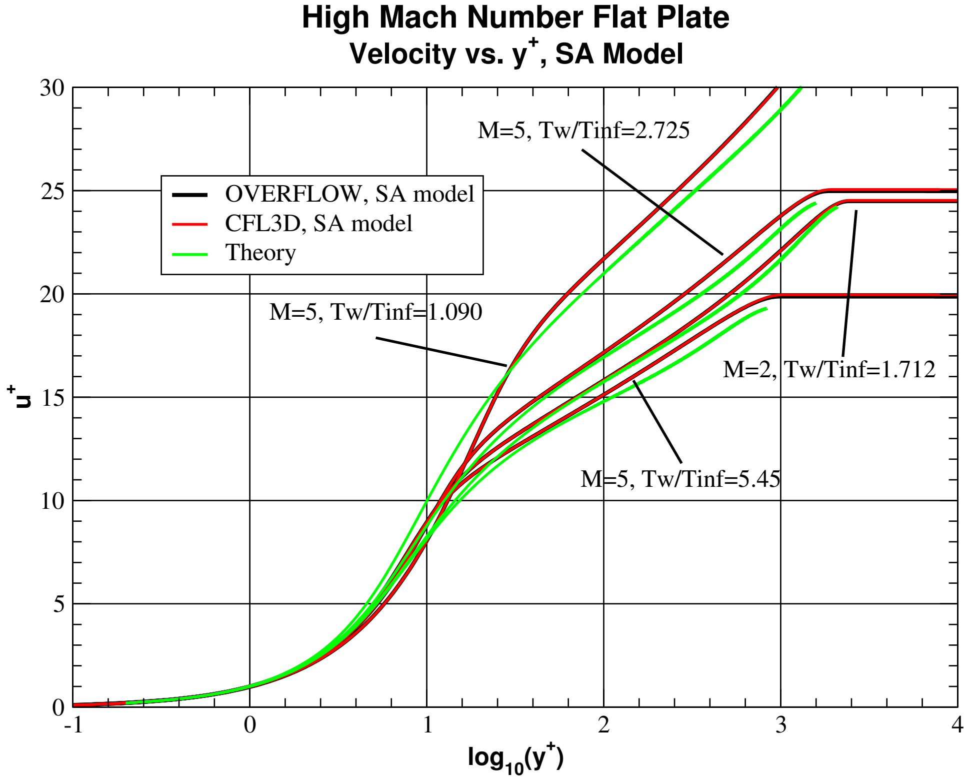

Figure 13.6: u^+, SA model.

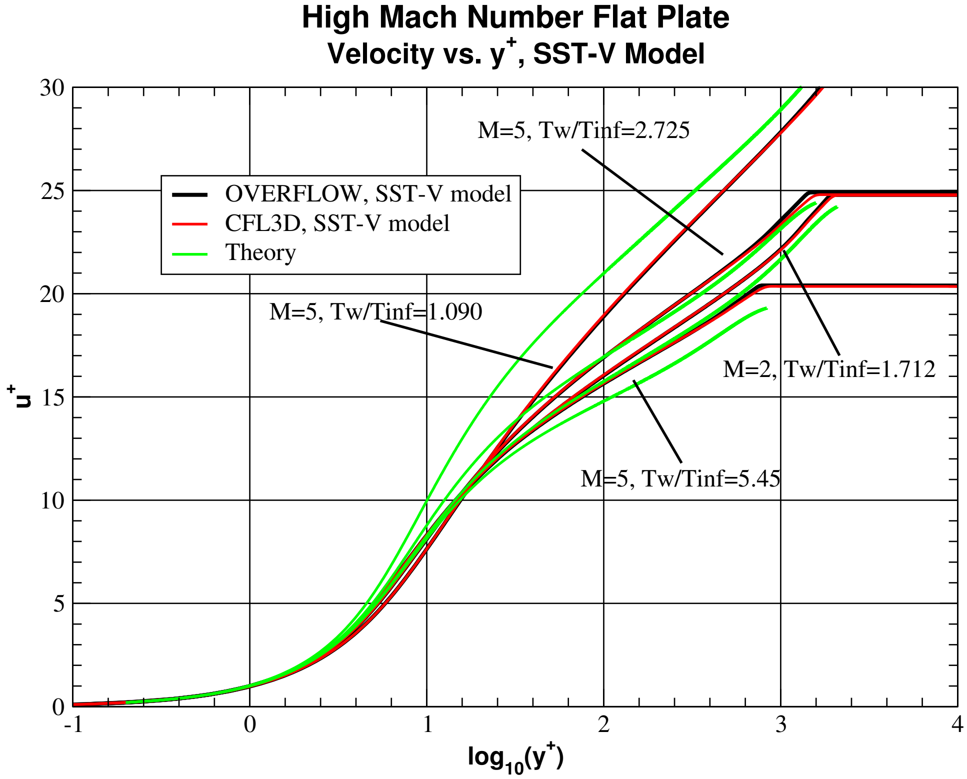

Figure 13.7: u^+, SST-V model.

14. 2D Backward Facing Step

In this section we present turbulence model validation for Overflow, performed using the LaRC Turbulence Modeling Resource (TMR) 2D Backward Facing Step case. This case has $M = 0.128$ and Reynolds number $Re = 36000$ based on a step height of 1. Figure 14.1 shows the layout of this case, along with the boundary conditions.

A grid provided by the TMR website is shown in Figure 14.2. For use with Overflow, the grid system was modified by combining zones 1 and 2 into one zone and zones 3 and 4 into another zone, with appropriate overlap between the two resulting zones. For the coarsest grid, the dimensions of the two zones were 49×33 and 65×57. For the finest grid, the dimensions of the two zones were 709×513 and 1025×897.

For Overflow and the SA model we used central differencing with low-Mach preconditioning and matrix dissipation. We used smoothing parameters `DIS2=0`, `DIS4=0.02`, `SMOO=0`, and time-step parameters `DT=1` and `CFLMIN=1`. The outflow boundary condition was `IBTYP=33`, the specified pressure outflow boundary condition, where after some experimentation we settled on a specified pressure ratio of 1.0035 at the outflow boundary to produce the desired Mach number of 0.128 at $x/H = -4$.

For Overflow and the SST and SST-V models we used Roe differencing with low-Mach preconditioning, and the time advance was time accurate with a physical time step (`DTPHYS`) of 0.1 and 40 subiterations per time step. We used `DT=5`, `CFLMIN=10`, `CFLMAX=500`, and `SMOO=0`. For these two models we found that a specified pressure ratio of 1.007073 at the outflow boundary would produce a Mach number close to 0.128 at $x/H = -4$.

The quantities to compare with experiment and with Cfl3d and Fun3d are: pressure coefficient C_p and skin friction coefficient C_f on the lower wall; and normalized u-velocity and turbulent shear stress $u'v'$ profiles upstream at $x/H = -4$ and downstream at the four locations $x/H = 1, 4, 6, 10$. The

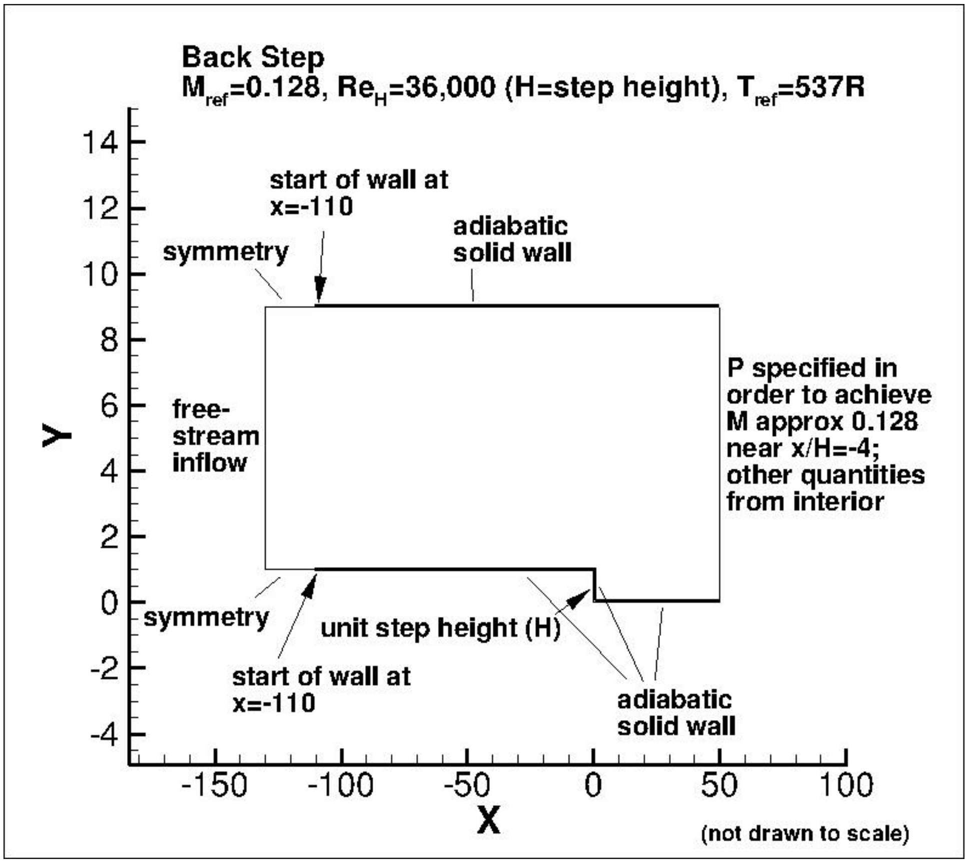

Figure 14.1: Backward facing step geometry and boundary conditions.

TMR website provides data from CFL3D and FUN3D on the second-finest grid.

In Figure 14.3 we show pressure coefficient and skin friction on the second-finest grid for the SA model, comparing OVERFLOW, CFL3D and experiment.

Figure 14.4 shows velocity profiles at five streamwise stations, comparing experiment with OVERFLOW and CFL3D using the SA model. The OVERFLOW and CFL3D results are in good agreement.

Figure 14.5 shows turbulent shear stress profiles at five streamwise stations for OVERFLOW and CFL3D using the SA model and experiment. At the upstream station, the two codes differ slightly while at the downstream stations the two codes are in close agreement.

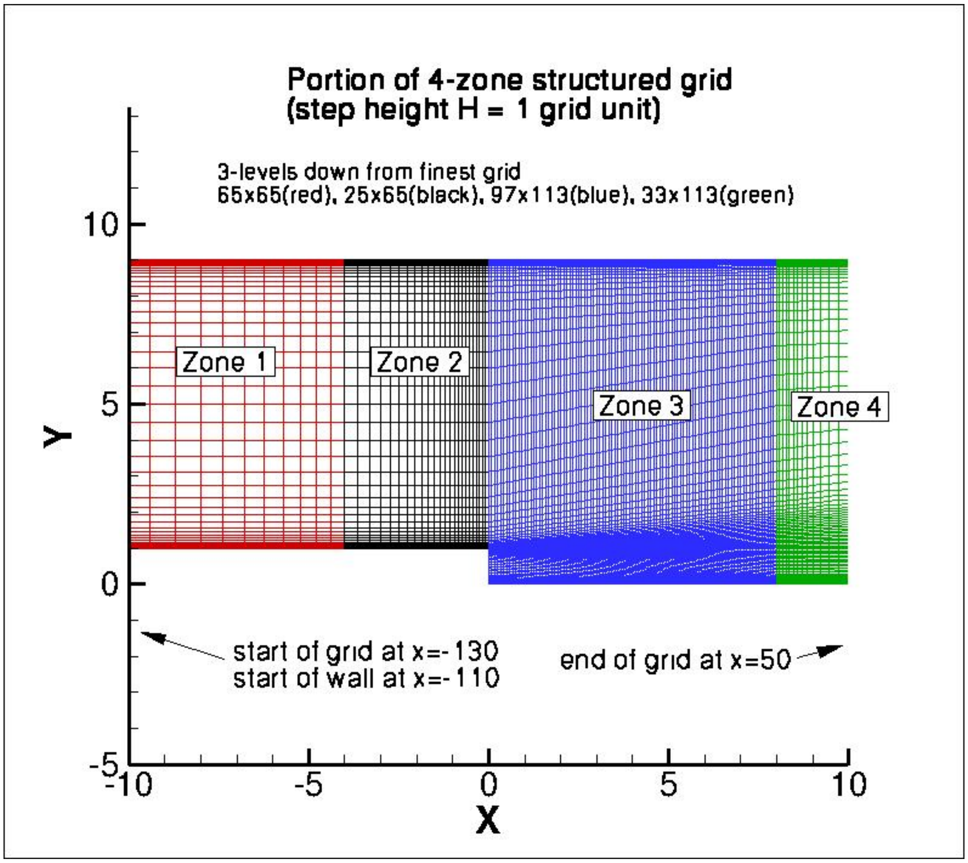

Figure 14.2: Grid system for backward facing step.

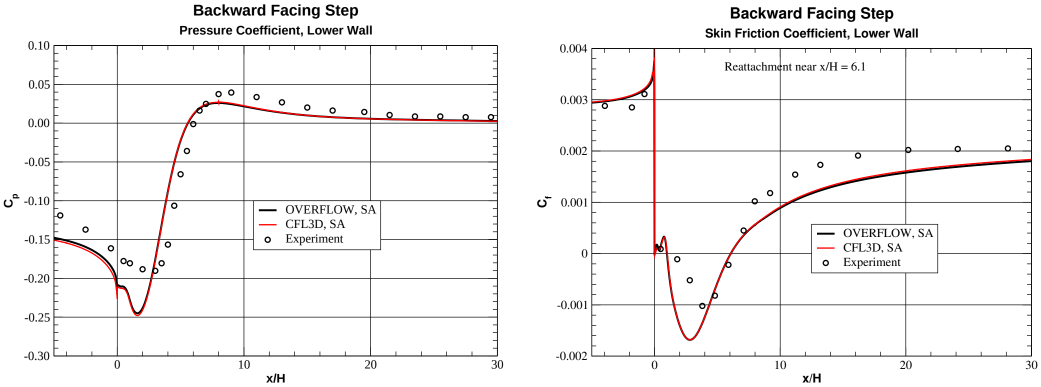

Figure 14.3: Pressure coefficient and skin friction, SA model.

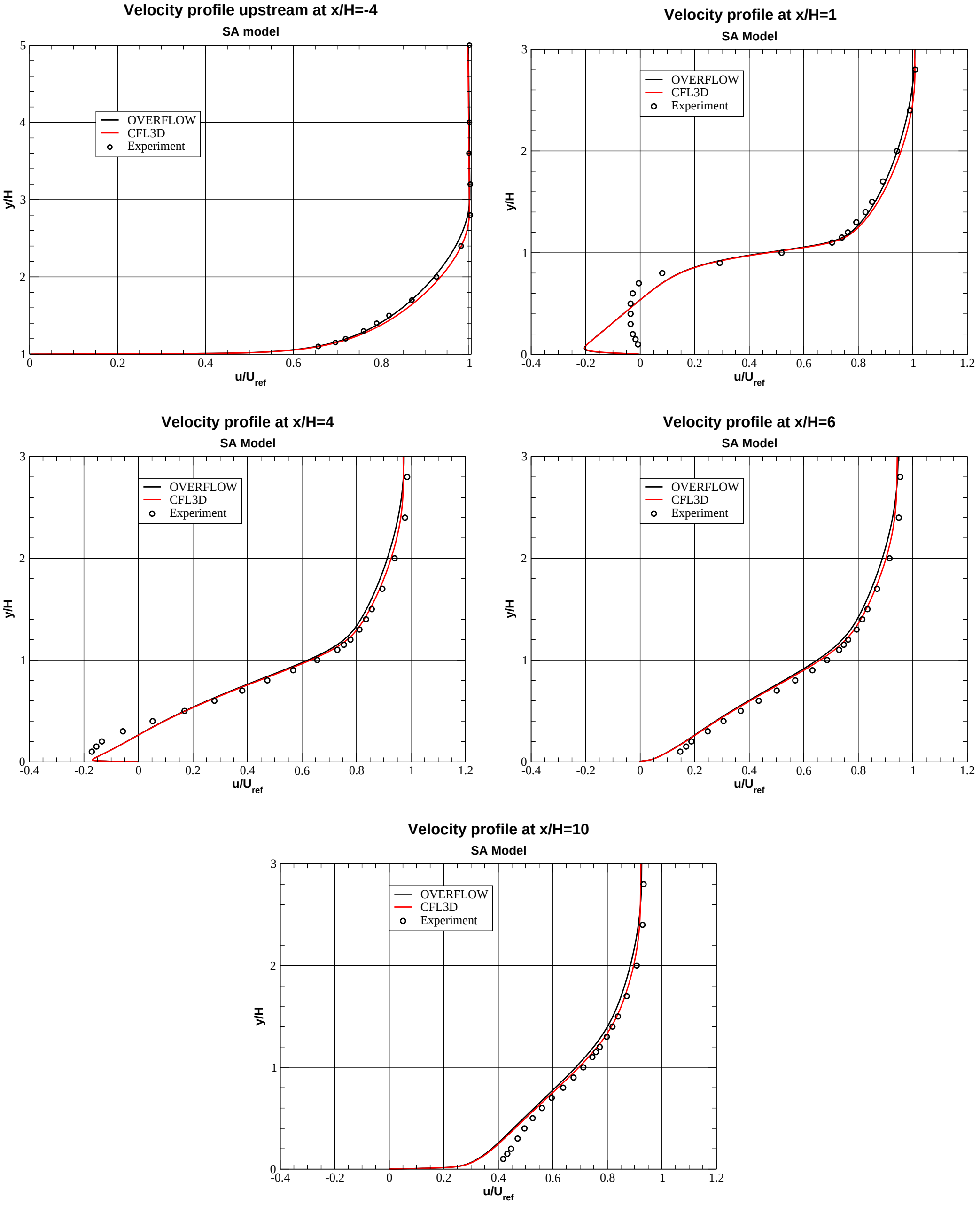

Figure 14.4: Velocity profiles, SA model.

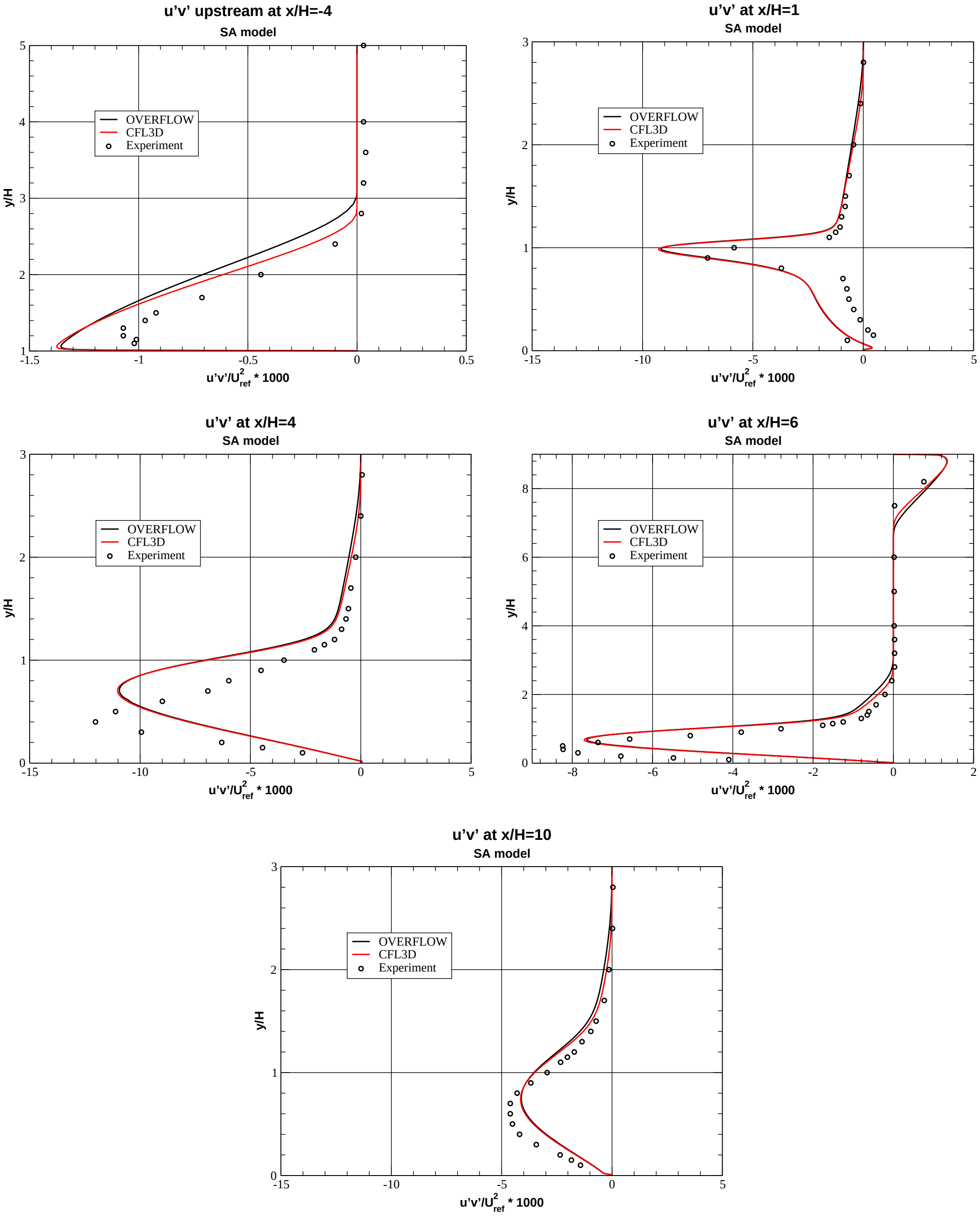

Figure 14.5: Turbulent shear stress profiles, SA model.

Figure 14.6 shows pressure coefficient and skin friction on the second-finest grid for the SST model, comparing Overflow, Cfl3d and experiment. The two codes are in good agreement.

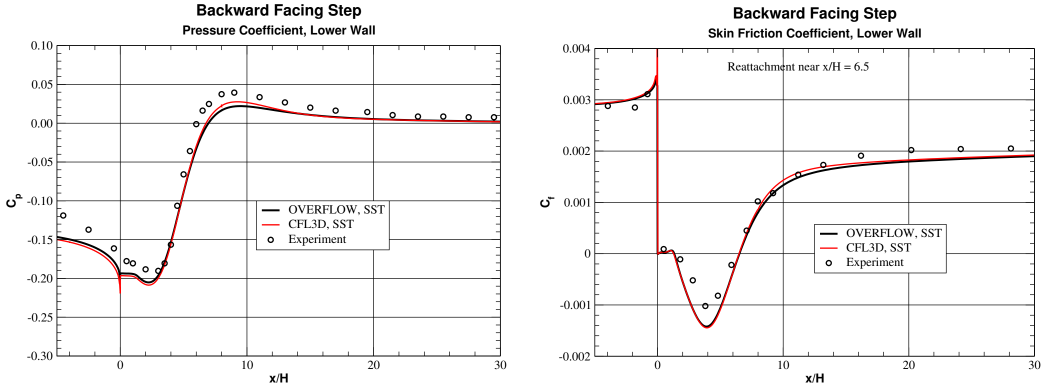

Figure 14.6: Pressure coefficient and skin friction, SST model.

Figure 14.7 shows velocity profiles at five streamwise stations for Overflow and Cfl3d using the SST model and experiment. The two codes agree well with one another.

Figure 14.8 shows turbulent shear stress profiles at five streamwise stations for Overflow and Cfl3d using the SST model and experiment. The codes are in close agreement at the first downstream station and differ slightly at the other stations.

Figure 14.9 shows pressure coefficient and skin friction on the second-finest grid for the SST-V model, comparing Overflow, Cfl3d and experiment. The two codes agree closely with one another.

Figure 14.10 shows velocity profiles at five streamwise stations for Overflow and Cfl3d using the SST-V model and experiment. The two codes are in good agreement with one another.

Figure 14.11 shows turbulent shear stress profiles at five streamwise stations for Overflow and Cfl3d using the SST-V model and experiment. As with the SST model, the codes are in close agreement at the first downstream station and differ slightly at the other stations.

All these results were for the second-finest grid. We also ran on the finest grid. For each of the SA, SST, and SST-V models, the results from the finest grid plot almost atop the results from the second-finest grid. We also ran SA-RC (Spalart-Allmaras with rotation/curvature correction [11]) on the finest

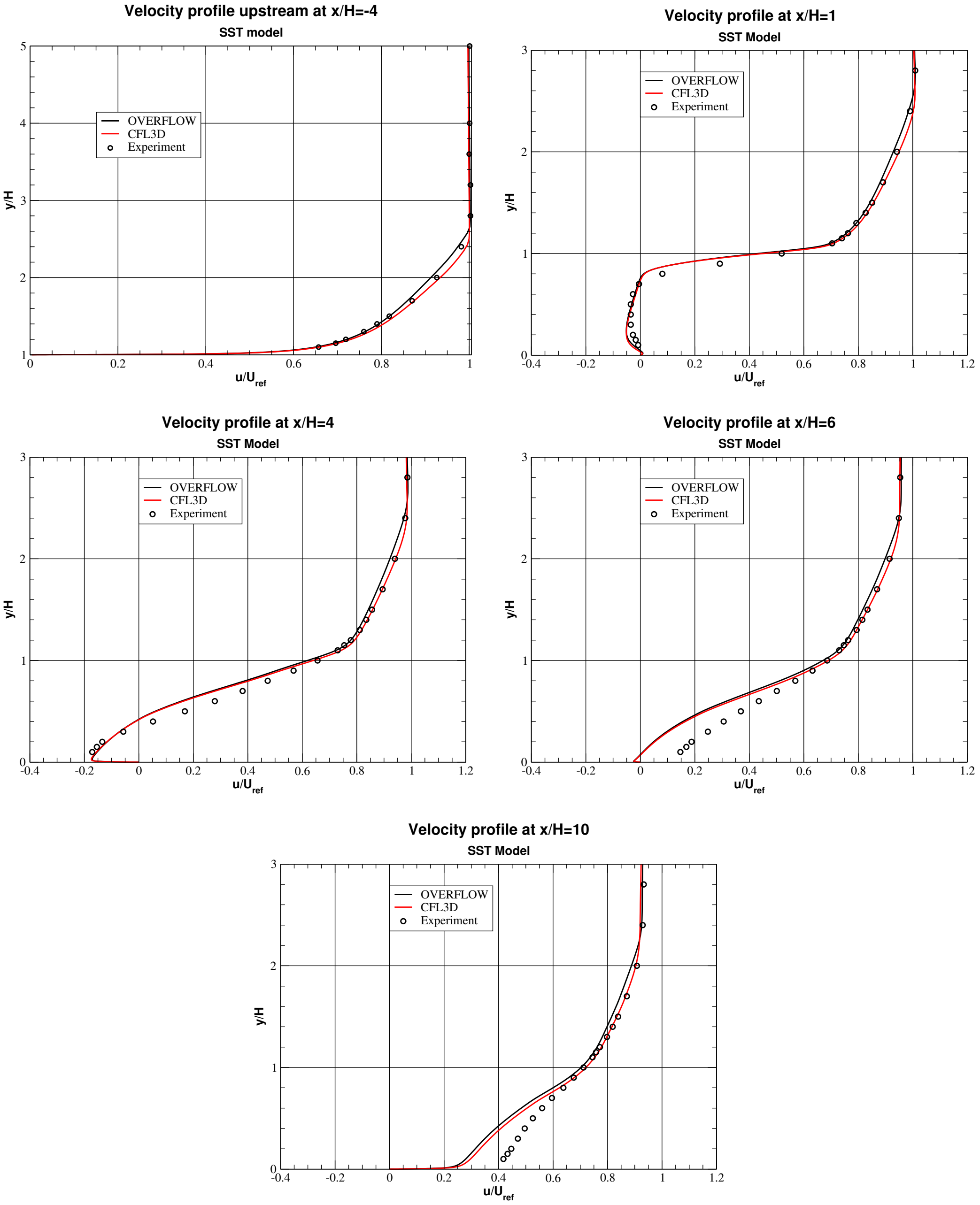

Figure 14.7: Velocity profiles, SST model.

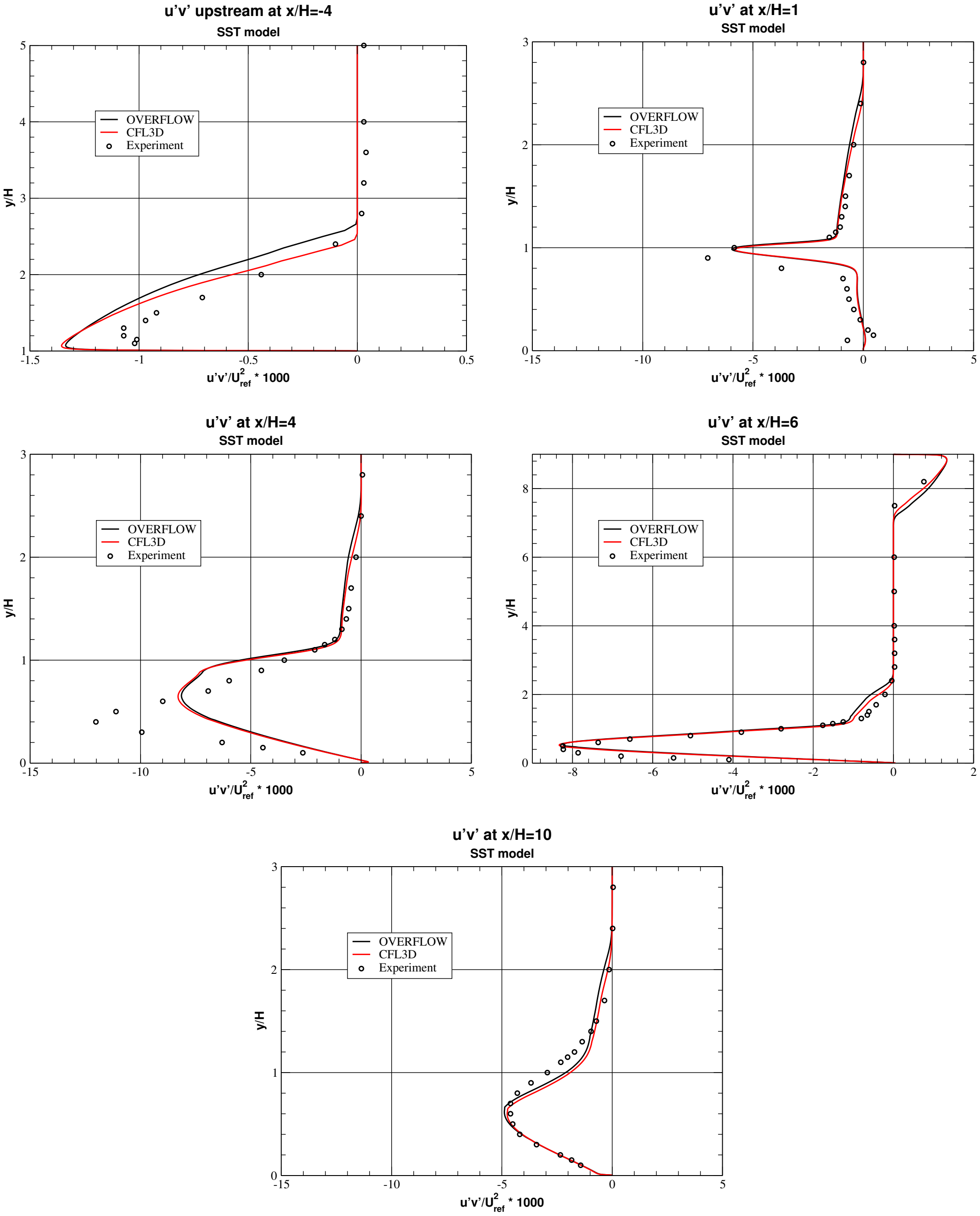

Figure 14.8: Turbulent shear stress profiles, SST model.

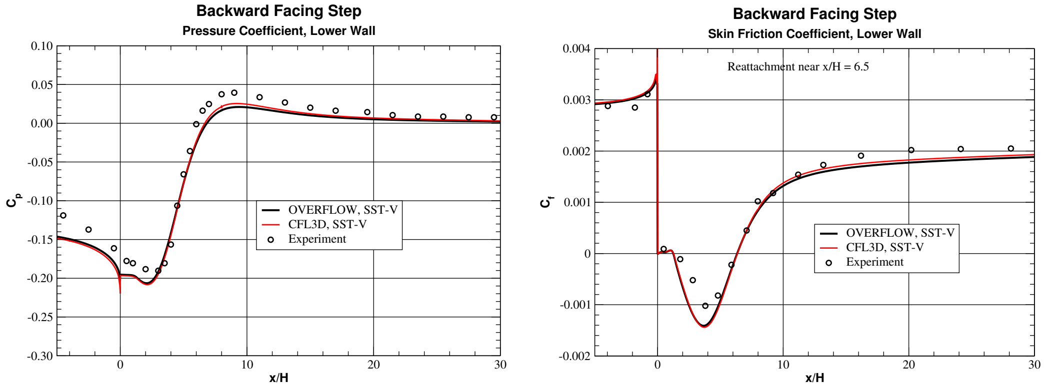

Figure 14.9: Pressure coefficient and skin friction, SST-V model.

grid. Figure 14.12 shows pressure coefficient and skin friction on the finest grid for OVERFLOW with the SA and SA-RC models.

Figure 14.13 shows velocity profiles at the five streamwise stations for OVERFLOW using SA and SA-RC, and Figure 14.14 shows turbulent shear stress profiles. The velocity profiles are nearly identical, while there are some differences in the turbulent shear stress profiles.

We also tried the SST model with rotational correction, SST-RC. On the second-finest grid with this model we were unable to get convergence to a steady state. Then we modified the implementation of SST-RC in OVERFLOW to change one of the constants in the model, c_{r2}, from 12 to 2 (see Section 16 on the Convex Curvature Boundary Layer for more information on this topic). With this modification, and with a specified outflow pressure ratio of 1.0035, we obtained a steady solution with the maximum Mach number at $x/H = -4$ very close to 0.128. The velocity and shear stress profiles for this SST-RC solution were very close to the profiles for the SST solution, while the reattachment point moved from about $x/H = 6.51$ for SST to about $x/H = 6.67$.

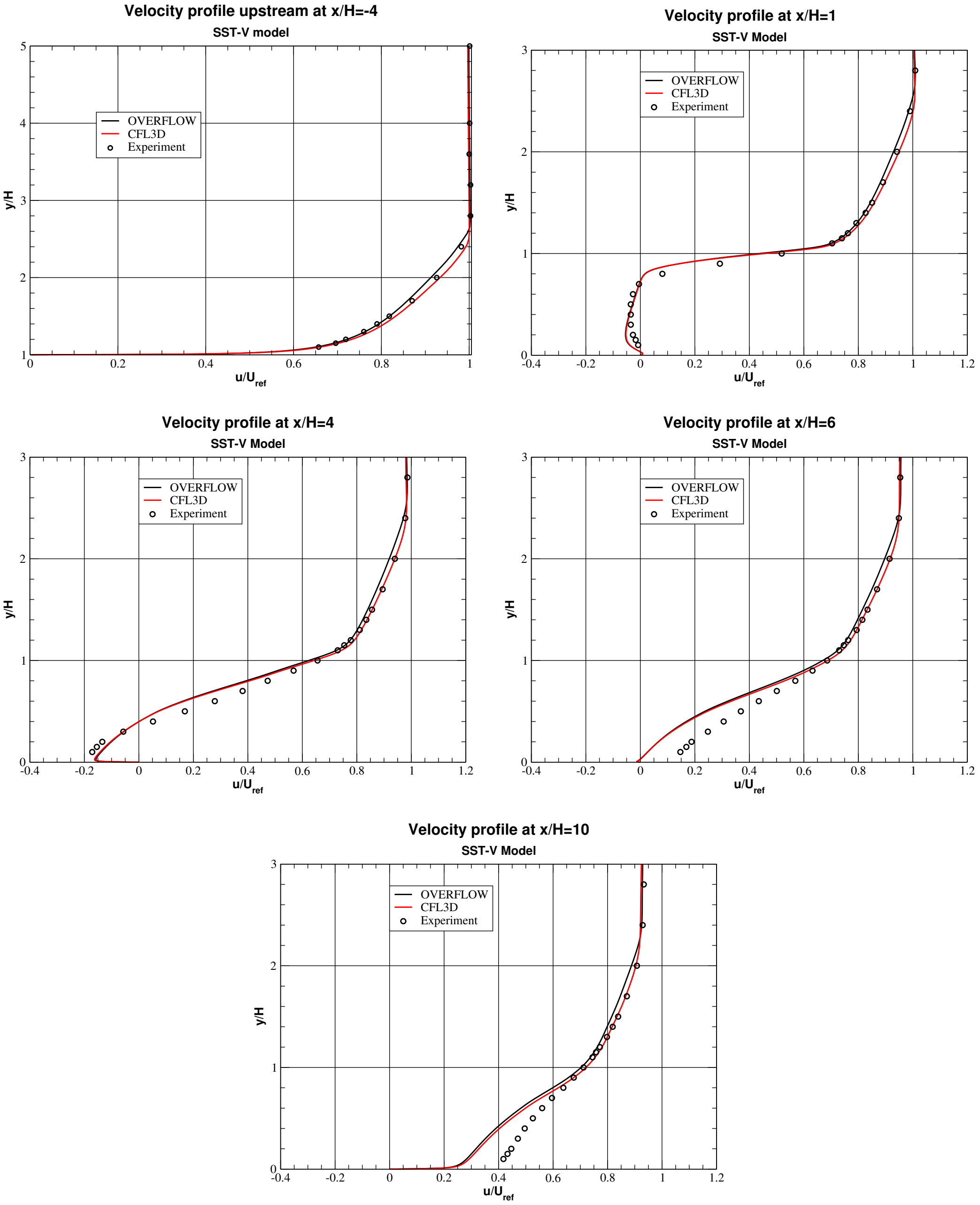

Figure 14.10: Velocity profiles, SST-V model.

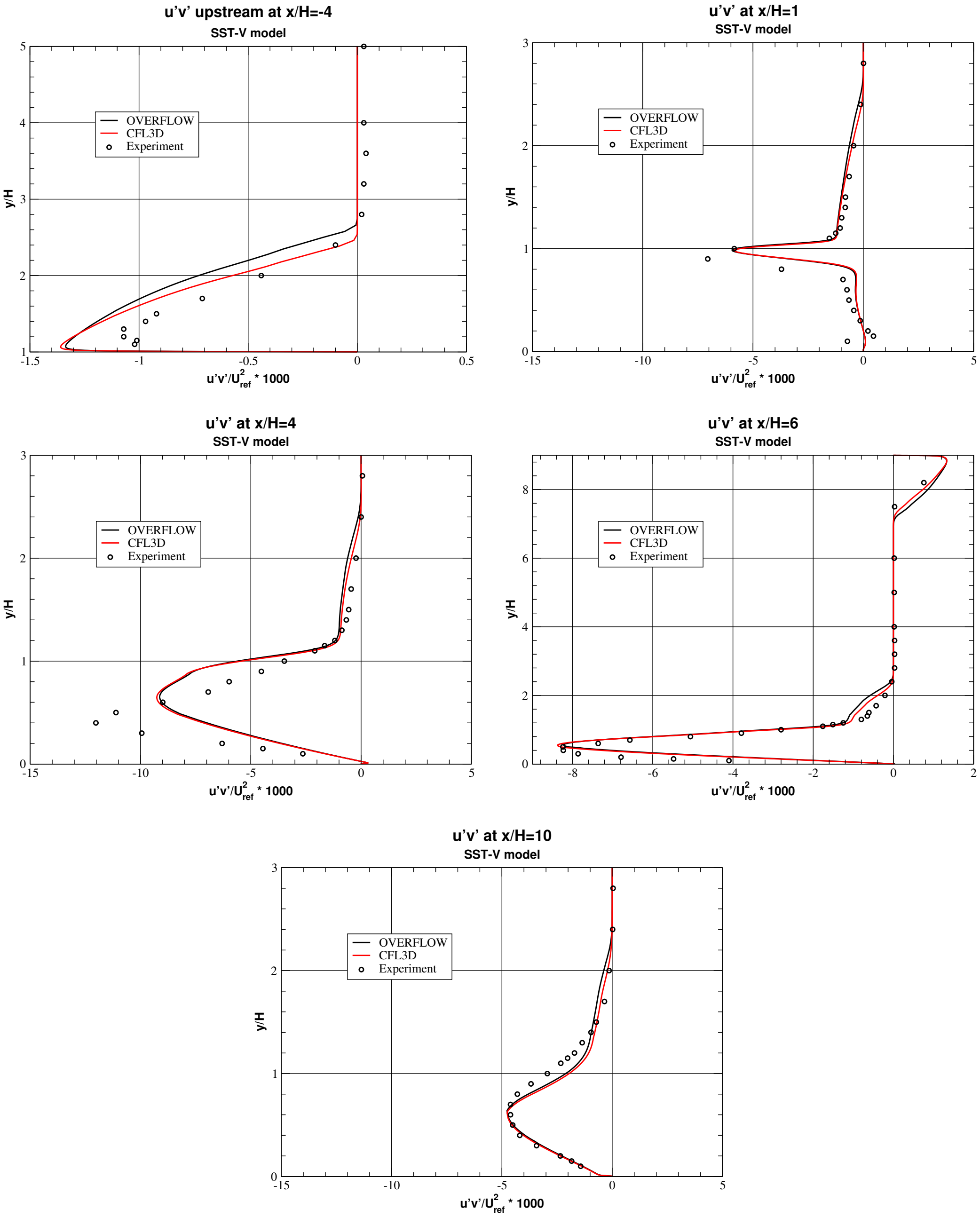

Figure 14.11: Turbulent shear stress profiles, SST-V model.

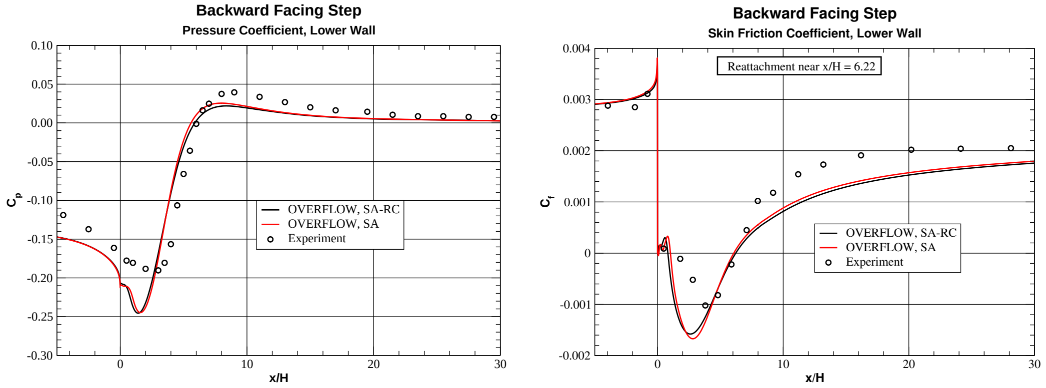

Figure 14.12: Pressure coefficient and skin friction, SA and SA-RC models, finest grid.

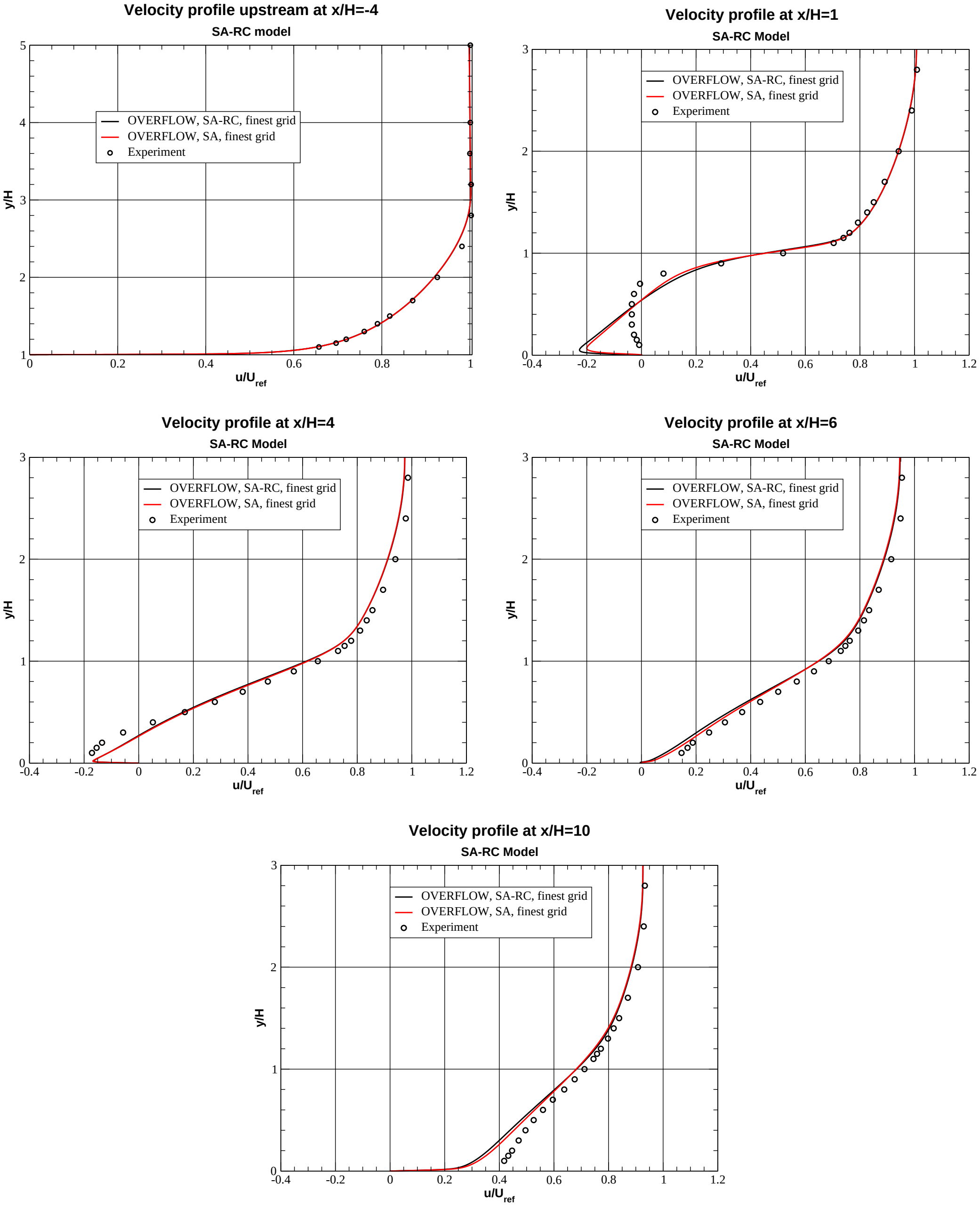

Figure 14.13: Velocity profiles, SA and SA-RC models.

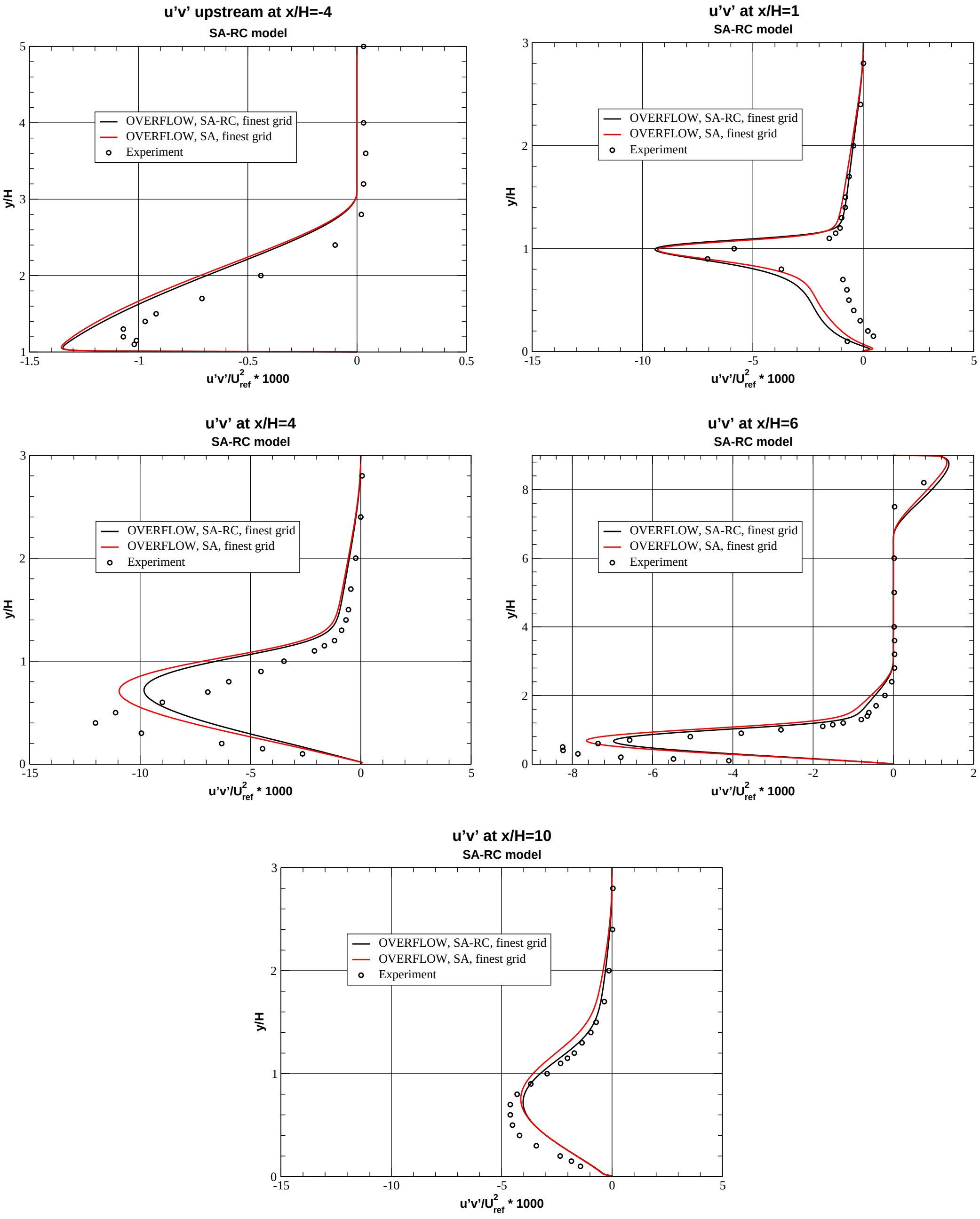

Figure 14.14: Turbulent shear stress profiles, SA and SA-RC models.

15. NACA4412 Airfoil

In this section we present turbulence model validation for Overflow using the LaRC Turbulence Modeling Resource (TMR) NACA4412 Airfoil validation case. This case has Mach number $M = 0.09$, angle of attack $\alpha = 13.87°$, and Reynolds number $Re = 1,520,000$ based on a chord of 1. The geometry and flow conditions are shown in Figure 15.1, taken from the TMR website. A close-up view of the grid system provided for this case is indicated in Figure 15.2. The Overflow calculations used third-order Roe differencing, and low-Mach preconditioning was activated. We used data surface grids at $x/c = 0.6753$, 0.7308, 0.7863, 0.8418, 0.8973, and 0.9528 to obtain data for plotting.

For the SA model we show the pressure coefficient on the airfoil in Figure 15.3, comparing Overflow with Cfl3d and experiment. The two codes give nearly identical results.

The next set of plots, Figure 15.4, show streamwise velocity profiles for the SA model, comparing Overflow, Cfl3d and experiment. The two codes give very similar results.

The next plots, Figure 15.5, show normal velocity profiles for the SA model, comparing Overflow, Cfl3d and experiment. The two codes give very similar results.

The next plots, Figure 15.6, show turbulent shear stress profiles for the SA model, comparing Overflow, Cfl3d and experiment. The two codes give very similar results.

The last plot for the SA model, Figure 15.7, shows streamlines and normalized streamwise velocity contours near the trailing edge of the airfoil. The normalized streamwise velocity values are defined as u-velocity values from Overflow divided by the freestream Mach number of 0.9 and further divided by an experimental normalization factor of 0.93, as noted on the TMR website.

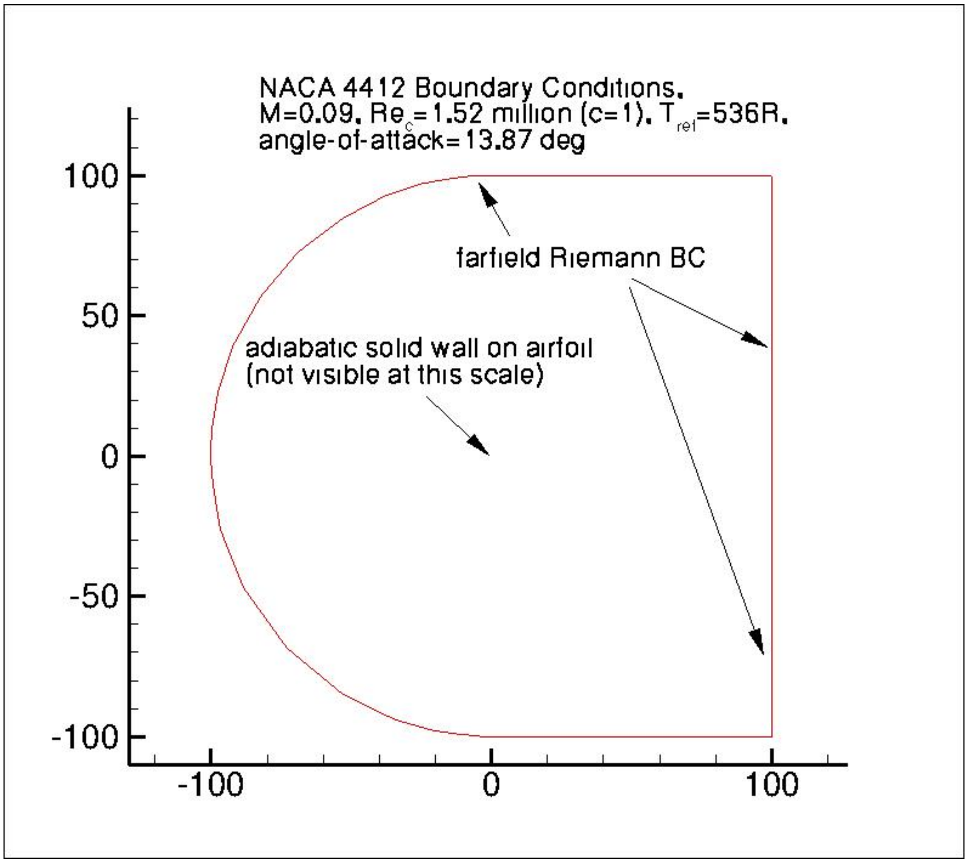

Figure 15.1: NACA4412 airfoil geometry.

For the second-finest grid, lift and drag coefficients for Cfl3d, Fun3d and Overflow are shown in Table 15.1, where the data for Cfl3d and Fun3d are taken from the TMR website.

With the SST model, the pressure coefficient on the airfoil is shown in Figure 15.8, comparing Overflow with Cfl3d and experiment.

Profiles of streamwise velocity are shown in Figure 15.9. The Overflow and Cfl3d results are very similar.

Normal velocity profiles for the SST model are shown in Figure 15.10.

Turbulent shear stress profiles for the SST model are shown in Figure 15.11.

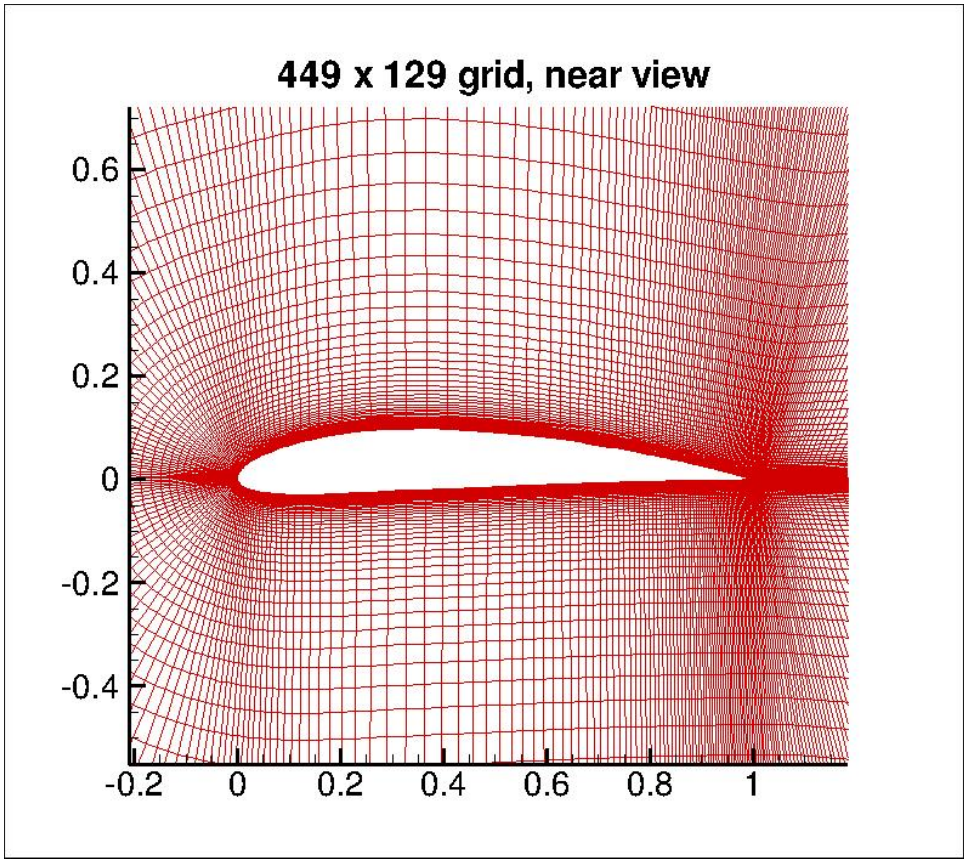

Figure 15.2: NACA4412 airfoil grid, near view.

Table 15.1: Lift and drag, SA model.

Code	C_L	C_D
CFL3D	1.7210	0.02861
FUN3D	1.7170	0.02947
OVERFLOW	1.7195	0.03009

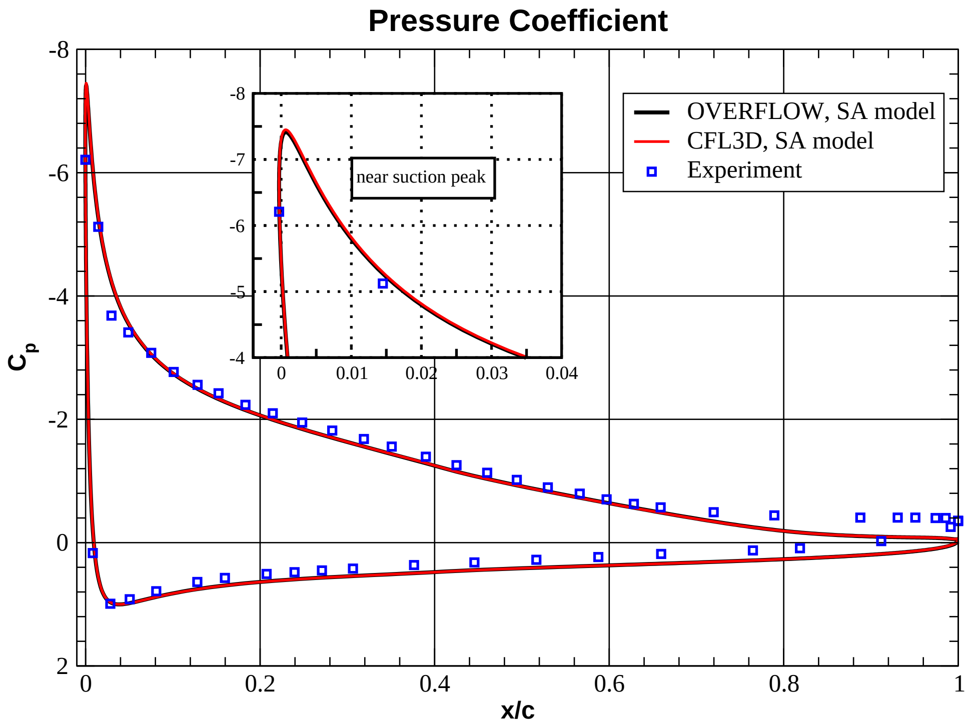

Figure 15.3: Pressure coefficient, SA model.

The last plot for the SST model, Figure 15.12, shows streamlines and normalized streamwise velocity contours near the trailing edge of the airfoil. The normalized streamwise velocity values are defined as noted above with the SA model.

For the second-finest grid, lift and drag coefficients for CFL3D, FUN3D and OVERFLOW are shown in Table 15.2, where the data for CFL3D and FUN3D are taken from the TMR website.

Table 15.2: Lift and drag, SST model.

Code	C_L	C_D
CFL3D	1.616	0.0311
FUN3D	1.615	0.0320
OVERFLOW	1.621	0.0321

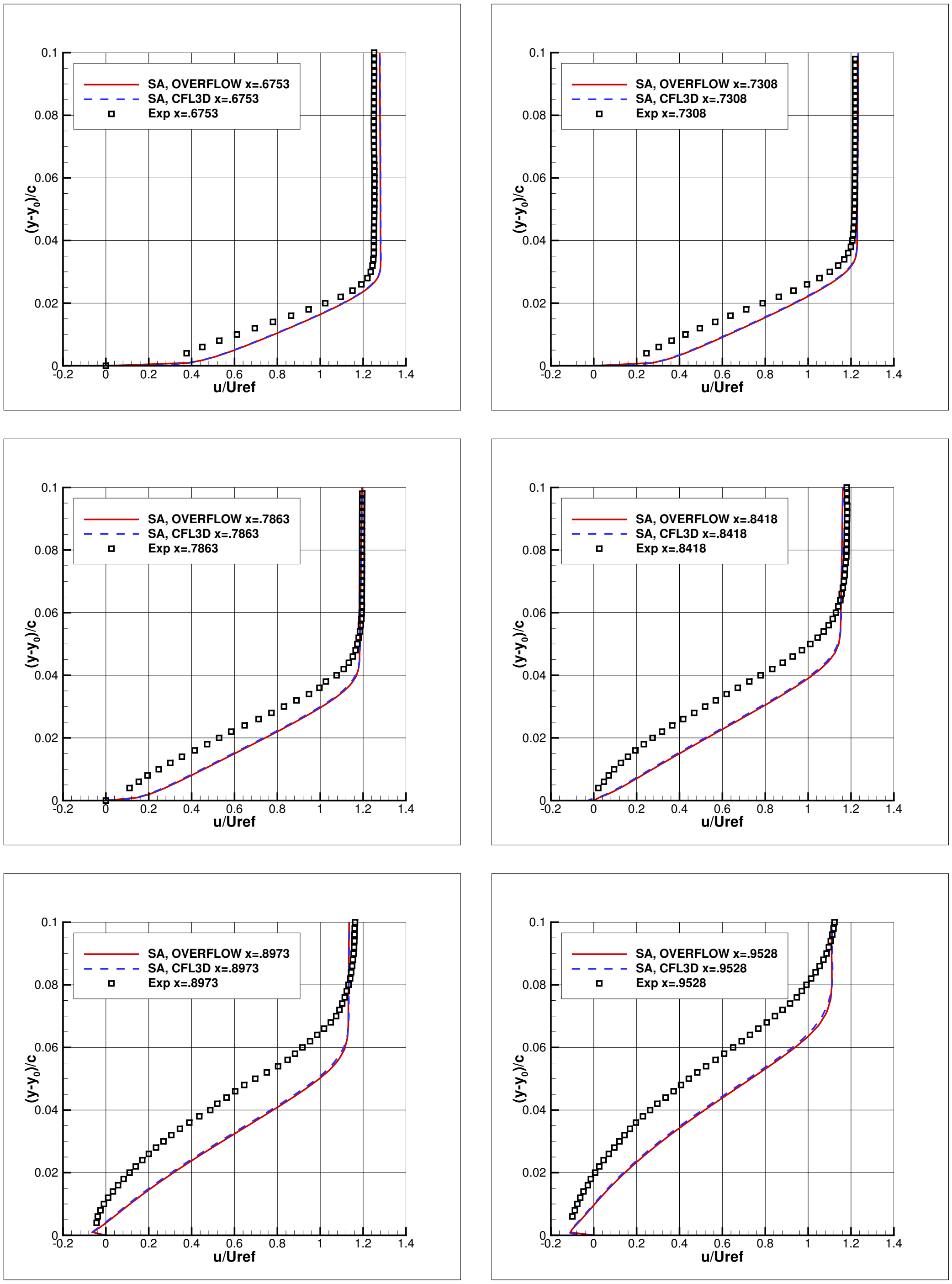

Figure 15.4: Streamwise velocity profiles, SA model.

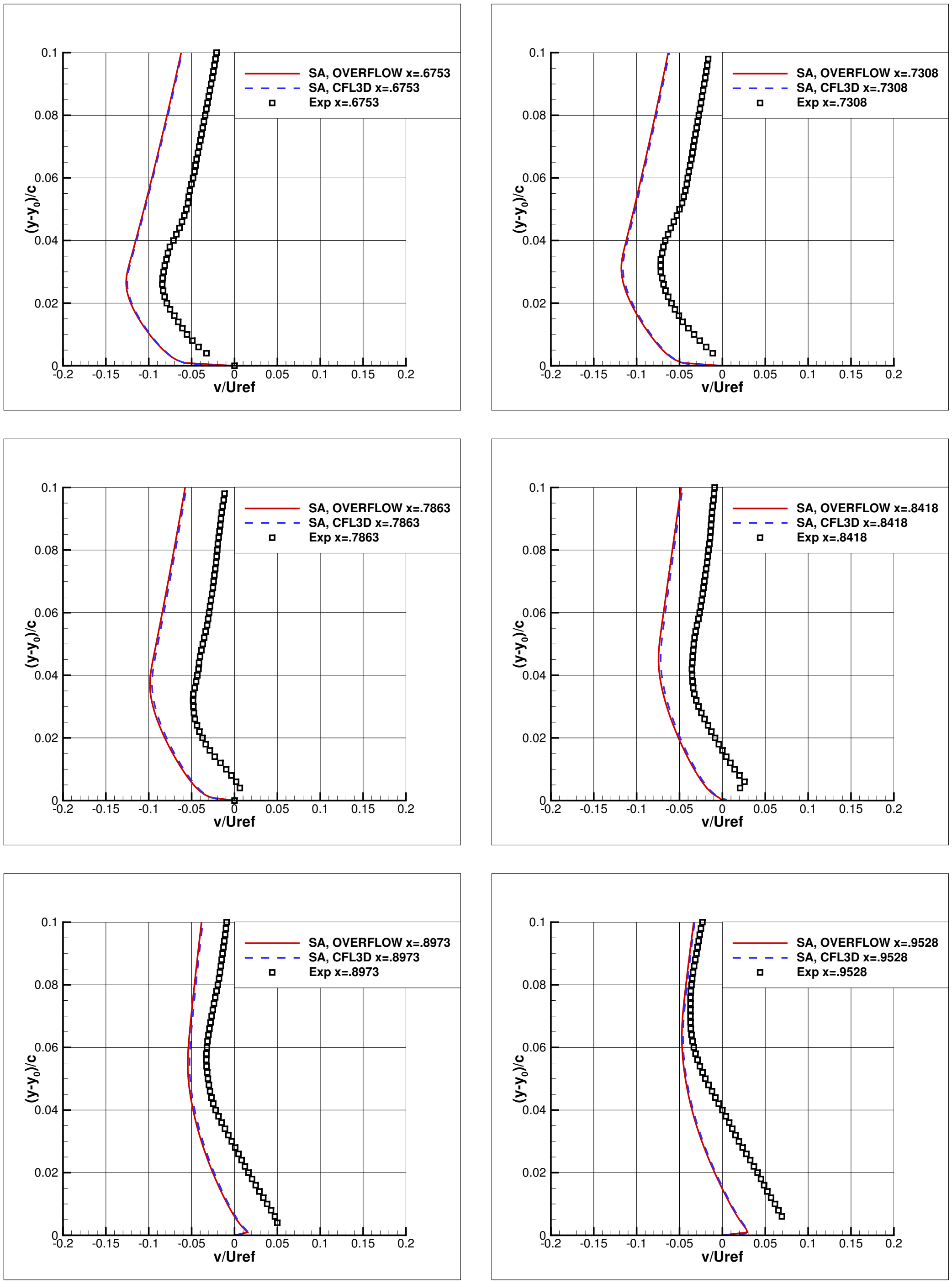

Figure 15.5: Normal velocity profiles, SA model.

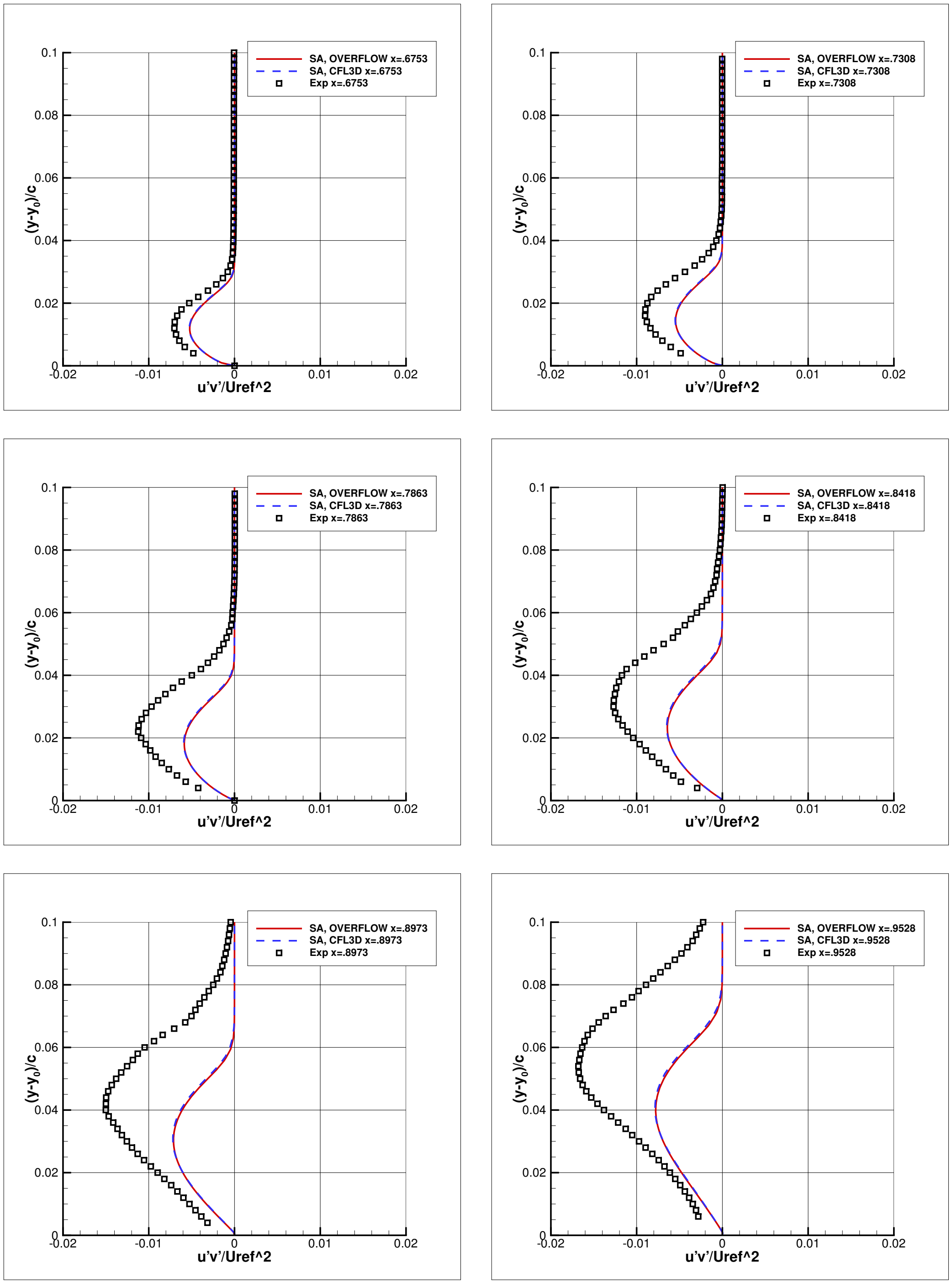

Figure 15.6: Turbulent shear stress profiles, SA model.

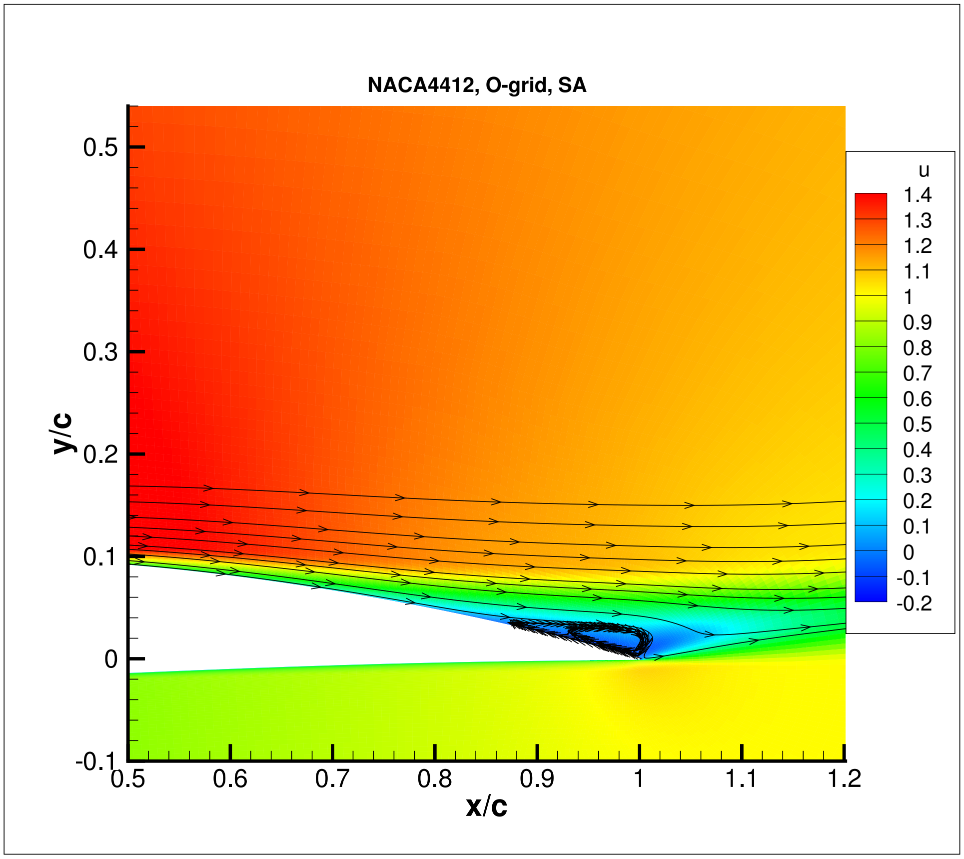

Figure 15.7: NACA4412 airfoil, streamwise velocity contours, SA model.

For this case we also ran the auxiliary 481 × 253 O-mesh provided at the TMR website. The pressure coefficient, velocity, and turbulent shear stress plots for this mesh were very close to the plots using the 897 × 257 C-mesh. For the O-mesh, we show lift and drag coefficients for Overflow and Cfl3d in Table 15.3.

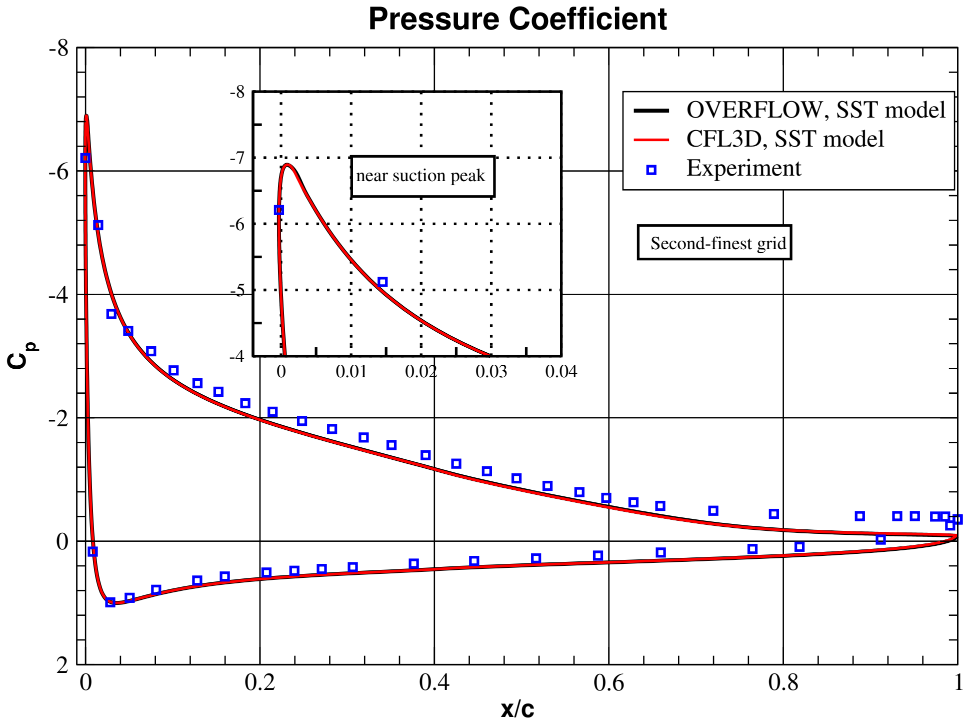

Figure 15.8: Pressure coefficient, SST model.

Table 15.3: Lift and drag, O-mesh.

	SA model		SST model	
Code	C_L	C_D	C_L	C_D
CFL3D	1.715	0.0285	1.621	0.0316
OVERFLOW	1.7167	0.02881	1.6294	0.03158

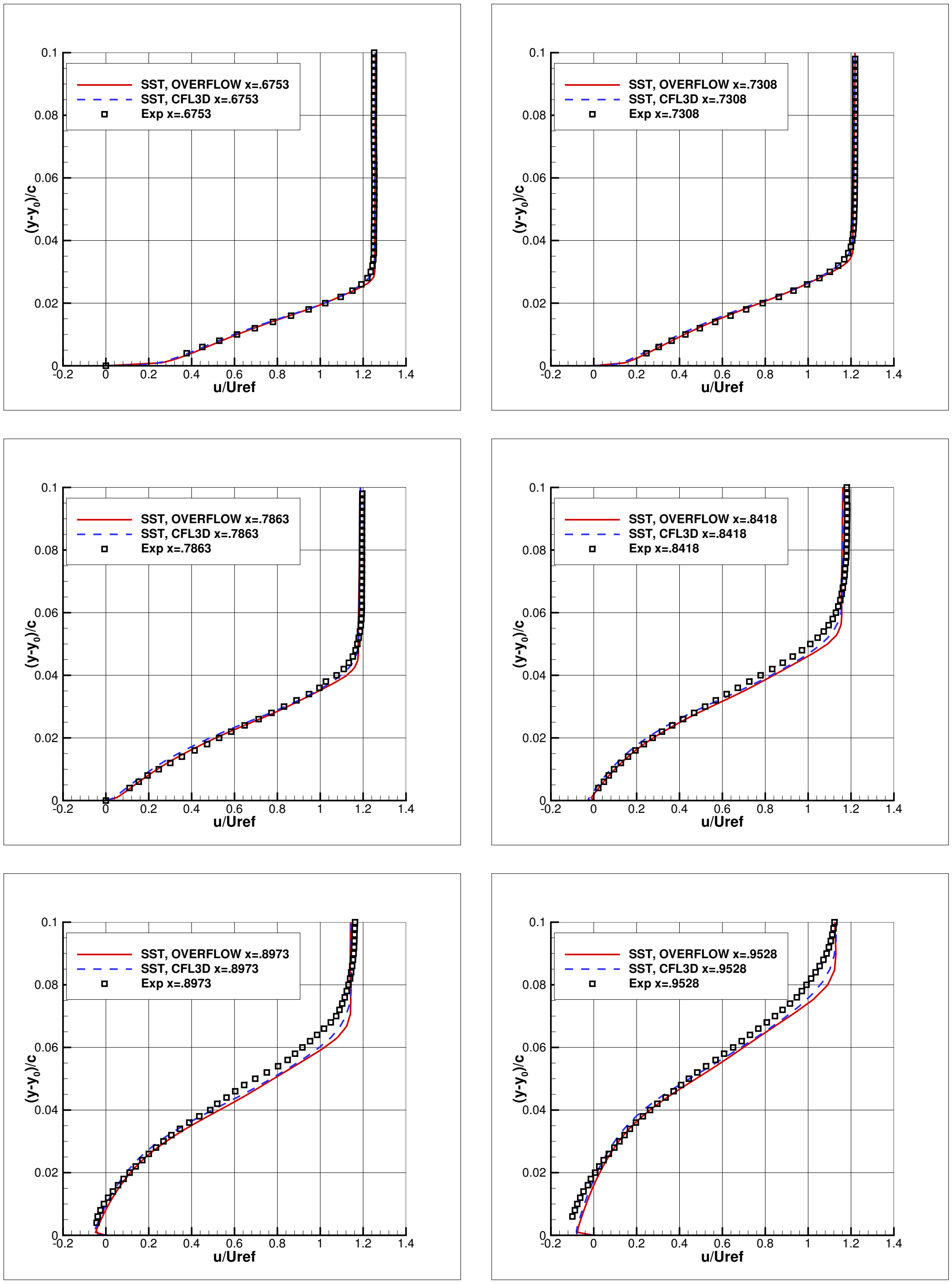

Figure 15.9: Streamwise velocity profiles, SST model.

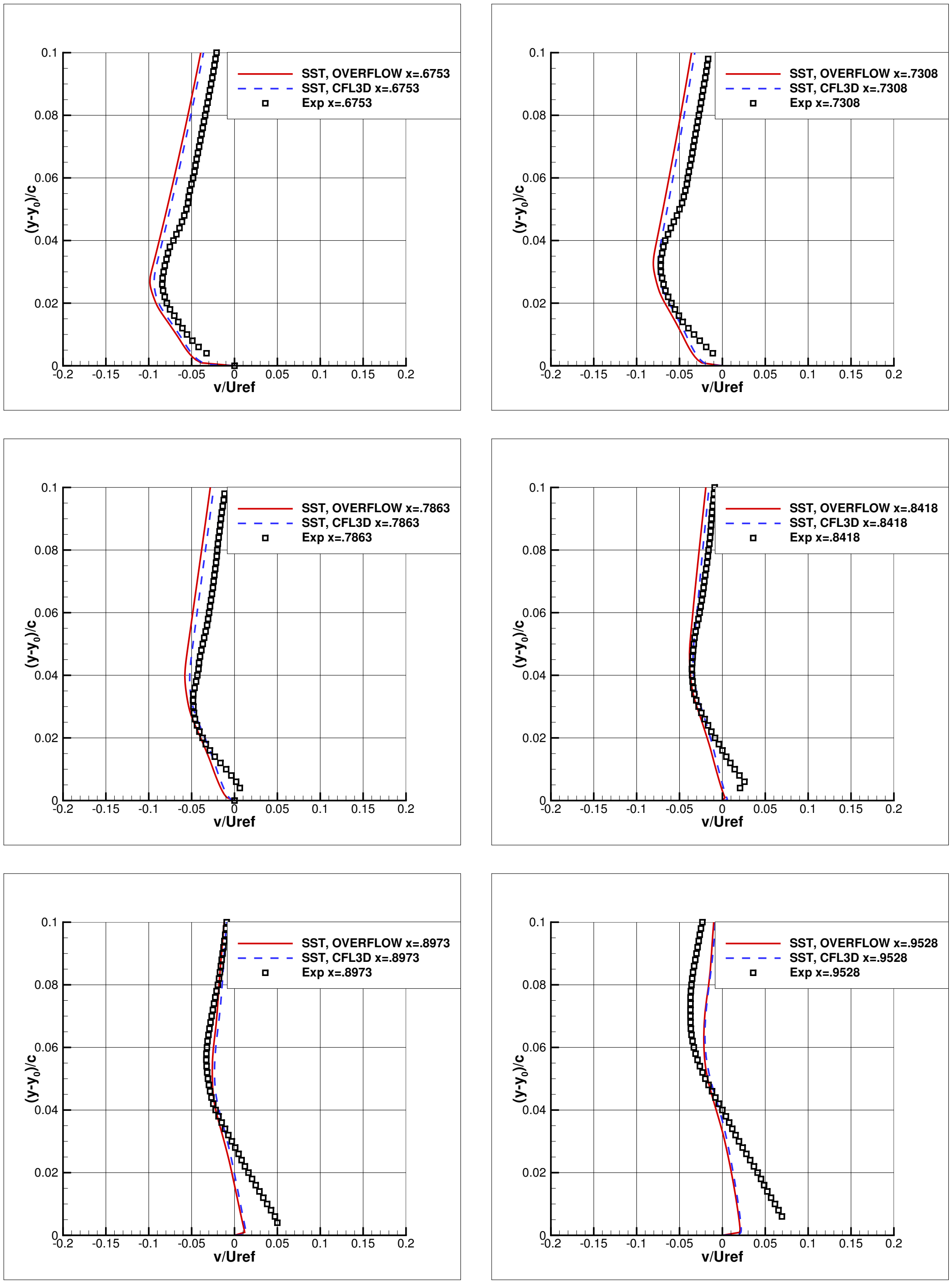

Figure 15.10: Normal velocity profiles, SST model.

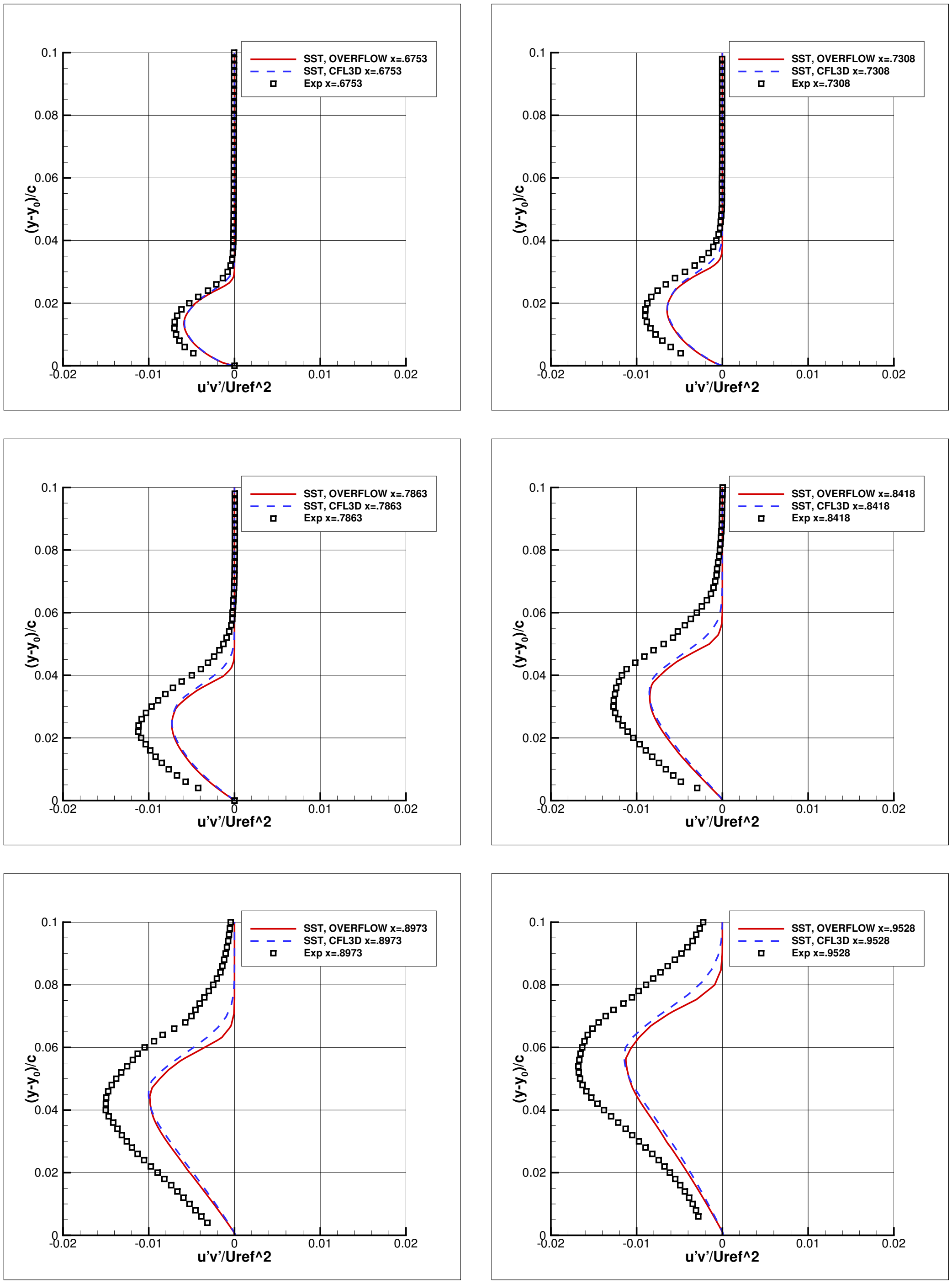

Figure 15.11: Turbulent shear stress profiles, SST model.

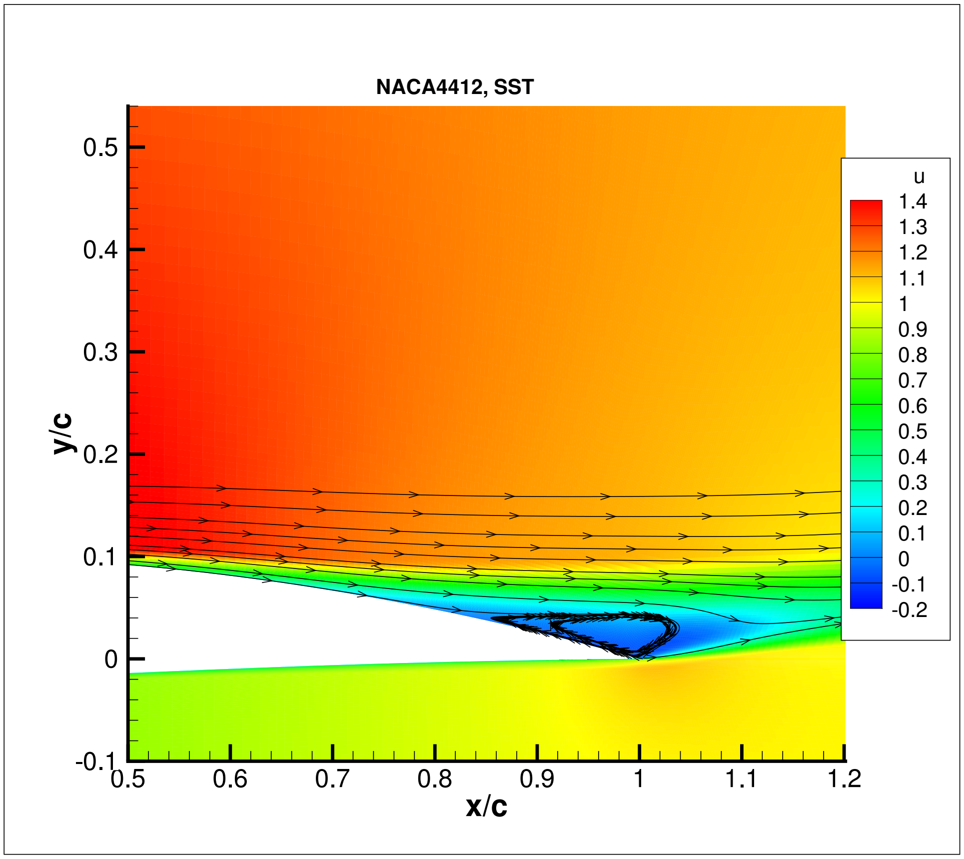

Figure 15.12: NACA4412 airfoil, streamwise velocity contours, SST model.

16. Convex Curvature Boundary Layer

In this section we present turbulence model validation for Overflow using the LaRC Turbulence Modeling Resource (TMR) Two-Dimensional Convex Curvature Boundary Layer validation case. This case is a channel flow with Mach number $M = 0.093$ and Reynolds number $Re = 2,100,000$. The geometry and flow conditions are shown in Figure 16.1, taken from the TMR website. A close-up view of the geometry of this case is indicated in Figure 16.2 and a view of the second-finest grid is shown in Figure 16.3.

The Overflow calculations used third-order Roe differencing. We used data surface grids at $x/c = -0.166124$, 0.030, 0.183, 0.335, 0.635, and 1.250 to obtain data for plotting. The data surface grids are defined as line segments perpendicular to the wall, meeting the lower surface of the wall at the indicated value of x. The lines of the grid are not perpendicular to the wall, so they cannot be used as the data surface grids.

The Overflow angle-of-attack input parameter `ALPHA` was set to 30, ensuring that the flow at the inflow boundary is parallel to the channel walls. The inflow boundary was specified with `IBTYP=41` and both parameters equal to 1, and the outflow boundary had `IBTYP=33` with parameter 0.9985. For all the Overflow cases on the second-finest grid, the code was run until the L_2 norm of the flow residuals was reduced by at least 12 orders of magnitude from its initial value.

It is worth noting that for Overflow the specified outflow pressure ratio of 0.9985 will not necessarily produce the desired inflow Mach number of 0.093. We found for Overflow on the second-finest grid that an outflow pressure ratio of 0.9985 gives a maximum Mach number at the inflow about 2.2% higher than the desired value. For Overflow on the second-finest grid an outflow pressure ratio of 0.99882 gives maximum Mach number at

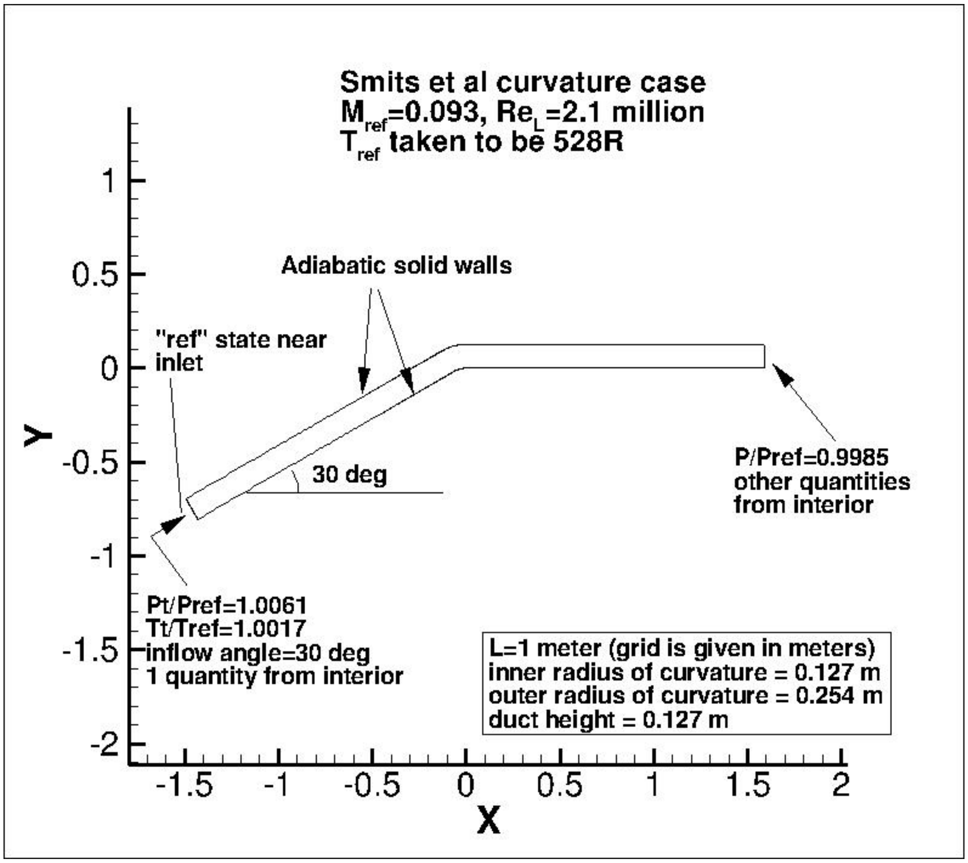

Figure 16.1: Convex curvature geometry.

the inflow within 0.05% of the desired value. Nevertheless, for the sake of consistency, all the OVERFLOW computations shown here used an outflow pressure ratio of 0.9985.

For this case, the TMR website shows turbulent stress tensor profiles at several streamwise stations, one of which is located upstream of the bend. At this upstream location, the turbulent stress tensor profile is taken with respect to the wall-parallel and wall-normal directions. The formula for this profile is given on the TMR website as

$$\overline{u'_p v'_p} = 0.5(\overline{v'v'} - \overline{u'u'})\sin(2\theta) + \overline{u'v'}\cos(2\theta),$$

where $\theta = 30°$. To obtain $\overline{v'v'}$ and $\overline{u'u'}$ from OVERFLOW we used the Boussi-

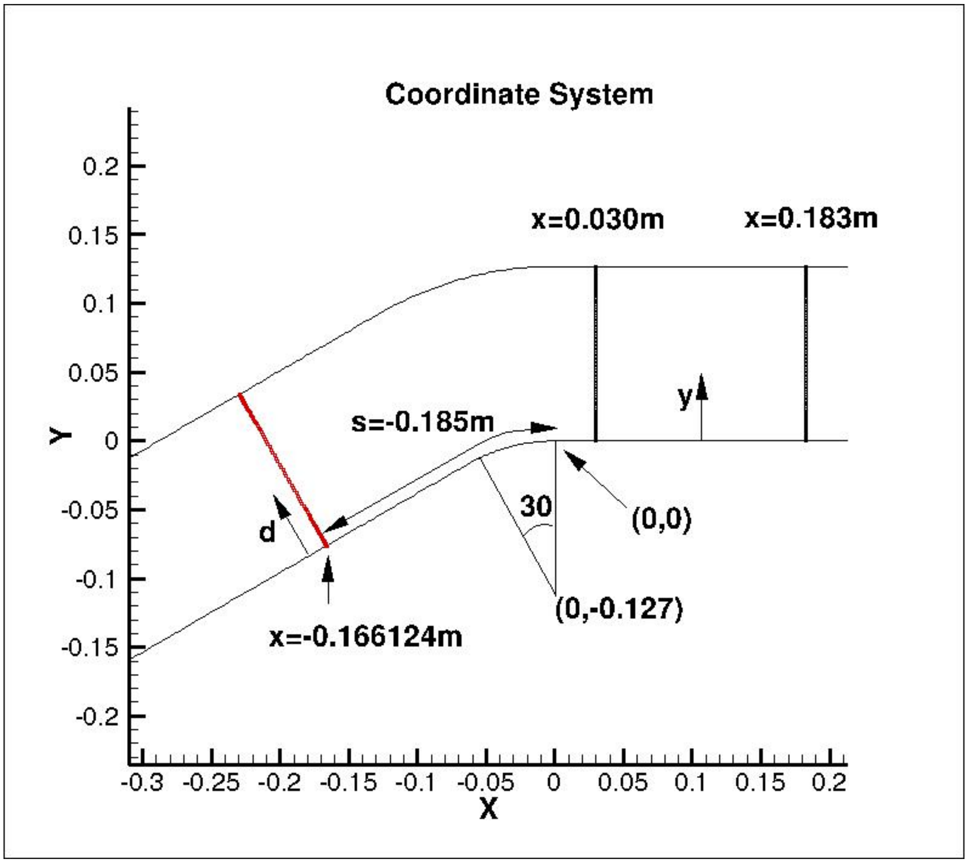

Figure 16.2: Convex curvature geometry, near view.

nesq relation (see section 3) and neglected the divergence term, which is close to zero for this nearly incompressible flow, and also neglected the turbulent kinetic energy term, since post-processing work indicated that at this location upstream of the channel bend the turbulent kinetic energy term is negligible compared to the strain tensor term. For the SA model, k is not even available and some approximation would be needed; for example (C. Rumsey, private communication) the approximation mentioned in [14].

The first set of plots,(16.4–16.7), uses the SA turbulence model and the second-finest grid. We show pressure coefficient and skin friction coefficient on the lower wall in Figure 16.4, velocity and turbulent shear stress profiles upstream of the bend in Figure 16.5, velocity and turbulent shear stress

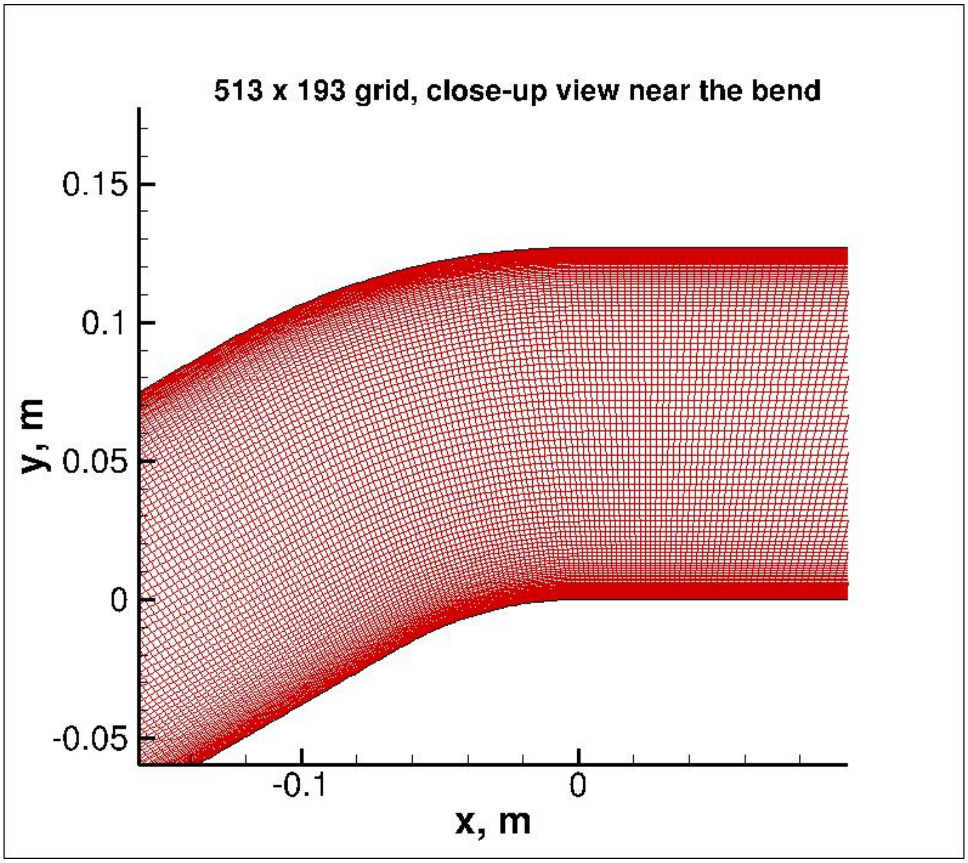

Figure 16.3: Convex curvature grid, near view.

profiles downstream of the bend in Figure 16.6, and skin friction coefficient on the upper wall in Figure 16.7. In all cases OVERFLOW and CFL3D agree very closely.

The next set of plots, (16.8–16.11), uses the SST turbulence model. We show pressure coefficient and skin friction coefficient on the lower wall in Figure 16.8, velocity and turbulent shear stress profiles upstream of the bend in Figure 16.9, velocity and turbulent shear stress profiles downstream of the bend in Figure 16.10, and skin friction coefficient on the upper wall in Figure 16.11. In all cases OVERFLOW and CFL3D agree very closely.

The next set of plots, (16.12–16.15), uses the SA model with rotational correction, denoted SA-RC on the TMR website. For OVERFLOW, this model

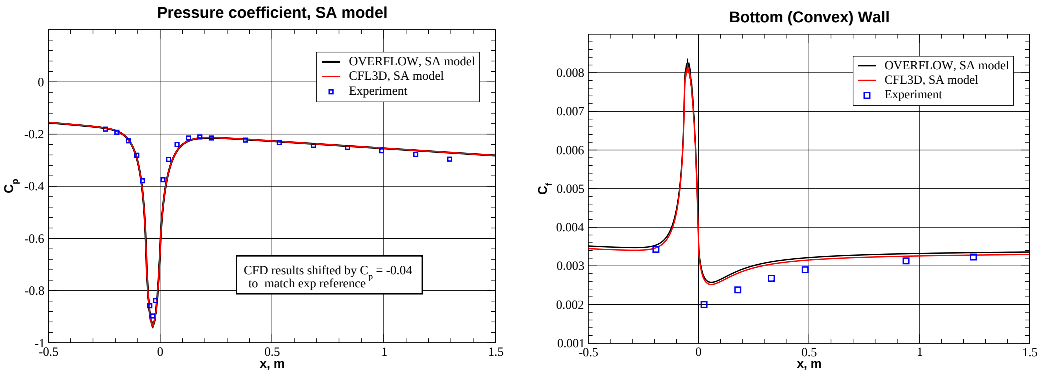

Figure 16.4: Pressure coefficient and skin friction on lower wall.

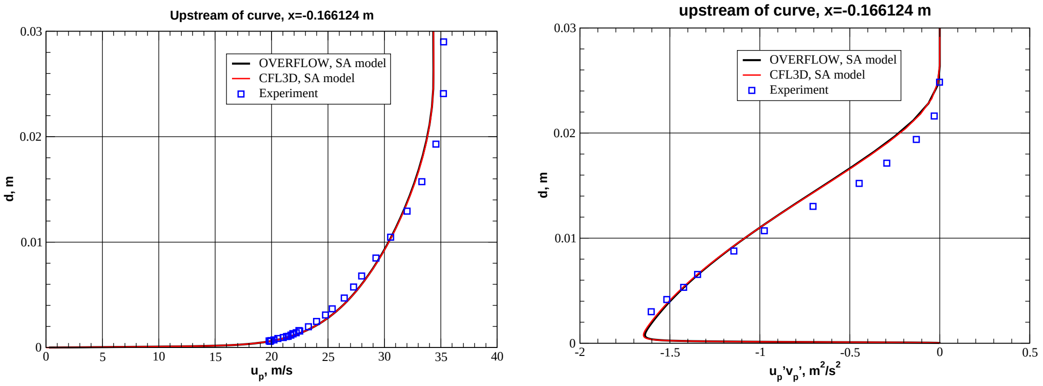

Figure 16.5: Velocity and turbulent shear stress profile upstream.

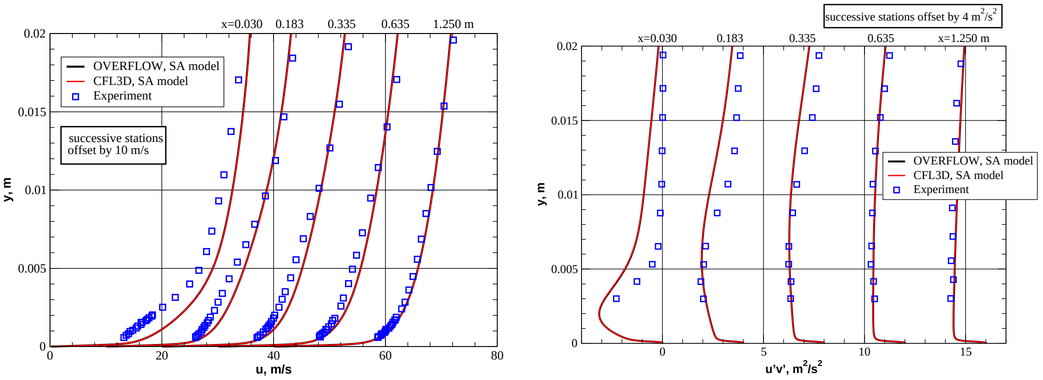

Figure 16.6: Velocity and turbulent shear stress profiles downstream.

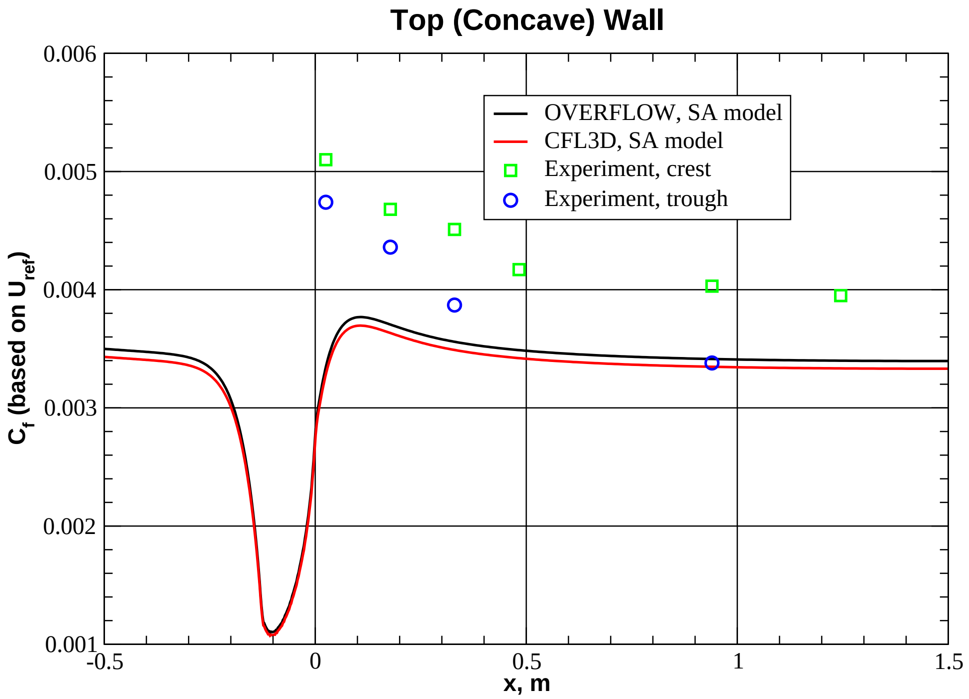

Figure 16.7: Upper wall skin friction, SA model.

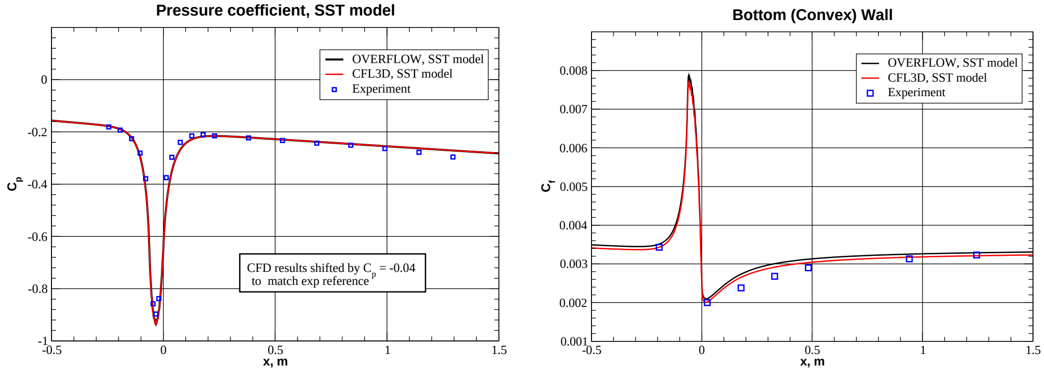

Figure 16.8: Pressure coefficient and skin friction on lower wall.

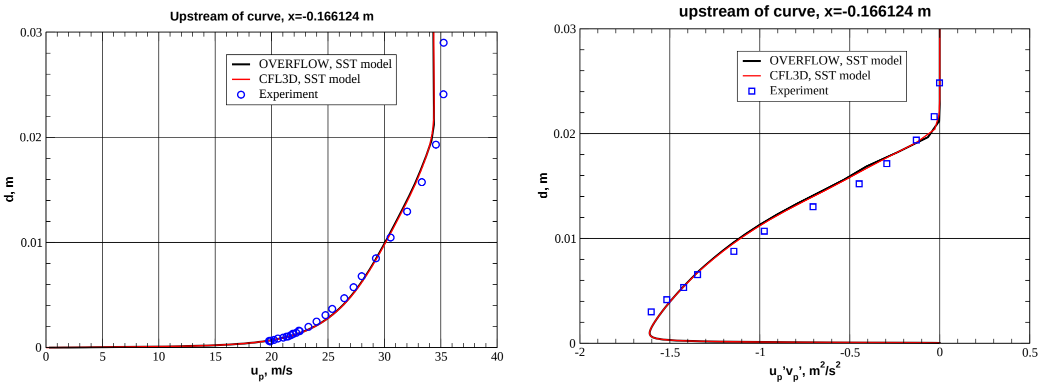

Figure 16.9: Velocity and turbulent shear stress profile upstream.

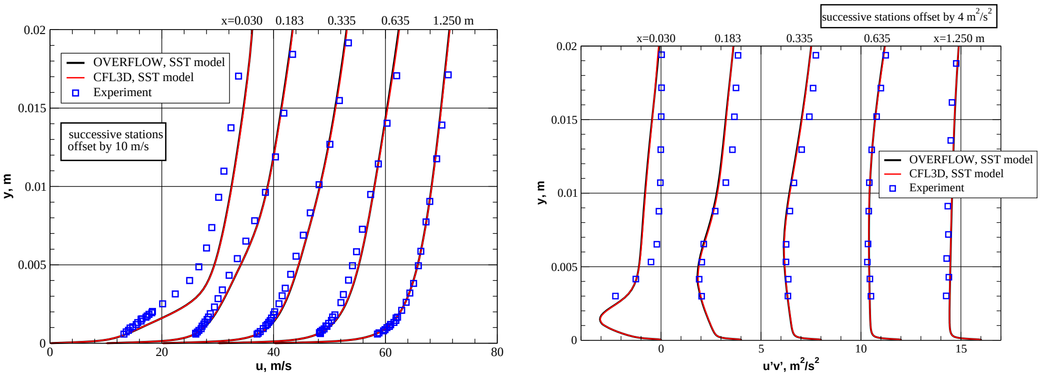

Figure 16.10: Velocity and turbulent shear stress profiles downstream.

is selected by setting the input parameter `IRC` to 1. We show pressure coefficient and skin friction coefficient on the lower wall in Figure 16.12, velocity and turbulent shear stress profiles upstream of the bend in Figure 16.13, velocity and turbulent shear stress profiles downstream of the bend in Figure 16.14, and skin friction coefficient on the upper wall in Figure 16.15. In all cases OVERFLOW and CFL3D agree very closely.

The next set of plots, (16.16–16.19), uses the SST model with rotational correction, denoted SST-RC on the TMR website. It should be noted that the SST-RC model implemented in the OVERFLOW versions that we used is not precisely the SST-RC model as defined on the TMR website. The SST-RC implementation in OVERFLOW is based on [15]. One of the differences is in the constant c_{r2}, which in OVERFLOW is set to 12 compared to the TMR website where c_{r2} is set to 2.

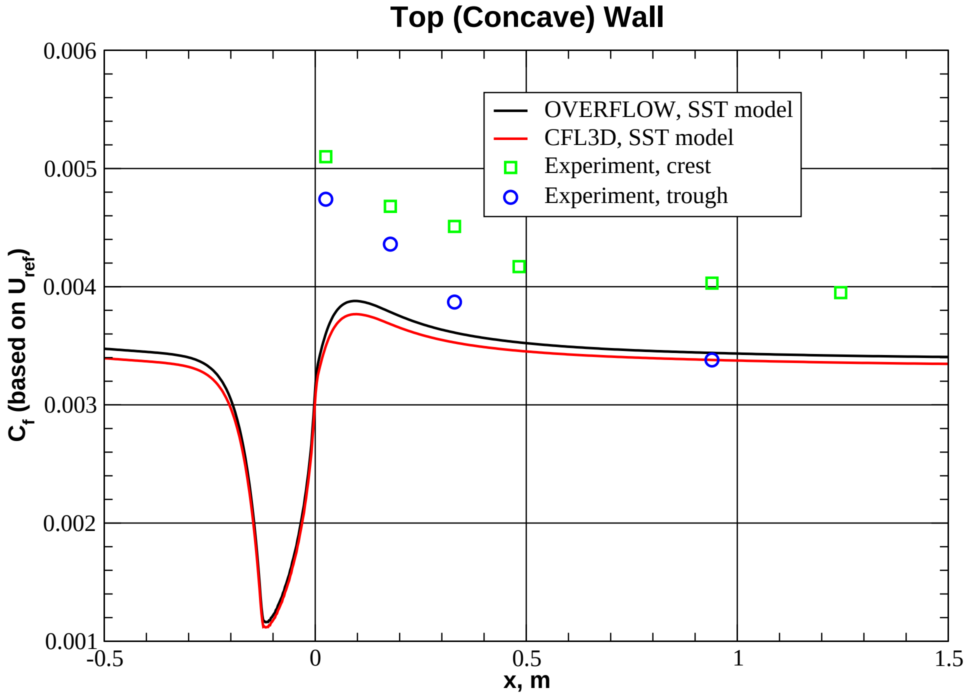

Figure 16.11: Upper wall skin friction, SST model.

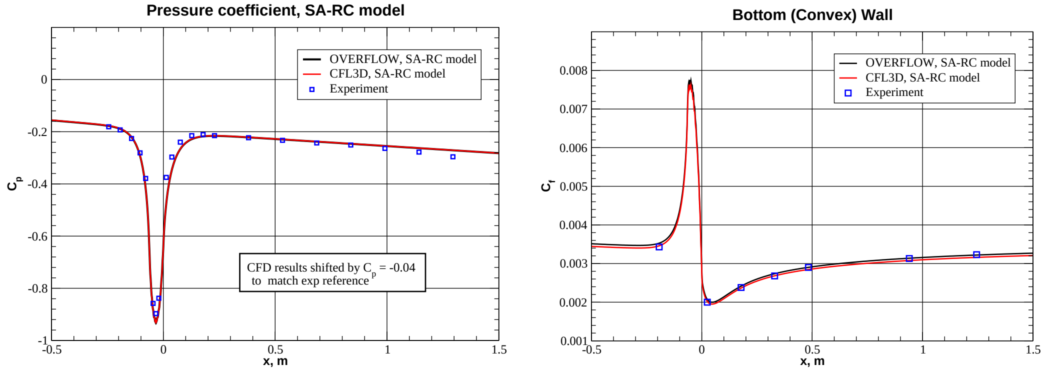

Figure 16.12: Pressure coefficient and skin friction on lower wall.

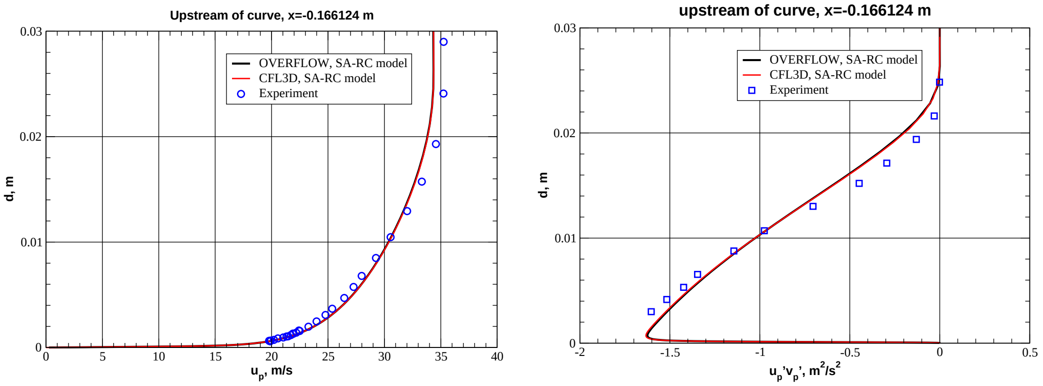

Figure 16.13: Velocity and turbulent shear stress profile upstream.

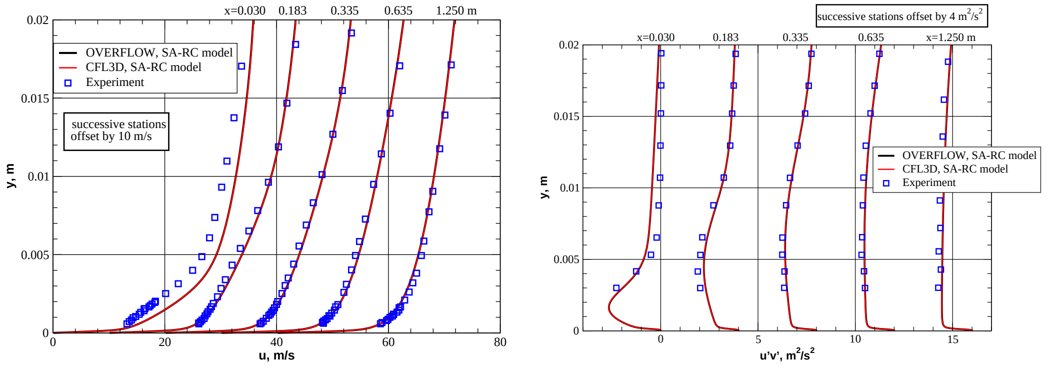

Figure 16.14: Velocity and turbulent shear stress profiles downstream.

We show pressure coefficient and skin friction coefficient on the lower wall in Figure 16.16, velocity and turbulent shear stress profiles upstream of the bend in Figure 16.17, velocity and turbulent shear stress profiles downstream of the bend in Figure 16.18, and skin friction coefficient on the upper wall in Figure 16.19. Evidently the skin friction coefficient on the lower wall from OVERFLOW is not as good compared to experiment as that from CFL3D.

In the next set of plots, (16.20–16.23), we show SST-RC results using a modified version of OVERFLOW, with the constant $c_{r2} = 2$. We show pressure coefficient and skin friction coefficient on the lower wall in Figure 16.20, velocity and turbulent shear stress profiles upstream of the bend in Figure 16.21, velocity and turbulent shear stress profiles downstream of the bend in Figure 16.22, and skin friction coefficient on the upper wall in Figure 16.23. The skin friction coefficient on the lower wall with $c_{r2} = 2$ is

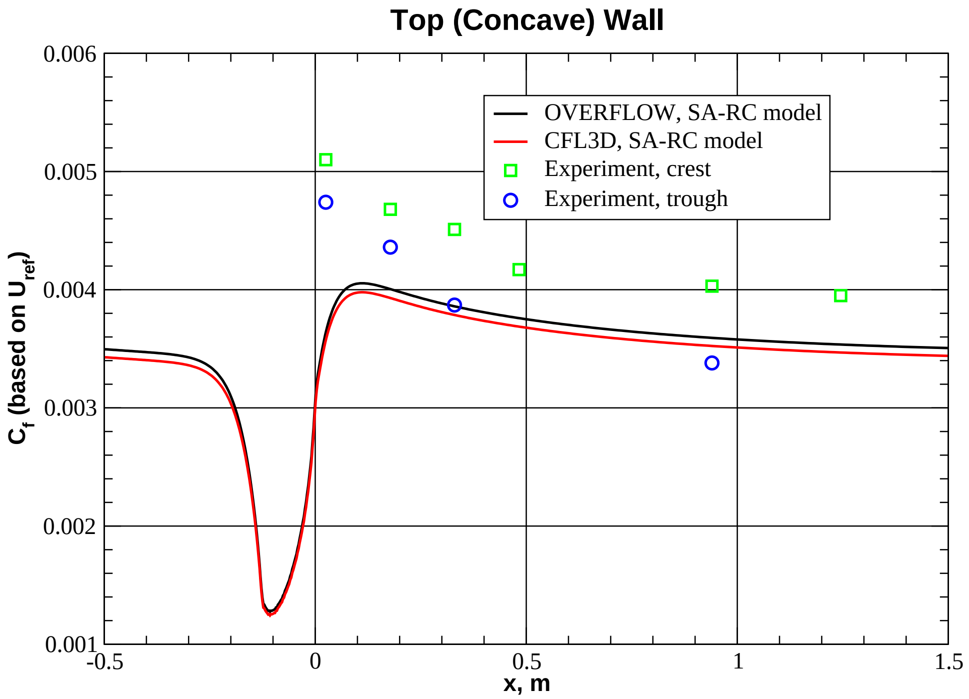

Figure 16.15: Upper wall skin friction, SA-RC model.

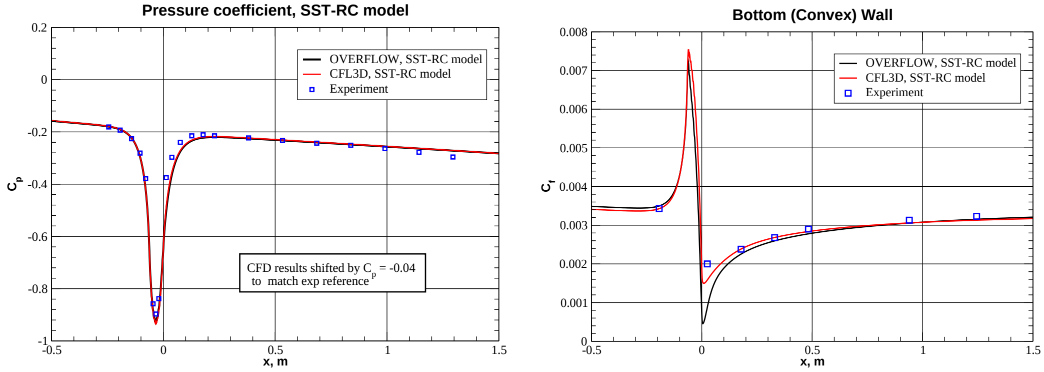

Figure 16.16: Pressure coefficient and skin friction on lower wall.

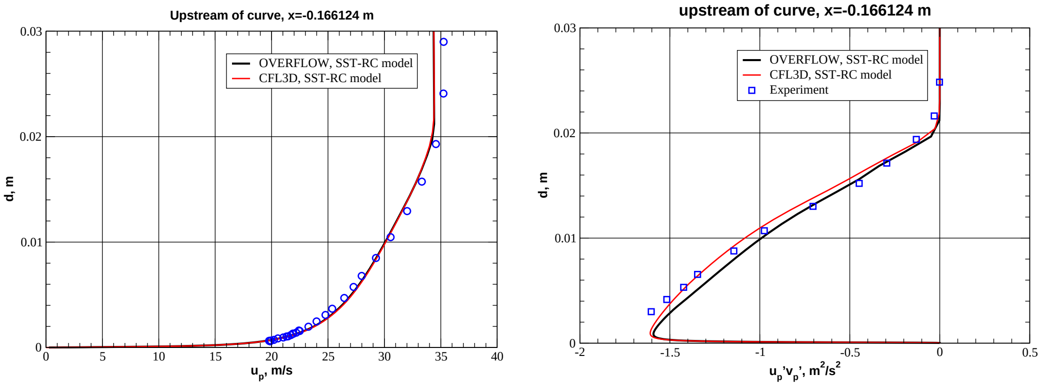

Figure 16.17: Velocity and turbulent shear stress profile upstream.

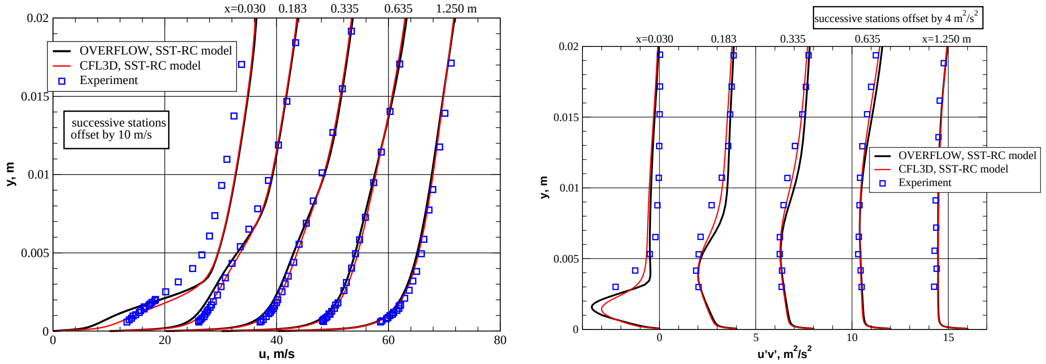

Figure 16.18: Velocity and turbulent shear stress profiles downstream.

closer to the experimental value, and there are some discernible changes in velocity and turbulent shear stress profiles.

There are several other possibilities for computation on this case. For example, the SA model in Overflow has an option for approximate rotational correction, selected with `IRC=2`. This model is denoted SA-R on the TMR website. The benefit of this model is a reduction in computation time compared to the SA-RC model. For one case with six MPI ranks on a Linux workstation, using the SA-RC model resulted in a 51% increase in compute time for the turbulence model as compared to the standard SA model, while using the SA-R model gave only a 9% increase in compute time over the SA model. The increase in overall time for numerics was 14% for the SA-RC model and 7% for the SA-R model. Of course these numbers are somewhat case dependent.

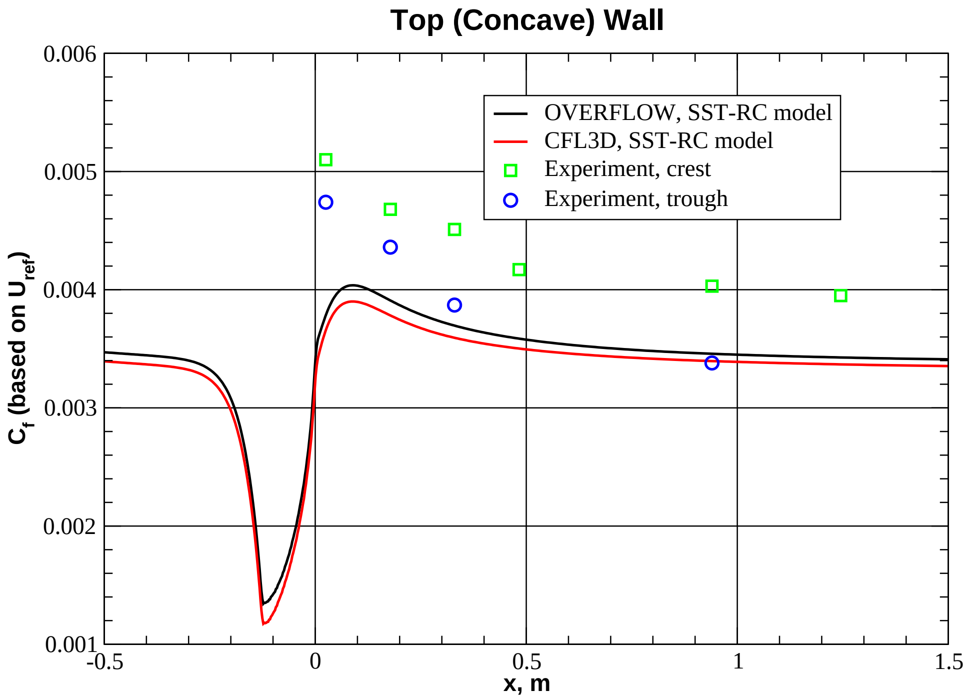

Figure 16.19: Upper wall skin friction, SST-RC model.

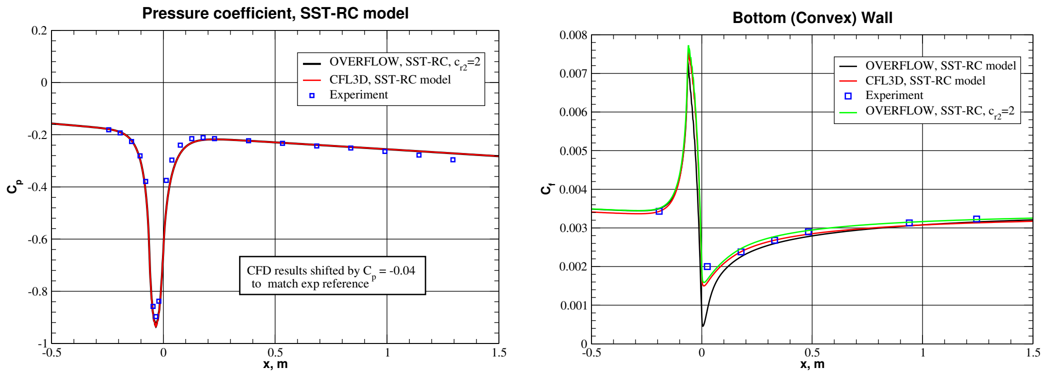

Figure 16.20: Pressure coefficient and skin friction on lower wall, $c_{r2} = 2$.

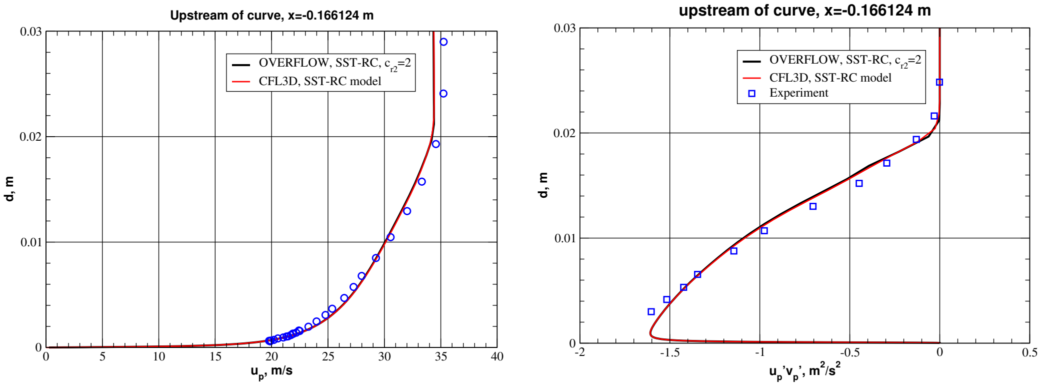

Figure 16.21: Velocity and turbulent shear stress profile upstream, $c_{r2} = 2$.

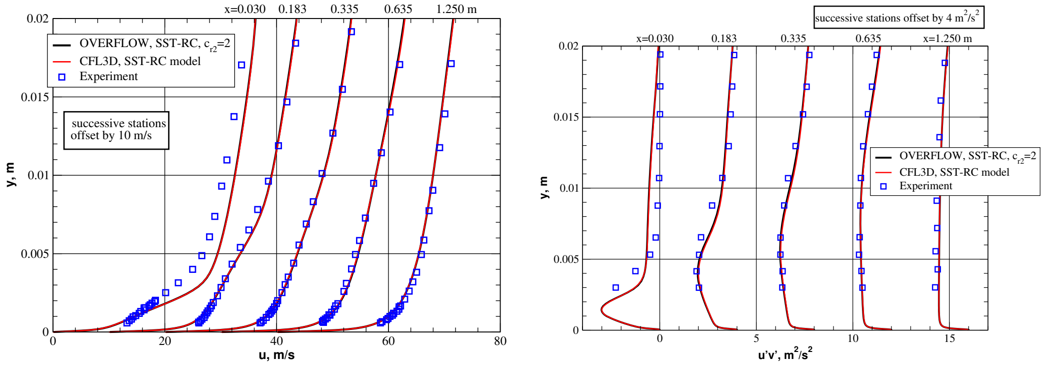

Figure 16.22: Velocity and turbulent shear stress profiles downstream, $c_{r2} = 2$.

The next set of plots,(16.24–16.27), compares OVERFLOW calculations with the SA, SA-RC, and SA-R models. We show pressure coefficient and skin friction coefficient on the lower wall in Figure 16.24, velocity and turbulent shear stress profiles upstream of the bend in Figure 16.25, velocity and turbulent shear stress profiles downstream of the bend in Figure 16.26, and skin friction coefficient on the upper wall in Figure 16.27. Some differences can be seen in the skin friction plots and in the velocity and turbulent shear stress profiles downstream of the bend. For these quantities the SA-RC model appears to give results closer to experiment than the SA or SA-R models. In some of the other plots, results from two of the variants, or even all three of the variants, plot atop one another.

To give some indication of the effect of grid refinement on the solution, in Figure 16.28 we show skin friction coefficient on the lower wall for the

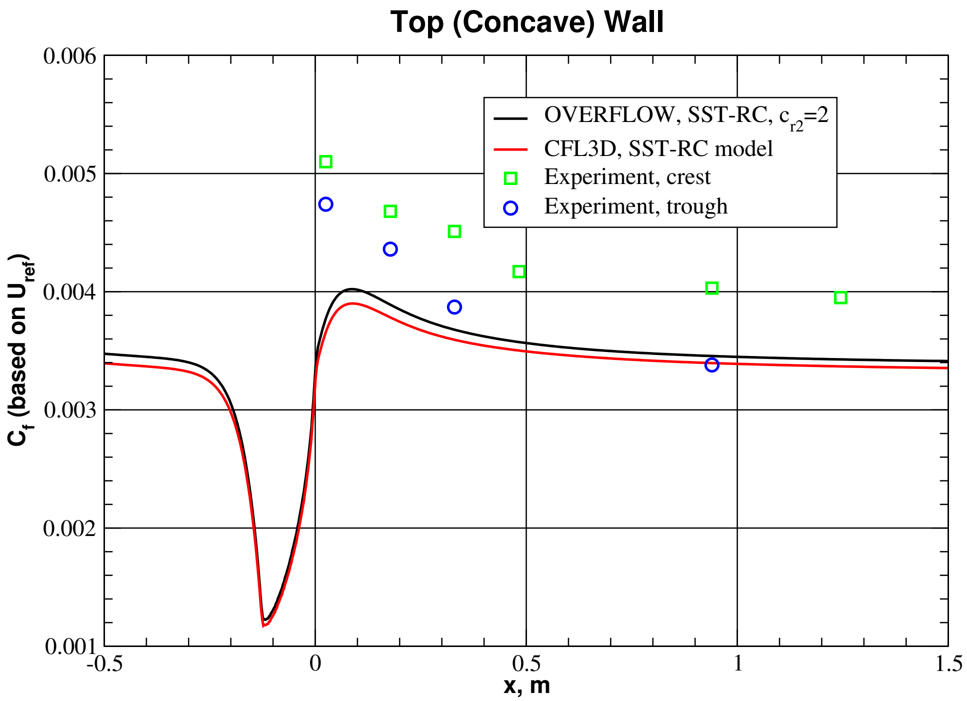

Figure 16.23: Upper wall skin friction, SST-RC model, $c_{r2} = 2$.

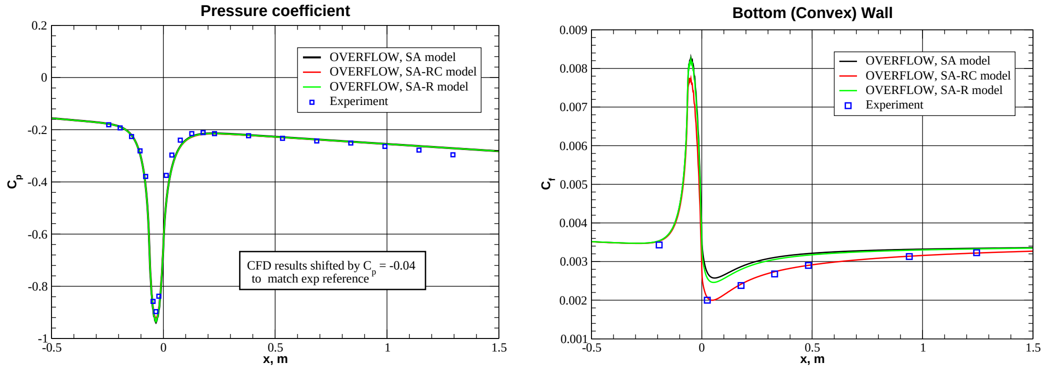

Figure 16.24: Pressure coefficient and skin friction on lower wall.

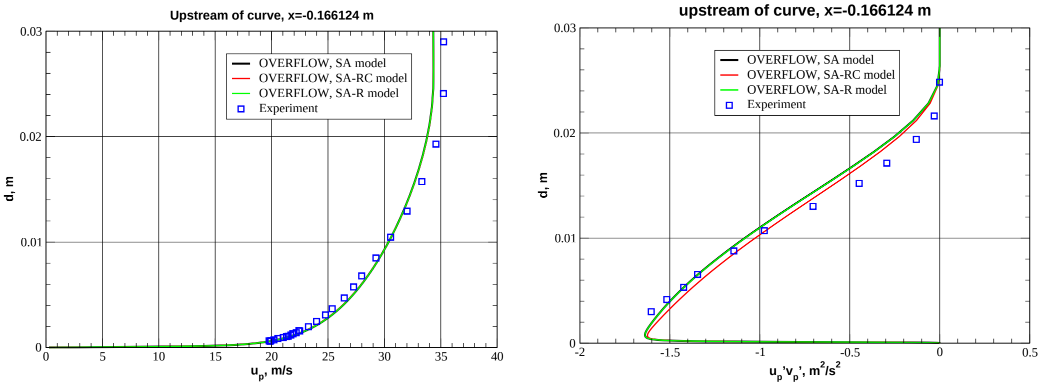

Figure 16.25: Velocity and turbulent shear stress profile upstream.

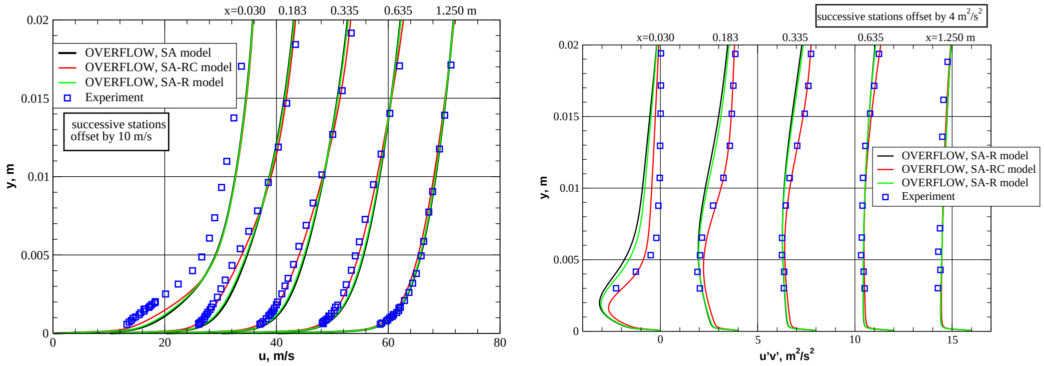

Figure 16.26: Velocity and turbulent shear stress profiles downstream.

SA-RC model, with five different grid sizes. Differences are noticeable for the coarser grid levels, but the results for the two finer grids are very close to one another.

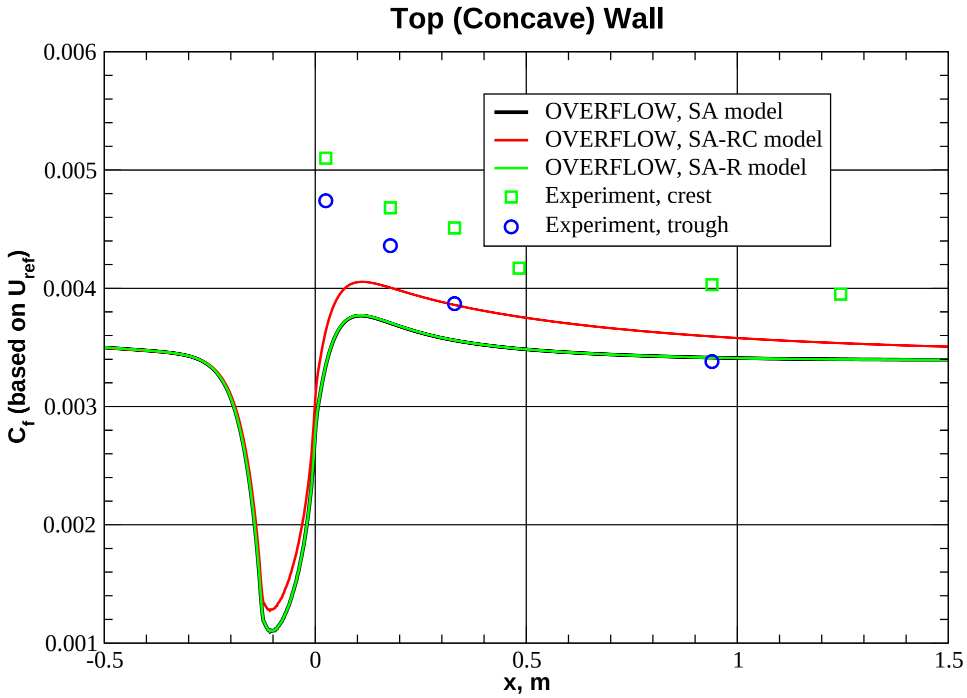

Figure 16.27: Upper wall skin friction, SA-RC and SA-R models.

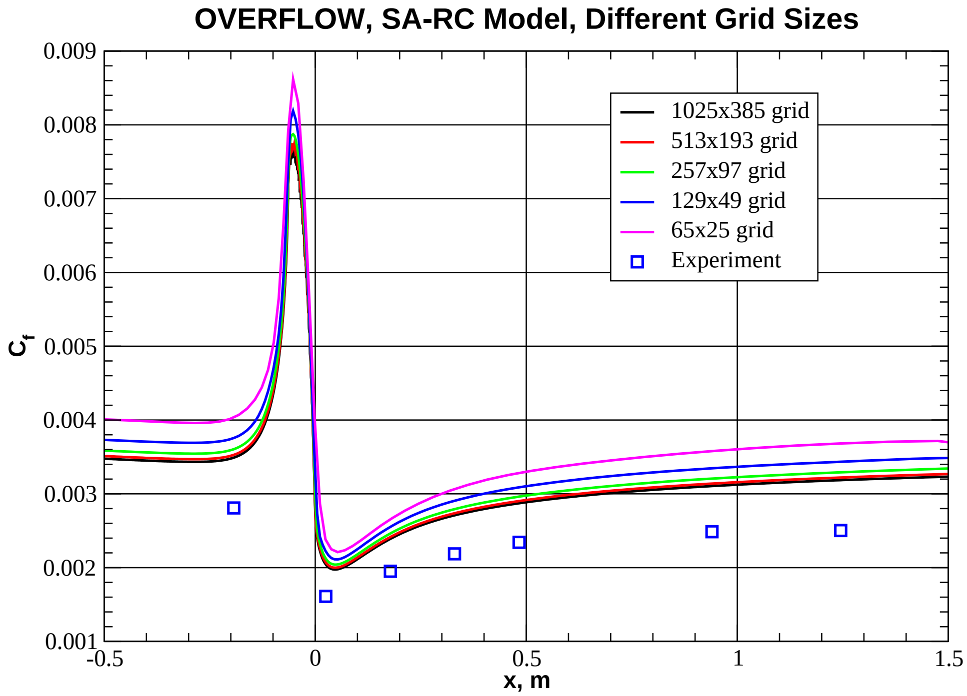

Figure 16.28: Lower wall skin friction, SA-RC, varying grid dimensions.

17. Two-Dimensional Wall-Mounted Hump

In this section we present turbulence model validation for Overflow using the LaRC TMR Two-Dimensional NASA Wall-Mounted Hump Separated Flow validation case. This case is a channel flow with Mach number $M = 0.1$ and Reynolds number $Re = 936,000$. The geometry and flow conditions are shown in Figure 17.1, taken from the TMR website. A close-up view of the geometry is indicated in Figure 17.2 and two views of the second-finest grid are shown in figures 17.3 and 17.4.

The Overflow calculations used central differencing with low-Mach preconditioning and matrix dissipation. We used data surface grids at $x/c = -2.1$, 0.65, 0.8, 0.9, 1.0, 1.1, 1.2, and 1.3 to obtain data for plotting. The data surface grids are defined as line segments perpendicular to the wall, meeting the lower surface of the wall at the indicated value of x. The lines of the grid are not necessarily perpendicular to the wall, so they cannot be used as the data surface grids.

The inflow boundary was specified with `IBTYP=41` and both parameters equal to 1, and the outflow boundary had `IBTYP=33` with parameter 0.99962. For Overflow on the finest grid with the SA turbulence model, the code was run until the L_2 norm of the flow residuals on each zone was reduced by at least five orders of magnitude from its initial value. With the SST turbulence model, the reduction factor was at least six orders of magnitude on each zone.

The first set of figures, (17.5–17.9), shows results with the SA turbulence model and the finest grid. We show pressure coefficient and skin friction coefficient in Figure 17.5, velocity profiles in Figures 17.6 and 17.7, and turbulent shear stress profiles in Figures 17.8 and 17.9. In all cases Overflow and Cfl3d agree very closely.

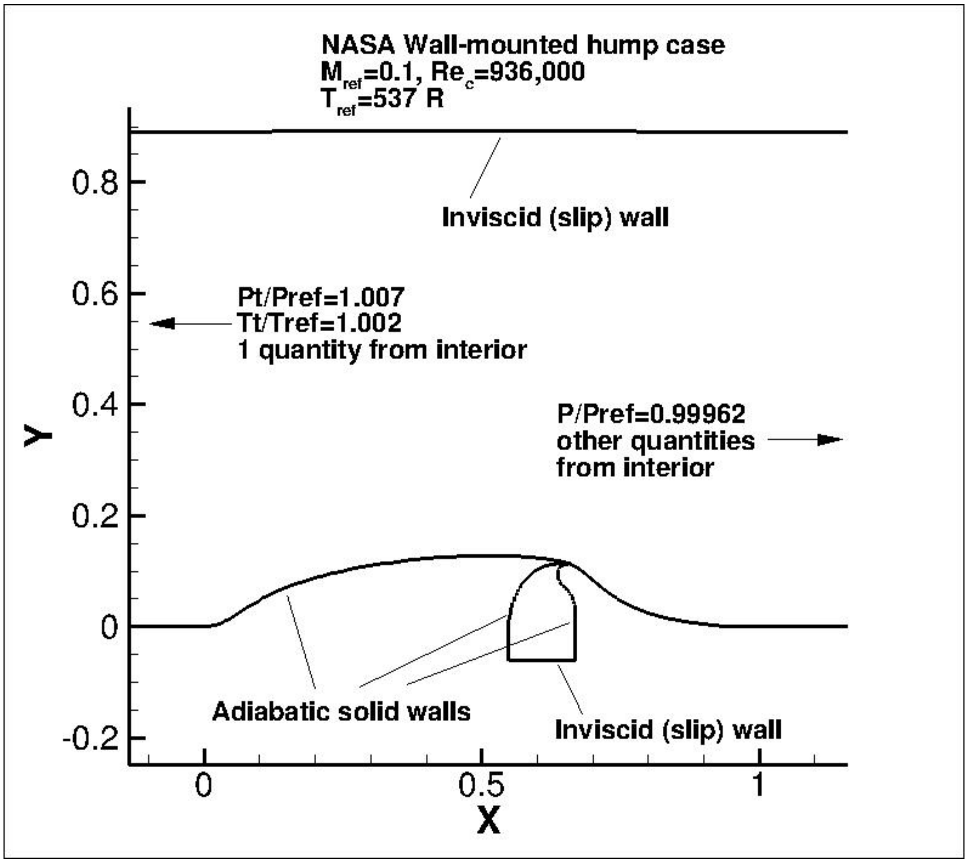

Figure 17.1: Wall-mounted hump geometry.

In Figure 17.10 we show contours of u-velocity along with some streamlines for the SA model on the finest grid, to indicate the extent of the recirculation region.

The next set of figures, (17.11–17.15), shows results with the SST turbulence model and the finest grid. We show pressure coefficient and skin friction coefficient in Figure 17.11, velocity profiles in Figures 17.12 and 17.13, and turbulent shear stress profiles in Figures 17.14 and 17.15. In all cases OVERFLOW and CFL3D are in good agreement.

In Figure 17.16 we show contours of u-velocity along with some streamlines for the SST model on the finest grid, to indicate the extent of the recirculation region.

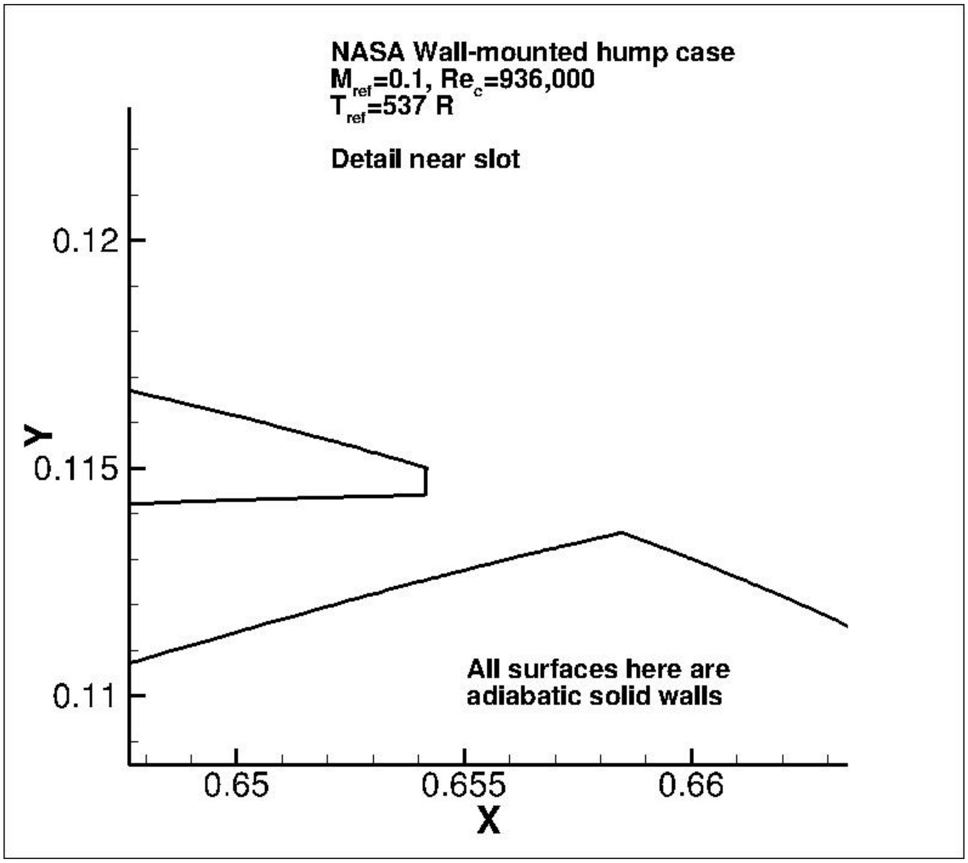

Figure 17.2: Wall-mounted hump geometry, near view.

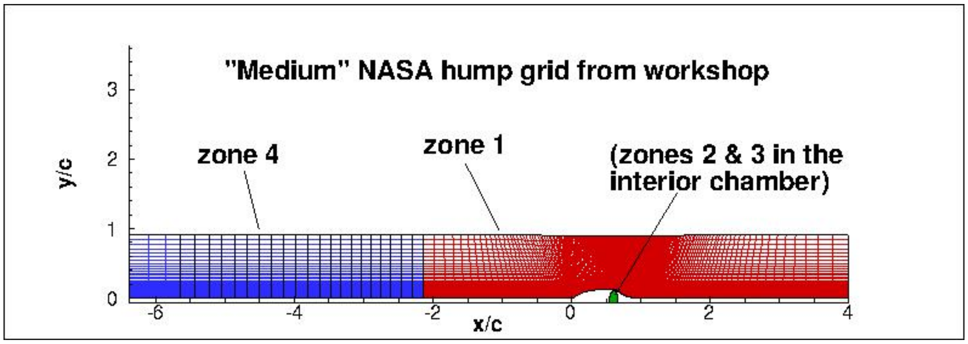

Figure 17.3: Wall-mounted hump grid.

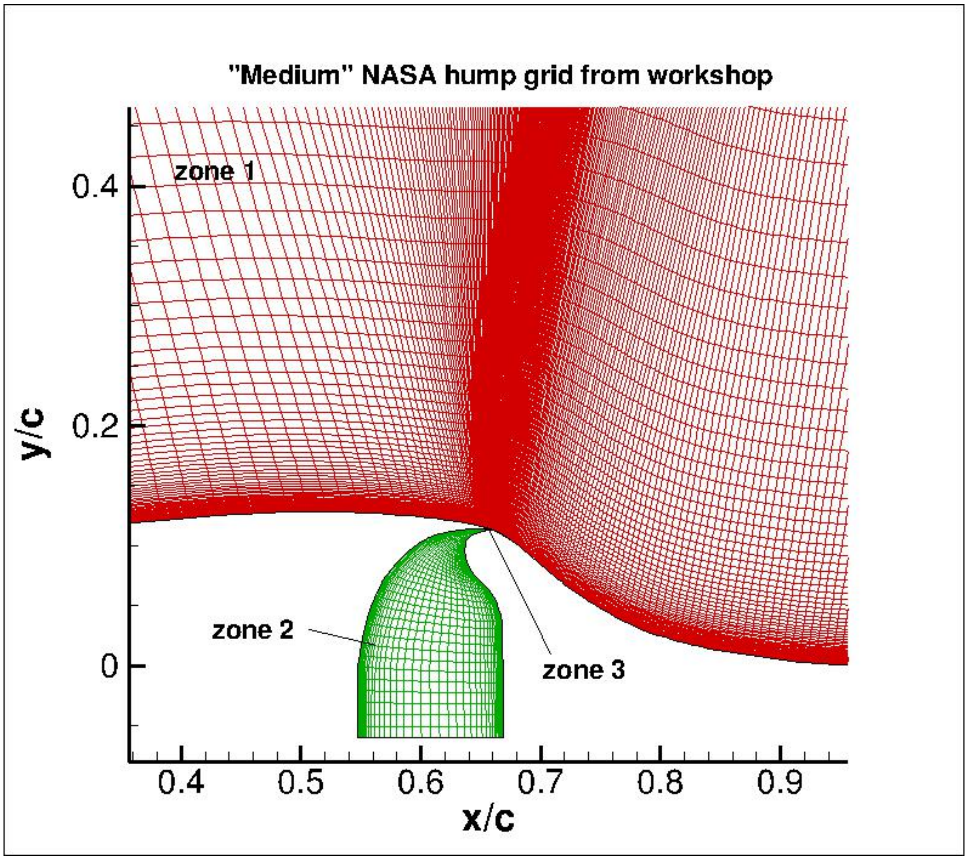

Figure 17.4: Wall-mounted hump grid, near view.

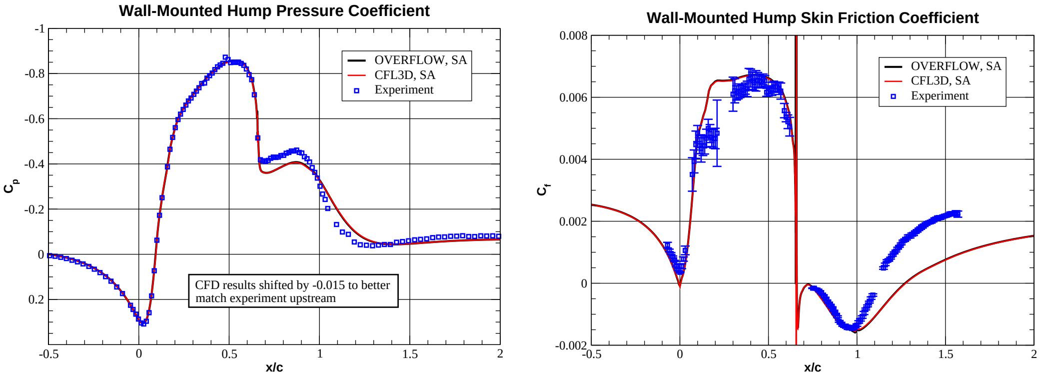

Figure 17.5: Pressure and skin friction coefficients, SA model.

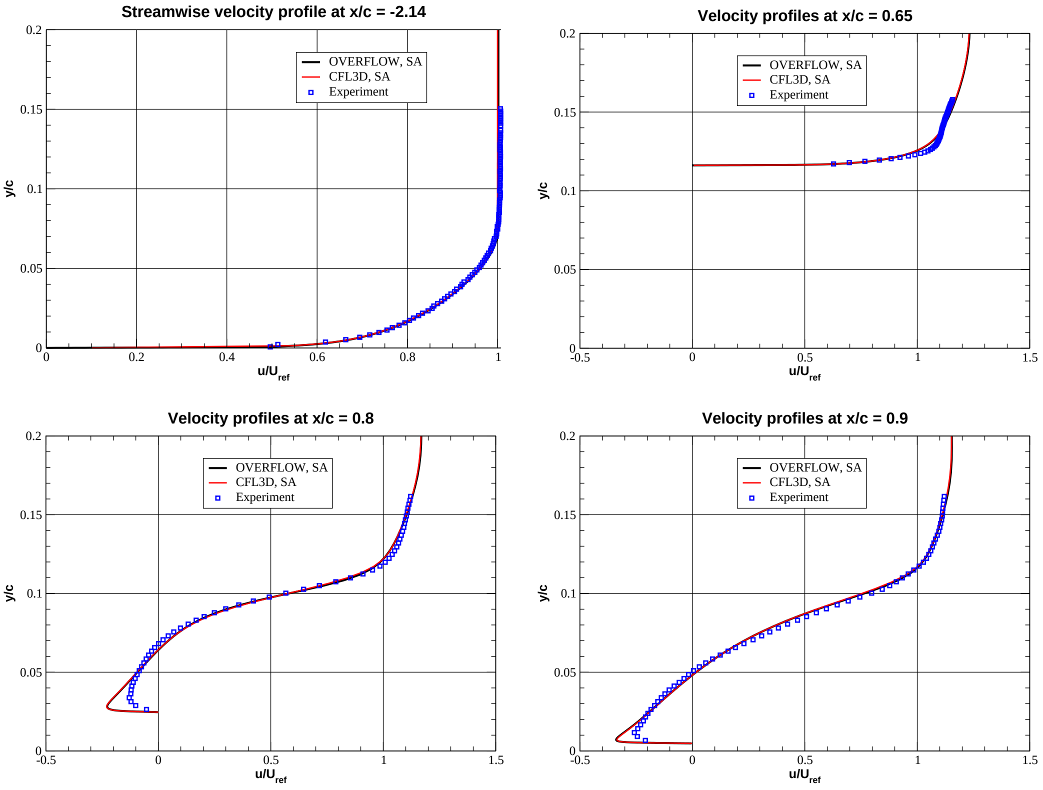

Figure 17.6: Velocity profiles, SA model.

For this case, the predicted reattachment location is of interest. In Table 17.1 we show data for the reattachment location from the experiment and from the computation.

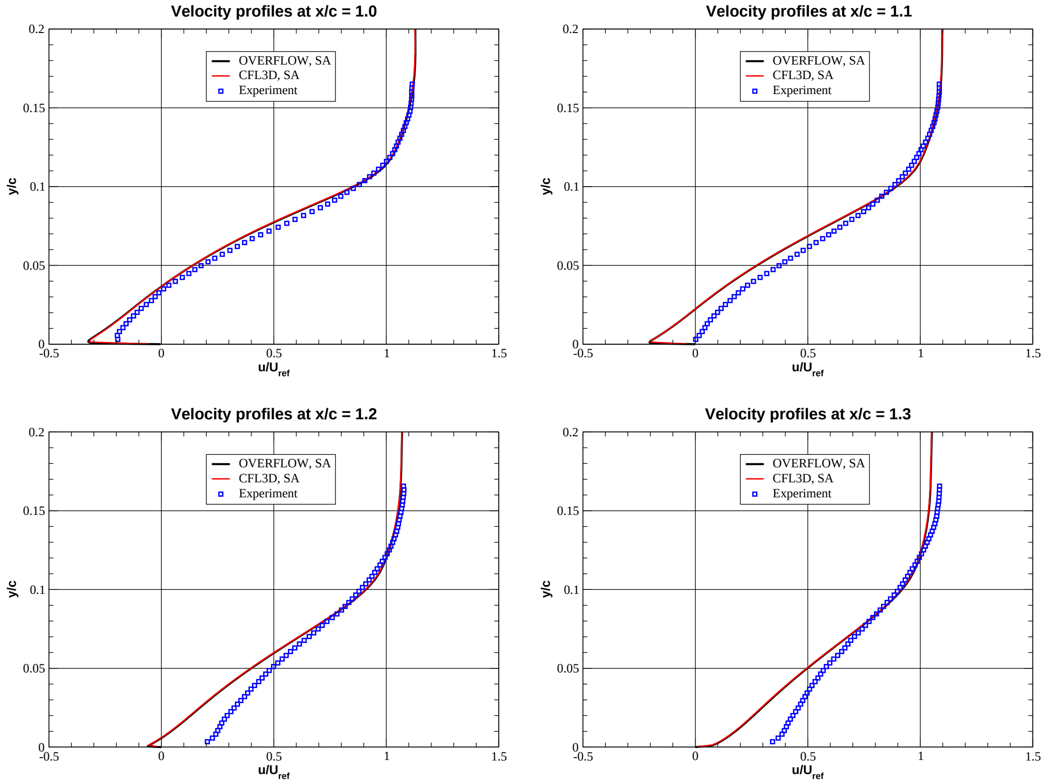

Figure 17.7: Velocity profiles, SA model.

Table 17.1: Reattachment location for wall-mounted hump.

Source	Reattachment
Experiment	1.1
CFL3D, SA	1.27 - 1.28
CFL3D, SST	1.25 - 1.27
OVERFLOW, SA	1.272
OVERFLOW, SST	1.271

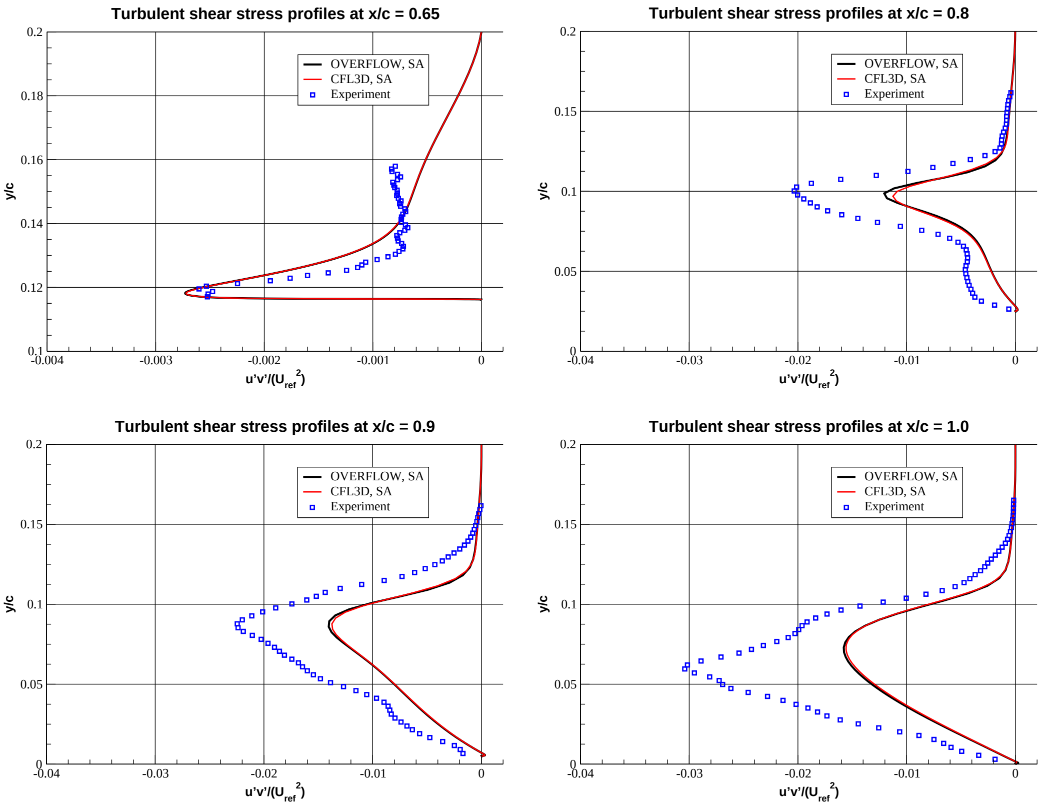
Turbulent shear stress profiles at x/c = 0.65

Turbulent shear stress profiles at x/c = 0.8

Turbulent shear stress profiles at x/c = 0.9

Turbulent shear stress profiles at x/c = 1.0

Figure 17.8: Turbulent shear stress profiles, SA model.

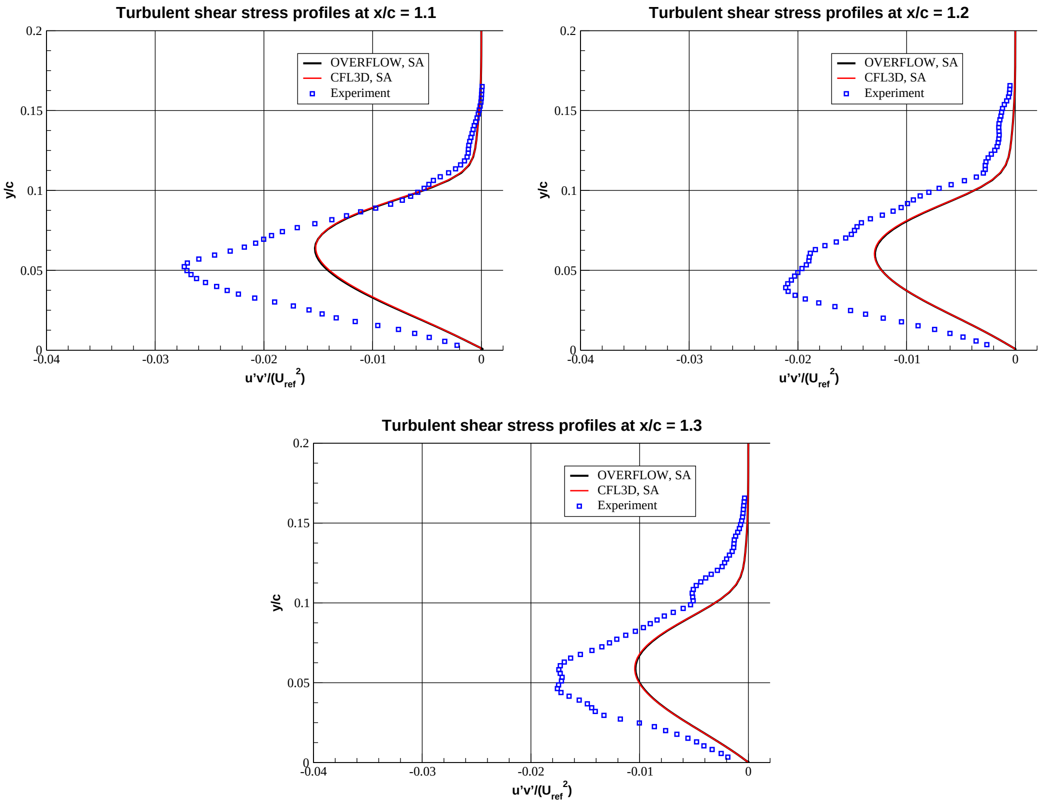

Figure 17.9: Turbulent shear stress profiles, SA model.

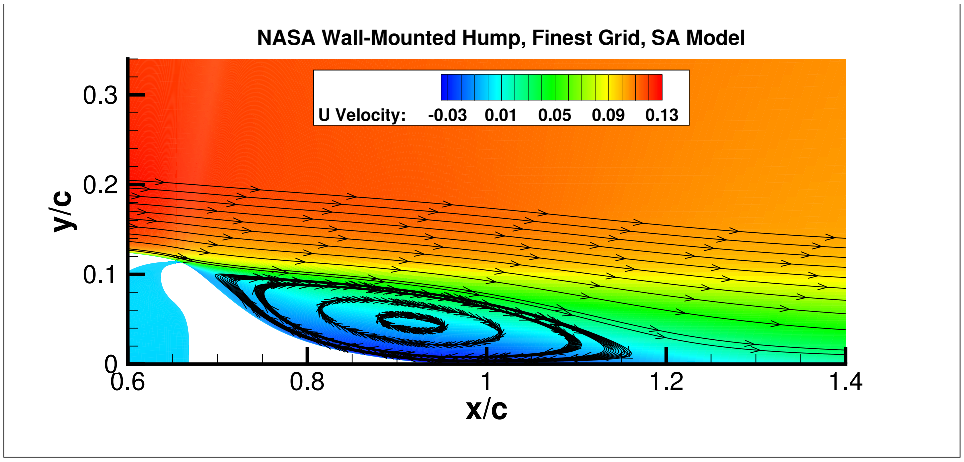

Figure 17.10: Streamlines and u-velocity contours, SA model.

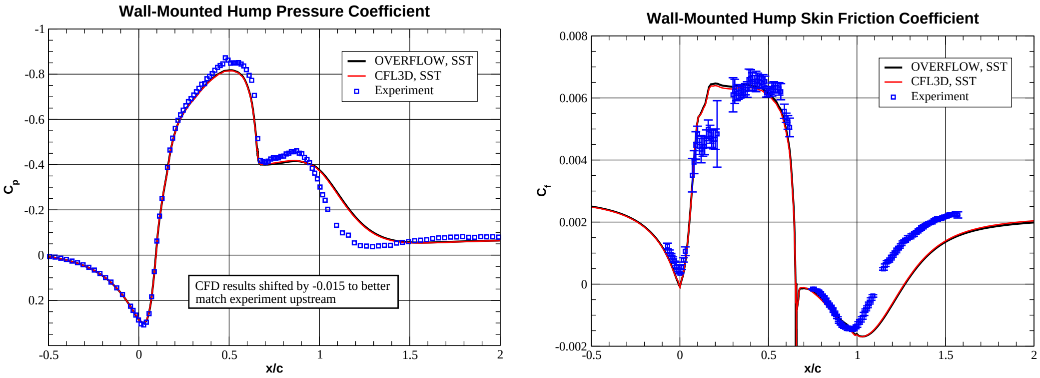

Figure 17.11: Pressure and skin friction coefficients, SST model.

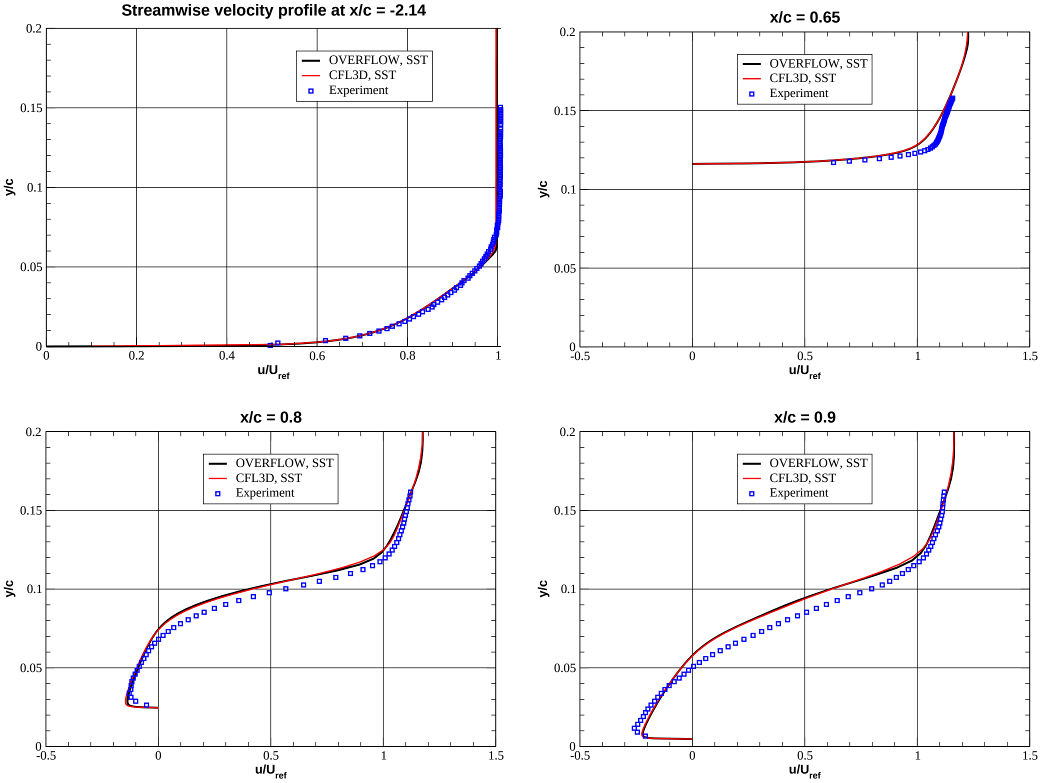

Figure 17.12: Velocity profiles, SST model.

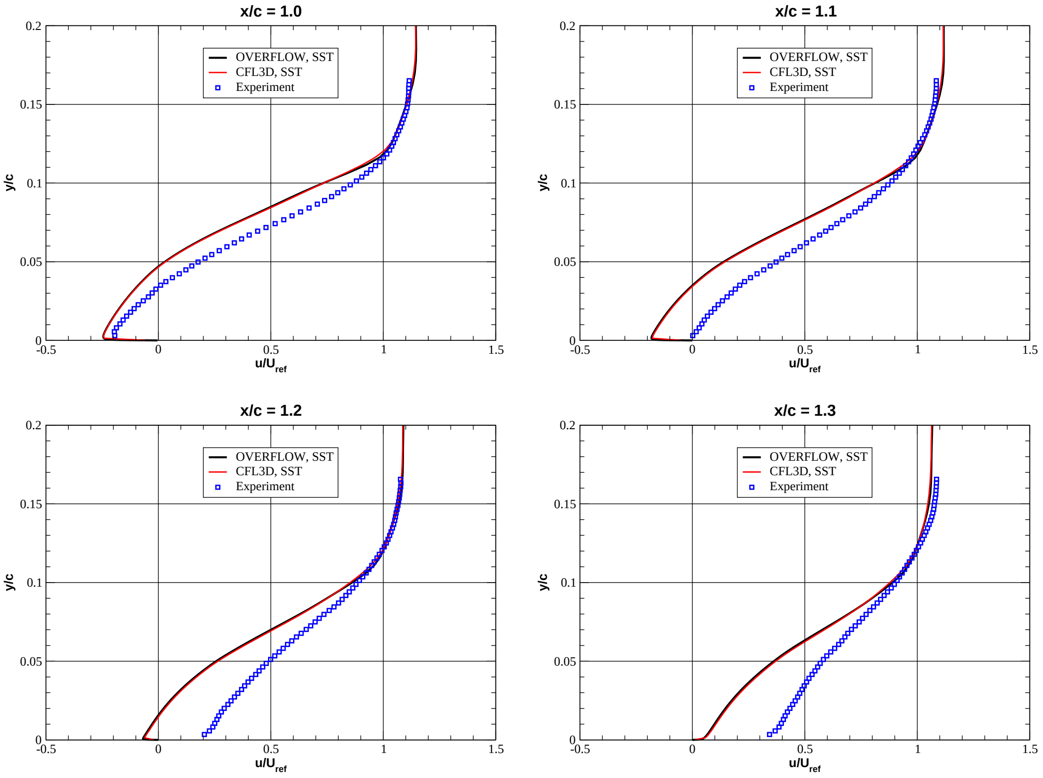

Figure 17.13: Velocity profiles, SST model.

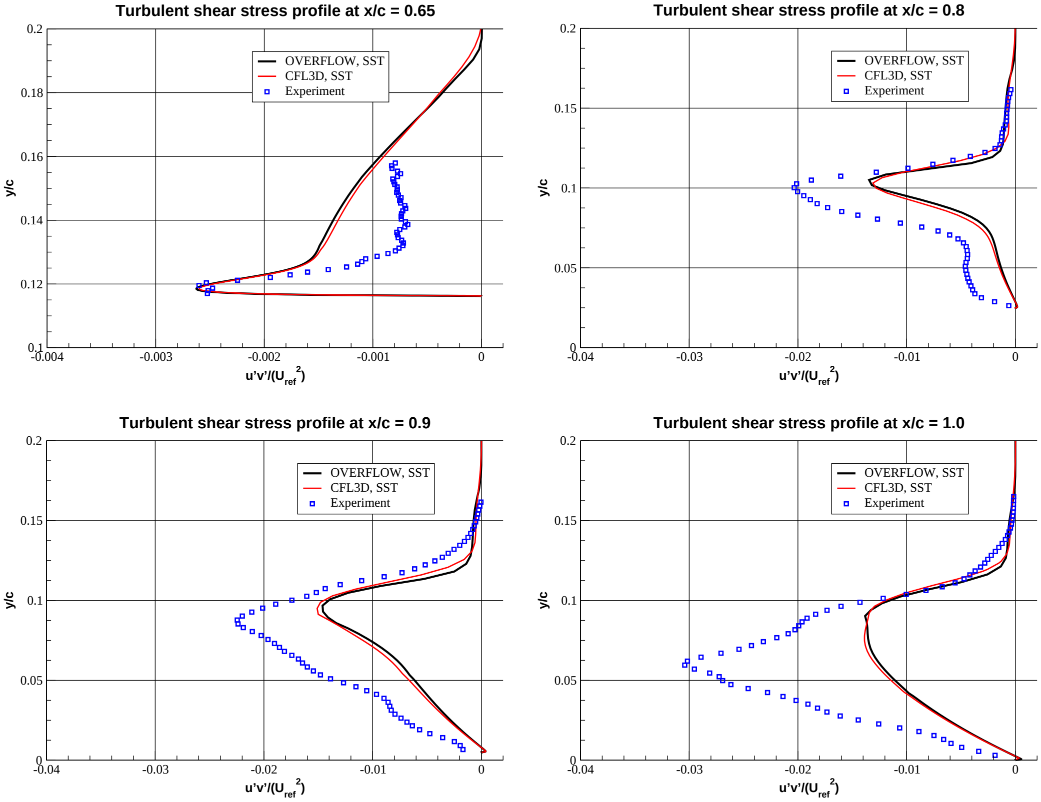
Turbulent shear stress profile at x/c = 0.65

Turbulent shear stress profile at x/c = 0.8

Turbulent shear stress profile at x/c = 0.9

Turbulent shear stress profile at x/c = 1.0

Figure 17.14: Turbulent shear stress profiles, SST model.

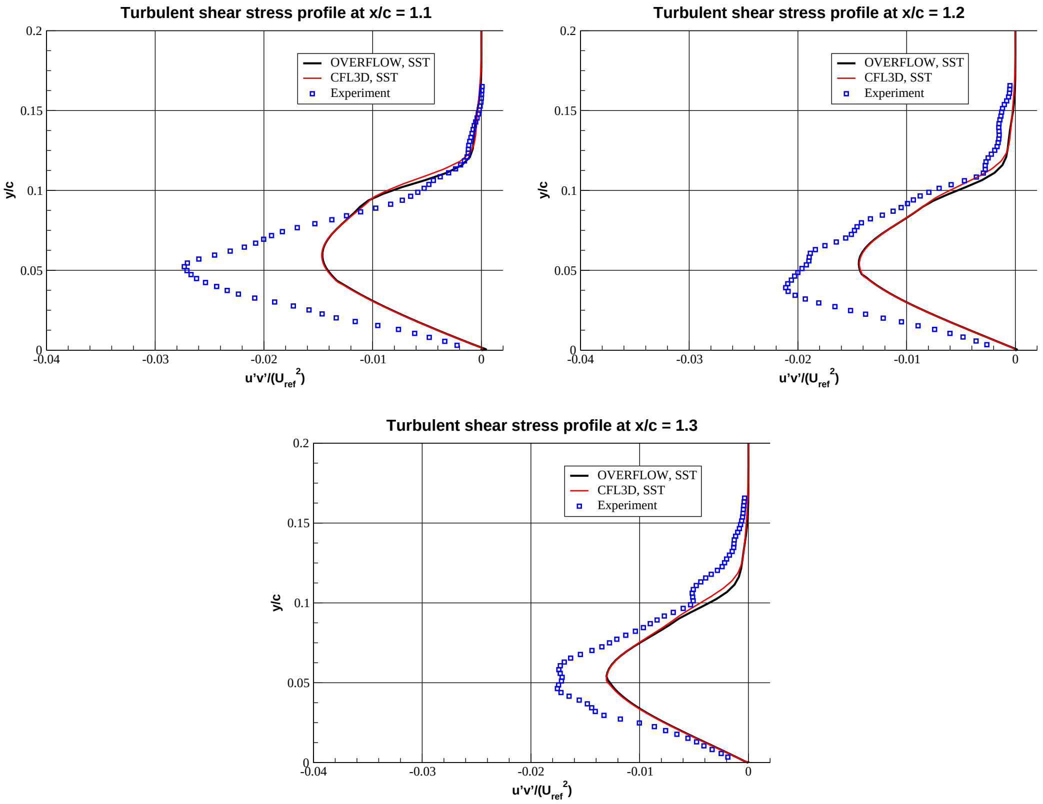

Figure 17.15: Turbulent shear stress profiles, SST model.

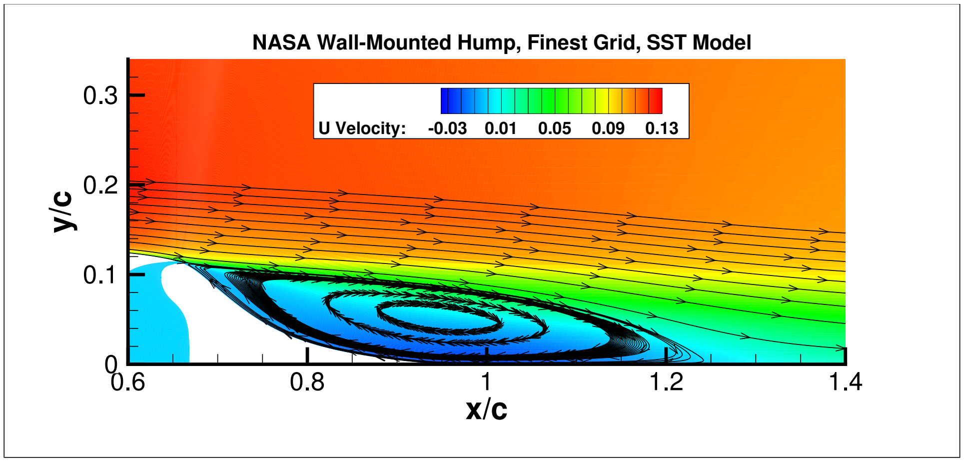

Figure 17.16: Streamlines and u-velocity contours, SST model.

18. Axisymmetric Shock Wave-Boundary Layer Interaction

In this section we present turbulence model validation for OVERFLOW using the LaRC Turbulence Modeling Resource (TMR) Axisymmetric Shock Wave Boundary Layer Interaction case. This case has Mach number $M = 7.11$ and Reynolds number $Re = 57,060$ per centimeter. The geometry and flow conditions are shown in Figure 18.1, taken from the TMR website. A close-up view of the grid system provided for this case is indicated in Figure 18.2. We used a data surface grid at $x = -6$ to obtain data for plotting velocity and total temperature profiles.

The first set of plots, figures 18.3–18.4, shows results with the SA model. The OVERFLOW calculations with the SA model used HLLE++ (`IRHS=6`) for spatial differencing and SSOR (`ILHS=16`) for the time-stepping. On the second-finest grid, enough time steps were taken so that the L_2 residuals of the mean flow equations and the turbulence model dropped at least ten orders of magnitude from their maximum values.

Figure 18.3 shows normalized streamwise velocity and temperature profiles upstream of the flare at $x = -6$, comparing OVERFLOW, WIND, and experiment. OVERFLOW and WIND agree closely with one another.

Figure 18.4 shows normalized pressures and heat transfer coefficients along the wall. There are some perceptible differences in pressure between OVERFLOW and WIND, while the heat transfer coefficients are in close agreement.

We tried OVERFLOW with various forms of the SST turbulence model, experimenting with rotational and compressibility correction. We used `IRHS=6`, `ILHS=5`, and the `DDADI` solver for the turbulence model, `NQT=203`. For the

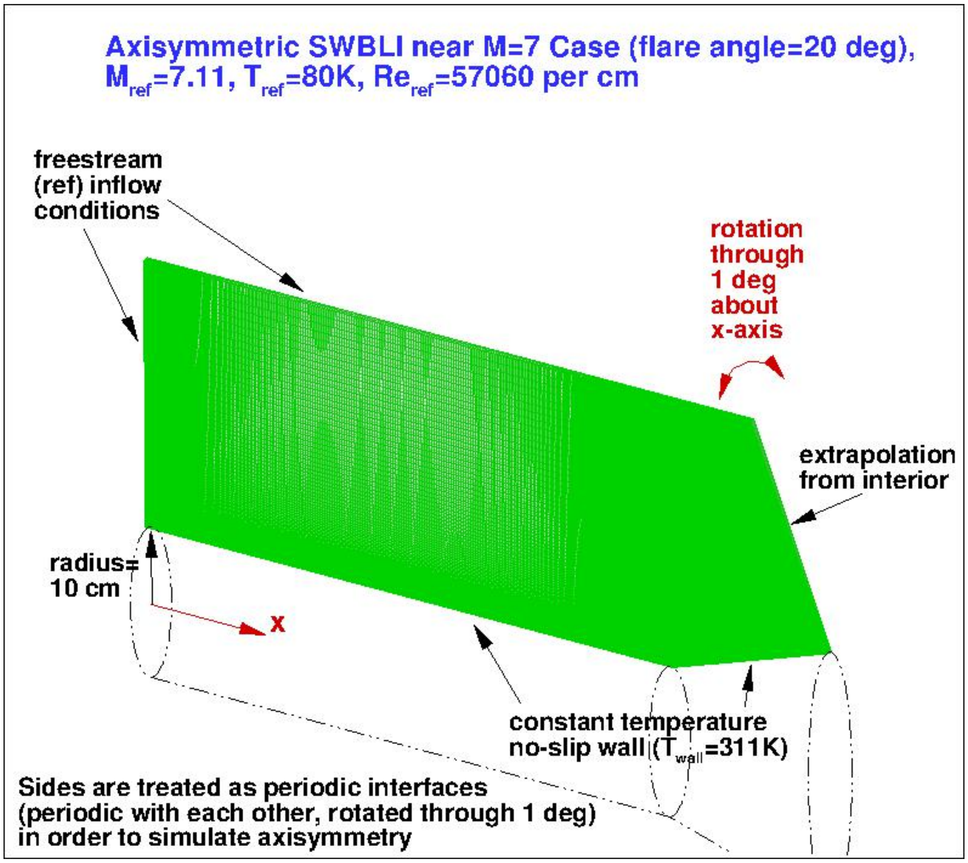

Figure 18.1: Axisymmetric shock wave boundary layer geometry.

SST model, we found that, in all cases, the model did not become steady. We found that the compressibility correction made little or no difference. With rotational correction, the heat transfer did not reach a steady state. Without rotational correction, the heat transfer reached a steady state but is significantly different from experiment.

For the SST-V model we found that the model does not reach a steady state and that the compressibility correction has little or no effect. With rotational correction, the heat transfer does not become steady, but without rotational correction the heat transfer does become steady and compares well with experiment. (For the SA model, rotational correction makes a slight difference in heat transfer, but both with and without rotational correction

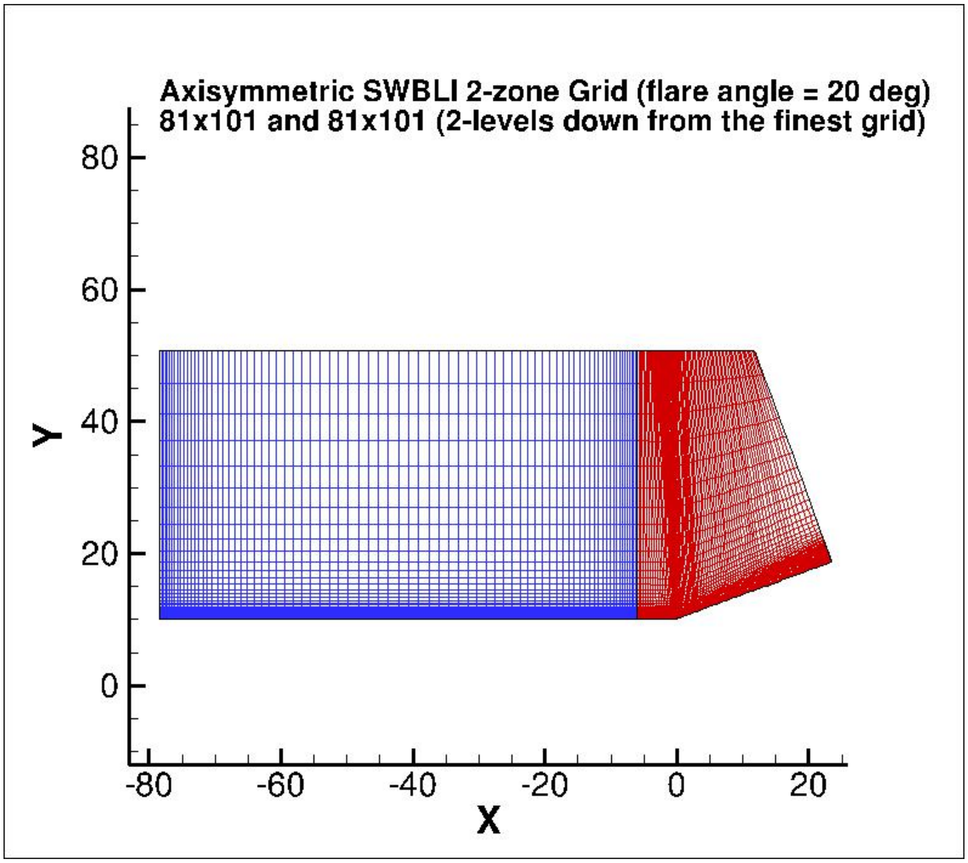

Figure 18.2: Axisymmetric shock wave boundary layer grid.

the heat transfer agrees with experiment. Also, the SA model reaches a steady state both with and without rotational correction.) Thus for this case the best form of the SST model appears to be SST-V without rotational correction and without compressibility correction.

The next set of plots, figures 18.5–18.6, shows results for the SST-V model. Figure 18.5 shows normalized streamwise velocity and temperature profiles upstream of the flare at $x = -6$, comparing Overflow, Wind, and experiment. Overflow and Wind agree closely with one another.

Figure 18.6 shows normalized pressure and heat transfer coefficients along the wall. There are some noticeable differences in pressure between Overflow and Wind, while the codes agree well for heat transfer.

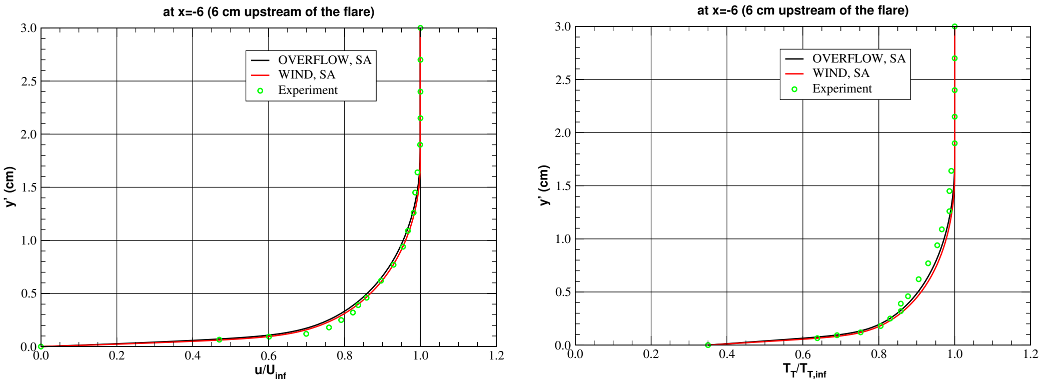

Figure 18.3: Normalized streamwise velocity and temperature profiles, SA model.

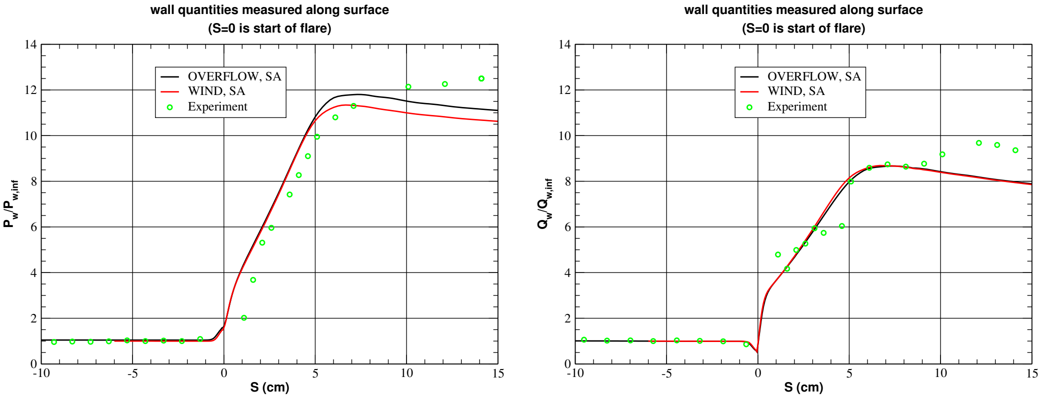

Figure 18.4: Normalized pressure and heat transfer on the surface, SA model.

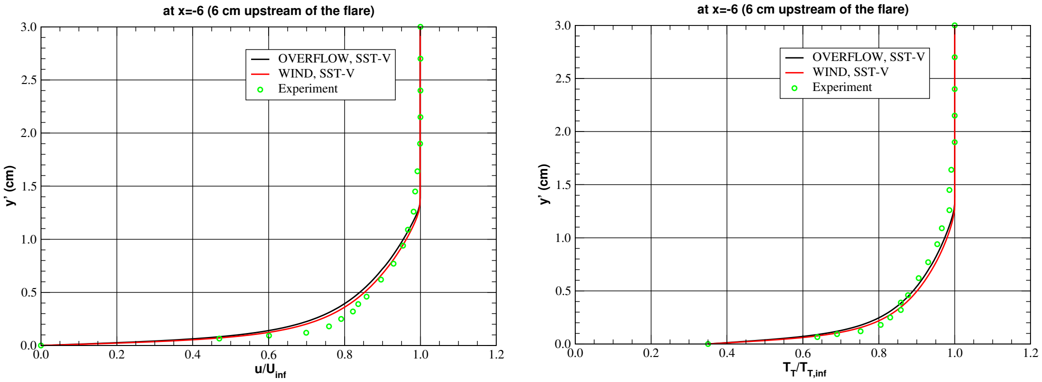

Figure 18.5: Normalized streamwise velocity and temperature profiles, SST-V model.

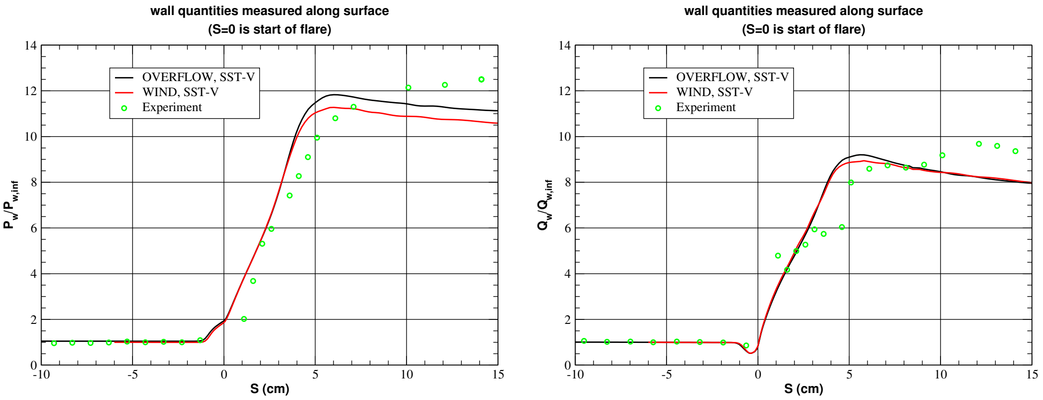

Figure 18.6: Normalized pressure and heat transfer on the surface, SST-V model.

19. Three-Dimensional Supersonic Square Duct

In this section we present turbulence model validation for Overflow using the LaRC TMR Three-Dimensional Supersonic Square Duct validation case. This case studies flow in a constant-area square duct with Mach number $M = 3.9$ and Reynolds number $Re = 508,000$. The geometry and flow conditions are shown in Figure 19.1, taken from the TMR website. A view of a cross-section of the grid for this case is indicated in Figure 19.2.

The Overflow calculations used Roe differencing. We used data surface grids at $x/D = 40$ and 50 to obtain data for plotting. At each of these two streamwise stations there were three data surface grids, one a 2D planar grid with x/D constant, one a diagonal line segment from the intersection of the solid walls to the opposite corner, and one a line segment along the symmetry boundary in the vertical (z) direction.

The inflow boundary was specified with `IBTYP=40` (freestream conditions imposed), and the outflow boundary had either `IBTYP=30` (pure extrapolation) or `IBTYP=31` (characteristic boundary condition using Riemann invariants). For this case it makes very little difference in the solution – except very near the outflow boundary – whether one uses `IBTYP=30` or `IBTYP=31`. We ran both the SA and SST models without and with the Quadratic Constitutive Relation (QCR) [10],[11]. The Overflow implementation of QCR is referred to as QCR2000 on the TMR website.

Overflow on the second-finest grid (dimensions 481 × 81 × 81), with both the SA and SST turbulence models, was run until the L_2 norm of the flow residuals was reduced by at least three orders of magnitude from its initial value and at least six orders of magnitude from its maximum value. In what follows, the term “crossflow velocity” refers to velocity transverse to the main flow direction, i.e., velocity in the (y, z) plane.

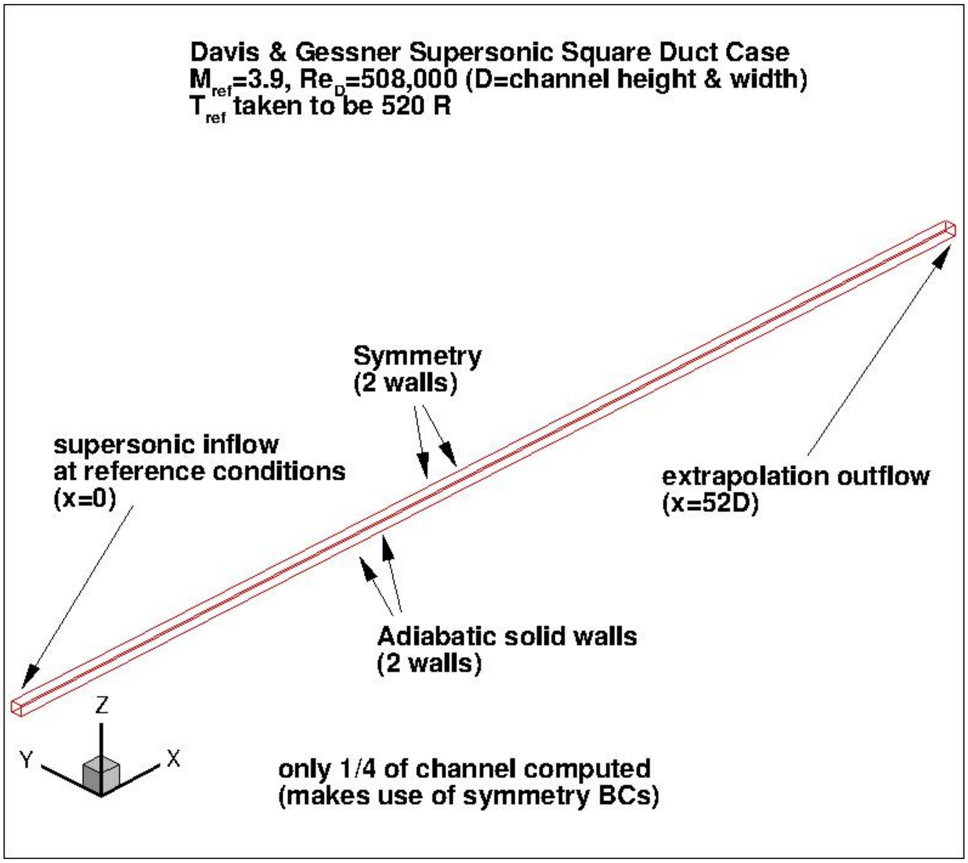

Figure 19.1: 3D duct geometry.

The first set of figures, (19.3–19.4), shows results for the SA model on the second-finest grid. We show velocity profiles along diagonal and vertical cuts at $x/D = 40$ and $x/D = 50$ in Figure 19.3. The skin friction coefficient along the vertical sidewall at $x/D = 50$ is shown in Figure 19.4. Crossflow velocity is also indicated in Figure 19.4. In all the line plots there is very good agreement between OVERFLOW and CFL3D. The crossflow velocity plot does not indicate any secondary recirculation regions, contrary to what is observed experimentally.

The next set of figures, (19.5–19.6), shows results for the SST model on the second-finest grid. We show velocity profiles along diagonal and vertical cuts at $x/D = 40$ and $x/D = 50$ in Figure 19.5. The skin friction coefficient

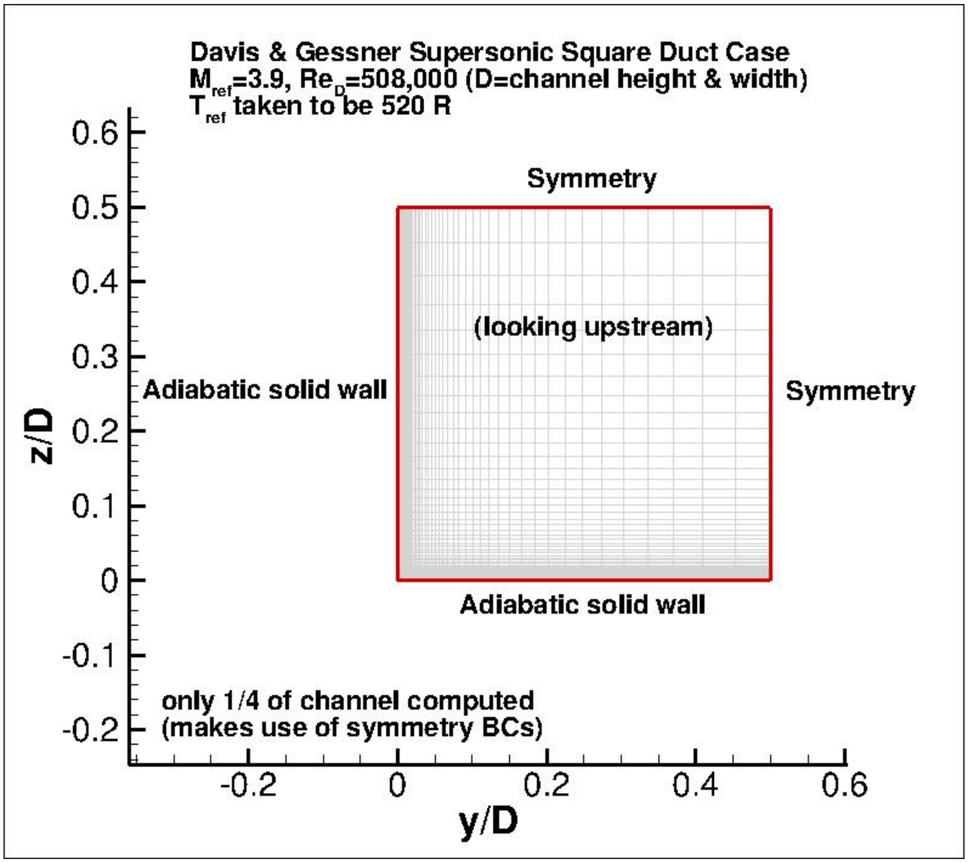

Figure 19.2: 3D duct, grid cross-section.

along the vertical sidewall at $x/D = 50$ is shown in Figure 19.6. Crossflow velocity is also shown in Figure 19.6. In all cases there is very good agreement between Overflow and Cfl3d, and as with the SA model the crossflow velocity plot for the SST model does not show any recirculation regions.

Figure 19.7 shows crossflow velocity on the finest grid for both the SA and SST models. Even with the increased grid resolution there is no secondary recirculation.

The next set of figures, (19.8–19.9), shows results for the SA-QCR model on the second-finest grid. We show velocity profiles along diagonal and vertical cuts at $x/D = 40$ and $x/D = 50$ in Figure 19.8. The skin friction coefficient along the vertical sidewall at $x/D = 50$ is shown in Figure 19.9.

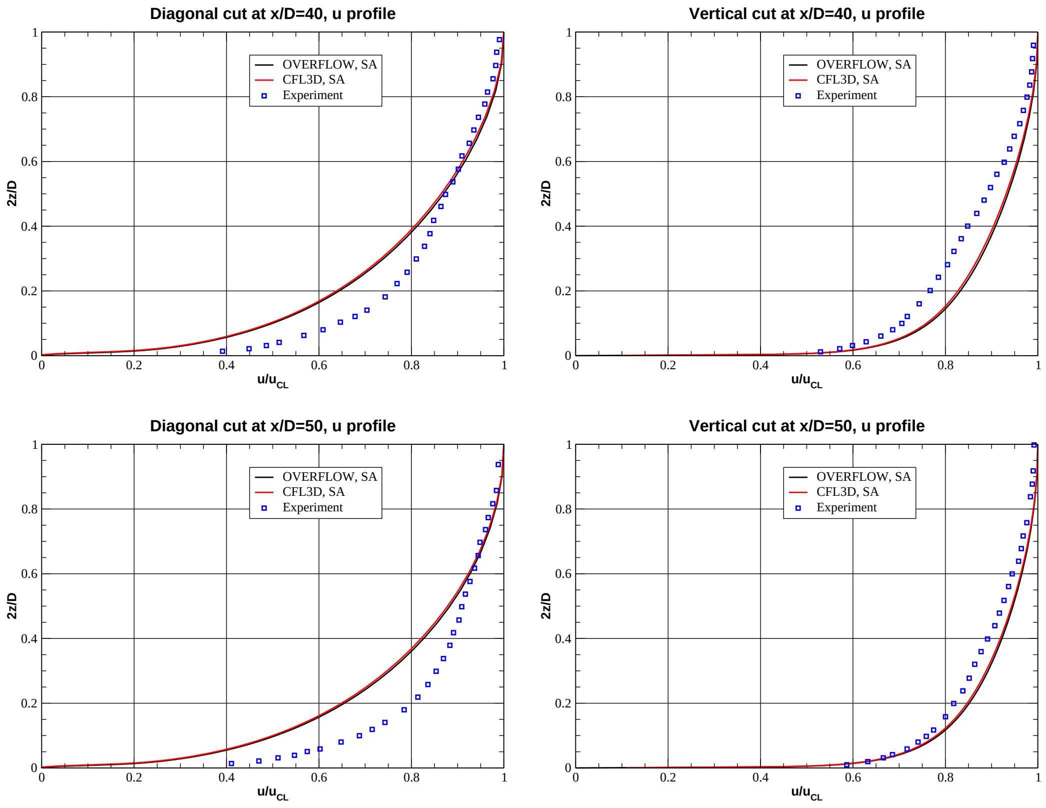

Figure 19.3: Velocity profiles, SA model.

Crossflow velocity is also shown in Figure 19.9. In all cases there is very good agreement between Overflow and Fun3d, and the agreement of Overflow with experiment is better with SA-QCR than with SA. The crossflow velocity plot shows recirculation regions with SA-QCR that did not occur with SA.

The next set of figures, (19.10–19.11), shows results for the SST-QCR model on the second-finest grid, with Overflow using central differencing for the mean flow equations. We define the SST-QCR model as having the same relation to SST as SA-QCR has to SA. The QCR idea does not change the turbulence model, rather it changes the way the eddy viscosity from the turbulence model enters into the viscous terms of the flow equations. Thus the QCR idea can be applied to the SST model.

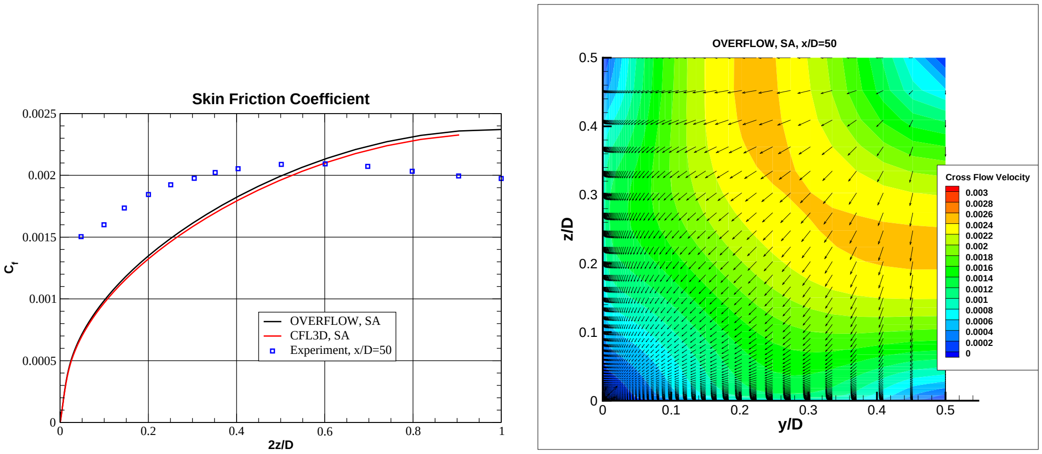

Figure 19.4: Skin friction and crossflow velocity, SA model.

We show velocity profiles along diagonal and vertical cuts at $x/D = 40$ and $x/D = 50$ in Figure 19.10. The comparisons shown here are with Fun3d using the SA-QCR model. The skin friction coefficient along the vertical sidewall at $x/D = 50$ is shown in Figure 19.11, which also shows crossflow velocity.

The next set of figures, (19.12–19.13), shows results for Overflow calculations using the SA-QCR model on the finest grid, with Roe differencing used for the mean flow equations. We show velocity profiles along diagonal and vertical cuts in Figure 19.12. The skin friction coefficient along the vertical sidewall at the plane $x/D = 50$ and crossflow velocity on the same plane are shown in Figure 19.13.

The final set of figures, (19.14–19.15), shows results for Overflow calculations using the SST-QCR model on the finest grid, with Roe differencing used for the mean flow equations. We show velocity profiles along diagonal and vertical cuts in Figure 19.14. The skin friction coefficient along the vertical sidewall at the plane $x/D = 50$ and crossflow velocity on the same plane are shown in Figure 19.15.

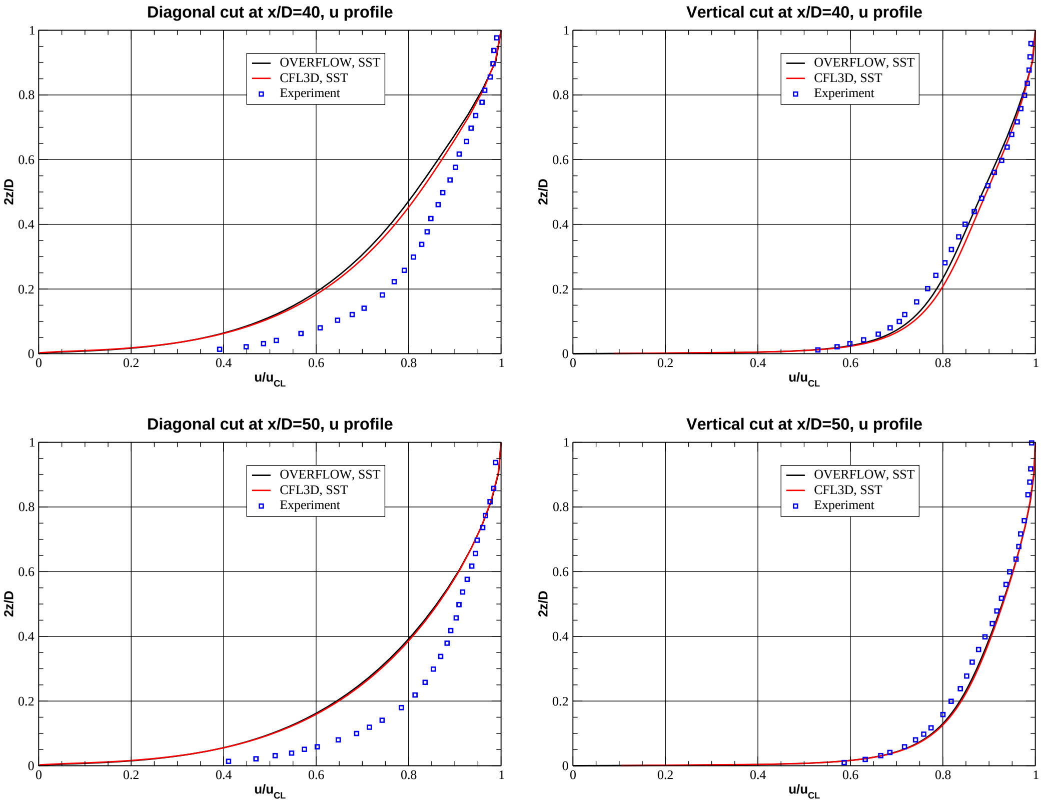
Diagonal cut at x/D=40, u profile

Vertical cut at x/D=40, u profile

Diagonal cut at x/D=50, u profile

Vertical cut at x/D=50, u profile

Figure 19.5: Velocity profiles, SST model.

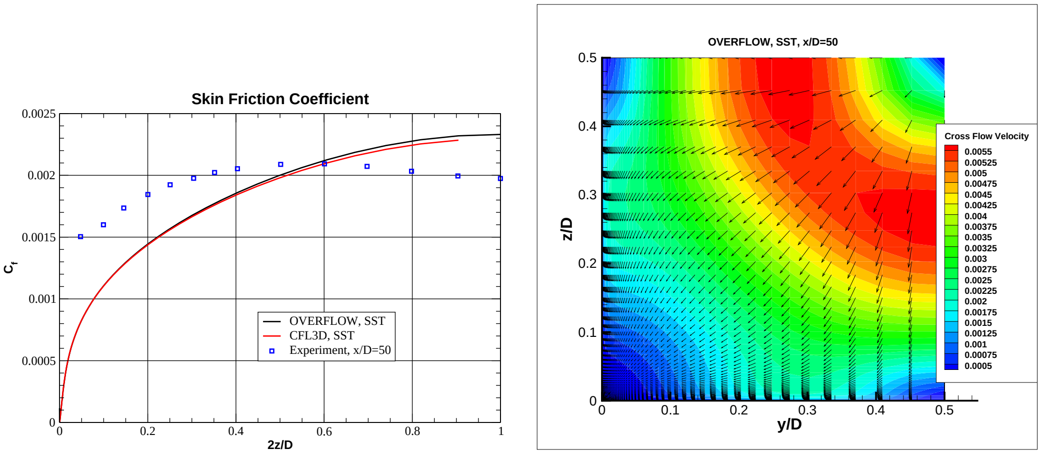

Figure 19.6: Skin friction and crossflow velocity, SST model.

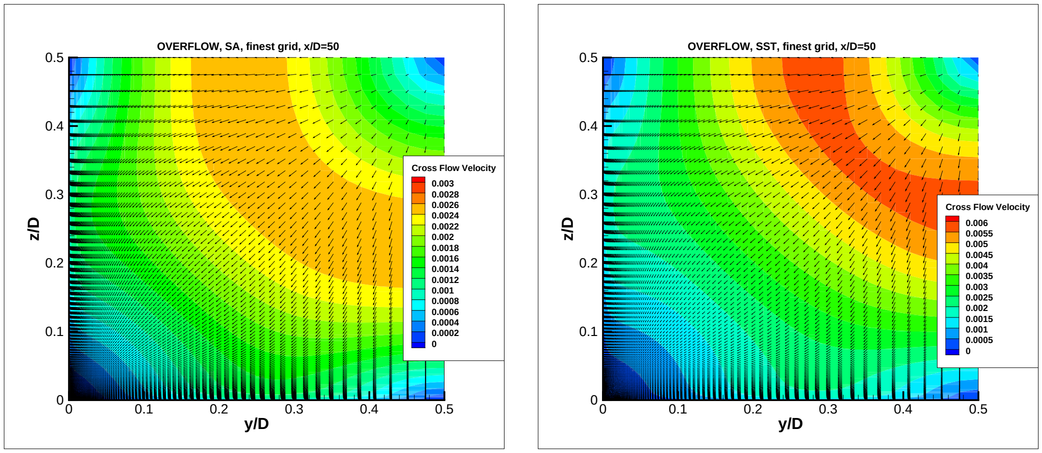

Figure 19.7: Crossflow velocity, finest grid, SA and SST.

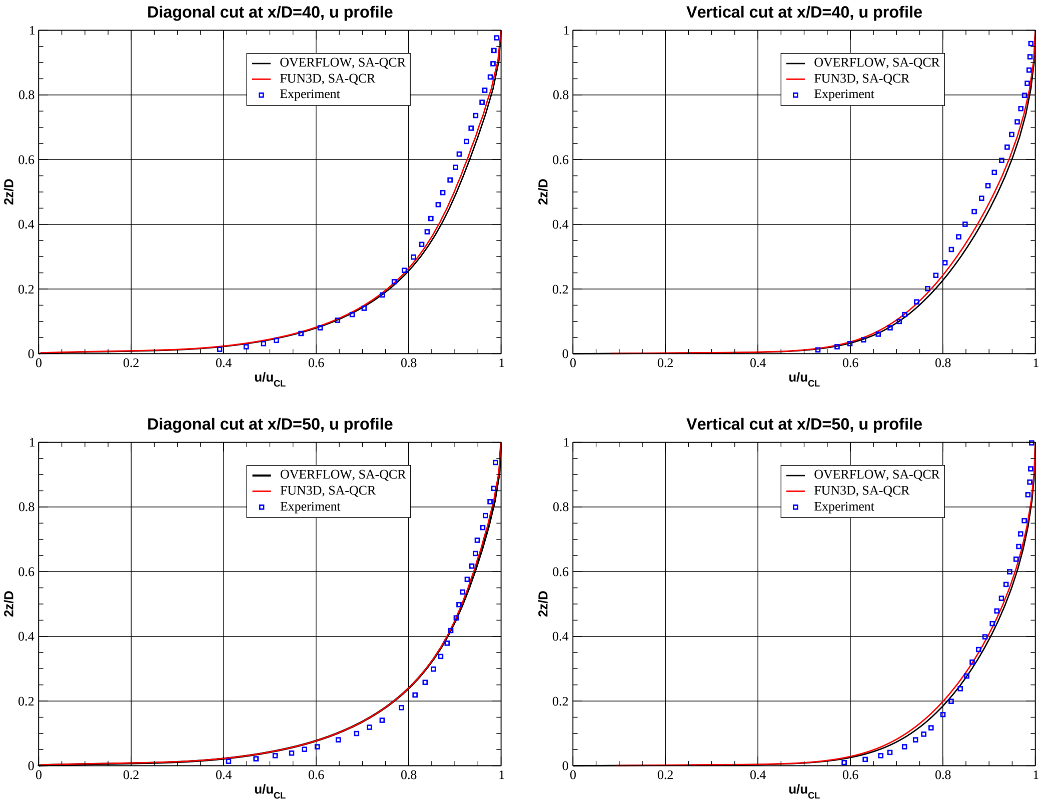

Figure 19.8: Velocity profiles, SA-QCR model.

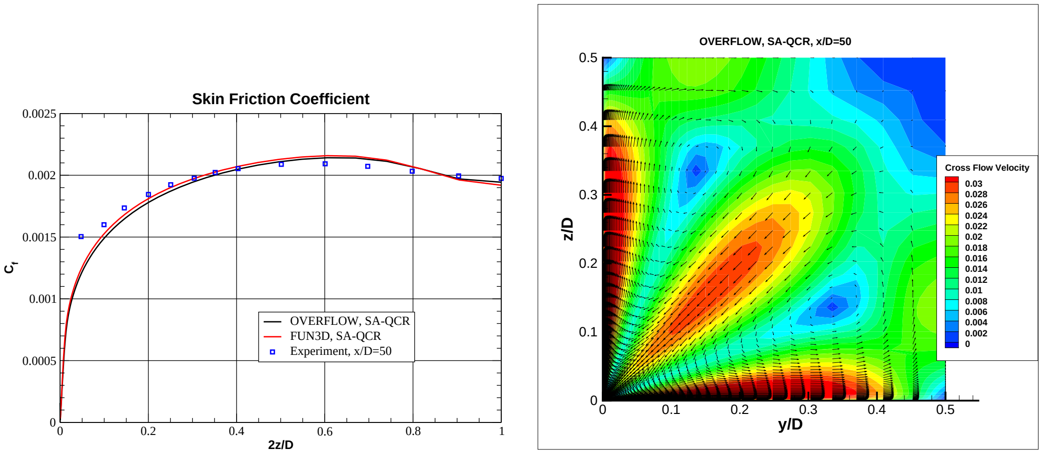

Figure 19.9: Skin friction and crossflow velocity, SA-QCR model.

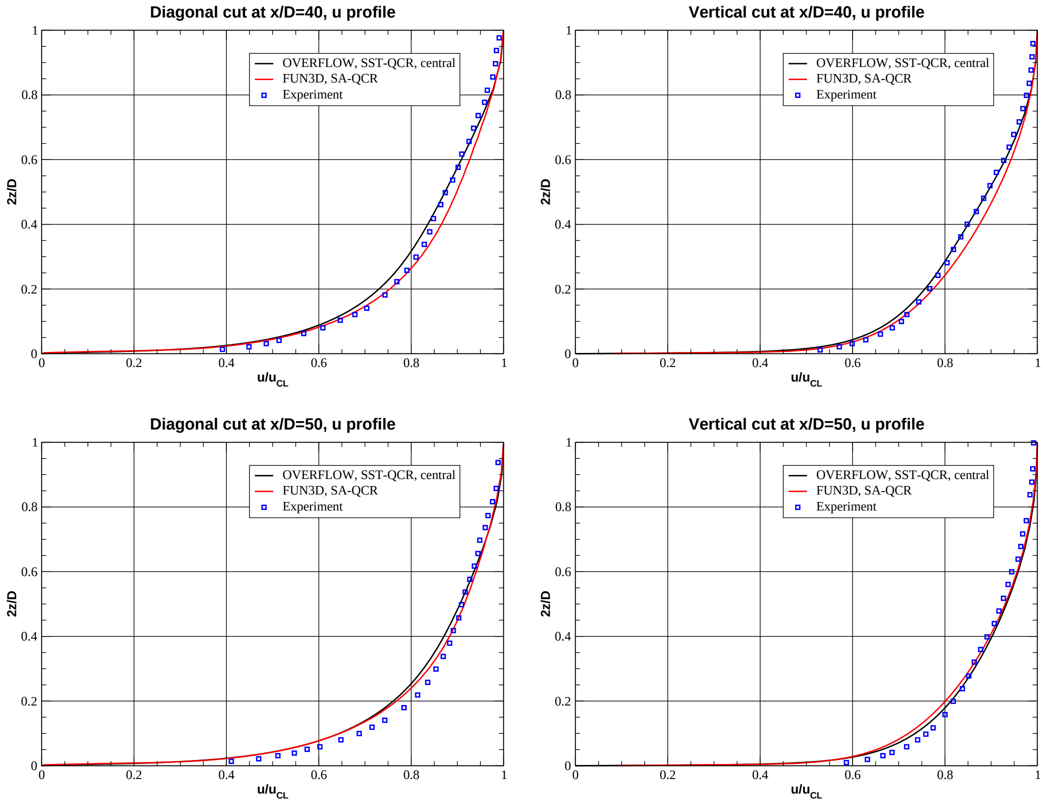

Figure 19.10: Velocity profiles, SST-QCR model.

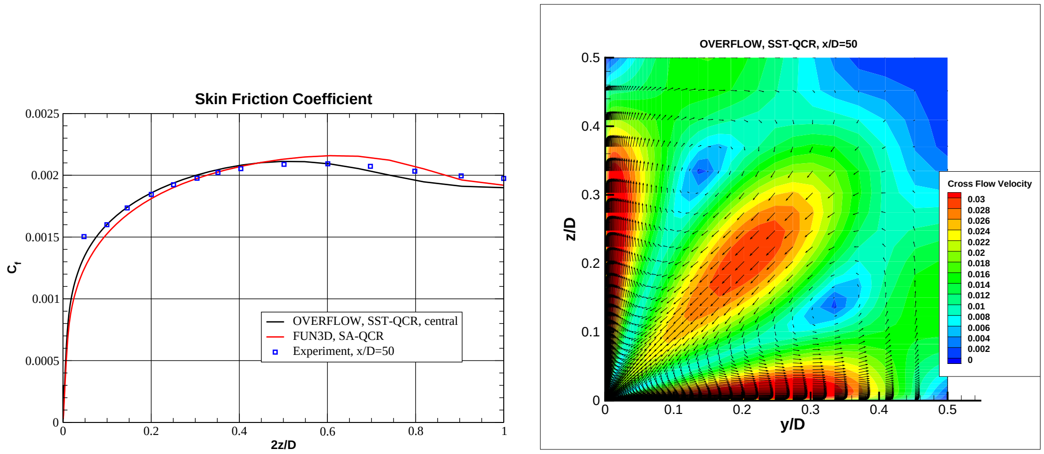

Figure 19.11: Skin friction and crossflow velocity, SST-QCR model.

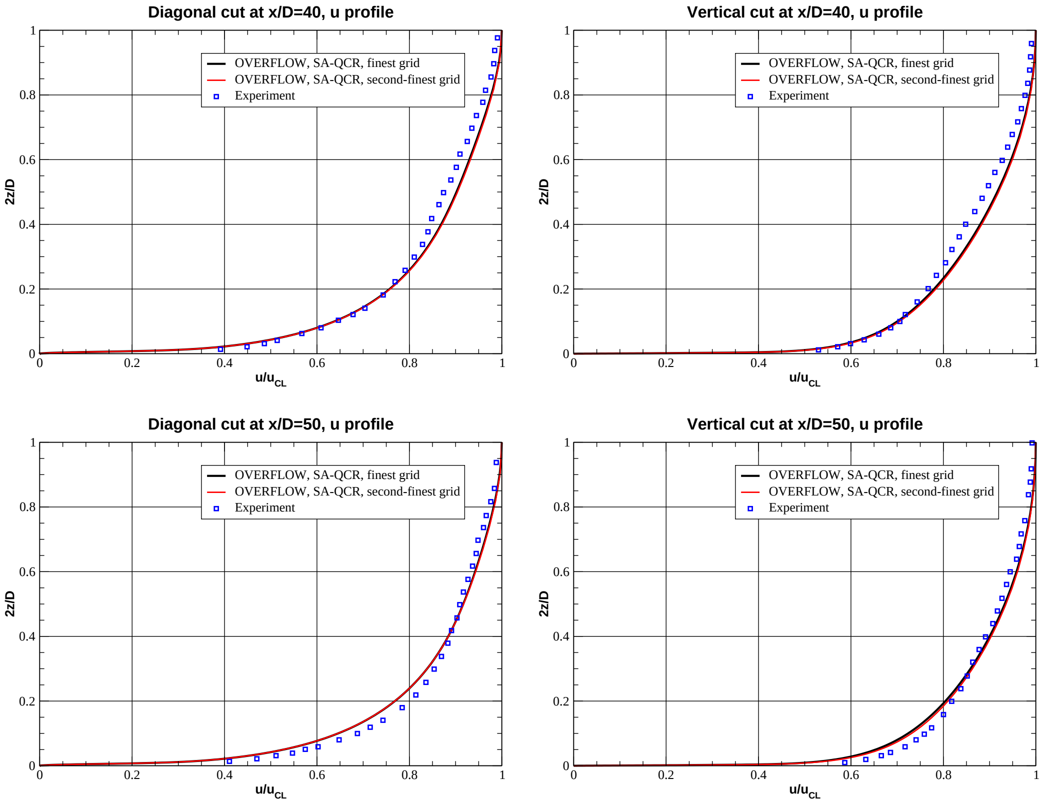

Figure 19.12: Velocity profiles, SA-QCR model, finest grid.

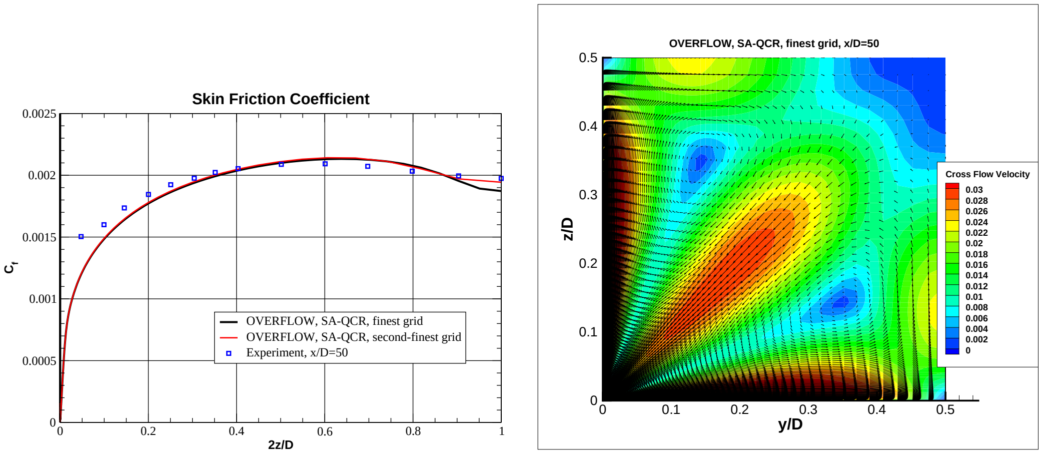

Figure 19.13: Skin friction and crossflow velocity, SA-QCR model, finest grid.

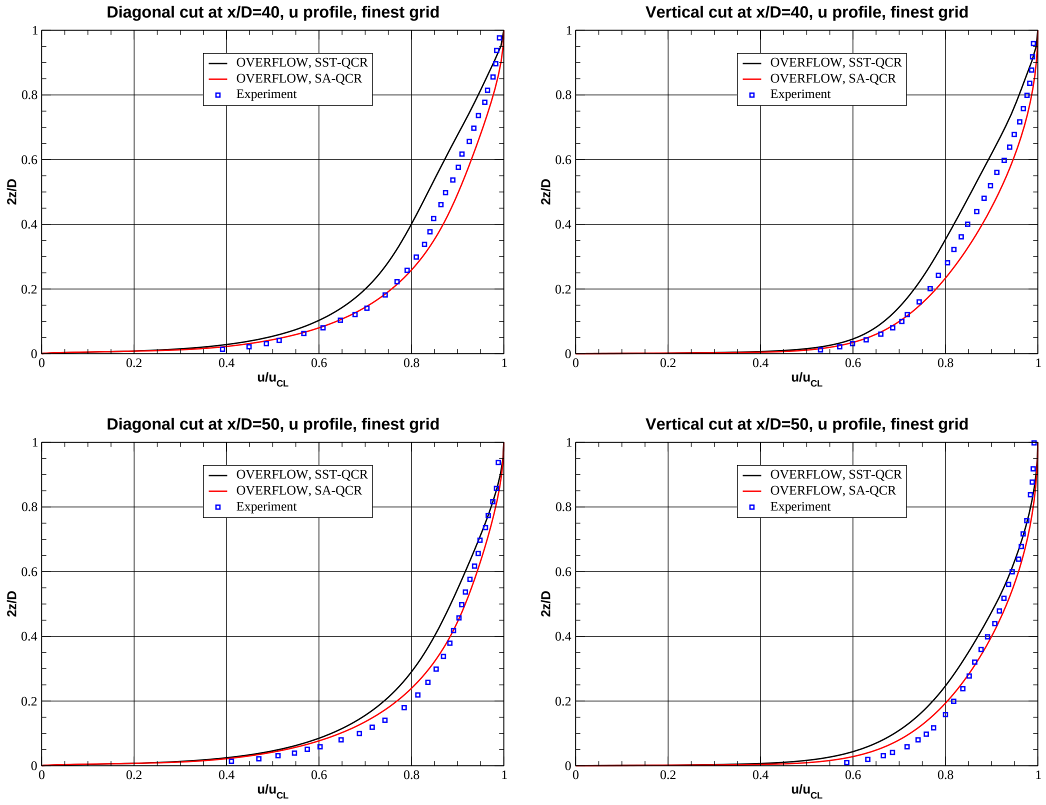

Figure 19.14: Velocity profiles, SST-QCR model, finest grid.

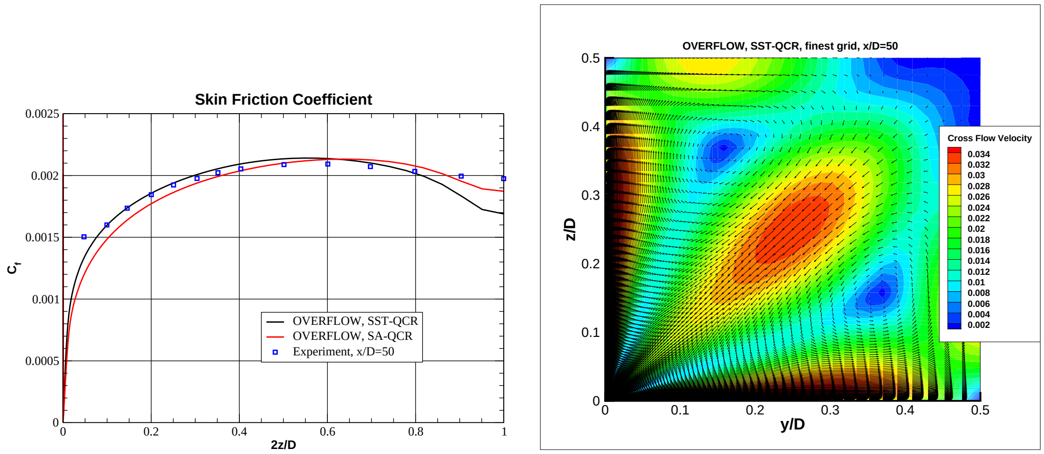

Figure 19.15: Skin friction and crossflow velocity, SST-QCR model, finest grid.

20. Conclusion

We have performed turbulence model validation for the NASA CFD code OVERFLOW on 16 validation test cases from the Langley Turbulence Modeling Resource collection. The results from OVERFLOW compare well with results from CFL3D, FUN3D, or WIND given on the TMR website, and the agreement of OVERFLOW with experiment is generally as good as that of those codes. The information we have presented for each case on grid construction, input parameters, and post-processing may be useful to others who wish to study OVERFLOW applied to these or other validation cases.

References

[1] NASA OVERFLOW CFD code website, http://overflow.larc.nasa.gov.

[2] NASA Langley Turbulence Modeling Resource website, http://turbmodels.larc.nasa.gov.

[3] CFL3D Version 6 website, http://cfl3d.larc.nasa.gov.

[4] FUN3D website, http://fun3d.larc.nasa.gov.

[5] Childs, M. L., Pulliam, T. H., and Jespersen, D. C., "OVERFLOW Turbulence Model Resource Verification Results", NAS Technical Report NAS-2014-03, June 2014, NASA Ames Research Center, Moffett Field, CA, http://www.nas.nasa.gov/publications/reports/2014/2014.html.

[6] "Equations, Tables, and Charts for Compressible Flow", NACA Report 1135, 1953.

[7] Coles, D., "The Law of the Wake in the Turbulent Boundary Layer", *J. Fluid Mech.*, vol. 1, 1956, pp. 191-226.

[8] Coles, D., "The Turbulent Boundary Layer in a Compressible Fluid", RAND Corp. Report R-403-PR, 1962.

[9] WIND CFD code website, http://www.grc.nasa.gov/WWW/wind.

[10] Spalart, P. R., "Strategies for Turbulence Modelling and Simulation", *International Journal of Heat and Fluid Flow* vol. 21, 2000, pp. 252-263.

[11] The Spalart-Allmaras Turbulence Model, http://turbmodels.larc.nasa.gov/spalart.html.

[12] Tramel, R. W., Nichols, R. N., and Buning, P. G., "Addition of Improved Shock-Capturing Schemes to OVERFLOW 2.1", AIAA-2009-3988, June 2009.

[13] Jespersen, D. C., Pulliam, T. H., and Buning, P. G., "Recent Enhancements to OVERFLOW", AIAA-97-0644, Jan. 1997.

[14] Spalart, P., and Allmaras, S., "A One-Equation Turbulence Model for Aerodynamic Flows", AIAA-1992-0439, January 1992.

[15] Nichols, R., "Algorithm and Turbulence Model Requirements for Simulating Vortical Flows", AIAA-2008-0337, January 2008.